Inaugural dissertation

for

obtaining the doctoral degree

of the

Combined Faculty of Mathematics, Engineering and Natural Sciences

of the

Ruprecht - Karls - University

Heidelberg

Presented by

Anusha Gopalan, M.Sc.

born in Srirangam, India

Oral examination on 15.05.2023

Heidelberg, Germany

The role of lipids in development and the control of cellular mechanics

Referees: Dr. Simone Köhler
Prof. Dr. Britta Brügger

Abstract

Lipids universally constitute biological membranes across the tree of life, yet the specific functions of distinct membrane lipid compositions are not clear.

Mammals synthesize thousands of chemically distinct lipids and maintain specialized lipidomes across various tissues. The brain requires specific lipid species to support membrane trafficking and neural function. This calls for a rewiring of the underlying lipid metabolic machinery during development, but when and how this occurs is unclear. To address this, I used mass spectrometry-based lipidomics to trace the establishment of the neural lipidome in both the developing mouse brain and in mouse embryonic stem cells differentiated into neurons *in vitro*. While orchestrated lipidome remodeling was observed across the embryonic and postnatal stages of brain development, neurons differentiated *in vitro* lacked remodeling and did not synthesize canonical neural lipids. Supplementing the cells with metabolic precursors of neural lipids prompted the synthesis of some but not all neural lipids, suggesting that both the availability of exogenous metabolic precursors and cell-intrinsic metabolic processes are limiting factors for the synthesis of neural lipids. Importantly, these results highlight the need to assess cells differentiated *in vitro* from a lipidomic perspective in order to inform differentiation procedures and generate cells that more closely resemble their *in vivo* counterparts.

It has been proposed that the unique lipid compositions of cellular membranes, such as those in neurons, serve to maintain mechanical properties critical to membrane function. In particular, cholesterol and lipid saturation are known to regulate membrane fluidity. As the plasma membrane is mechanically coupled to the active actomyosin cortex through membrane-to-cortex linker proteins, I next investigated how the lipid composition-mediated fluidity of the plasma membrane affects the cortex. To this end, I perturbed cholesterol and lipid saturation in cultured mouse fibroblasts and found that lowering plasma membrane fluidity via either perturbation resulted in increased cortical tension and cell rounding. These findings suggest that membrane fluidity could be a potential regulator of cortical mechanics. Since the actomyosin cortex is a central regulator of cell shape and integrity, these findings highlight the importance of the homeostatic regulation of plasma membrane lipid composition, which constrains membrane fluidity to a narrow, favorable range in cells.

Zusammenfassung

Lipide bilden biologische Membranen in allen Lebensformen, doch die spezifischen Funktionen unterschiedlicher Membranlipidzusammensetzungen sind unklar.

Säugetiere synthetisieren tausende chemisch unterschiedliche Lipide und bewahren spezialisierte Lipidome in verschiedenen Geweben. Das Gehirn benötigt bestimmte Lipidarten, um Membranverkehr und neuronale Funktion zu unterstützen. Dies erfordert ein Umschalten des Lipid-metabolismus während der Gehirnentwicklung, aber wann und wie dies geschieht, ist unklar. Um dies zu untersuchen, habe ich Massenspektrometrie-basierte Lipidomik verwendet, um die Entstehung des neuralen Lipidoms sowohl im sich entwickelnden Mausgehirn als auch in aus embryonalen Stammzellen differenzierten Mausneuronen *in vitro* zu verfolgen. Während des embryonalen und postnatalen Stadiums der Gehirnentwicklung wurde ein eine orchestrierte Umstrukturierung des Lipidoms beobachtet, während *in vitro*-differenzierte Neuronen ihr Lipidom nicht umstrukturierten und keine kanonischen neuronalen Lipide synthetisierten. Eine Ergänzung der Zellen mit Stoffwechselvorläufern neuronaler Lipide löste die Synthese einiger, aber nicht aller neuronalen Lipide aus, was darauf hinweist, dass sowohl die Verfügbarkeit von exogenen Stoffwechselvorläufern als auch zell-intrinsische Stoffwechselprozesse die Synthese neuronaler Lipide begrenzen. Diese Ergebnisse betonen die Notwendigkeit, *in vitro*-differenzierte Zellen aus einer lipidomischen Perspektive zu bewerten, um Differenzierungsverfahren zu verbessern und Zellen zu generieren, die ihren *in vivo*-Gegenstücken ähnlicher sind.

Es wird angenommen, dass die komplexe Lipidzusammensetzung von Zellmembranen dazu dient, mechanische Eigenschaften aufrechtzuerhalten, die für die Membranfunktion entscheidend sind. Insbesondere Cholesterin und Lipidsättigung regulieren die Membranfluidität. Da die Plasmamembran über Membran-zu-Cortex-Linker-Proteine mechanisch mit dem aktiven Aktomyosin-Cortex gekoppelt ist, habe ich untersucht, wie die durch die Lipidzusammensetzung vermittelte Fluidität der Plasmamembran den Cortex beeinflusst. Zu diesem Zweck störte ich Cholesterin und Lipidsättigung in kultivierten Mausfibroblasten und stellte fest, dass eine Absenkung der Plasmamembranfluidität durch beide Störungen zu einer erhöhten kortikalen Spannung und Zellabrundung führte. Diese Ergebnisse legen nahe, dass die Membranfluidität ein potenzieller Regulator der kortikalen Mechanik sein könnte. Da der Aktomyosin-Cortex ein zentraler Regulator der Zellform und -integrität ist, betonen diese Ergebnisse die Bedeutung der homöostatischen Regulation der Lipidzusammensetzung.

Acknowledgements

A number of people are responsible for making the work described in this thesis possible. I'd like to take this opportunity to express my gratitude to everyone who touched my life in big, small and unquantifiable ways over the last few years.

Firstly, I'd like to thank my advisor, Dr. Alba Diz-Muñoz for giving me the opportunity to work in her lab, for the resources that made this work possible, and for all her input and feedback. I'd also like to thank Dr. Christer Ejsing for opening the doors of his lab and lipidomics to me.

Thanks to my TAC members, Prof. Dr. Britta Brügger, Dr. Pierre Neveu, Dr. Simone Köhler and Dr. Kyung-Min Noh for valuable discussions and suggestions.

I'm indebted to my colleagues for great discussions and fun times, both in the lab and outside, and for sharing their time and knowledge with me. In particular, to Lisa for teaching me how to culture cells; to Martin for the AFM training and the endless troubleshooting that came with all of my AFM experiments; To Richard for all the hours spent in the cold room, at the mass spectrometer and in analysing lipidomics data during my visits to Odense; To Sergio, Ewa and Léanne for help in the lab in all shapes and forms; To Alex, Manuel and Stefan at the ALMF for teaching me all I know about microscopes; And to Srishti for taking me on board in her explorations of the actomyosin cortex.

Much of the work presented here is a result of the collaborations that tend to blossom so well at EMBL. In particular, Emilia, Juan and Vikram performed the mouse brain dissections, and Lisa and Nadine performed neuronal differentiation of mESCs; Their combined efforts allowed me to generate and analyze some very interesting data, which would not have been possible otherwise. Per, Henrik and Frank performed all the proteomics experiments and Richard generously performed lipidomics experiments for me when I could not travel to Odense. Ewa and Diana helped me generate and sort GFP-CAAX-expressing cells. Jia kindly helped me write the Zusammenfassung for this thesis. I'd like to thank each of these individuals for their invaluable contributions.

I'm also very grateful to everyone who gave me the opportunity to contribute to their exciting projects. My discussions with Srishti, Maria, Annamarie and Julio were always scientifically enriching and gave me a glance into the fascinating worlds of *in vitro* reconstitutions and simulations. For this, I thank them profusely.

I would also like to extend my gratitude to the members of the Prevedel lab over the years for being wonderful neighbours to us and for the many fun coffee breaks I spent in their office. It was my great pleasure to work alongside Fan, whose boundless patience and persistence are most inspiring.

The best week of my PhD was without a doubt spent in the Physical Biology of the Cell course, which can only be described as life-changing. Many thanks to Rob Phillips and Jane Kondev for the endless inspiration.

My acknowledgements would be incomplete if I weren't to mention my immensely supportive friends who helped me enjoy life despite the overwhelming difficulties that I faced in my PhD. Thank you, Michelle, for being a pea in my pod, through and through, and for offering the best advice in every situation. Mukthi, thank you for the much-needed coffee breaks, all the reassurance and the pep talks. Ewa and Kuba, some of my best memories from my time in Heidelberg are of the evenings spent in your company and I miss you both very much. Dorothy, I have and will always look forward to our dinner dates. Sid, your company, humour and gossip are sorely missed. Barbara, Mario and Anna, you have been like family to me in the last few years and my home away from home. I'm so lucky and grateful to have gotten to know all of you.

Lastly, I'd like to thank my family for their unconditional love and support. Thank you for keeping me close despite the geographical distance, and for believing that I am capable of so much more than I often think. Appa, Amma, Varsha and Srihari, you inspire me in so many ways. Thanks to both my wonderful Paattis for being such strong women and for bringing music into all our lives. And Yashas, you are a real superhero, for turning Nunu's every frown upside down since 2021.

And thank you, Keerthan, for being a great partner and my biggest cheerleader. I would not have made it this far if it weren't for your unwavering support and encouragement.

To my parents,
Gopu and Indu.

Contents

List of Figures

List of Tables

List of Abbreviations

AA	Arachidonic Acid
ACar	Acyl Carnitine
ACSL	Fatty Acyl-Coenzyme A Synthetase
AF	Ammonium Formate
AFM	Atomic Force Microscope
AGPAT	Acylglycerolphosphate Acyltransferase
ANOVA	Analysis of Variance
BAEC	Bovine Aortic Endothelial Cell
BCA	Bicinchoninic Acid
β-ME	β-Mercaptoethanol
BSA	Bovine Serum Albumin
CC	Cellular Component
CE	Cholesterol Ester
Cer	Ceramide
CerS	Ceramide Synthase
CL	Cardiolipin
DAG	Diacylglycerol
DAPI	4′,6-Diamidino-2-Phenylindole
DB	Double Bond
DBF	Double Bond Fragment
del FBS	delipidated Fetal Bovine Serum
DGAT	Diacylglycerol Acyltransferase
DHA	Docosahexaenoic Acid
DMEM	Dulbecco′s Modified Eagle Medium
DMPC	Dimyristoylphosphatidylcholine
DMSO	Dimethyl Sulfoxide
DOPC	Dioleoylphosphatidylcholine
DOPS	Dioleoylphosphatidylserine
DPPC	Dipalmitoylphosphatidylcholine
ECL	Enhanced Chemiluminescence
EDTA	Ethylenediaminetetraacetic acid

EGFP	Enhanced Green Fluorescent Protein
EGTA	Ethylene Glycol-bis(β-aminoethyl ether)-N,N,N′,N′-Tetraacetic Acid
EPA	Eicosapentaenoic Acid
ER	Endoplasmic Reticulum
ERM	Ezrin-Radixin-Moesin
FA	Fatty Acid
FACS	Fluorescence-Activated Cell Sorting
FABP	Fatty Acid Binding Protein
FBS	Fetal Bovine Serum
FDFT1	Farnesyl-Diphosphate Farnesyltransferase 1
FRAP	Fluorescence Recovery After Photobleaching
FTMS	Fourier Transform Mass Spectrometry
GAPDH	Glyceraldehyde-3-Phosphate Dehydrogenase
GFP	Green Fluorescent Protein
GL	Glycerolipid
GO	Gene Ontology
GPAT	Glycerol-3-Phosphate Acyltransferase
GPL	Glycerophospholipid
HCD	High-energy C-trap Dissociation
HEK	Human Embryonic Kidney
HEPES	4-(2-hydroxyethyl)-1-piperazineethanesulfonic acid
HexCer	Hexosylceramide
HIV	Human Immunodeficiency Virus
HRP	Horseradish Peroxidase
IACUC	Institutional Animal Care and Use Committee
IS	Internal Standard
LatA	Latrunculin A
LCF	Lipid Class Fragment
LCMS	Liquid Chromatography Mass Spectrometry
LIF	Leukemia Inhibitory Factor
LPA	Lysophosphatidic Acid
LPC	Lysophosphatidylcholine
LPE	Lysophosphatidylethanolamine
LPI	Lysophosphatidylinositol
LPS	Lysophosphatidylserine
MβCD	Methyl β-Cyclodextrin
MCA	Membrane-to-Cortex Attachment
MD	Molecular Dynamics

MEF	Mouse Embryonic Fibroblast
MES	2-(N-morpholino)ethanesulfonic acid
mESC	mouse Embryonic Stem Cell
MLF	Molecular Lipid Fragment
MLS	Molecular Lipid Species
MOPS	3-(N-Morpholino) Propanesulfonic Acid
MS	Mass Spectrometry
NEAA	Non-Essential Amino Acid
NEFA	Non-Esterified Fatty Acid
NSI	Nanoelectrospray Ionization
OBL	Olympus Biolever
OLS	Optical Light Sensitivity
PA	Phosphatidic Acid
PAGE	Polyacrylamide Gel Electrophoresis
PAP	Phosphatidic Acid Phosphohydrolase
PBS	Phosphate-Buffered Saline
PC	Phosphatidylcholine
PC1, PC2	Principal Component 1,2
PCR	Polymerase Chain Reaction
PDL	Poly-D-Lysine
PDMS	Polydimethylsiloxane
PE	Phosphatidylethanolamine
PG	Phosphatidylglycerol
PI	Phosphatidylinositol
PIP	Phosphatidylinositol phosphate
PIP2	Phosphatidylinositol bisphosphate
PIP3	Phosphatidylinositol trisphosphate
PL	Phospholipid
PLL-PEG	Poly L-lysine - Polyethylene glycol
PM	Plasma Membrane
POPC	Palmitoyloleoylphosphatidylcholine
POPS	Palmitoyloleoylphosphatidylserine
PS	Phosphatidylserine
PUFA	Polyunsaturated Fatty Acid
PVDF	Polyvinylidene Difluoride
RIPA	Radio Immunoprecipitation Assay
rpm	rotations per minute
SA	Stearic Acid

SCAP	SREBP Cleavage Activation Protein
SCD	Stearoyl Coenzyme A Desaturase
SDS	Sodium Dodecyl Sulfate
SHexCer	Sulfated Hexosylceramide
SL	Sphingolipid
SM	Sphingomyelin
SOPC	Stearoylloleoylphosphatidylcholine
SPTLC1	Serine Palmitoyl Transferase Long Chain Base Subunit 1
TAG	Triacylglycerol
TBS	Tris-Buffered Saline
TBST	Tris-Buffered Saline - Tween
TC	Tissue Culture
TMT	Tandem Mass Tag
TxR	Texas Red
WASP	Wiskott–Aldrich syndrome protein
WCL	Whole Cell Lysate

Chapter 1

Introduction

Compartmentalization is ubiquitous in biology. Robert Hooke is famously known to have coined the term 'cell' when peering through his microscope into the compartmentalized structure of cork in 1665 [1]. Careful examination of plant and animal tissues under the microscope in the 19th century confirmed the notion that cells make up all living matter, and ultimately lead to the formulation of the cell theory, two centuries after cells had first been observed [2].

Closely linked to the cell theory is the idea that the cell boundary must allow the selective transport of material. Jean-Antoine Nollet had already discovered the phenomenon of osmosis in pig bladders in 1748, which had subsequently been observed in living plant cells by René Dutrochet in 1828 [3]. Hence, it was conceived that cells must be bound by a *semi-permeable membrane*.

Incidentally, the idea that the cell membrane could be made of a *thin oil film* was born here in Heidelberg, when Georg Quincke attempted to explain the movement of amoeba using physical laws in 1888 and noted their similarity to oil droplets in an oil-water emulsion [4, 5]. Although unpopular at the time it was proposed, evidence for this theory soon followed at the turn of the century. The pharmacologist Hans Meyer discovered that the potency of an anesthetic could be predicted by its partition coefficient between oil and water [6]. In the meantime, Ernest Overton had independently examined the permeability of plant and animal cells to over 500 chemical compounds and found the same dependence on partition coefficient [7, 8]. It was hence proposed that cell membranes were composed of lipids.

It is now known that lipid membranes are an essential feature of all organisms across the tree of life. It is also widely thought that the emergence of molecules capable of spontaneously self-organizing into membranes was a key event in the early evolution of life [9–11].

The unique molecular properties of lipids endow biological membranes with unique material properties [12, 13]. Our everyday encounters with the natural world provide us with little intuition for how a two-dimensional fluid would behave. In the following sections, I will discuss the key features of this unusual material and the molecules that constitute it.

1.1 The study of lipids

Historically, the term lipid has been used to refer to a chemically diverse group of biomolecules characterized by their solubility in nonpolar solvents and their strong hydrophobicity, such as oils, waxes, and oil-soluble vitamins. A more precise definition has been proposed based on the chemical motifs present in the molecules, rather than on solubility. Based on this proposal, lipids can be defined as "hydrophobic or amphipathic[1] small molecules that may originate entirely or in part by carbanion-based condensations of esters (e.g., fatty acyls) and/or by carbocation-based condensation of isoprene units (e.g., sterols)" [14].

Lipids are one of the four kinds of molecular building blocks of cells, along with nucleic acids, amino acids, and monosaccharides. In contrast to the other building blocks, lipids do not have a molecular design that allows them to form larger polymers analogous to DNA, RNA, proteins, or polysaccharides. However, they can spontaneously self-organize into much larger structures that can span the surface of entire cells in an aqueous medium, as we will discuss later.

1.1.1 Lipid diversity

Contrary to amino acids, nucleic acids, and monosaccharides, lipid molecules come in a lot more flavors, with the average mammalian cell containing $\sim 10^4$ distinct lipid species [15]. It is therefore useful to classify them on the basis of their chemical constitution, and to use standard nomenclature that reflects their molecular features [16, 17].

Most lipids contain a head group and one or more fatty acyl chains. Based on the chemical backbone and head group, each lipid can be assigned to a lipid class. The defining chemical motifs of the major lipid classes in mammals are shown in Fig.1.1, which is also intended to serve as a reference chart for the lipids that appear throughout this thesis.

---

[1] A molecule having both hydrophobic and hydrophilic parts is termed amphipathic.

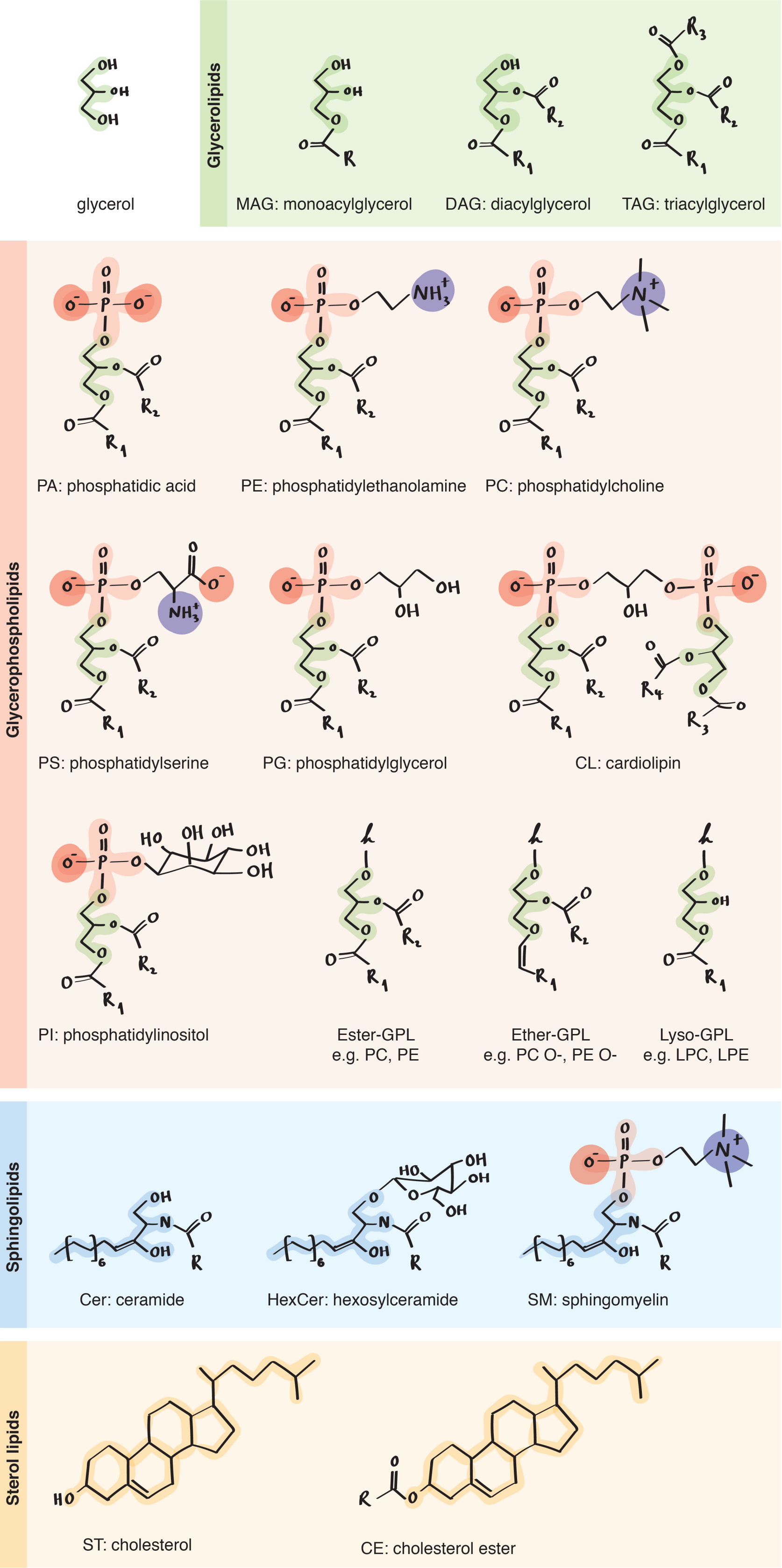

Figure 1.1: Major lipid classes in mammalian cells. *Contd.*

Figure 1.1: *Contd.* Structures of the chemical backbones of various lipid classes are shown. The glycerol backbone, highlighted in green is a common feature across glycerolipids and glycerophospholipids. The phosphate group common to all glycerophospholipids is highlighted in pink. Red and dark blue circles denote negatively and positively charged groups, respectively. The sphingosine and cholesterol backbone are shown in light blue and yellow, respectively. *R* is used to denote acyl chains and *h* is used to denote the headgroup.

The above lipid classes can be grouped into the following categories based on their chemical composition [18]:

- ***Glycerolipids.*** Glycerolipids are neutral lipids derived by the condensation reaction of one or more hydroxyl groups with fatty acids. Of these, DAGs are an important reaction intermediate to the formation of both TAGs and glycerophospholipids. TAGs are the major constituents of lipid droplets and serve as storage lipids that can be broken down for the release of energy when required by the cell.
- ***Glycerophospholipids (GPLs).*** GPLs, like glycerolipids, contain a glycerol backbone and additionally contain a phosphate headgroup, making them hydrophilic at one end and therefore suitable for constituting membranes. GPLs are the major constituents of biological membranes across the tree of life. The presence of phosphate lends a negative charge to most GPLs (e.g. PA, PG, CL, PI), whereas some others exist in zwitterionic form through the presence of an additional positively charged motif in their headgroup, making them effectively neutral (e.g. PE and PC). The inositol headgroup in PI provides several positions for phosphorylation, making it an important signaling molecule that can exist unphosphorylated or in the form of PIP (PI 4-phosphate), PIP2 (PI 4,5-bisphosphate), or PIP3 (PI 3,4,5-trisphosphate), respectively. These phosphorylated PIPs are strongly anionic and known to bind several proteins depending on their phosphorylation state.

  While most GPLs contain two fatty acyl chains, cardiolipin, present predominantly in the inner mitochondrial membrane, has four. Further, the acyl chains of GPLs may be connected to the glycerol backbone via an ester bond as in most GPLs, or an ether bond in the sn-1 position, which is the case for the ether lipid classes PC O- and PE O-. Each GPL class also has an associated lysolipid class where one of the two fatty acyl chains is hydrolyzed, leaving just one chain in place.

- ***Sphingolipids.*** Sphingolipids are made of a sphingoid base backbone with an acyl chain substitution. Fig. 1.1 shows examples with one of several possible bases. As we will discuss in chapter 2, sphingolipids are highly enriched in the brain and its constituent cells.

  As shown for HexCer, sugars and long chains thereof can constitute head groups for sphingolipids, yielding cerebrosides (HexCers) and gangliosides, respectively. These are collectively termed glycosphingolipids and are known to be present at the outer surface of the plasma membrane where they are involved in cell recognition and signaling.

  Sphingolipid metabolites such as sphingosine-1-phosphate are known to act as signaling molecules participating in a number of cellular processes such as apoptosis, proliferation, stress responses, inflammation, senescence, and differentiation [19–21].

- ***Sterol lipids.*** Sterol lipids are a unique lipid category where the backbone is constituted by cholesterol in mammalian cells. Condensation of the hydroxyl group in cholesterol with a fatty acid results in the formation of cholesterol esters, which are present in lipid droplets along with TAGs. Cholesterol is an essential component of all mammalian cell membranes, and we will look very closely at this molecule and its effect on the bulk properties of membranes in chapter 3.

The nomenclature used for individual lipids depends on the structural information available and usually conveys all available information on the structure of the lipid at hand. Consider the lipid shown in Fig.1.2. The name assigned to this molecule would be PC 16:0/18:1(9Z), indicating that it is a phosphatidylcholine (PC) with a fatty acyl chain in the sn-1 position of the glycerol backbone that is 16 carbon atoms long with no double bonds (16:0), and with a fatty acyl chain in the sn-2 position that is 18 carbon atoms long with 1 double bond on the 9th carbon atom (18:1(9Z)). However, we may not necessarily have access to all this structural information, depending on the methods used for analyzing the lipid at hand. As we will see in the next section, in such cases, the lipid name reflects only the available information.

1.1.2 Mass spectrometry-based lipidomics

The large-scale quantification of all lipids in a sample is termed lipidomics, analogous to genomics and proteomics, where the *lipidome* refers to the repertoire of all lipids in a cell or tissue, analogous to the genome and proteome.

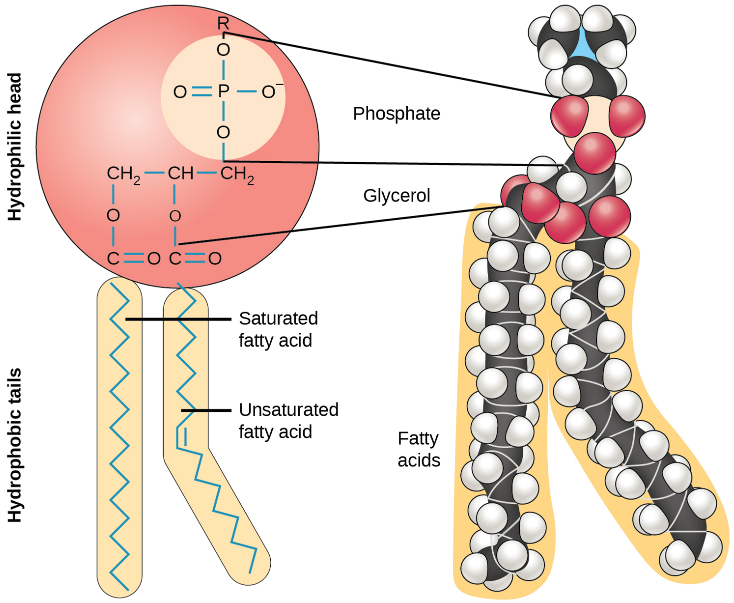

Figure 1.2: Structure of the representative membrane phospholipid PC 6:0/18:1(9Z). The structural formula (left) and space-filling atomic model (right) of phosphatidylcholine (PC) 16:0/18:1(9Z), showing the hydrophobic acyl chains and hydrophilic head group. Notice the kink produced by the double bond in *cis* configuration in the sn-2 acyl chain. Image from [22].

Together, the -omics methods enable a quantitative data-driven systems-level view of living systems.

Advances in mass spectrometry allowing the analysis of lipid extracts from biological samples are largely responsible for making the study of entire lipidomes possible [23]. Mass spectrometry relies on the interactions of charged particles with electromagnetic fields. To illustrate the basic principle, let us consider a simple design for a mass spectrometer as shown in Fig. 1.3.

Consider an unknown mixture of molecules whose composition we are interested in. Let us start by ionizing the molecular components of this mixture. Recall that the force acting on a particle carrying a charge q and moving with velocity $\vec{v}$ is described by

$$\vec{F} = m\vec{a} = q(\vec{E} + \vec{v} \times \vec{B}) \tag{1.1}$$

where m is the mass of the particle, $\vec{a}$ is its acceleration, and $\vec{E}$ and $\vec{B}$ are electric and magnetic fields, respectively.

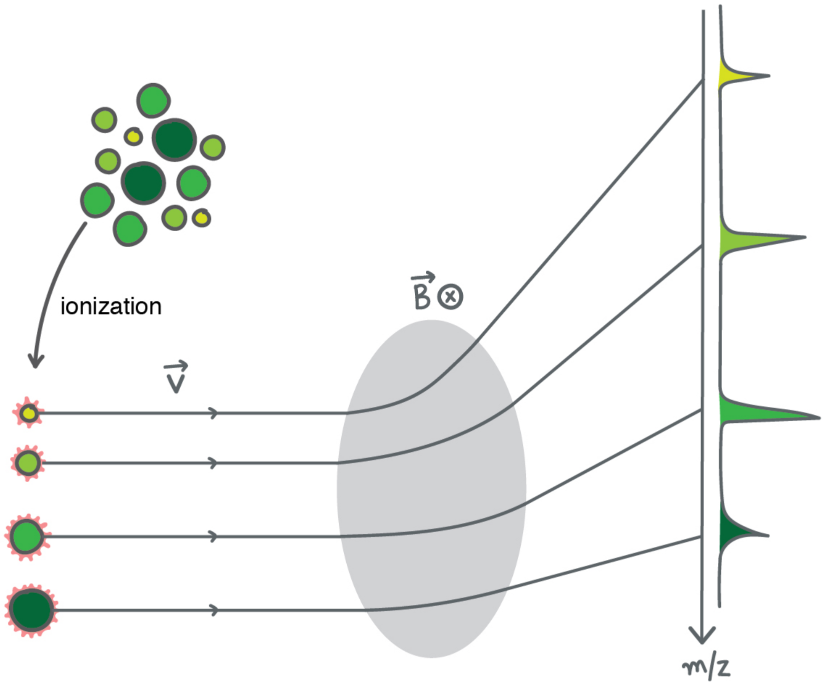

Figure 1.3: The principle behind mass spectrometry. A mixture of unknown molecules can be analyzed by mass spectrometry if they are first converted to ions. The ions are then accelerated to the velocity $\vec{v}$ and allowed to pass through a uniform magnetic field, $\vec{B}$ (grey ellipse) perpendicular to the plane of the page. The particles experience an acceleration perpendicular to their direction of motion and inversely proportional to their mass-to-charge ratio, m/z, and detecting the ion flux for each m/z value reflects their concentrations in the mixture.

The above equation tells us that the application of an electric field $\vec{E}$ produces a force along the field and can be used to accelerate the ionized particles. Once the particles are accelerated to a uniform velocity v, the application of a perpendicular magnetic field $\vec{B}$ can be used to produce an acceleration perpendicular to both $\vec{v}$ and $\vec{B}$. Due to this centripetal acceleration, the particles traverse a circular path within the magnetic field, whose radius is obtained by equating the strength of the centripetal force to that of the force due to the magnetic field above.

$$F = \frac{mv^2}{r} = qvB \tag{1.2}$$

yielding

$$r = \frac{mv}{qB} \tag{1.3}$$

Note that v and B are constant for all the ions in the mixture, meaning that r is directly proportional to m/q. Expressed in units of mass per unit charge of an electron, this is the m/z. Hence, once the ionic flux can be separated in this manner according to m/z, the relative abundances can be determined.

While modern mass spectrometers may not use the same scheme with static electric and magnetic fields to separate the ions by m/z, the basic principle is the same. The use of Fourier transform mass spectrometry in particular is advantageous to obtain sub-ppm resolutions along m/z. This is important for distinguishing signatures from a mixture of a large number of lipids that overlap closely in m/z.

By compiling a database of the m/z values of ions of purified lipids (e.g. ALEX123, [24]), one can match the peaks obtained in m/z spectra of unknown samples to identify the lipids they originate from. The peak height is then used to determine relative abundance. However, this must be done with caution, as different lipids have different propensities for ionization. One strategy to account for these differences is to use internal standards with similar ionization characteristics at known concentrations and normalize all peak intensities to the respective internal standard (See section 4.4.3 for a detailed discussion).

While assigning lipids to m/z spectra, it is important to reckon with the question of isomers, where chemically distinct lipids could give rise to peaks at the exact same m/z. Consider our example lipid from the previous section (Fig. 1.2), PC 16:0/18:1. A different lipid, PC 16:1/18:0 would have the exact same molecular weight as PC 16:0/18:1. If only the m/z is available, then we cannot distinguish between these two lipids and use the nomenclature of sum composition, i.e., the peak is assigned to the lipid PC 34:1, where the identity of the individual acyl chains is not known.

Fragmentation of the ions and analysis of the m/z spectrum of ion fragments (termed MS^2 spectra) can resolve the above isomeric lipids. Fragment ions provide additional information on the headgroup and individual acyl chains, as shown in Fig. 1.4. Depending on the information provided by each fragment ion, they are annotated as lipid class fragments (LCFs), molecular lipid fragments (MLFs) or double bond fragments (DBFs). As per the nomenclature used here [25], the acyl chains are separated by a '/' when the positions of the acyl chains on the lipid backbone are known (e.g., sn-1, sn-2), and a '-' is used in its place when the positions of the acyl chains are not known.

In this thesis, I have extensively used the MS^{ALL} approach that combines MS^1, MS^2 and an MS^x mode specially developed for the detection and quantification of cholesterol (See 4.4 for a detailed description of the methods) [26].

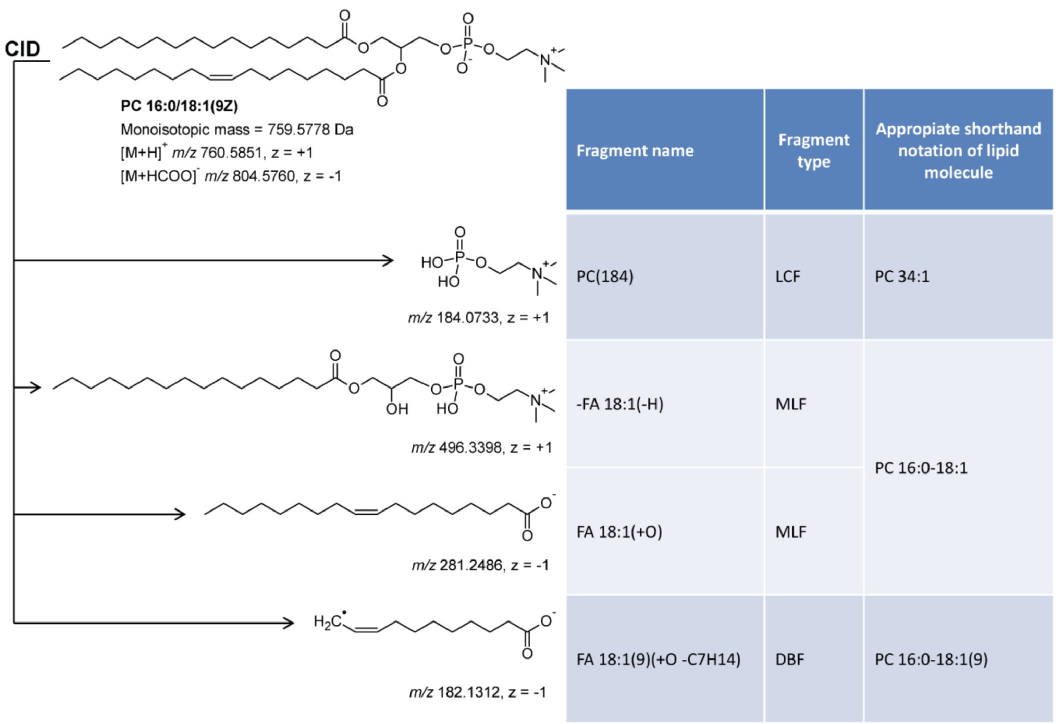

Fragment name	Fragment type	Appropiate shorthand notation of lipid molecule
PC(184)	LCF	PC 34:1
-FA 18:1(-H)	MLF	PC 16:0-18:1
FA 18:1(+O)	MLF	
FA 18:1(9)(+O -C7H14)	DBF	PC 16:0-18:1(9)

Figure 1.4: An example of lipid ion fragmentation. MS^2 spectra of fragment ions can provide structural information and help distinguish isomeric lipids. Image from Pauling *et al*, 2017 [25].

1.2 Biological membranes

Lipids are known for their characteristic hydrophobicity due to the presence of one or more long hydrocarbon chains. Since hydrocarbon chains do not have a polarized distribution of charges, their insertion into an aqueous environment is disruptive to the solvent hydrogen-bond network. This suggests that lipid molecules should have a tendency to aggregate and minimize their interface with water. What then causes the arrangement of lipid molecules into the vast membranous structures so ubiquitous in biology?

Hydrophobicity alone is insufficient to explain the assembly of lipids into membranes. It is only *amphipathic* lipids containing a hydrophilic head in addition to the long hydrophobic tail that are capable of this feat. The spontaneous organization of amphipathic lipids into a bilayer allows for the interaction of polar head groups with the solvent and the 'burying away' of hydrophobic chains into a solvent-free zone in the middle. A closer look at Fig. 1.1 reveals that the vast majority of lipids capable of forming membranes contain a polar headgroup.

The structure of the lipid bilayer makes it apparent that biological membranes are only two molecules thick while spanning areas as large as hundreds of μm^2. In fact, the unique ability of amphipathic lipids to spread into thin sheets covering large expanses fascinated scientists long before they were thinking of cells and the membranes that enclose them, and ultimately led to the discovery of the bilayer organization of lipids in biological membranes [27, 28].

1.2.1 Oil on water

The pouring of oil on water is a simple experiment that has led to many a scientific discovery on the behavior of lipids over the centuries. In 1774, Benjamin Franklin, inspired by stories from seafarers on the use of oil to still turbulent waters, performed the experiment of pouring a teaspoon of olive oil into a lake [29]. He made the observation that the oil spread to coat nearly half an acre of the lake's surface. The immediate and forceful spreading of the oil on the surface of water was a most remarkable phenomenon that could not be fully explained by Franklin at the time.

A century later, the independent efforts of Lord Rayleigh and Agnes Pockels resulted in scaled-down table-top versions of the experiment that could be carried out in a laboratory[2][30, 31]. The first estimates for *molecular size* emerged as a result of these experiments, assuming that the oil spreads until it forms a monolayer of molecules.

When Irving Langmuir repeated the experiment with a variety of lipids in 1917, he further gleaned insight into the shape and size of the lipid molecules and their orientation within the monolayer [32, 33]. This allowed him to understand how molecular properties of lipids, such as the number of hydrocarbon chains, their lengths, and the presence of double bonds, could affect their interactions with water and hence their molecular organization within the monolayer.

Remarkable though these findings were for their time, their direct relevance to cell membranes was not realized until the experiment of Gorter and Grendel in 1925 [34]. They proposed that the cell membrane is made of a lipid bilayer with the arrangement of lipids as shown in Fig.1.5, by monitoring the spreading of lipids extracted from red blood cells of animals on water and comparing it to the total surface area of the cells from which they were extracted. The resulting factor of two suggested that the cells were covered

---

[2] Or in a kitchen, which is where Agnes Pockels carefully performed her experiments, owing to her circumstances as a woman of her time.

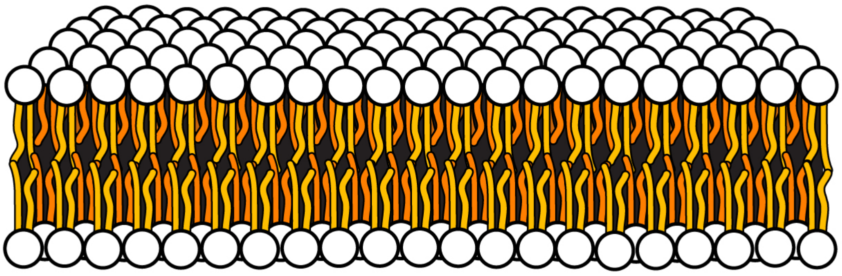

Figure 1.5: A phospholipid bilayer. Schematic of phospholipids arranged in a bilayer, with the lipid headgroups (white circles) at the aqueous interfaces and the acyl chains (yellow strings) buried in the hydrophobic core of the bilayer. Image from [35].

with a membrane two molecules thick. Gorter and Grendel further took into consideration the molecular properties of lipids and deduced that the only feasible arrangement of the lipids in the membrane would be with their hydrophobic tails in the middle and the hydrophilic heads forming interfaces with water both inside and outside of the cell.

In the 1950s, electron microscopy images confirmed the universality of lipid bilayer membranes and disproved competing hypotheses [36, 37]. Early experiments on model membranes in the 1960s shed light on the fluid nature of membranes [38] and the experiments of Frye and Edidin using fluorescent tags in 1970 established this to be true in cells [39]. These ideas, along with the knowledge of ion pumps and other membrane proteins, precipitated the formulation of the fluid mosaic model by Singer and Nicolson in 1972, which describes the plasma membrane as fluid lipid bilayers with embedded and anchored proteins, where the lipids and proteins can diffuse laterally [40]. This idea of the plasma membrane is widely regarded as valid to this day, with some notable additions over the years:

1. ***Bilayer Asymmetry.*** Lipid bilayers in cells are found to be asymmetric, with different lipid abundances in the inner and outer leaflets of the bilayer, maintained actively by ATP-dependent flippases [41–43].

2. ***Fences and pickets***. Anomalies have been observed in the lateral diffusion of membrane components, attributed to picketing by the cytoskeleton [44] and the existence of lipid domains within the membrane [45].

3. ***The raft hypothesis***. It has been proposed that membrane domains enriched in cholesterol and sphingomyelin function as signaling hubs for membrane proteins in the plasma membrane of cells [45].

4. ***Integral membrane proteins***. It is now recognized that a lot more of the membrane area is covered by proteins than previously thought, where proteins can be likened to cobblestones surrounded by thin rims of lipids on the cobblestone membrane, as opposed to sparse icebergs floating in a vast sea of lipids [46].

1.2.2 Membrane diversity

While the bilayer structure is a universal feature of lipid membranes, there is a lot of variability in the chemical composition of individual membranes at all levels of organization [18, 28, 47, 48]. Distinct lipid compositions can be observed for biological membranes from different organisms [49], different tissues within the same organism [50, 51], different organelles within the same eukaryotic cell [47, 52, 53] and even different domains of the same continuous membrane [45, 54, 55].

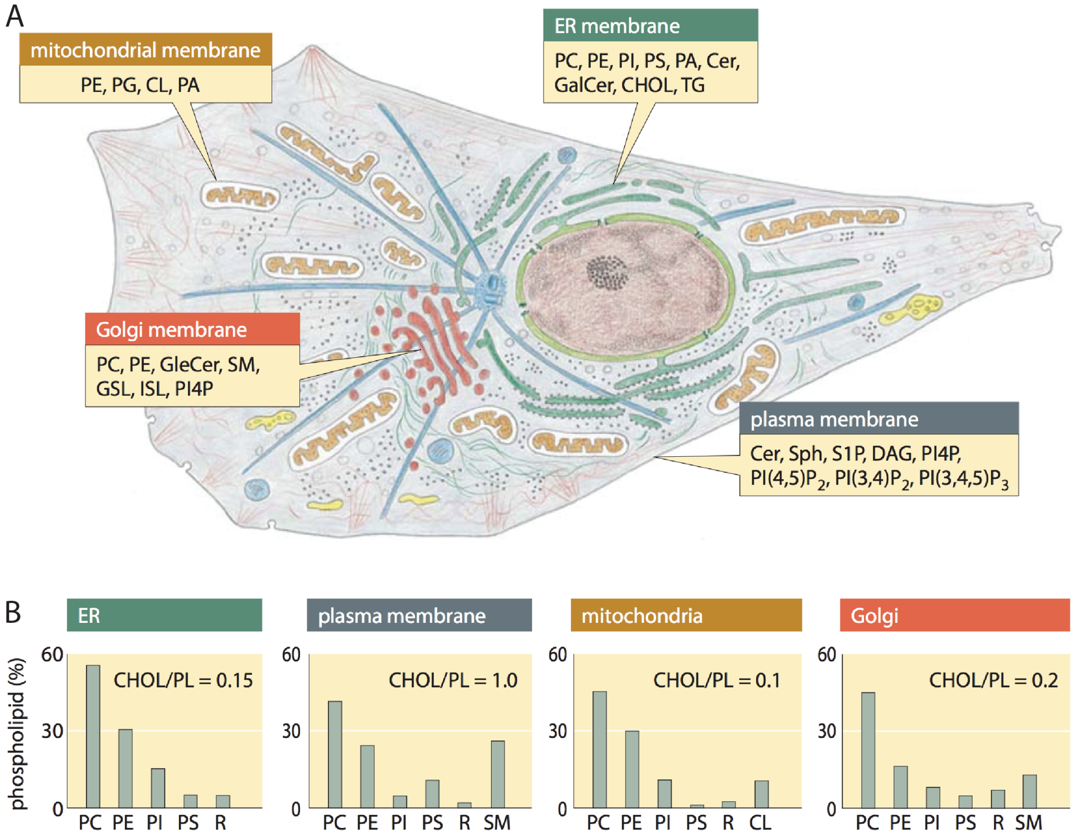

Figure 1.6: Compositional diversity of organellar membranes. A) Schematic of a mammalian cell showing the sites of cellular synthesis of various lipids, with the bulk of phospholipid and cholesterol synthesis occurring in the endoplasmic reticulum (ER). B) Membrane lipid composition of organellar membranes, as a % of all phospholipids (PL). R denotes remaining lipids. Figure from Phillips, 2018 [28], adapted from van Meer *et al*, 2008 [47].

Since organellar membranes are subject to continuous exchange due to membrane trafficking, the observed variations in organellar lipid composition are necessarily maintained by active processes in cells, whose conservation suggests a critical function. It is widely thought that precise lipid compositions regulate the geometrical and mechanical properties of the individual bilayers as required for their specific functions [48, 50]. For example, it is known that the plasma membrane is especially enriched in sphingolipids and cholesterol (lipids with tight packing) relative to membranes of other organelles. This is thought to endow the plasma membrane with the capacity to withstand higher stresses [18, 48].

Why do cells maintain distinct membrane compositions? What happens if these carefully maintained lipid compositions are tinkered with and perturbed? These questions remain open and are central to the explorations of this thesis.

1.2.3 Phase behavior

Early X-ray studies in the 1940s and 50s revealed that lipid bilayers can exist in one of several possible phases [56–58], which have since then been further characterized both experimentally [59] and by Molecular Dynamics (MD) simulations[3] [61]. Fig. 1.7 shows the major phases of pure, single-component phospholipid membranes, determined by the interplay of temperature, pressure, hydration, and interactions between individual lipid molecules. The resulting phases are characterized by the spacing, orientation, and fluidity of the molecules within the plane of the bilayer, which can undergo large discontinuous changes during phase transitions.

Under standard experimental conditions, most phospholipids form bilayers that exist in either the gel phase or the liquid crystalline phase. Thus, the transition between these two phases has been referred to as the main phase transition of the lipid bilayer, and is analogous to the solid-to-liquid transition of 3D materials [65, 66]. The characteristic *melting temperature* for this phase transition under standard pressure for various lipid species are plotted in Fig. 1.7. Here it is clear that the melting temperature increases with acyl chain length and is decreased by the presence of double bonds, which do not favor the formation of crystal lattices due to the kinks they generate in the acyl chain structure (Fig. 1.2).

---

[3] Molecular Dynamics is a computer simulation method first developed in the late 70s for analyzing the physical movements of atoms and molecules.[60]

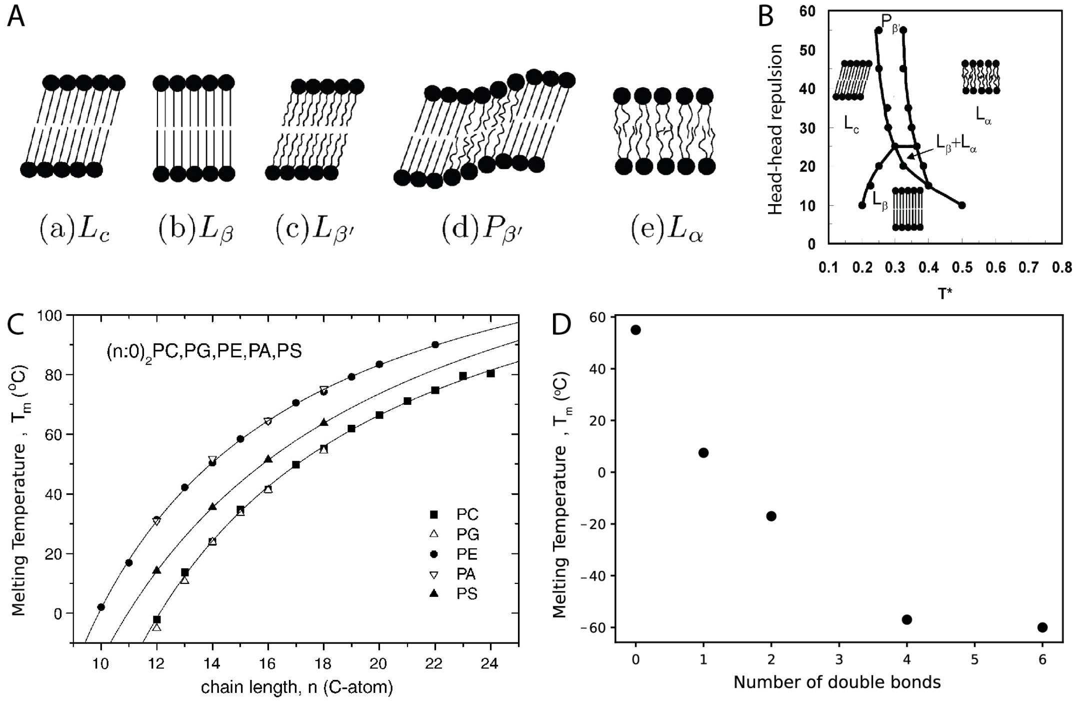

Figure 1.7: Phase behavior of lipid bilayers. A) Five known bilayer phases for phospholipids. B) Representative phase diagram with respect to temperature and head-head repulsion between phospholipid molecules. Panels A and B from Kranenburg and Smit, 2005 [62]. C) Melting temperature as a function of acyl chain length for phospholipids with identical saturated acyl chains in the sn-1 and sn-2 positions. Plot from Marsh, 2010 [63]. D) Melting temperature as a function of the number of double bonds per acyl chain for PC with two identical 18C acyl chains. Data from Silvius *et al*, 1982 [64].

We will revisit the topic of lipid bilayer phases in the context of perturbations to membrane cholesterol and lipid saturation in chapter 3.

1.3 Aims of this thesis

Our ability to read, edit and rewrite the genetic code has ushered in a golden age of the gene and gene products. Modern tools in molecular biology allow us to routinely probe the role of proteins by mutating them, overexpressing them, or knocking them down or out in cells. In contrast, it is relatively harder to target lipids and to probe changes to lipid composition.

The chemical diversity among the lipids that cells generate and the compositional diversity meticulously maintained by cells among their membranes suggest an important functional role underlying such regulation. In particular, it has been observed that distinct tissues and cell types maintain distinct lipid compositions. This prompts the question of when and how they acquire these distinct lipid compositions during development. For instance, it is not understood how lipidomic changes are encoded within the differentiation programs of specialized cell types.

Then there is the question of why cells should maintain specialized lipid compositions at all. The fluidity, elasticity, hydration and surface charge at the membrane all depend on its lipid composition. Since lipid composition affects these bulk properties of membranes, it is possible that the composition is tuned to provide those properties which serve membrane function and optimal functioning of membrane-associated proteins. Perturbational studies similar to those described above for proteins could shed light on the need for homeostatic control of membrane lipid composition in cells.

In this thesis, I have chosen different model systems to tackle different aspects of the above questions:

1. ***The developing mouse brain.*** I used the developing mouse brain as a setting for studying the timing of lipidomic changes during development. This question is particularly interesting in the context of the brain as it is a lipid-rich organ with a very distinct lipid composition relative to other tissues and a site of extensive membrane trafficking between cells [67, 68].

   Seeking the answer to this question of *when* is similar in spirit to trying to balance a light switch in the exact position between *on* and *off* and catching what happens at that transition; except that in developmental biology, we are dealing with a thousand switches in a complex circuit tuned precisely to produce a magnificent orchestra of lights over time. The lipidomics approach outlined in section 1.1.2 allows us to trace over a thousand lipids in the mouse brain over developmental time.

2. ***Mouse embryonic stem cells (mESCs).*** To probe lipidomic changes at the cellular level in relation to the differentiation program of stem cells, I used mESCs being differentiated into neurons *in vitro* [69].

   While stem cells differentiated *in vitro* are typically benchmarked by mRNA and protein expression, their lipidomes are largely ignored. Here, I have characterized the lipidome of neurons differentiated from stem cells *in vitro*.

3. ***3T3 mouse fibroblasts.*** In this thesis, I have used 3T3 mouse fibroblasts in culture as microscopic chemistry labs for tinkering with lipids.

> The actomyosin cortex is a ∼200nm-thick meshwork of actin filaments and associated proteins beneath the plasma membrane that governs cell shape and the mechanics of the cell surface [70–72]. Since the actomyosin cortex is tethered to the plasma membrane, I posited that plasma membrane lipid composition could in turn affect the cortex. Thus, I perturbed cellular cholesterol and lipid saturation and studied the impact of these perturbations on the mechanical prroperties of the plasma membrane and actomyosin cortex.

The thesis is divided into two parts, one concerning the onset of lipidomic changes during development and the other focusing on perturbational studies of lipid compostion and their impact on cellular mechanics. Chapter 2 deals with tracing lipids through the course of neural development. Here, I describe my efforts to characterize lipidome remodeling in the developing mouse brain and in neurons differentiated from stem cells *in vitro*. In Chapter 3, I discuss the response of the actomyosin cortices of mouse fibroblasts to perturbations in cholesterol levels and lipid saturation. While I focus on the rationale behind the experiments, their outcomes, and the interpretation of the results in Chapters 2 and 3, detailed descriptions of all experimental procedures are provided in Chapter 4.

Chapter 2

Lipids in neural development

2.1 Lipids in the brain

The brain is a remarkable and enigmatic organ that regulates a vast array of complex processes from sensation to cognition and behavior. The cells constituting the brain can be grouped into two broad categories, namely neurons, and glia. Of these, neurons are the processing units while the glia provide structural, metabolic, and immune support to the neurons and come in three main flavors (Fig 2.1A):

1. ***Astrocytes***. Astrocytes play a role in maintaining nutrient and ion concentrations and interact closely with endothelial cells of the blood vessels in the brain.
2. ***Oligodendrocytes***. Oligodendrocytes are primarily responsible for the formation of membrane stacks known as the myelin sheath around neuronal axons (Fig. 2.1C).
3. ***Microglia***. Microglia are the immune cells of the central nervous system which are involved in the detection and destruction of bacteria and other foreign cells.

Overall, it has been estimated that the human brain is composed of about 67-86 billion neurons and 40-50 billion glia [74].

Underlying all of the complex functions carried out by the brain is the transmission of information through large networks of neurons, where each neuron shares points of contact termed synapses with several thousand other neurons. This transmission occurs via electric signals called action potentials along the axons of neurons and chemical signals through the release of neurotransmitters at the synapses between neurons (Fig. 2.1). Interestingly, lipids

---

Parts of the text in this chapter are adapted from my contribution to Gopalan *et al*, 2022 [73].

are a crucial structural element that aid both of these events. They constitute the myelin sheaths that act as insulation around neuronal axons to ensure efficient transmission of action potentials [75] and they form the synaptic vesicles which carry and release neurotransmitters. These synaptic vesicles are present at μM concentrations in the brain [68] and lipids constitute more than half of the human brain in dry weight [67].

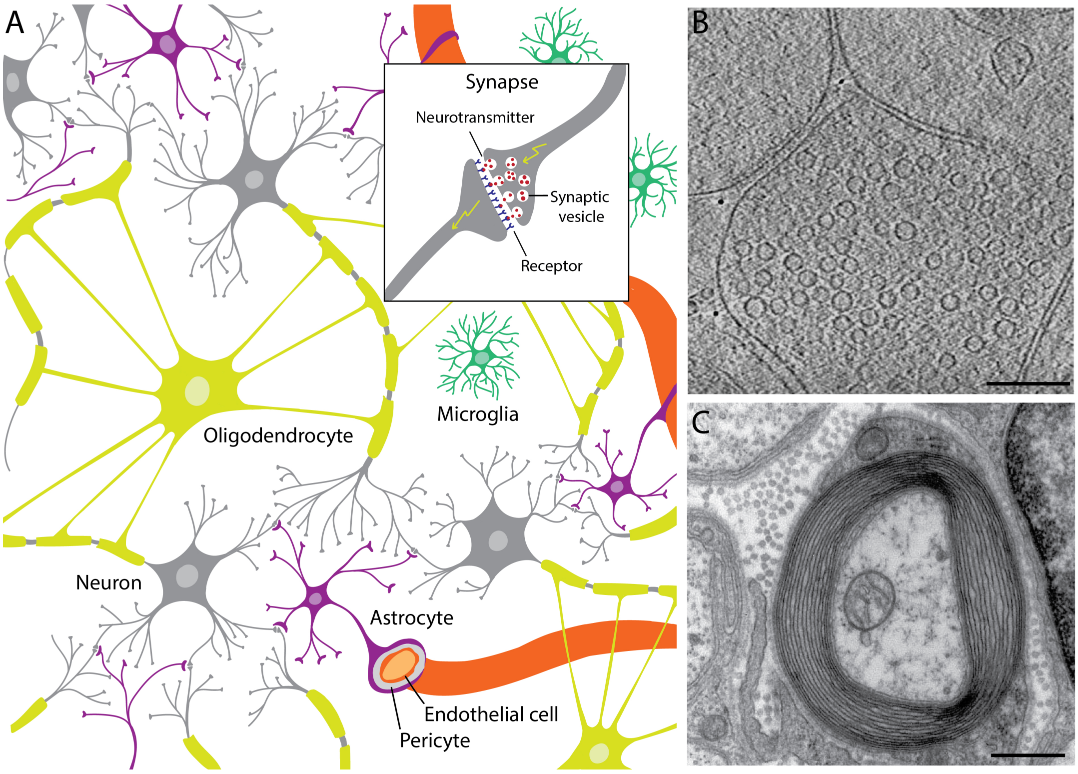

Figure 2.1: Cellular composition of the brain. A) The major cell types in the brain include glial cells, neurons, and the endothelial cells which constitute the blood-brain barrier. The inset shows the release of neurotransmitters at the synapse between two neurons. B) Cryo-electron tomographic slice of a synapse with synaptic vesicles from Schrod *et al*, 2018 [76]. C) Transmission electron micrograph of a cross-section of a myelinated axon from the Electron Microscopy Facility at Trinity College.

2.1.1 Lipid metabolism in the brain

Considering the structural importance of lipids in the brain, it comes as no surprise that defects in lipid metabolism cause impairments to brain development and function [77]. In particular, metabolism of the following lipids has been reported to be crucial to brain function:

1. ***Sphingolipids.*** A large body of work shows that defects in sphingolipid metabolism are associated with a number of neurological pathologies.

Mutations in Serine Palmitoyl Transferase Long Chain Base Subunit 1 (SPTLC1), a key enzyme in sphingolipid biosynthesis are found to cause neurodegeneration of motor neurons leading to neuropathy in humans [78, 79]. Further, a loss of myelination is observed when the expression of Ceramide Synthase 2 (CerS2, specific to very long fatty acid residues 22–24 carbon atoms in length) is inactivated in mice [80].

Metabolism of monoglycosylated ceramides and their sulfated forms (HexCer and SHexCer) in particular, must be kept in check for the maintenance of myelination and normal brain function. Overexpression of the enzymes that synthesize both HexCers and SHexCers has been shown to cause demyelination and severe neurological symptoms in mice [81–83].

Further, Sphingomyelin (SM) and the ganglioside GM1 are also found to be involved in triggering differentiation programs in neuronal stem cells [21]. It has also been found that exposure to the myotoxin fumonisin during pregnancy leads to neural tube defects in embryos via inhibition of sphingolipid synthesis [84, 85].

2. ***Cholesterol.*** Complete loss of function of several enzymes specific to cholesterol biosynthesis is lethal during embryonic development [86, 87]. However, conditional mutations in specific cell types have allowed scientists to decipher the role of cholesterol in the nervous system. Conditional loss of function of the enzyme Farnesyl Diphosphate Farnesyltransferase 1 (FDFT1) in oligodendrocytes [88] and SCAP (SREBP cleavage activation protein) in Schwann cells[1] [89] have both been reported to result in severely defective myelination leading to neuropathy.

   Further, cholesterol transport from glial cells to neurons has been identified as a rate-limiting step for synapse formation [67, 90, 91] and axonal growth [92]. Inhibition of cholesterol synthesis has also been shown to impair the exocytosis of synaptic vesicles in cultured neurons [93]. Accumulating evidence shows that defective cholesterol metabolism plays a role in several developmental disorders [94] and neurological diseases such as Niemann-Pick C, Huntington's, and Alzheimer's disease [95–98].

3. ***n-3 polyunsaturated fatty acids (PUFAs).*** n-3 PUFAs have the first double bond at the third C atom from the free end of the chain and are

---

[1] A major glial cell type of the peripheral nervous system, where they surround neurons and act akin to oligodendrocytes and astrocytes of the central nervous system.

> all either taken up directly from the diet or generated from the 18:3(n-3) essential acid[2], linolenic acid. Due to this dietary dependence, a lot of the work on studying the role of n-3 PUFAs has been done by modulating the availability of linolenic acid in the diet rather than using genetic approaches. Early studies identified linolenic acid and its longer-chain derivatives as essential for brain development [99].
>
> In particular, the role of docosahexaenoic acid (DHA, 22:6) has been studied extensively in this context [100, 101]. Studies performed *in vitro* [102–106] as well as *in vivo* [104, 105, 107–110] have demonstrated that DHA (22:6) provided through the diet or supplemented in cell culture media, aids neurogenesis, the formation of synapses and the modulation of ion currents in neurons.
>
> Notably, the effects of DHA on brain function are also reflected at the level of behavior. In particular, a number of studies have shown that rats on a diet deficient in DHA perform poorly in learning and spatial tasks compared to the control group [111–114] and show distressed behaviors [115]. On the other hand, rats whose diets were enhanced with DHA showed improved memory-related learning ability [116].

As is evident from the above studies, the approach of manipulating lipid metabolic genes or diet and studying the resulting neuropathologies and behavioral changes in rodent models has contributed greatly to our qualitative understanding of the role of various lipids in brain function. Investigation of brain cells isolated from these animals and cultured *in vitro* has further made it possible to access morphology, gene expression, protein localization and activity, and electrical activity of individual cells in response to interventions modulating lipid composition. Next, we turn to a complementary approach taken by analytical chemists, which has helped construct a quantitative description of the brain's unique lipid composition.

2.1.2 Lipid composition of the brain

Chemists had already begun investigating the composition of the brain from deceased humans and animals in the late 1700s. In 1884, Johann Thudichum published his findings in *A treatise on the chemical constitution of the brain* [117], where he described painstakingly elaborate methods for the extraction of

---

[2] Essential acids cannot be synthesized by the organism and need to essentially be consumed in the diet.

various fractions and their chemical analysis by monitoring solubility, precipitation, and crystallization of the extracted substances and their reactivity with several laboratory reagents. As the extractions were performed by dissolving tissue in alcohol, what resulted from this work was a quantitative analysis of brain lipids.

The chemical analysis of individual lipid classes in the brain by these traditional methods continued well into the 20th century [118–123]. However, the advent of chromatography revolutionized the separation and analysis of lipids [124, 125] and made it possible to analyze many more lipids in great structural detail. Brain lipids were extensively analyzed in the 1960s and 1970s using chromatographic methods [126–129]. Studies in this period also sampled brain tissue from various animals [130–132] and examined the changes to lipid composition across development and aging [132, 133] and in response to dietary restrictions [134]. Notably, synaptic plasma membrane fractions were also isolated and analyzed by chromatography [135, 136].

The second major technical advancement came with the use of mass spectrometry (MS) for the analysis of lipid mixtures. Advances in ionization techniques [137, 138] made it possible to analyze lipid mixtures using MS in combination with chromatographic separation in the 1990s, and revealed that cells maintain a far more diverse repertoire of lipids than previously thought. Mass spectrometry has been extensively used to analyze the lipid composition of tissues, cells and sub-cellular fractions ever since, earning lipidomics a prominent spot alongside the other -omics disciplines (section 1.1.2) [23, 139].

Mass spectrometry-based lipidomics has provided a detailed account of the lipid composition of brain regions and their constituent cells [140], and of synaptic membrane fractions [141] and the vesicles themselves, which are accessible for purification and analysis owing to their high abundance and uniform size [46]. There has been much interest in studying lipidome-wide changes in the brain associated with aging [142] and in neurodegenerative diseases such as Alzheimer's [143–146]. Further, recent developments in mass spectrometric imaging have enabled the study of spatial distributions of lipids in brain slices [147–150].

Upon going through data acquired using various methods on brain tissue and cells over the years [46, 126–132, 135, 136, 140, 141], one can converge on a list of lipids that are consistently enriched in the healthy adult brain compared to other organs:

1. Sphingolipids with an 18:0 acyl chain

2. Monoglycosylated ceramides and their sulfated forms (HexCer and SHexCer)

3. Cholesterol

4. Glycerophospholipids (GPLs) containing n-3 and n-6 polyunsaturated fatty acyl chains

5. Ether-linked GPLs such as phosphatidylethanolamines (PE O-)

Further, neurodegenerative brain tissue shows alterations in the levels of these same lipid groups [143–146]. These findings are in line with what studies involving genetic and dietary perturbations to lipid metabolism have taught us about the lipids that play a role in brain development and function [67, 80, 89–92, 99, 104, 105, 107–116]. However, it is not clear when these lipid features arise during development and how they are coupled to the differentiation and maturation of cells within the brain. In order to address this question, I chose the mouse as a model organism.

2.1.3 The developing mouse brain

The mouse has a gestation period of 19-21 days and a typical litter size of 6 to 8 pups. The timeline for brain development extends across embryonic and postnatal development periods over about 40 days in total until adolescence, as outlined in Fig. 2.2A. Some of the key events involved in this process are briefly introduced below:

1. ***Neurulation.***The first morphogenic event that forms the basis for brain development is the folding and fusing of a layer of neuroepithelial cells to form the hollow neural tube - the structure which will eventually form the brain and spinal cord of the central nervous system.

2. ***Neurogenesis, gliogenesis and apoptosis.*** Neural progenitor cells are stem cells that can differentiate into both neurons and glia and these differentiation events are termed the 'genesis' of the respective cell type. In fact, these cells are produced in excess and then killed off to restore the desired numbers. This process of programmed cell death is termed apoptosis and occurs extensively during development of the central nervous system. Neural progenitor cells, differentiated neurons, and glia have all been found to undergo apoptosis in order to establish the desired population size of each cell type [152, 153].

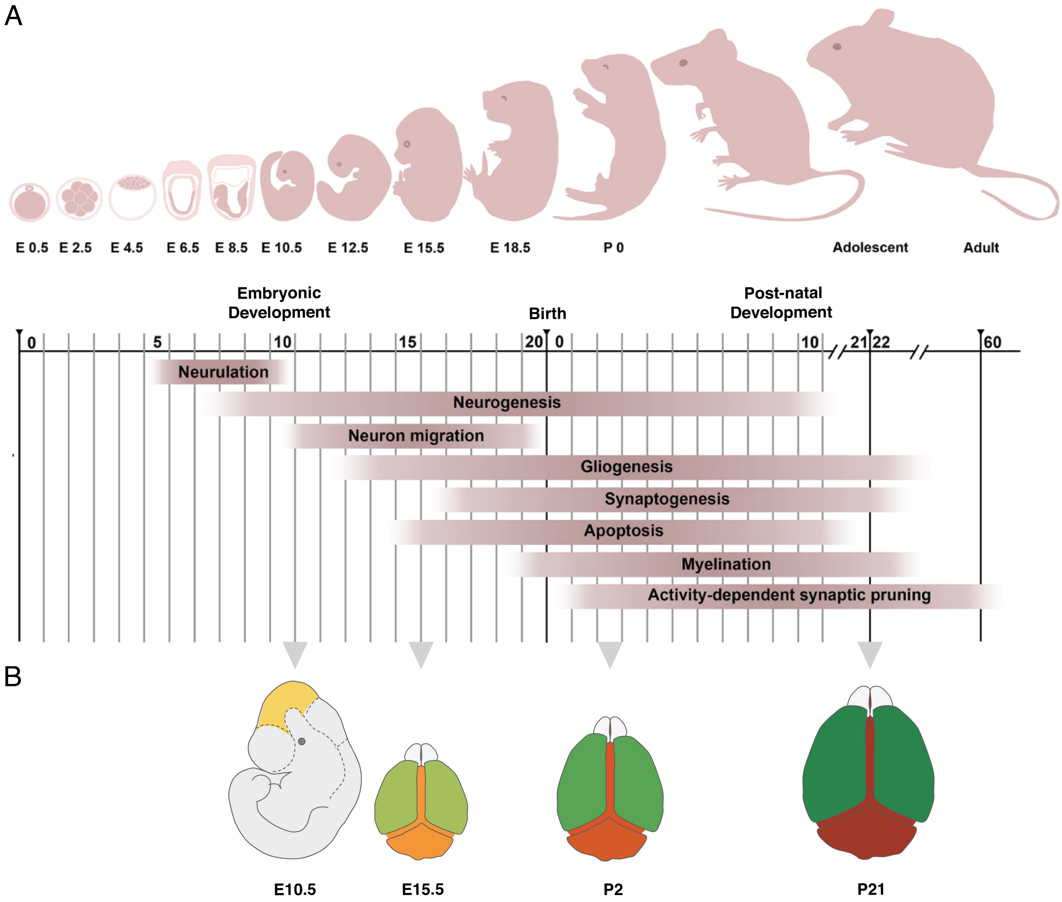

Figure 2.2: Timeline of brain development in mice. A) Timeline of the events connected with brain development in mice from Wen *et al*, 2022 [151]. B) Samples collected at various time points over development for the lipidomics analysis reported in this thesis. Schematic by Lisa van Uden.

3. ***Synaptogenesis and synaptic pruning.*** Differentiated neurons in isolation cannot achieve any brain function without physical connections to other neurons through synapses. The growth of neural processes and formation of these points of contact, where synaptic vesicles can carry information in a controlled one-way street over to an adjacent cell is termed synaptogenesis [154]. Similar to neurogenesis and gliogenesis followed by apoptosis, synapses are produced in excess and the unnecessary synapses are then destroyed or pruned away [155]. Further, synapses display plasticity in that the strength of synaptic connections can change over time, throughout the lifetime of the organism, and depending on reinforcement from learning and memory [156].

2.2 Lipidomics of the developing mouse brain

To trace lipidome-wide changes during brain development, I performed a quantitative mass spectrometry-based lipidomics analysis (Sections 1.1.2, 4.4) [26, 157] of brain tissues obtained from mice at the four developmental time points indicated in Fig. 2.2B and traced lipidome-wide changes across these samples[3].

The time points for sampling were chosen such that embryonic and postnatal changes in lipid composition could be identified. It is worth noting that lipidome-wide changes during the embryonic phase of brain development have not been studied thus far. I chose E10.5 as the first time point as it was the earliest time point in which a distinct brain tissue could be dissected out of the embryo. The brain tissue (yellow) and rest of the embryo post removal of the brain tissue (grey) were both analyzed at this time point. At all other time points, it was possible to dissect cerebral hemispheres (green) from the rest of the brain (brown) and these were analyzed as separate samples.

The experiment was performed on five biological replicates, and detailed experimental procedures are described in section 4.4. The lipidomics analysis allowed us to identify and quantify 1488 lipid molecules from 26 lipid classes.

Hence, each sample in the dataset can be defined as a point in a 1488-dimensional space, where each coordinate corresponds to the mole percent abundance of one lipid. It is then interesting to ask where in this space the samples lie with respect to each other, and what the trajectory taken by the mouse brain in the lipid space over the course of development is. As it is challenging to capture these changes in such a high-dimensional space, I used the principal component analysis for dimensionality reduction, to identify a few axes along which most of the changes could be captured.

The PCA revealed that 39 principal components are required to completely describe the variation between the samples, but 77% of the variation between samples can be captured in the first two principal components, PC1 and PC2, which account for 49% and 28% of the variation, respectively.

A PCA plot of samples along these leading principle components PC1 and PC2 shows the clustering of samples as per sample group, with a notably large separation between E10.5 and E15.5 samples and between P2 and P21 samples (Fig. 2.3B). E15.5 and P2 samples cluster closer to each other in comparison. Further, E10.5 and E15.5 samples show a large separation

---

[3] Mouse brain tissues were dissected by Emilia Esposito, Vikram Singh Ratnu and Juan Carlos Boffi at EMBL, Heidelberg.

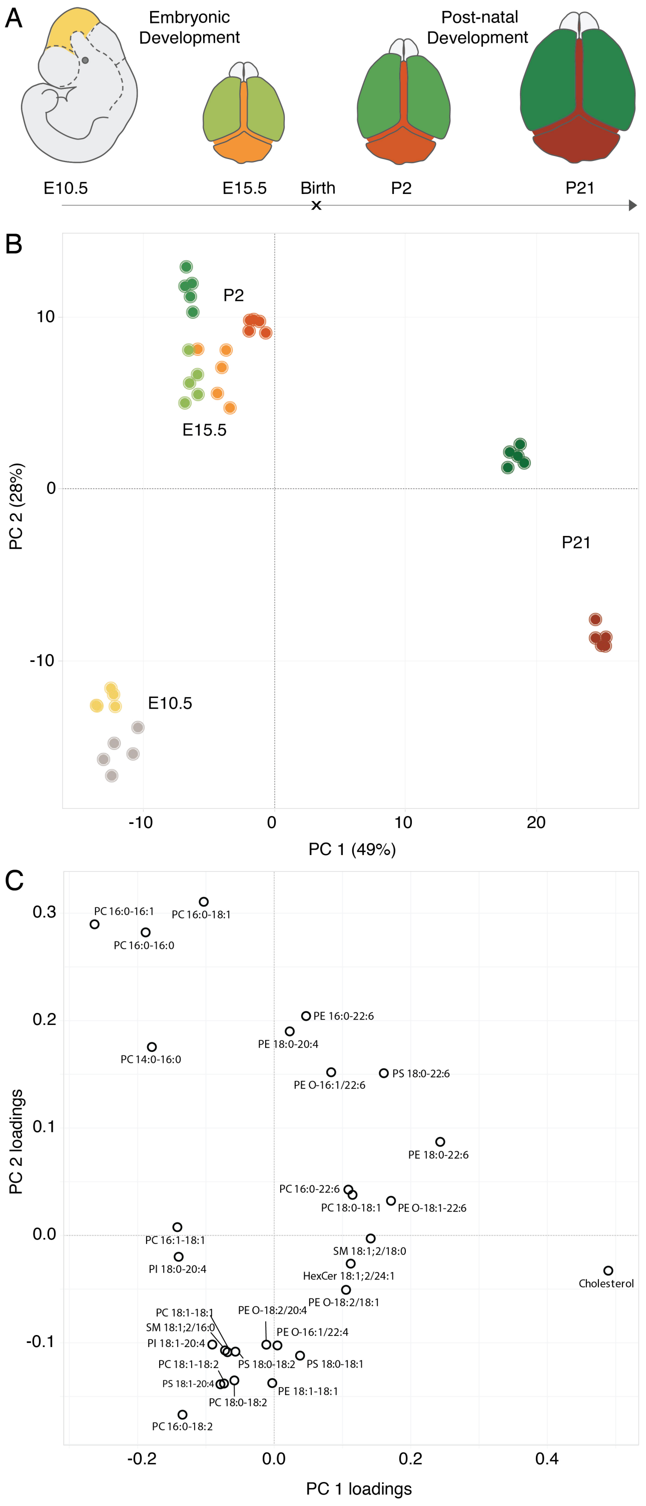

Figure 2.3: Principal component analysis. A) Samples were collected at the indicated time points from the regions shown in distinct colors in the schematic. Schematic by Lisa van Uden. B) PCA scores of samples along Principal components 1 and 2 (PC1 and PC2), where each point denotes a sample and is colored as per A. C) Loadings of individual lipid species to PC1 and PC2. Only lipids having an absolute loading ≥ 0.1 along at least one of the axes are plotted. Data from n = 5 replicates.

along the PC2 axis, whereas P2 and P21 are separated along both axes. Examining the loadings of lipids to PC1 and PC2 can inform us about the lipids contributing to differences between samples along each of these axes. For instance, from Fig. 2.3C, it is clear that cholesterol is a strong contributor to PC1.

Among samples from the same time-point, there is further clustering as per tissue group. The distinction between hemispheres and the rest of the brain is observed to be negligible at E15.5 but grows subsequently in the post-natal samples, as the different brain regions begin to acquire more specialized lipidomes. Interestingly, the E10.5 brain tissue and the rest of the embryo cluster very close to each other. This indicates that the developing brain has not yet acquired a lipidome distinctly dissimilar to the rest of the embryo at E10.5.

This is also confirmed by a statistical test for significant differences in the molar abundances of individual lipids between the E10.5 brain and the rest of the embryo. A total of 13 lipids (0.9% of all quantified lipids) were identified to be significantly lower in the brain as compared to the rest of the embryo and no lipids were found to be enriched (Fig. 2.4, $p \leq p_c = 0.0025$, as determined by a Student's t-test. The cut-off $\mathrm{p_c}$ was determined by a Benjamini-Hochberg procedure to account for multiple hypothesis testing. See section 4.4.7 for details on statistical analysis). Thus, it appears that the enrichment of brain-specific lipids has not begun as of E10.5, making the brain tissue from E10.5 an ideal starting point from which to trace lipidomic changes.

A similar statistical comparison of samples from later time points against the E10.5 brain tissue reveals large-scale lipidome remodeling over development. 451 lipids in the cerebral hemispheres and 445 lipids in the rest of the brain (30% of detected lipids in both cases) show a significant two-fold or larger change in abundance at P21 compared to the E10.5 brain (Fig. 2.5A and C, $p \leq p_c = 0.04$ and 0.041, respectively, as determined by one-way ANOVA. See section 4.4.7 for details on statistical analysis). Of these, 133 (9%) lipids are increased and 318 (21%) lipids are decreased in the P21 cerebral hemispheres relative to the E10.5 brain. Similarly, 162 (11%) and 283 (19%) lipids are found to increase and decrease in the rest of the P21 brain, respectively.

To identify common molecular features among lipids that increase and decrease in abundance over the course of development, I performed an enrichment analysis of lipid features, as previously described [157] (See section 4.4.7 for details). The occurrence of structural features such as lipid class and

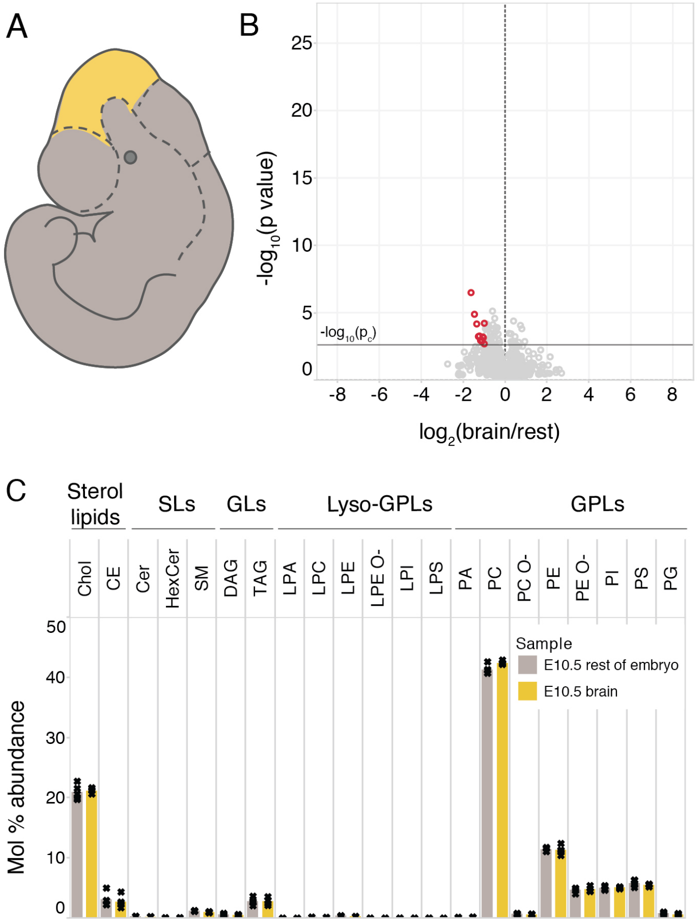

Figure 2.4: The E10.5 brain lipidome. A) Schematic of the dissected E10.5 brain tissue and the rest of the embryo used for lipidomics. Schematic by Lisa van Uden. B) Volcano plot where each circle corresponds to one lipid and its abundance is compared between the E10.5 brain and the rest of the E10.5 embryo. Lipids with $p \leq p_c = 0.0025$ (Student's t-test followed by the Benjamini-Hochberg procedure) and average fold-change across replicates greater than two-fold are colored red. C) Lipid class profile of the two tissue samples collected at E10.5. Data from n = 5 replicates.

category and fatty acyl chains was examined in the pools of increasing and decreasing lipids and compared to their occurrence in the pool of all detected lipids. The over- and under-represented structural features in cerebral hemispheres and the rest of the brain are plotted in Fig. 2.5B and D, respectively.

Nearly the same lipid features were found to be significantly enriched and depleted from the pools of increasing and decreasing lipids in both the brain regions examined here. In both cases, membrane glycerophospholipids (GPL) and sphingolipids (SP) are enriched among increasing lipids whereas storage glycerolipids (GL) are depleted from this pool. Moreover, the lysolipids LPC, LPE, and LPS are enriched in the pool of increasing lipids, in addition to Monoglysylceramides (HexCer) and ether-linked phosphatidylethanolamines (PE O-). The polyunsaturated structural attribute 22:6, corresponding to DHA, is also significantly enriched among the increasing lipids in both brain regions, as are sphingolipids with a sphingosine 18:1;2 chain.

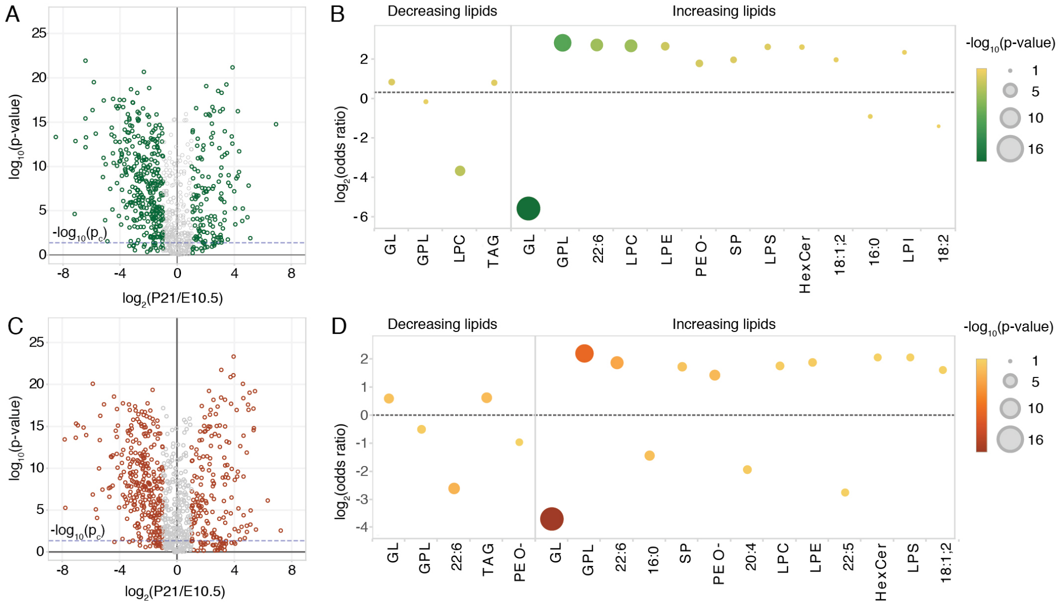

Figure 2.5: Lipidome remodeling during brain development. A) and C) Volcano plots where each circle corresponds to one lipid and its abundance is compared between P21 and E10.5 for the cerebral hemisphere (A) and the rest of the brain (C). Lipids with an average fold-change across replicates smaller than two-fold are colored grey and the dashed blue line indicates the threshold for significance, $-\log_{10}(p_c)$, determined by a Benjamini-Hochberg procedure. B) and D) Enrichment analysis of lipid features among the groups of significantly decreasing and increasing lipids from (A) and (C), respectively, where $-\log_2$(odds ratio) is plotted in the y-axis and the color and size of the points correspond to the $-\log_{10}$(p-value). Data from n = 5 replicates.

These features are in line with previous observations of lipids characteristic of the brain (section 2.1.2). In order to trace their evolution in time, I looked at the abundances of the relevant lipid classes and individual lipid species over time in cerebral hemispheres (Fig. 2.6) and the rest of the brain (Fig. 2.7).

Assessing the bulk abundance of lipid classes in both brain regions across development, I observed a 1.5-fold increase in cholesterol and a 2-fold increase in PE O- as well as a corresponding decrease in phosphatidylcholines (PC) in the postnatal phase between P2 and P21. The sphingolipid classes SM, HexCer, and SHexCer also show a post-natal increase in both brain regions, with HexCers and SHexCers attaining a two-fold higher abundance in the rest of the brain as compared to the cerebral hemispheres at P21 (Fig. 2.6B and 2.7B).

Low levels of cholesterol esters (CE) and triacylglycerol (TAG) present at E10.5 were further diminished thereafter and the total level of phosphatidylinositols (PI), precursors of signaling phosphoinositides, gradually decreased in abundance throughout development to half their initial abundance (Fig. 2.6B and 2.7B).

At the level of individual lipids, one can observe consistent patterns in the establishment of lipid traits unique to the brain (listed previously in section 2.1.2). The sphingolipids Cer 18:1;2/18:0 and SM 18:1;2/18:0, containing an 18:0 acyl chain increase in abundance throughout development in the cerebral hemispheres (Fig. 2.6C), and during embryonic development in the rest of the brain (Fig. 2.7C), replacing Cer 18:1;2/16:0 and SM 18:1;2/16:0 as the most abundant species within their respective lipid classes.

Similarly, upon tracing the abundance of 22:6 among all acyl chains across glycerophospholipids (See section 4.4.7 for detailed methods), I found that 22:6 gets increasingly incorporated into PA, PE, PE O- and PS lipids throughout embryonic and post-natal development in the cerebral hemispheres (Fig. 2.6D). A similar increase is observed in the rest of the brain during embryonic development, but it is followed by a drop in 22:6 levels among PA, PS, and PE O- lipids during post-natal development (Fig. 2.7D).

The lipidomic changes outlined above can be broadly grouped under two categories depending on when they begin to occur:

- Embryonic changes:
    1. Decrease in PI
    2. Decrease in CE and TAG
    3. Increase in 18:0-sphingolipids
    4. Increase in 22:6-GPLs
- Post-natal changes:
    1. Increase in cholesterol
    2. Increase in PE O-
    3. Increase in SM, HexCer and SHexCer

The dataset generated here provides access to the lipidomic landscape of the mouse brain during development, starting from the early embryonic

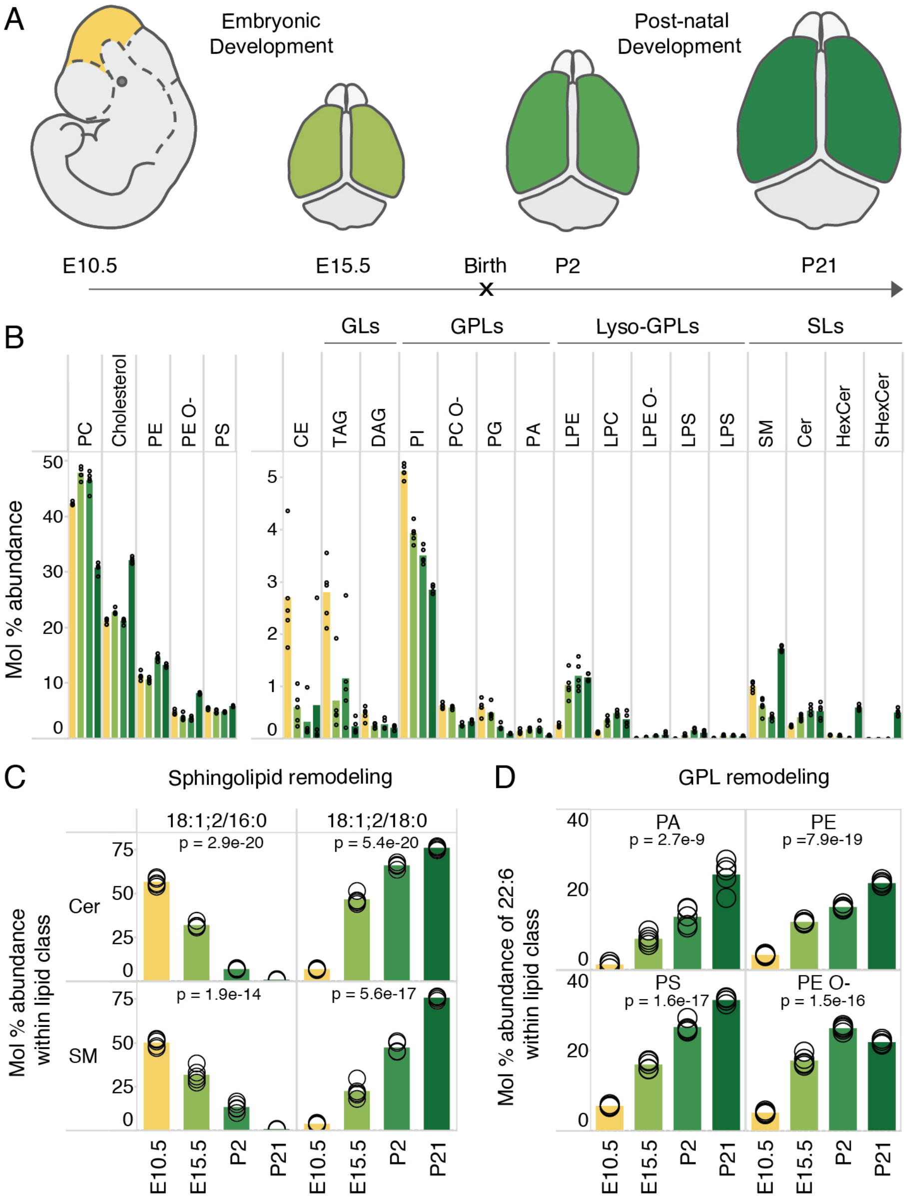

Figure 2.6: Lipidomics of the developing cerebral hemisphere. A) Schematic showing the analyzed samples, drawn by Lisa van Uden. B) Mol % abundance of lipid classes across developmental time. C) Profile of the most abundant Cer and SM species across samples, containing an 18:1;2 sphingoid chain and either a 16:0 or 18:0 acyl chain. D) Profile of 22:6 (DHA) among fatty acyls constituting PA, PE, PE O- and PS species. Data was collected on n = 5 replicates. p-values were obtained using a one-way ANOVA test and changes were considered significant if $p \leq p_c = 0.04$, as determined by the Benjamini-Hochberg procedure.

stage, E10.5. If one were to interpret the lipidomic changes in light of developmental events in the mouse brain (Fig. 2.2), it is clear that early embryonic changes in lipid abundances between E10.5 and E15.5 are concurrent with the differentiation of neurons and glia, whereas later time-points reflect the mixed effect of other developmental events such as synaptogenesis and

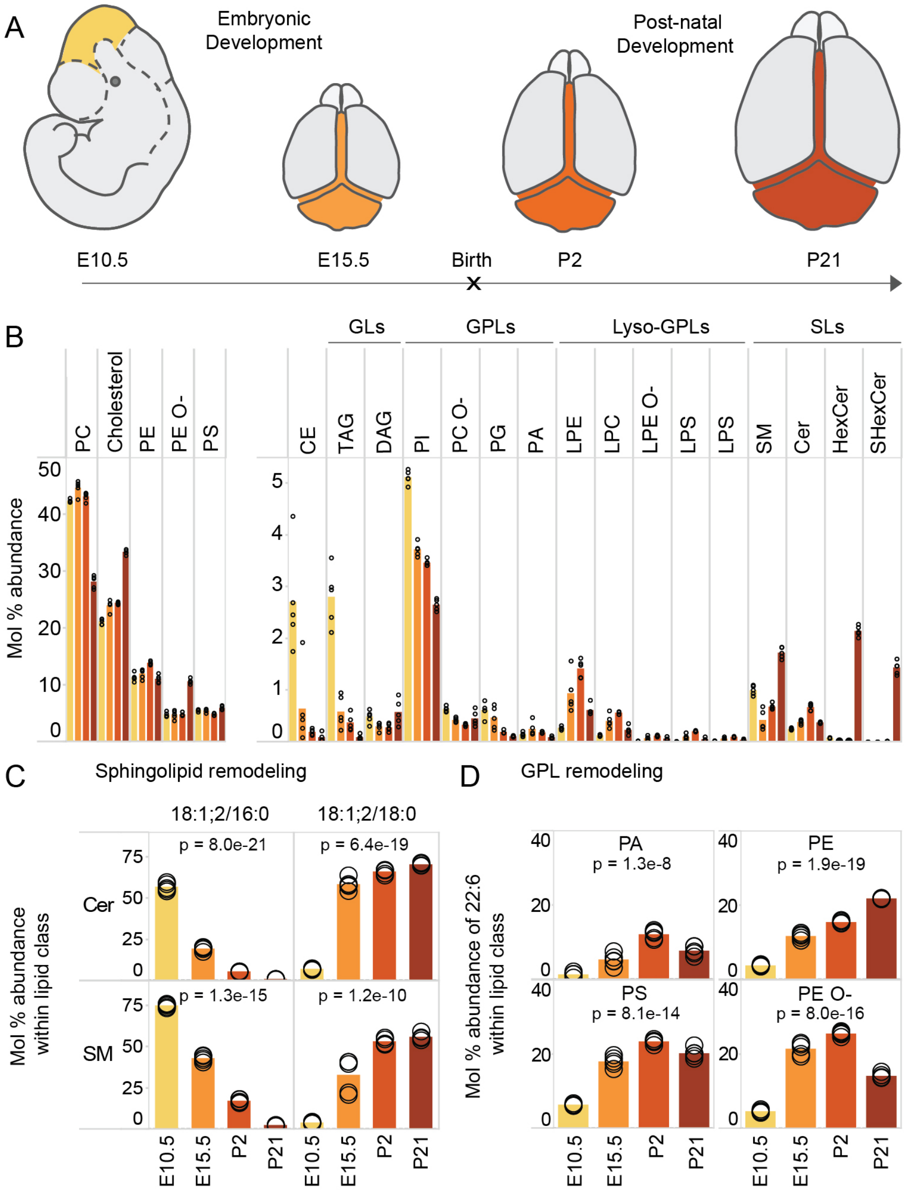

Figure 2.7: Lipidomics of the rest of the brain across development. A) Schematic showing the analyzed samples, drawn by Lisa van Uden. B) Mol % abundance of lipid classes across developmental time. C) Profile of the most abundant Cer and SM species across samples, containing an 18:1;2 sphingoid chain and either a 16:0 or 18:0 acyl chain. D) Profile of 22:6 (DHA) among fatty acyls constituting PA, PE, PE O- and PS species. Data was collected on n = 5 replicates. p-values were obtained using a one-way ANOVA test and changes were considered significant if $p \leq p_c = 0.041$, as determined by the Benjamini-Hochberg procedure.

myelination.

The early increase in 18:0-sphingolipids and 22:6-GPLs in the developing brain and their enrichment in primary neurons over other cell types [140], in particular, raise the question of their role in neuronal differentiation and how their metabolism is coupled to the differentiation program of neural stem cells. To investigate this further, I turned to the *in vitro* neuronal differentiation of embryonic stem cells.

2.3 Lipidomics of differentiating neurons

2.3.1 Making neurons in a dish

It has been proposed that switches in lipid metabolism are closely linked to the differentiation programs of stem cells [158–160]. In order to study the link between lipid metabolism and neuronal differentiation at the cellular level, I characterized lipidomic changes occurring during neuronal differentiation *in vitro*. For this, mouse Embryonic Stem Cells (mESCs) isolated from the inner cell mass of the mouse blastocyst at E3.5 were subjected to *in vitro* differentiation in aggregates known as embryoid bodies[4] [69]. The detailed differentiation procedure is described in section 4.3.1 and Fig. 2.8A shows a schematic of the process. Staining with the neuronal marker β-tubulin III was used to ascertain whether differentiation by this procedure yielded neurons on day 12[5] (Fig. 2.8B). By counting the cell bodies positive for β-tubulin III relative to the cell nuclei stained by DAPI, it was found that 84 ± 1 % of the cells were positive for β-tubulin III across 16 images from two independent replicates of the differentiation procedure.

2.3.2 Lipidomics of neurons differentiated *in vitro*

To assess lipidome remodeling, samples were collected on days 0, 4, 8 and 12 of the differentiation protocol as shown in Fig. 2.8A and subjected to lipid extraction and MS^{ALL}-based lipidomics similarly to homogenized mouse brain tissue (See section 4.4 for a detailed description of the methods). A total of 1355 lipids from 26 lipid classes were quantified. One-way ANOVA was used to determine statistically significant changes in the lipidomes of samples across the differentiation timeline. The cut-off $p_c = 0.023$ was determined by a Benjamini-Hochberg procedure to account for multiple hypothesis testing (See section 4.4.7 for details on statistical analysis). In all, the abundance of 431 lipids (32% of the detected lipids) was significantly altered over the course of differentiation, showing a two-fold or greater change between

---

[4] Stem cell differentiation was performed by Lisa van Uden and Nadine Fernandez-Novel Marx.

[5] Immunofluoresence stainings, imaging, and analysis were performed by Nadine Fernandez-Novel Marx.

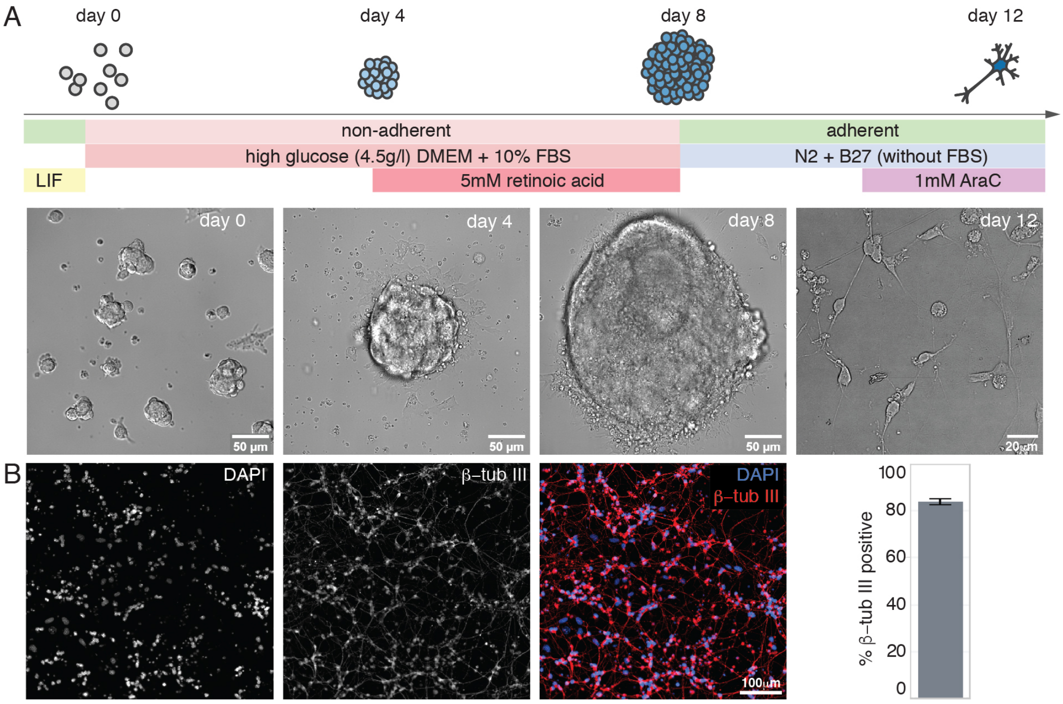

Figure 2.8: Neuronal differentiation of mESCs in embryoid bodies. A) Schematic of the neuronal differentiation protocol for mESCs with representative bright-field images at stages in the differentiation protocol where samples were collected for lipidomics. Schematic by Lisa van Uden. B) Representative fluorescence images of cells on day 12 stained for nuclei (DAPI) and the neuronal marker βtub-III. Quantification of βtub-III positive cells is shown on the right, based on 16 images from n = 2 biological replicates; LIF, Leukemia inhibitory factor; FBS, Fetal bovine serum; AraC, Cytarabine.

days 0 and 12 of differentiation. Of these, 200 (15%) increased in abundance, whereas 231 (17%) decreased in abundance (Fig. 2.9A).

To identify common molecular features among lipids that increase and decrease in abundance over the course of differentiation, I performed an enrichment analysis of lipid features as in the case of mouse brain tissue [157] (See section 4.4.7 for details). The occurrence of structural features such as lipid class and category and fatty acyl chains was examined in the pools of increasing and decreasing lipids identified above, and compared to their occurrence in the pool of all detected lipids. The over- and under-represented structural features thus obtained are plotted in Fig. 2.9B.

The structural features GPL, 16:1, PE O- and PS were enriched in the pool of increasing lipids. The increase in 16:1 is indicative of *de novo* lipid synthesis [161–163], which coincides with the removal of serum from the culture medium and a switch to using glucose as the primary substrate for *de novo* lipogenesis on day 8 (Fig. 2.8A). Further, the polyunsaturated features 20:4

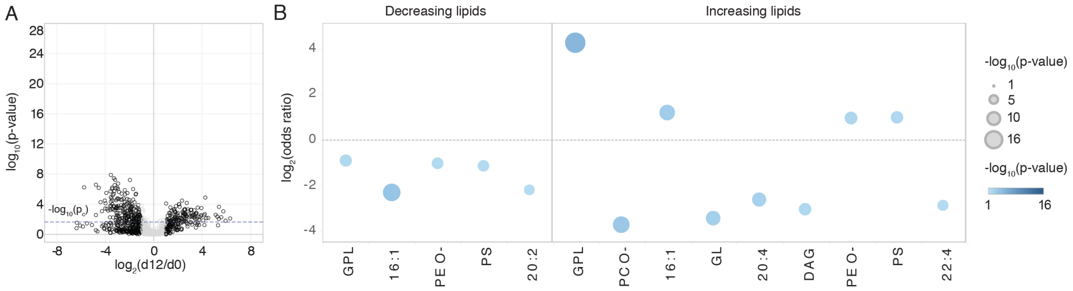

Figure 2.9: Lipidome remodeling during *in vitro* neuronal differentiation of mESCs. A) Volcano plot where each circle corresponds to one lipid and its abundance is compared between day 12 and day 0 of differentiation. Lipids with an average fold-change smaller than two-fold across replicates are colored grey and the dashed line indicates the threshold for significance, -$\log_{10}(p_c)$, determined by a Benjamini-Hochberg procedure. B) Enrichment analysis of lipid features among the groups of significantly decreasing and increasing lipids from (A) where -$\log_2$(odds ratio) is plotted in the y-axis and the color and size of the points correspond to the -$\log_{10}$(p-value). Data from n = 4 replicates.

and 22:4 were depleted among the pool of increasing lipids (Fig. 2.9B). Notably, these structural attributes do not resemble those that are found in the remodeling of brain tissue lipidome (Fig. 2.5).

In order to trace the levels of the canonical neural lipids in the differentiating cells, I looked at the abundances of the relevant lipid classes and individual lipid species over time (Fig. 2.10). At the level of lipid class, I observed a small increase in cholesterol from 19 mol % on day 0 to 22 mol % on day 12 (Fig. 2.10B). Apart from this, a significant increase in cholesterol esters (CE) and TAGs was observed on day 4 and day 8, indicating that the cells were storing fat in the embryoid bodies at these stages. Both 18:0-sphingolipids and 22:6-GPLs were relatively low in abundance at all time points (Fig. 2.10C and D). In particular, the abundance of 22:6 in PE O- and PE classes was further decreased on day 12 of differentiation compared to earlier time points (Fig. 2.10D). Overall, these changes were contrary to those observed early in brain development (section 2.2) and expected for cells differentiating into neurons based on previously published work [46, 140, 141].

Apart from the lack of remodeling similar to developing brain tissue and the synthesis of neural lipid markers, I found that the cells in culture also varied in the fatty acid composition of PIs as compared to brain tissue, with elevated levels of 18:1 and reduced levels of 20:4 chains (Fig. 2.11). The general lack of polyunsaturated fatty acyl chains (PUFAs) in the lipidomes of mESCs *in vitro* (Fig. 2.10D and Fig. 2.11) prompted me to look into the available fatty acids in the growth media of these cells. While the precursors to $\omega 3$ and $\omega 6$

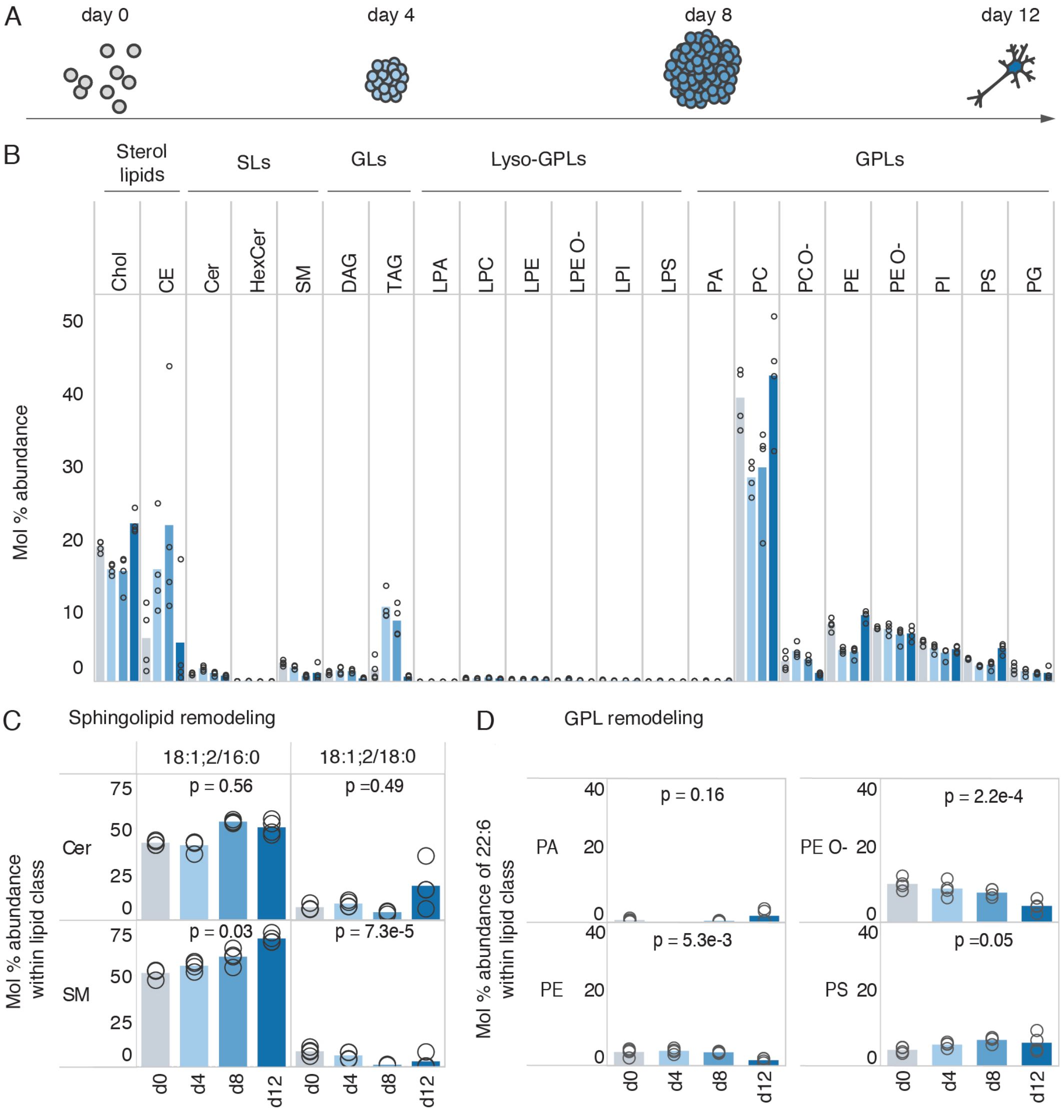

Figure 2.10: Lipidomics of mESCs differentiated into neurons *in vitro*. A) Schematic of the neuronal differentiation protocol for mESCs showing the stages at which samples were collected for lipidomics. Schematic by Lisa van Uden. B) Profile of different lipid classes across time. C) Profile of sphingolipids of interest within their respective lipid classes. D) Profile of 22:6 (DHA) among fatty acyls constituting PA, PE, PE O- and PS species. Data was collected on n = 4 replicates. p-values were obtained using a one-way ANOVA test and changes were considered significant if $p \leq p_c = 0.023$ as determined by the Benjamini-Hochberg procedure.

fatty acids, linolenic acid (18:3ω3) and linoleic acid (18:2ω6) were present in the media, their downstream products were not. Studies using primary rat neurons and astrocytes have previously shown that the PUFAs 22:6ω3 and 20:4ω6 are not produced by neurons, but rather by astrocytes from 18:3ω3 and 18:2ω6, respectively, and supplied thereafter to neurons [164, 165]. The culture media for *in vitro* neuronal differentiation of mESCs, containing the B27 supplement, are devoid of the essential polyunsaturated fatty acids DHA

(22:6ω3) and arachidonic acid (20:4ω6). Instead, the B27 supplement contains only the precursors, linolenic acid (18:3ω3) and linoleic acid (18:2ω6) [166, 167]. Hence, it is possible that the lack of the PUFA chains 22:6 and 20:4 in the lipids of cultured cells is due to a lack of the same fatty acids in the media. I wondered if the lack of 18:0-sphingolipids could similarly be due to a deficiency in dietary 18:0 from the media. In order to answer these questions, we next supplemented the cells with 18:0, 20:4 and 22:6 fatty acids and probed their lipidomes[6].

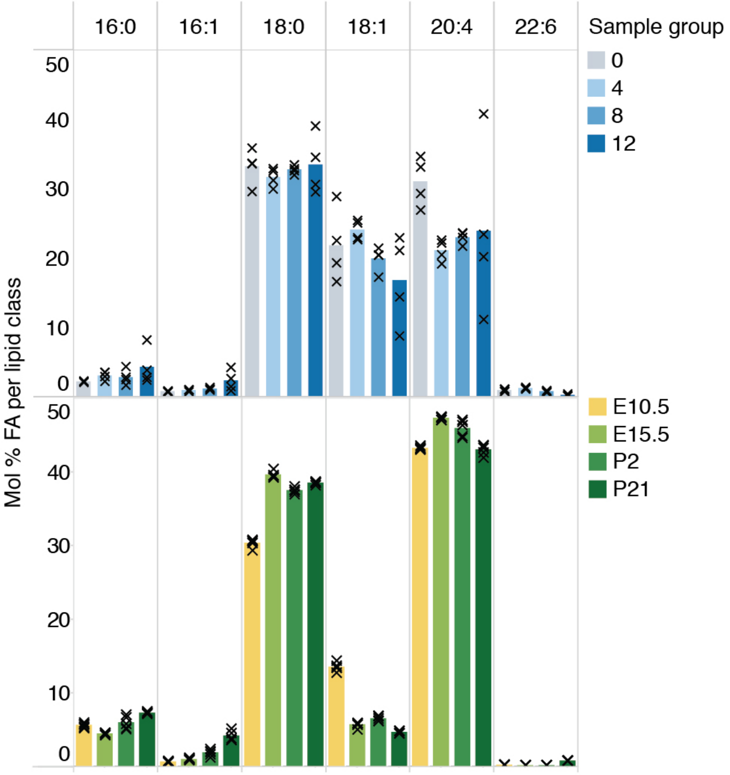

Figure 2.11: Fatty acid composition of PIs in mESCs differentiated into neurons *in vitro*. Comparison of the mol% abundances of various fatty acyl chains among PIs in mESCs being differentiated *in vitro* into neurons and mouse cerebral hemispheres over development. Data was collected on n = 4 replicates of cells and n = 5 replicates of brain tissue.

2.3.3 Fatty acid supplementation

Fatty acid (FA) supplementation to the cells in culture was performed by the widely used method of loading fatty acids to bovine serum albumin (BSA) and then adding the BSA-FA mix to culture medium [106, 168, 169]. The following fatty acids were supplemented by this method:

---

[6] Stem cell differentiation with fatty acid supplementation was performed by Nadine Fernandez-Novel Marx.

- Stearic acid (18:0) for incorporation into sphingolipids.
- Arachidonic acid (20:4) for incorporation into PI.
- DHA (22:6) for incorporation into PA, PE, PE O- and PS.

A mix of 18:0, 20:4, and 22:6 was used to obtain final concentrations of 30, 10, and 20 μM in the cell culture media, respectively, along with 30μM BSA (See section 4.3.4.1 for a detailed description of the method). The fatty acids were supplemented in cell culture media from day 8 of differentiation once the embryoid bodies were dissolved and cells were plated in N2 media, and the cells were collected for lipidomics on day 12 of differentiation (Fig. 2.12A).

Lipid extraction and MS$^{\text{ALL}}$-based lipidomics was performed on control and FA-supplemented cells from day 12 of differentiation as before. A total of 1200 lipids belonging to 26 lipid classes were quantified. The Student's t-test was used to find lipids significantly altered in abundance between control and FA-supplemented cells ($p \leq p_c = 0.029$, determined using a Benjamini-Hochberg procedure to account for multiple hypothesis testing, see section 4.4.7 for details). 310 lipids (26% of those detected) were significantly altered 2-fold or more in mol % abundance due to FA supplementation, of which 124 (10%) were increased and 186 (16%) were decreased in abundance (Fig. 2.12B).

In order to determine how many of these lipids contained a polyunsaturated acyl chain, I used the criterion that at least one of the acyl chains had 4 or more double bonds, and where acyl chain information was not available, that the lipid had a total of 4 or more double bonds. 112 out of 124 increasing lipids (90%) satisfied this criterion, suggesting that the increase in these lipids was largely due to supplementation with the PUFAs 20:4 and 22:6 (Fig. 2.12B).

Examining the relative abundances of lipid classes as a whole showed no changes due to FA supplementation (Fig. 2.12C). While the incorporation of supplemented fatty acids into lipids is not expected to change the relative levels of the lipid classes in itself, mammalian cells have been reported to alter these levels as a compensatory response to the resulting change in membrane packing and fluidity, known as *homeoviscous adaptation* [169–171]. In particular, Levental *et al* have reported that an increase in cellular cholesterol is a common response across several cell types including neurons, to both loading with DHA as well as arachidonic acid, in similar concentrations as those used here [169]. However, I did not observe an increase in cholesterol,

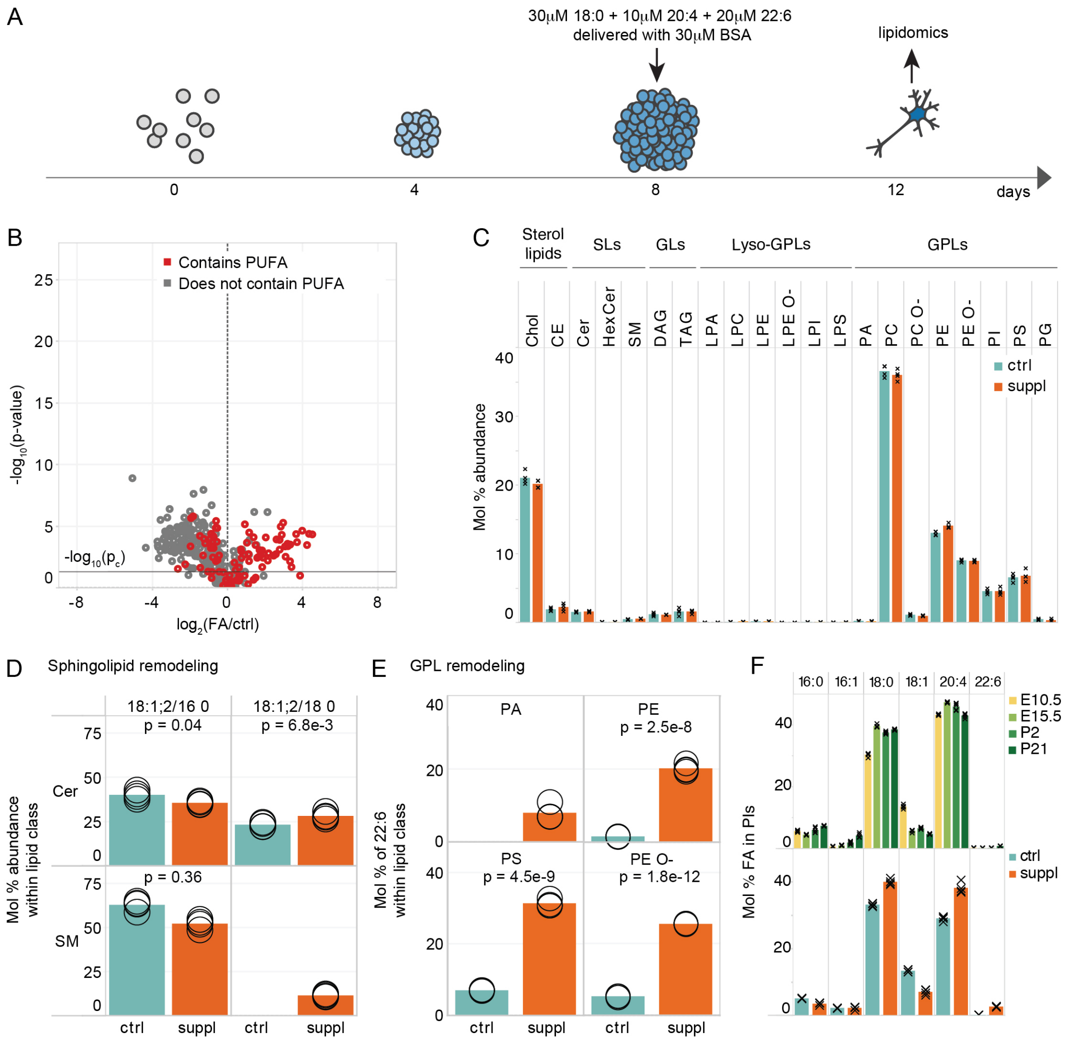

Figure 2.12: Fatty acid supplementation to mESCs undergoing neuronal differentiation *in vitro*. A) Schematic of the differentiation protocol where cells were supplemented with fatty acids. Schematic by Lisa van Uden. B) Volcano plot where each circle corresponds to a lipid. The fold-change in mol% abundance of each molecular lipid species was calculated between the FA-supplemented and control cells. The dashed line indicates the threshold for significance, $-log\_10(p_c)$, determined by a Benjamini-Hochberg procedure. C) Profile of lipid classes in control vs FA-supplemented cells. D) Profile of Cer and SM 18:1;2/16:0 and 18:1;2/18:0 in control and FA-supplemented cells on day 12 of differentiation. E) Profile of 22:6 among fatty acyls constituting PA, PE, PE O- and PS species. F) Mol % abundances of various fatty acyl chains among PIs in the developing cerebral hemisphere and in FA-supplemented *in vitro*-differentiated neurons. Data was collected on n = 4 replicates. p-values were obtained using Student's t-test and considered significant if $p \leq pc = 0.029$, as determined by the Benjamini-Hochberg procedure.

perhaps due to simultaneously loading the cells with the saturated stearic acid. Moreover, since both cholesterol and PUFAs are enriched in the brain and neural cell types, it is interesting to consider whether this feature is a result of homeoviscous adaptation. However, one finds that these events are not coupled in the developing brain, with PUFA enrichment starting much earlier in the embryonic phase as compared to cholesterol enrichment, which occurs only post-natally.

I next traced the incorporation of the loaded fatty acids into the desired lipids and found that 18:0 was incorporated only to a small extent into sphingolipids (Fig. 2.12D), whereas 22:6 and 20:4 were incorporated into the desired lipid classes (Fig. 2.12E and F). Specifically, the abundance of 22:6 increased to 8, 20, 31, and 25 mol % among all fatty acyl chains of PA, PE, PS, and PE O- classes (Fig. 2.12E), and 20:4 abundance in PIs increased from 29 to 38 mol % (Fig. 2.12F), making the distribution of fatty acyl chains in these classes similar to that observed in brain tissue.

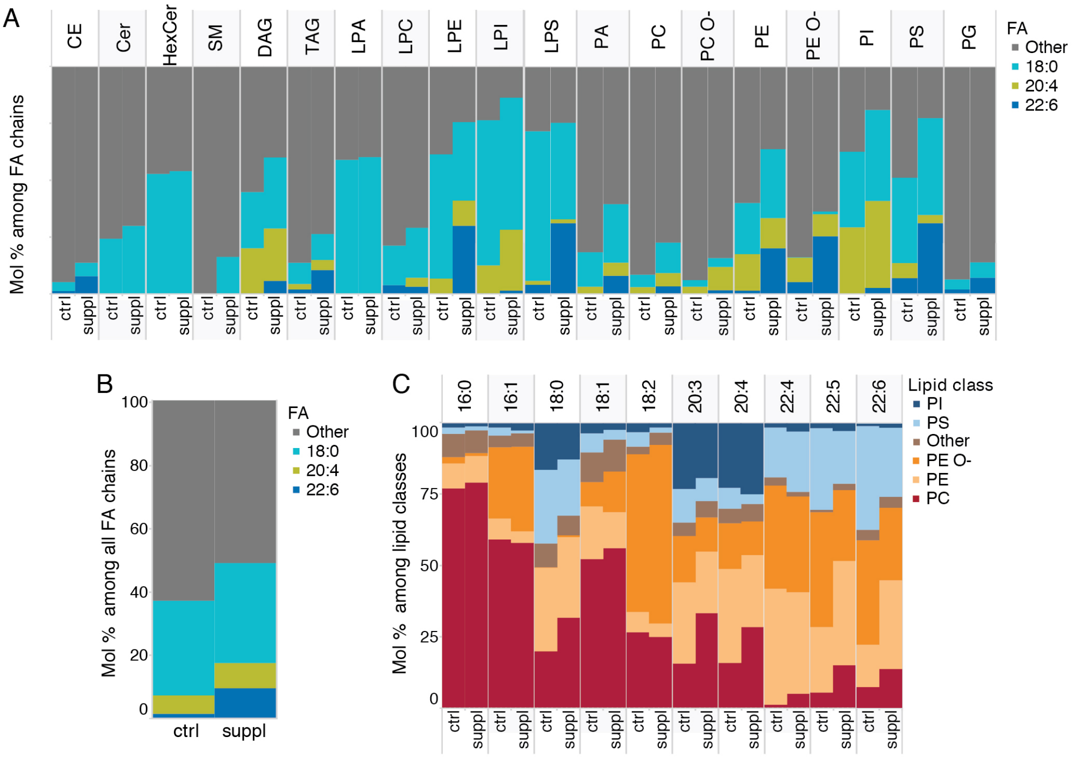

Figure 2.13: Fatty acid distribution within the cell lipidome A) Abundance of the three supplemented fatty acids among all those present in individual lipid classes of FA-supplemented cells, showing specificity in the incorporation of the supplemented fatty acids into lipids. B) The total abundance of the three supplemented fatty acids in the FA pool of FA-supplemented cells. C) Distribution of fatty acyl chains among the prominent lipid classes in which they are present. All values are averages from n = 4 replicates.

The relative abundances of the loaded fatty acids across lipid classes is shown in Fig. 2.13. Here, it is clear that there is high specificity in the incorporation of the loaded fatty acids:

- 18:0 is preferentially incorporated into SM and PC.

- 20:4 is preferentially incorporated into LPI, PI, and PC.
- 22:6 is most preferentially incorporated into PE, PE O-, LPE, PS, LPS, PA, and LPA, and to a lesser extent in other classes.

The outcome of the fatty acid supplementation experiment suggests some reasons for the absence of characteristic neural lipids in the neurons differentiated *in vitro*. While supplementation with the PUFAs 20:4 and 22:6 led to their preferential incorporation into the expected lipid classes, supplementation with 18:0 did not similarly induce the production of 18:0-sphingolipids. This indicates that the metabolic pathways necessary to generate 22:6-GPLs are established in the neurons differentiated *in vitro*, whereas those responsible for the synthesis of 18:0-sphingolipids are not established to the same extent. Hence, the absence of 22:6-GPLs in these neurons can be explained by a lack of suitable precursors in the culture medium, which also readily suggests a method for remedying this deficiency. To the contrary, the supply of 18:0 is not the limiting factor in the synthesis of 18:0-sphingolipids, and a change in the expression levels or activity of the corresponding metabolic enzymes is necessary to prompt the synthesis of 18:0-sphingolipids in these cells.

It is known that the Cer synthase CerS1 is specific for stearoyl-CoA [174], which results in the production of 18:0-sphingolipids, while the synthases CerS5 and CerS6 are responsible for 16:0-sphingolipid production. During brain development, one observes a 35-fold increase in the expression of CerS1 and down-regulation of CerS5 and CerS6 compared to embryonic tissue [172] (Fig. 2.14A). In contrast, during *in vitro* neuronal differentiation, between day 8 and 12, CerS1 expression increases only by 5-fold and, contrary to expectation, CerS6 expression is upregulated and CerS5 expression is unchanged [175](Fig. 2.14B). This could underpin the observation that 16:0-sphingolipids remain elevated whereas brain-specific 18:0-sphingolipids only increase marginally, despite supplementation with stearic acid. Overall, this suggests that appropriate programming of the sphingolipid metabolic machinery is not fully established in stem cell-derived neurons.

2.4 Conclusions and outlook

I began this chapter with the goal of answering two questions regarding the acquisition of a lipidome characteristic of neurons and brain tissue:

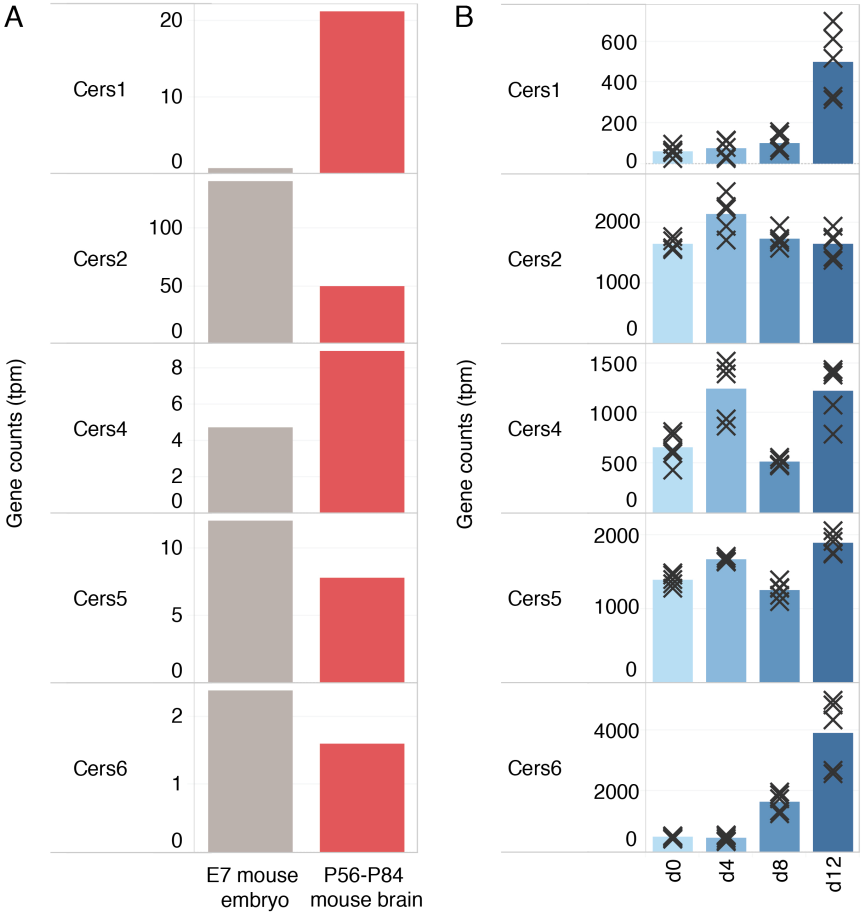

Figure 2.14: Expression levels of the ceramide synthases involved in sphingolipid synthesis. Expression levels are compared between E7 mouse embryos and pooled brain samples from P56-P84 mice. The data is from n =1 replicate and taken from the RNA-seq resource of Sladitschek and Neveu, 2019 [172]. B) Expression levels are compared across the *in vitro* differentiation of mESCs into neurons in embryoid bodies. The data is from n = 5 replicates and taken from the RNA-seq resource of Gehre et al., 2020. CerS1 and CerS4 are responsible for incorporating C18 chains into sphingolipids whereas CerS5 and CerS6 incorporate C16 chains [173].

1. When in development does the mouse brain acquire its unique lipid composition?
2. How are these changes in lipid composition coupled to neuronal differentiation?

And so in pursuit of these answers, I generated a lipidomic resource tracing the lipidome of developing mouse brain tissue, starting at the early embryonic stage. This resource complements previous lipidomic investigations of brain regions, cell types, and membrane fractions obtained from postnatal pups and adolescent animals [46, 136, 140, 141, 176, 177], and adds to the emerging multi-omics picture of neural development [178]. The time series further allowed me to trace the enrichment of neural lipid biomarkers across developmental time, based on which two groups of lipids could be identified: those that increased throughout development, starting in the embryonic stages (e.g., 22:6-GPLs and 18:0-SLs) and those that increased only post-natally (e.g., cholesterol and PE O-). Importantly, the dataset presented here is the first to look into the early embryonic mouse brain and make this distinction.

The early orchestrated changes to the lipidome of brain tissue coincide with the onset of neurogenesis and underscore the important role of lipids and their metabolism in the acquisition of function *in vivo*. To investigate this further on the cellular scale and answer the second question stated above, I turned to *in vitro* neuronal differentiation of mESCs following an established protocol [69]. Here, I did not find lipidomic changes similar to those observed *in vivo* and the canonical neural lipid biomarkers, previously shown to be present in primary neurons [140] and synaptic membranes [46, 136, 141] were lacking in the neurons differentiated *in vitro*. While this prevented me from further probing the coupling between lipid metabolism and cell identity, it brought to light a potentially important deficiency of stem cells differentiated into neurons *in vitro*.

To probe this deficiency further, I reasoned that two factors could result in impaired lipidome acquisition in this case, namely inappropriate programming of the underlying lipid metabolic machinery required for the biosynthesis of neural lipids, or the absence of required metabolic precursors, or a combination thereof. The causes can be delineated by delivering missing metabolites in the culture media and measuring the lipidomic response of the cells. Supplementing the cells with the necessary precursor fatty acids, I was able to determine that the metabolic pathways for incorporating PUFAs into specific lipid classes were established in the stem cell-derived neurons, whereas the metabolic pathways responsible for generating a dominant pool of 18:0-sphingolipids over 16:0-sphingolipids were not.

Modifications to the differentiation protocol may be required to induce the acquisition of a neural lipidome in neurons differentiated *in vitro*. Supplementation with DHA has been shown to improve neuronal function and the formation of synapses *in vivo* [104, 105, 107–110] as well as in primary cultures of neurons *in vitro* [102–106]. Together with the finding that neurons differentiated *in vitro* use supplemented DHA to generate the same 22:6-GPLs enriched *in vivo*, this suggests that DHA supplementation could improve *in vitro* neuronal differentiation. It would be important to assess gene expression and synaptic activity in response to such supplementation and the timing and dose need to be further optimized. The synthesis of 18:0-sphingolipids is another area where potential improvements are needed in order to generate neurons with neural lipidomes. Here, it would be important to identify and regulate the transcription factors responsible for controlling the expression of Cers1, Cers5, and Cers6.

More generally, these results highlight the need to assess *in vitro* differentiation protocols from a lipidomic perspective and to dissect the environmental and intrinsic cellular factors underlying the acquisition of cell type-specific lipidomes, and their impact on cellular function. While the concept of *cell identity* has traditionally revolved around the transcriptional state of gene expression, it is important to integrate the cell's metabolic state and lipidome into this view.

Here, it is important to note that the lipidomic and transcriptional axes of information are not orthogonal. The transcription of lipid metabolic enzymes, together with the availability of metabolic precursors from the environment determines the cell lipidome. This makes lipids important integrators of environmental and cellular signals during events like differentiation. At the same time, it is also known that lipids and their metabolic intermediates affect the transcriptional state of cells [20, 21]. D'Angelo and La Manno have recently proposed that membrane lipid composition could also affect the cellular response to environmental cues to differentiation via modulation of membrane-embedded receptor signaling activity [160]. In doing so, they suggest that cellular lipid composition is coupled bidirectionally to the transcriptional state of the cell.

Technical advances in spatial and single-cell lipidomics, alongside spatial and single-cell transcriptomics, can shed light on correlations between the two [179]. Developments in imaging mass spectrometry are particularly promising as lipids are not suitable targets for labeling and imaging by conventional methods like fluorescence microscopy [150]. Further, by doing away with lipid extraction and separation, this method can vastly improve throughput and allow for lipidomic screening over a large number of conditions, much like imaging-based screening methods for proteins. Rapid developments at both the technological frontier and the development of new differentiation models [180, 181] and organoid cultures [182, 183] make it an interesting time to study lipids in a developmental context.

Chapter 3

A role for lipids in the regulation of the actomyosin cortex

Having discussed neurons and the brain at great length, we now turn our attention to a different kind of cortex, namely the cell cortex or actomyosin cortex, which consists of a thin actin network ($\sim 0.2\mu m$) that is bound to the plasma membrane of cells. Such a structure is present in nearly all animal cells and serves to regulate cell shape (Fig. 3.1) by the action of double-headed myosin motors which generate contractile forces in the actin network by consuming energy from the hydrolysis of ATP molecules. The structure of the actomyosin cortex is remodeled on the order of 10s of seconds, in part due to the action of myosin and in part due to protein turnover, including the continuous polymerization and depolymerization of the actin filaments themselves. The dynamic actomyosin cortex is a subject of great interest to both biologists and physicists alike, for the key role it plays in cells [70–72], and for the interesting properties it exhibits as an adaptive and active material [184].

The regulation of cell shape by actomyosin is critical for a range of biological processes, such as cell division and migration, and faulty force generation in the network leads to a failure in these events [185–187]. In particular, the adhesion of the cortex to the plasma membrane is important for effecting cell shape changes [70, 188, 189] and has been proposed to restrict lateral diffusion in the membrane [190]. In this context, it is interesting to ask if tethering to the plasma membrane in turn affects the behavior of the cortex, and to what extent the composition and mechanical properties of the plasma membrane influence the cortex. This is the focus of the present chapter.

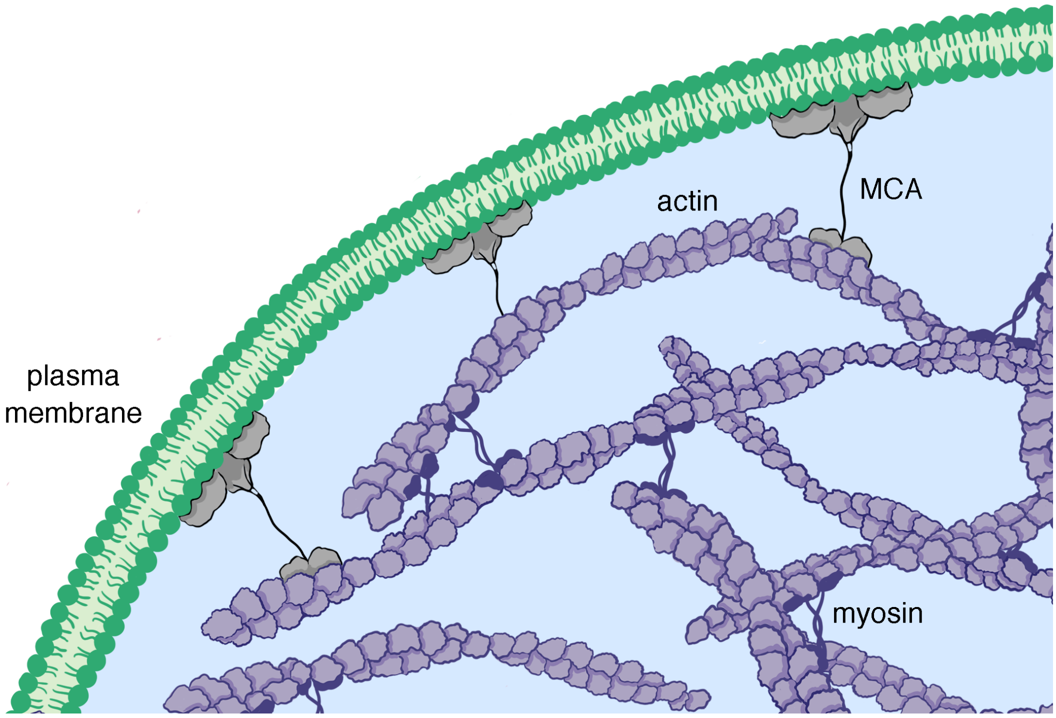

Figure 3.1: The animal cell surface. Simplified schematic of the animal cell surface, consisting of the plasma membrane, actomyosin cortex its associated proteins. The membrane-to-cortex attachment (MCA) proteins shown here tether the cortex to the membrane.

3.1 Perturbations to lipids in cells

A very powerful approach to studying the role of a molecule in a living system is to perturb its steady-state level and observe the response of the system. This approach has been used for decades to study genes and the proteins they encode.

Since proteins are the direct products of genes, their concentration in cells is subject to gene regulation. Advances in our understanding of molecular biology and the modern tools born from it allow us to routinely overexpress and mutate proteins and to knock in, knock down, and knock out genes, or place them under inducible promoters to control their expression at will. These sophisticated genetic techniques have made it possible to perturb protein levels and thereby elucidate the function of $\sim 10^4$ individual proteins in genetically tractable model organisms.

In comparison, it is more difficult to perturb the levels of individual lipids in living cells, since they are metabolites. Individual lipid levels depend on the activity of a series of enzymes involved in their synthesis and the concentration of other metabolites from which they are made. Perturbing enzymes

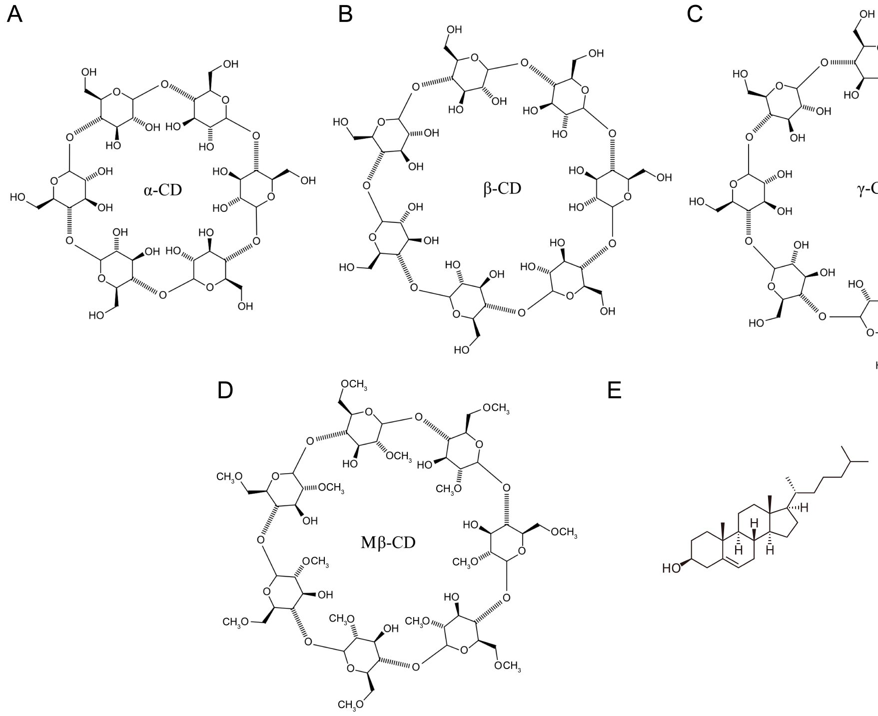

Figure 3.2: Cyclodextrins. Structures of (A)$\alpha-$, (B)$\beta-$ and (C)$\gamma-$ cyclodextrin, which are hexameric, heptameric, and octameric rings of glucose, respectively. (D) Methyl β-cyclodextrin, which forms an inclusion body with (E) cholesterol in its hydrophobic core.

in the pathway therefore generally has the effect of redirecting the metabolic flux and altering the levels of other related molecules.

Another approach is to control the concentrations of available precursors in the diet, such as with the supplementation of fatty acids discussed in the previous chapter. However, as several lipids share precursor metabolites and are interconvertible through enzymatic reactions, it is not always possible to achieve selectivity using this approach.

A class of molecules known as cyclodextrins has proved to be useful with regard to perturbing lipid levels in cells. Cyclodextrins are water-soluble cyclic oligosaccharides, consisting of 5 or more glucose monomers arranged around a hydrophobic core (Fig. 3.2). They were first described as crystalline products in the enzymatic degradation of potato starch by Antoine Villiers in 1891 [191]. Today, they are widely used in various industries for catalysis, nanotechnology, and drug delivery [192, 193]. Over 30 approved drugs in circulation include cyclodextrin as an ingredient. This is due to the ability of cyclodextrins to form inclusion complexes with hydrophobic molecules at their core and screen these molecules from ambient water in an aqueous solution, making it possible to deliver otherwise insoluble drugs.

Cyclodextrins also form inclusion complexes with lipids and can be used as vehicles for the delivery of exogenous lipids, and in some cases, to deplete lipids from cells by their encapsulation into inclusion complexes. For the latter, high selectivity towards the targeted lipid is required. The selectivity of cyclodextrins towards molecules depends on the size and hydrophobicity of the cavity. For instance, the cavity in α-cyclodextrin accommodates molecules with aliphatic chains such as phospholipids relatively well but is too small to accommodate cholesterol, which is preferentially bound by β-cyclodextrins [194, 195]. γ-cyclodextrin can bind more varied and larger molecules and has been used to deliver fluorescently labeled phospholipids and sphingolipids to cells in culture [196–198].

Several chemical derivatives of the cyclodextrins shown in Fig. 3.2 have been synthesized, where cavity size and hydrophobicity can be tuned by chemical modifications to achieve higher specificity towards particular molecules. For instance, methylation increases hydrophobicity in the ring, and hence the affinity of cyclodextrins to lipids. Methyl α-cyclodextrin has been successfully used to exchange endogenous phospholipids and sphingolipids of the outer leaflet of the plasma membrane for exogenous lipids in mammalian cells [199]. Given the size and hydrophobic similarity of various phospholipids and sphingolipids, it is still a challenge to target individual species with high specificity. However, its unique molecular structure makes cholesterol a suitable target.

In particular, methyl β-cyclodextrin (MβCD) shows high affinity towards cholesterol and has been widely used to both deplete and deliver cholesterol in cells [195, 200–202]. It binds cholesterol in a 2:1 ratio, likely since the height of an individual MβCD ring (0.8nm) can screen only half the cholesterol molecule (1.8nm) from solvent [195, 203–205].

Given the unique molecular structure and synthesis pathway of cholesterol, it is an ideal target for all forms of perturbation, including enzymatic intervention using statins[1], modulation of lipoprotein levels in the media of cultured cells[2], and direct acute intervention using MβCD. Even so, statin- and lipoprotein-based approaches require several hours of treatment to produce the desired perturbation to cholesterol, whereas MβCD is effective

---

[1] Statins are small-molecule inhibitors of the enzyme HMG-CoA reductase, which catalyzes the rate-limiting step in the mevalonate pathway, responsible for the synthesis of cholesterol and other isoprenoids.

[2] Lipoproteins are biomolecular assemblies consisting of a core formed from cholesterol and triglycerides, surrounded by a monolayer of phospholipids and lipoproteins. They serve to transport lipids in extracellular fluids and are usually present in the media of cultured mammalian cells.

within an hour and acts with high specificity towards cholesterol directly at the membrane.

The unique molecular properties of cholesterol, its proposed role in the formation of ordered membrane domains, and its importance in physiology and disease all make it a very interesting candidate for perturbative studies. The use of MβCD has further made it the most widely studied lipid in cell biology. In the following section, we take a closer look at cholesterol and the emerging view of its role in cell mechanics.

3.2 Cholesterol

Cholesterol was postulated to be a component of the outer membrane of cells by Charles Overton in the late 19th century, long before the lipid bilayer structure of membranes was described [7, 8]. Today, we know that it is an essential component of animal cell membranes which is synthesized in all animal cells. It is notably distinct in molecular structure compared to all other membrane lipids, due to the absence of fatty acyl chains and the presence of hydrophobic rings (Fig. 1.1).

The unique structure of cholesterol lends unique properties to the membranes it is a part of, as I shall discuss in the following sections.

3.2.1 Role in lipid bilayers

Much of what we know about the behavior of cholesterol in membranes comes from the careful characterization of artificial lipid membranes and Molecular Dynamics (MD) simulations [211, 212]. The following observations have been made with regard to the presence of cholesterol in lipid bilayers:

1. ***Condensation effect.*** The condensation effect of cholesterol has been known for nearly a century. One of the earliest observations of this phenomenon was made using a mixture of egg-lecithin and cholesterol at the air-water interface (similar to the experiments discussed in section 1.2.1) by John Leathes in 1925 [213]. He observed that the binary mixtures have average molecular surface areas much smaller than that expected for ideal mixtures, and the same has been observed for various cholesterol-phospholipid mixtures in bilayers (Fig. 3.3A, B). X-ray [214–217] and neutron scattering [218–220] have shed light on the orientation of molecules within the bilayers, showing that the

acyl chains of the phospholipids orient perpendicular to the plane of

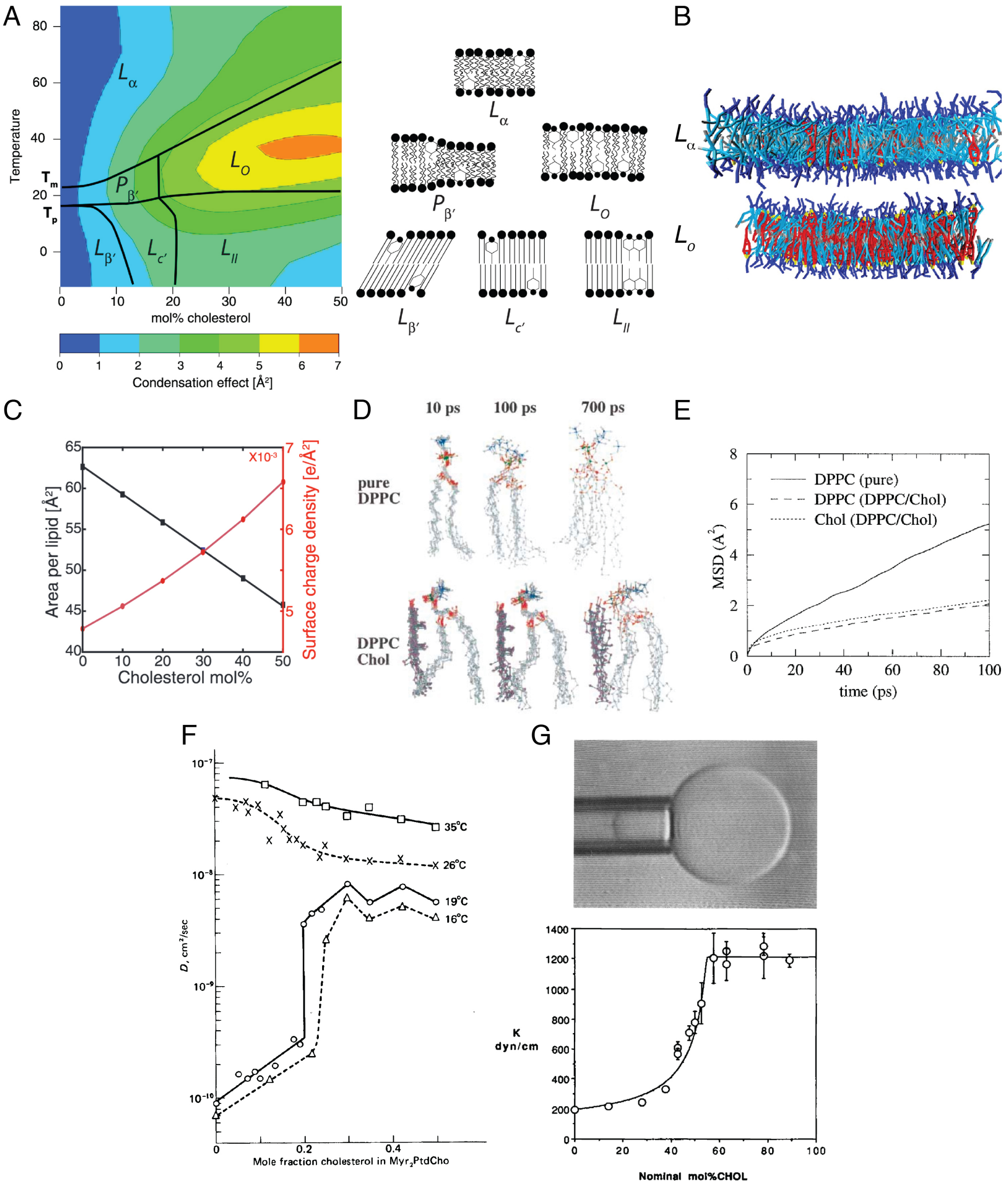

Figure 3.3: The effect of cholesterol on phospholipid bilayers. A) Phase diagram for a binary mixture of DMPC (PC 14:0-14:0)–cholesterol obtained by molecular dynamics simulations. B) Snapshots from the molecular dynamics simulations of PC 14:0-14:0-cholesterol bilayers containing 10% (top) and 40% cholesterol (bottom) and existing in the liquid crystalline phase L_α and liquid-ordered phase, L_o, respectively. The condensation effect is made clear by displaying the same number of lipid molecules in both membranes. Panels A and B are from de Meyer and Smit, 2009 [206]. C) Plot from Doktorova *et al*, 2017 [207] showing the calculated area per lipid (black) and surface charge density of the membrane as a function of cholesterol abundance in a POPC (PC 16:0-18:1)/POPS (PS 16:0-18:1)/cholesterol mixture. *Contd.*

Figure 3.3: *Contd.* D) Snapshots of configurations sampled by individual DPPC (PC 16:0-16:0) molecules in the molecular simulation of either a pure DPPC bilayer (top row) or one containing 12.5 mol % cholesterol over 10, 100, and 700ps of simulation, demonstrating the loss of molecular motions in the phospholipid when interacting with a cholesterol molecule. E) A plot of mean square displacement of the center of mass of the molecules in D. Panels D and E are from Tu *et al*, 1998 [208]. F) Plot of the Diffusion coefficient (D) of a fluorescent lipid probe in DMPC (PC 14:0-14:0)-cholesterol membranes over a range of temperatures, from Rubenstein *et al*, 1979 [209]. G) Micropipette aspiration-based measurements of membrane elastic modulus, κ, as a function of cholesterol concentration in SOPC (PC 18:0-18:1)-cholesterol vesicles from Needham and Nunn, 1990 [210].

the lipid layer in the presence of cholesterol. The condensation phenomenon has been explained by the formation of complexes between cholesterol and membrane phospholipids [221, 222]. It has been proposed that this could result from the need to screen the hydrophobic cholesterol molecule from solvent, which is enabled by closer packing of the phospholipids around cholesterol [223]. MD simulations show that cholesterol restricts the thermal motion of the adjacent phospholipids and their acyl side-chains [206, 208, 224] (Fig. 3.3D, E).

2. ***Increased thickness.*** The decreased surface area of individual molecules is accompanied by the thickening of the bilayer, which has been reported using x-ray and neutron scattering and is also observed in MD simulations [206, 220–222, 225]. Since membrane proteins tune the length of their hydrophobic membrane-spanning domains to the membrane thickness, this has important consequences for membrane protein structure and function [226, 227]. The enrichment of cholesterol in the plasma membrane is thought to account for the increased length of trans-membrane domains in plasma membrane proteins, compared to proteins residing in the internal membranes of eukaryotic cells. For instance, the membrane-spanning α-helices of proteins residing in the plasma membrane of cells are typically 20 residues long, whereas similar helices are only 15 residues long for Golgi membrane proteins [228].

3. ***Surface hydration and charge.*** The headgroups of phospholipids form the interface with water molecules on both sides of the lipid bilayer, and are involved in the formation of hydrogen bonds with solvent molecules that constitute a hydration layer [229]. This hydration layer also penetrates into the bilayers, at packing defects between fatty acyl

chains [230]. Studies using fluorescent probes show that the presence of cholesterol reduces the hydration of the bilayer [231, 232].

The pursuit of molecular mechanisms governing the assembly of HIV (human immunodeficiency virus) particles has further revealed interesting effects of cholesterol on membrane hydration and surface charge density. The assembly of infectious HIV particles requires the interaction of the viral structural protein Gag with headgroups of lipids in the inner leaflet of the plasma membrane, and it is known for decades that cholesterol is essential for this process [233, 234]. A 2017 study combining small-angle neutron scattering experiments with molecular dynamics simulations shed light on the role of cholesterol in this process [207]. Cholesterol reduces the hydration of the phospholipid headgroups, which in turn reduces screening of the surface charge on anionic lipid headgroups that interact electrostatically with the positively charged amino acid residues on Gag (Fig. 3.3C). This phenomenon likely plays an important role in determining the interactions of several peripheral membrane proteins with the membrane.

4. ***Bending rigidity and elasticity.*** Mechanically, membranes can be characterized in terms of their response to two kinds of mechanical perturbations: stretching and bending. Both of these perturbations cost energy and the energy cost to deform the membrane by a fixed amount is an intrinsic property of the membrane which can be expressed in the form of an elastic modulus, termed bending rigidity in the case of a bending deformation and the elastic modulus in the case of stretching. By studying membrane deformations in lipid vesicles, it has been found that the incorporation of cholesterol into the bilayer increases both the bending rigidity and elastic modulus for a number of phospholipids, meaning that cholesterol makes membranes more resistant to both bending as well as stretching (Fig. 3.3G) [210, 235–239].

5. ***Membrane packing and fluidity.*** All of the above phenomena result from a change in the packing of lipids when cholesterol is present in the bilayer and are different manifestations of the fact that cholesterol-phospholipid mixtures form a phase distinctly different from the liquid crystalline and the gel phases described in section 1.2.3. This is termed the liquid-ordered phase [240] and is characterized by a fluidity lower than that in the liquid crystalline phase but higher than in the gel phase.

Hence, cholesterol buffers membrane fluidity over a range of temperatures and prevents the abrupt change in membrane fluidity that occurs with the main phase transition of the bilayer [241]. Above the melting temperature of a phospholipid bilayer, cholesterol causes a decrease in membrane fluidity and below the melting temperature, it causes an increase in the bilayer fluidity (Fig. 3.3F) [209, 242, 243].

6. ***Phase separation.*** In 1987, Subramaniam and McConnell visualized the coexistence of two immiscible phases in monolayers made of binary mixtures of dimyristoyl phosphatidylcholine (DMPC or PC 14:0-14:0) and cholesterol [244]. The phase space of binary phospholipid-cholesterol mixtures in monolayers and bilayers has been studied in detail [245–249]. Some of the phase diagrams hence constructed are qualitatively similar to those of regular three-dimensional liquid mixtures while others show the unusual existence of two upper miscibility critical points, which has not been experimentally observed for any other liquid mixture [248]. Importantly, at ambient and physiological temperatures (above 20°C), only mixtures of saturated lipids and cholesterol are reported to phase-separate. The complex mixtures of lipids in biological membranes are likely to offer rich possibilities, but live in a high-dimensional phase space and are exceedingly complex to model.

   Domains rich in cholesterol and sphingomyelin and insoluble to certain detergents have been isolated from plasma membranes of cells [55], in line with the lipid raft proposal [45], but the direct observation of distinct lipid phases in the plasma membrane of live cells has been elusive and continues to be widely debated [250–253]. Hence, it remains unclear to what extent perturbations to the cholesterol composition of live cells change the phase behavior of cell membranes, although observations from such experiments have extensively been interpreted as resulting from disruptions to rafts [254–268].

3.2.2 Role in cell mechanics

As discussed in section 3.1, MβCD has been widely used to perturb cholesterol levels in mammalian cells and effects have been reported on the morphology, motility, and mechanical properties of cells. These observations point to changes in the actomyosin cytoskeleton responsible for the regulation of cell shape, motility, and mechanics and are summarized below:

1. ***Polarization and migration.*** Studies have demonstrated that cholesterol depletion using MβCD inhibits polarization and migration in several cell types including MCF-7 adenocarcinoma cells [254], T cells [257, 258], Jurkat cells [257], neutrophils [259], endothelial cells [269] and HL-60s [261]. Cholesterol-loading has been found to both enhance and suppress migration, depending on the cell type and the amount loaded [270–272].

2. ***Cell spreading.*** It has been observed in several cell types including fibroblasts, neutrophils, and cancer-derived cells that cholesterol depletion causes cells to spread less and round up, whereas cholesterol-loading causes increased cell spreading [255, 256, 262–264, 273]. In a recent paper by Sun *et al*, the opposite effect was reported in human mesenchymal stem cells, where cholesterol depletion caused cells to be more spread and cholesterol loading caused them to round up [268]. The former was found to abrogate adipogenic differentiation while the latter facilitated the same.

3. ***Adhesion.*** Although cell rounding due to cholesterol depletion was initially interpreted to be an effect of reduced adhesion, it has been shown that cholesterol-depleted cells form larger focal adhesions and register higher traction forces on the substrates compared to control cells, despite their rounded morphology [267, 274]. In contrast to cell-substrate adhesion, cholesterol depletion has been shown to disrupt the formation of cell-cell adherens junctions between cells in a monolayer [275].

4. ***F-actin***[3]. Conflicting reports have been made on the effect of membrane cholesterol on F-actin levels in cells. Kwik *et al* report on the effects of cholesterol depletion on the cytoskeleton, by culturing human skin fibroblasts (5659) and B-lymphoblasts over days in LDL-depleted medium or with acute depletion using MβCD and found fewer F-actin stress fibers in both cases [276]. To the contrary, Chubinskiy-Nadezhdin *et al* find that F-actin levels increase upon cholesterol depletion using MβCD in human myeloid leukemia cells (K562), predominantly in the cell cortex [277]. Studies have also reported on increased F-actin in stress fibers of mouse osteoblasts (MC3T3-E1), human prostate cancer cells (PC3), and mouse fibroblasts (WTCL3) in response to cholesterol

---

[3] Filamentous actin in the polymerized form, as opposed to globular G-actin in monomeric form.

depletion [265, 266]. Despite conflicting reports on F-actin concentration in cholesterol-depleted cells, data from Kwik *et al* and others are in agreement when it comes to the rate of actin turnover, indicating that cholesterol-depleted cells have a faster actin turnover as compared to control cells [266, 276].

5. ***Cortical Properties.*** Cholesterol depletion has been reported to cause increased cortical stiffness in BAECs [278], human embryonic kidney (HEK 293) cells [279], mouse fibroblasts (WTCL3) [266] and human mesenchymal stem cells [268], and analysis of fluctuations at the surface of a variety of cholesterol-depleted mammalian cell lines has demonstrated a loss of amplitude and lengthening of relaxation time due to this stiffening [266, 280]. On the other hand, loading the cells with cholesterol has been reported to make the cell surface more deformable in human neutrophils and HL-60s [273]. Cholesterol is also found to play a role in modulating membrane-to-cortex adhesion strength, which is increased upon cholesterol depletion and weakened by cholesterol loading to BAECs and HEK cells [281, 282].

Despite similarities in the observations made by independent research groups, a number of diverging mechanisms have been proposed. The effects are commonly attributed to a disruption of lipid rafts upon cholesterol depletion. The phosphorylated forms of PIs, PIP (PI 4-phosphate), PIP2 (PI 4,5-bisphosphate), and PIP3 (PI 3,4,5-trisphosphate) are important groups of strongly anionic membrane lipids which act as a substrate for several signaling proteins and are thought to form clusters associated with rafts, which sort proteins and help maintain cell polarity [283–289]. Notably, several regulators of actomyosin such as the Ezrin-Radixin-Moesin (ERM) family of membrane-to-cortex attachment (MCA) proteins and WASP are binding partners of PIP2 [290, 291], and the redistribution of PIP2 following cholesterol depletion is therefore thought to explain the effect of cholesterol depletion on actomyosin [259, 260, 268, 276].

The unclustering of integrins and other membrane proteins upon disruption of lipid rafts has also been observed and linked to the effect of cholesterol depletion on actomyosin, particularly in the form of stress fibers [254, 257, 258, 261]. Some authors have proposed that rafts influence the strength of integrin binding to the extracellular matrix and the cytoskeleton [255, 256, 262–264], whereas others propose mechanisms that involve the activation of signaling pathways via Rac, Rho, Rho GTPases, Src kinases, Ca^{2+} influx and caveolin [265–267].

A handful of papers propose that the effects caused by perturbations to cholesterol could result from a change to plasma membrane viscosity [269, 270, 272]. For example, Kanayasu-Toyoda *et al* observed that the suppression of cell migration caused by cholesterol-loading to BAECs could be reversed by concomitantly loading the cells with eicosapentaenoic acid (EPA, 20:5), a known membrane fluidizer [270]. Vasanji *et al* show that the viscosity of the membrane in the leading edge of migrating BAECs is lower than at the trailing edge, whereas cholesterol depletion disrupts this regulation by decreasing membrane viscosity at the trailing edge [269]. They further demonstrate that phospholipid membrane vesicles encapsulating actin made with cholesterol are more deformable than those lacking cholesterol. Interestingly, this supports a purely physical influence of membrane cholesterol independent of downstream cell signaling and suggests that cells could spatially regulate membrane viscosity to achieve shape changes and migratory behavior.

Another physical effect involving the ERM family of MCA proteins has been proposed by Sun *et al* [268]. The ERM proteins are active in their phosphorylated state and bind to PIP2 in the plasma membrane via their FERM domain and to actin via a different domain. Sun *et al* propose that cholesterol concentration in the membrane can regulate the activity of ERM proteins, as suggested by altered levels of phosphorylated ERM proteins in response to cholesterol depletion and loading observed in human mesenchymal stem cells [268], and changes to membrane-to-cortex adhesion measured by tether pulling in BAECs and HEK cells [281, 282].

Although there has been extensive research into the role of cholesterol in regulating signaling and mechanics at the mammalian cell surface over the last three decades, there are conflicting reports and a variety of mechanisms have been proposed. As a result, a complete understanding of how membrane cholesterol impacts the organization and behavior of the actomyosin cortex and its interaction with the plasma membrane continues to remain elusive. I address this question in the present chapter of my thesis, using 3T3 mouse fibroblasts as a model system.

While nearly all studies have relied on MβCD to perturb cholesterol levels, the concentrations used and duration of treatment vary. Additionally, lipid composition and cholesterol levels vary with cell type [18, 160], and the controls used vary between studies. Since membrane properties are further affected in a non-monotonic and non-linear manner relative to cholesterol concentrations (section 3.2.1), depletion of varying amounts of cholesterol from varied cell types could contribute to the heterogeneity in the observed effects. Therefore, thorough quantification of the relevant parameters is required.

In the above studies, cholesterol levels have predominantly been quantified by indirect methods, such as filipin staining [254, 257, 258, 268, 280, 292] or by assessing cholesterol oxidation [256, 262–264, 266, 273, 275, 279, 282], or not quantified at all [261, 265, 267, 270, 274, 276]. The use of mass spectrometry can allow direct and more precise quantification of cholesterol. It is also of interest to characterize the effect of MβCD on other lipids, to observe off-target interactions of MβCD [293] as well as any compensatory homeostatic response of the cell [169]. To address these questions, I first set up a pipeline combining the biochemical isolation of the plasma membrane, quantitative lipidomics and proteomics[4], in order to characterize the complete effect of MβCD treatment on the plasma membrane lipidome and proteome.

3.3 Cholesterol depletion in 3T3 mouse fibroblasts

3.3.1 Optimisation of MβCD treatment

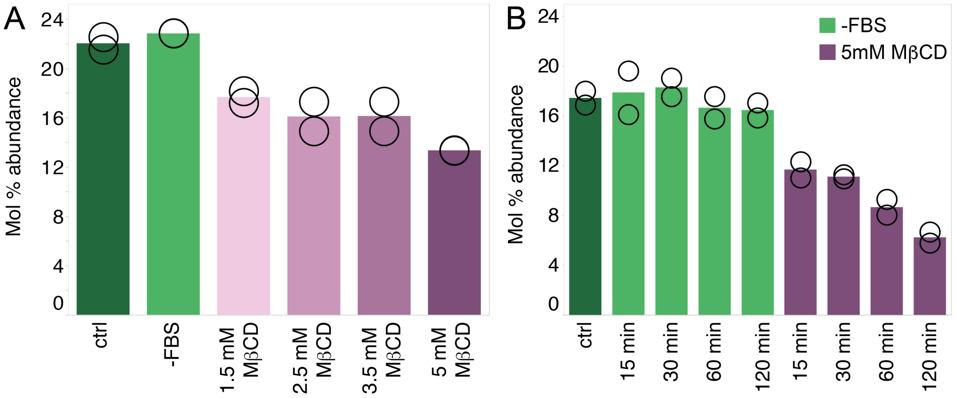

Figure 3.4: Optimisation of MβCD treatment in serum-free media. A) Mol % cholesterol abundance in whole-cell lipid extracts as measured using MS^{ALL}-based lipidomics. Cells treated for 30 minutes with varying concentrations of MβCD were analyzed. B) Mol % abundance of cholesterol in whole-cell lipid extracts from cells treated with 5mM MβCD over varying durations. Cells cultured in serum-free media (-FBS) for an equal duration were used as controls.

---

[4] Lipid extraction and mass spectrometry for all lipidomics experiments described this chapter were performed by Richard R. Sprenger at SDU, Odense. Proteomics was performed by Per Haberkant, Henrik Hammaren, and Frank Stein at the Proteomics core facility at EMBL, Heidelberg.

As a first step towards addressing the above questions, I determined the appropriate conditions for cholesterol depletion from 3T3 mouse fibroblasts using MβCD. Since MβCD binds to lipids present in the serum of cell culture medium, it has extensively been delivered to cells in media lacking serum [254, 256, 257, 261–268, 273, 274, 278–282]. Initially, I treated cells with 1.5mM, 2.5mM, 3.5mM, and 5mM concentrations of MβCD in serum-free media (denoted -FBS for fetal bovine serum) and harvested the cells after 30min of treatment. Then a lipidomics analysis of these samples was performed to quantify cholesterol abundance in whole cells relative to a control sample of cells grown in complete medium, and an additional control sample of cells treated with serum-free medium but no MβCD for 30 minutes (Fig. 3.4A). No difference in cholesterol abundance was observed due to serum starvation alone, and 5mM MβCD showed the strongest effect, resulting in the depletion of 40% of cellular cholesterol.

Next, I collected cells treated with 5mM MβCD 15, 30, 60, and 120 minutes into the treatment and analyzed the whole-cell lipidomes. In accordance with previous reports [200, 294, 295], one observes a biphasic efflux of cholesterol from the cells, where a sharp decline of 33% of cellular cholesterol levels occurred within the first 15 minutes of treatment, followed by a slower decline, resulting in the depletion of 36%, 50% and 64% of cellular cholesterol at 30, 60 and 120-minute time points (Fig. 3.4B).

When I started working on cholesterol, Sun *et al* had recently reported on changes to MCA via the phosphorylation of ERM proteins in response to modifying cholesterol content of cells, and MCA was emerging as an important factor in the regulation of several biological processes [296–300]. Therefore, I decided to test the impact of cholesterol depletion on MCA and ERM phosphorylation in 3T3 mouse fibroblasts.

3.3.1.1 Dynamic tether pulling to measure MCA

To measure the strength of MCA, I used atomic force microscopy (AFM) and performed dynamic tether pulling [301, 302]. The experimental procedure is described in detail in section 4.10.1 and Fig.3.5A shows a schematic of the experiment from Diz-Munoz *et al*, 2010 [187].

To perform dynamic tether pulling using AFM, a cantilever is used to pull tethers from the plasma membrane of cells at varying speeds, and the dynamic tether force, F_d is measured during tether breakage, as a function of the pulling speed, v. The dynamic tether force has been modeled by Brochard-Wyart *et al* in terms of the speed-invariant equilibrium tether force F_0 that would be measured if the tether were allowed to break when the cantilever is at rest, and the viscous term α that is determined by membrane-to-cortex adhesion in case of the cell membranes, as follows [303]:

$$F_d(F_d^2 - F_0^2) = \alpha v \tag{3.1}$$

By fitting the above equation to the Force-velocity plot, one can obtain the MCA parameter, α, which is expressed as

$$\alpha = 2(2\pi)^3\kappa^2\nu\eta_e ln\frac{r_c}{r_t} \tag{3.2}$$

where κ is the bending rigidity of the membrane, ν is the density of MCA proteins, η_e is the effective viscosity, and r_c and r_t are the cell and tether radii, respectively.

For an ideal elastic membrane with no viscous losses, the tether force would not depend on pulling speed, and would always yield F_0. It is noteworthy that the above model captures the non-linear dependence of dynamic tether force on velocity, consistent with experimental observations. Brochard-Wyart *et al* explain that the non-linearity is a consequence of the tether radius depending on pulling speed, $r_t(v)$ [303]. It is also important to note that the parameter α also depends on membrane bending rigidity, κ, and the viscosity of the lipid bilayer (this contributes to η_e) which are assumed to remain unchanged when interpreting α as a measure of membrane-to-cortex adhesion.

When I performed dynamic tether pulling on MβCD-treated cells, I observed no significant change in the value of the fitted parameters α between control cells under serum-free conditions (-FBS) and MβCD-treated cells (Fig. 3.5B). Following this, I performed a western blot (see section 4.5 for a detailed description of the method) to assess the phosphorylation of ERM proteins during 30 minutes of treatment with 5mM MβCD. While I did not find a significant change in phosphorylated (pERM) levels due to the MβCD treatment, I could observe a 2.7-fold decrease in pERM levels normalized to GAPDH[5] due to serum-starvation. In order to test if this was due to a change in the phosphorylation state alone, or a change in the concentration of ERM proteins, I also performed a western blot and stained for ERM proteins, independent of their phosphorylation state and found that their net level did not change significantly due to serum starvation. This confirmed that the observed reduction in pERM levels as a result of serum starvation was due

---

[5] GAPDH: Glyceraldehyde-3-Phosphate Dehydrogenase

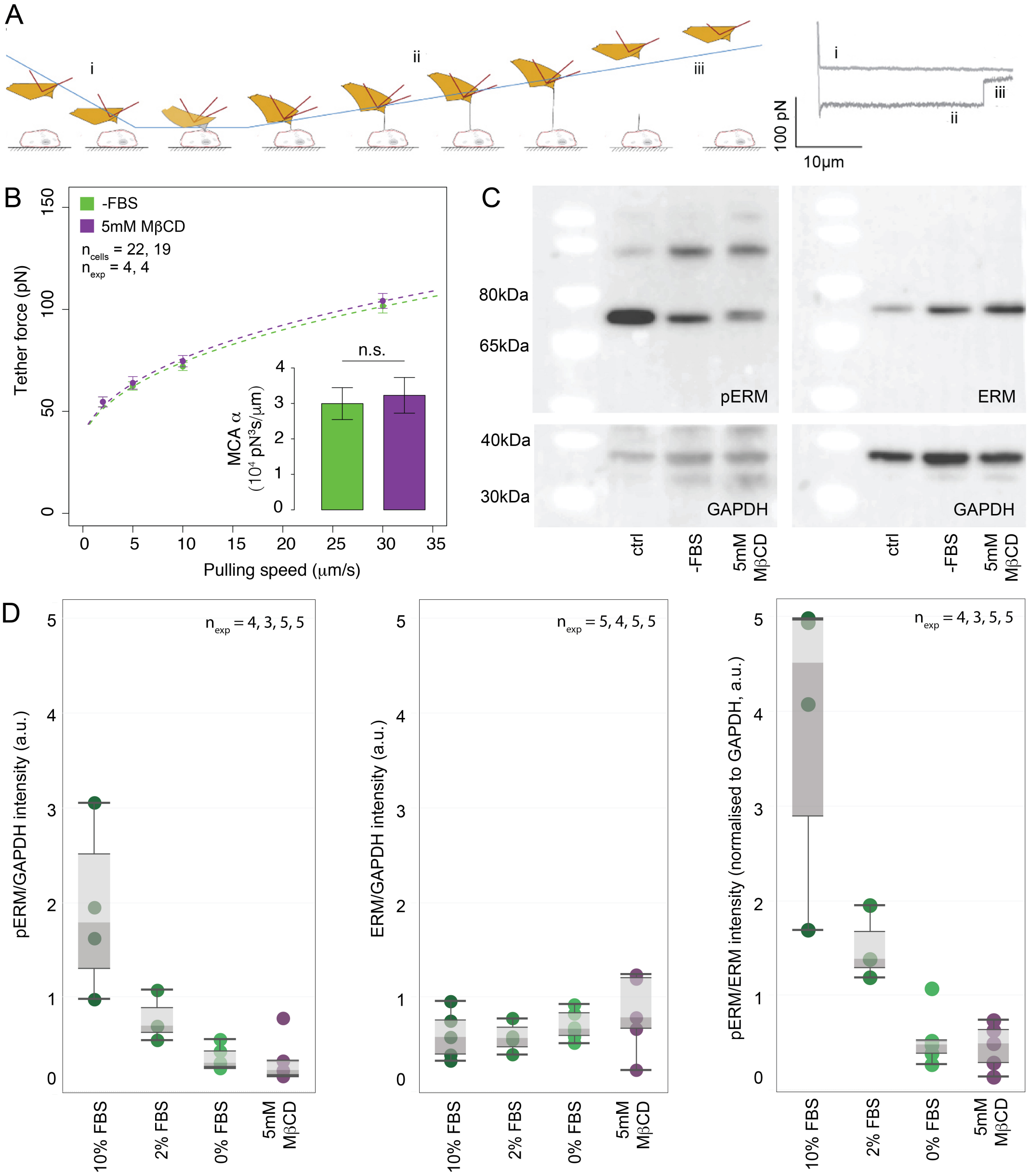

Figure 3.5: The effect of MβCD on MCA in serum-free media. A) Schematic of a dynamic tether-pulling experiment showing i) approach, ii) retraction, and iii) tether breakage. A corresponding force curve with force (y-axis) as a function of cantilever height (x-axis) is shown on the right. Schematic from Diz-Munoz *et al*, 2010 [187]. B) Average tether force as a function of pulling speed for control (green) and MβCD-treated cells (purple). The dotted lines correspond to fitted curves and the inset shows the value of the MCA parameter α obtained from the fits. C) Representative western blots against pERM and ERM with GAPDH as a loading control. D) Quantification of bands from western blots like those shown in C. Bands that showed artifacts were not quantified and all pERM and ERM intensities were normalized to the GAPDH intensity from the corresponding lane.

to a change in the phosphorylation state, which resulted in a 9-fold decrease in the pERM/ERM ratio (Fig. 3.5C,D). A dose-dependent decrease in ERM phosphorylation due to the removal of serum was confirmed by measuring pERM levels in cells grown in media containing 2% FBS (as opposed to 10% FBS present in complete media) for 30 minutes.

3.3.1.2 MβCD treatment using delipidated FBS

Due to the dramatic decrease in ERM phosphorylation observed as a result of serum starvation, I looked for an alternative method to perform cholesterol depletion without using serum-free media. I found that Kwik *et al* had used lipoprotein-deficient FBS for MβCD treatment instead of completely removing serum from the cell culture media. Therefore, I used commercially available delipidated FBS (Table 4.2) and measured pERM levels in cells grown with 10% delipidated FBS in place of regular FBS. I found that the use of delipidated FBS (del FBS) did not significantly alter pERM levels in the cells (Fig. 3.6A, B). Therefore, 5mM MβCD treatment in media prepared with 10% del FBS was preferred over serum starvation, and the impact of this treatment on the cell lipidome was assessed using mass spectrometry-based lipidomics, as before. A similar level of cholesterol depletion was achieved in the presence of 10% del FBS as previously observed in serum-free conditions, with 13%, 38%, 51%, and 63% of cellular cholesterol being depleted 15, 30, 60, and 120 minutes after the addition of MβCD (Fig. 3.6C).

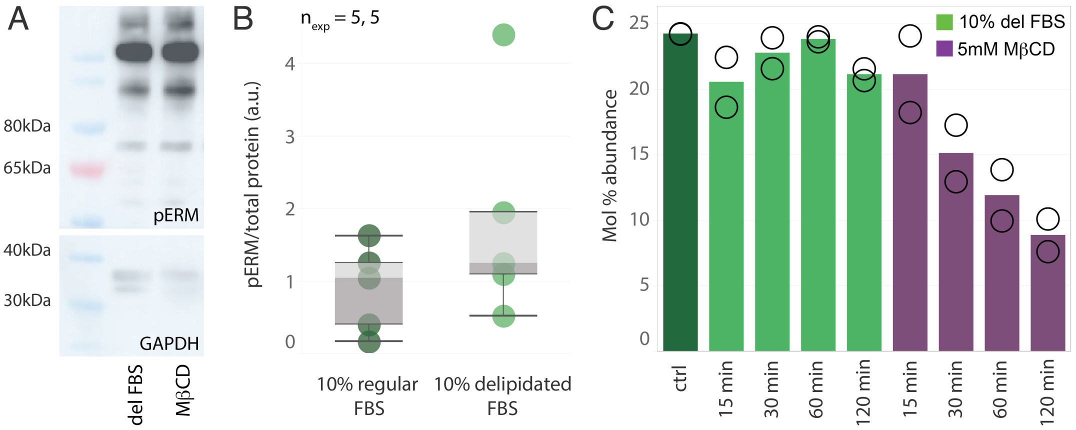

Figure 3.6: MβCD treatment using delipidated FBS. A) Representative western blot stained for pERM and GAPDH. B) Quantification of pERM bands from western blots such as the one shown in A. Since several of the GAPDH bands showed artifacts similar to that seen in A, the pERM signal was normalized to the total protein amount present in the loaded samples, measured by BCA. C) Mol % cholesterol abundance determined by MS^{ALL} lipidomics of whole-cell lipid extracts.

A total of 1577 lipids from 25 lipid classes were quantified by lipidomics. I performed a one-way ANOVA on the abundances of individual lipid species as well as lipid classes to identify lipids significantly altered in abundance between sample groups, followed by a Benjamini-Hochberg procedure for multiple-hypothesis testing (See section 4.4 for details on statistical methods). This analysis yielded no other significantly altered lipids, demonstrating the specificity of MβCD to cholesterol, as well as the lack of any lipidome remodeling response within the first two hours of cholesterol depletion in the cells.

3.3.2 Plasma membrane isolation

In addition to optimizing MβCD treatment for cholesterol depletion in 3T3 mouse fibroblasts, I also optimized a pipeline for isolating plasma membranes from these cells, in order to study the effect of cholesterol on plasma membrane lipids and proteins in particular. For this, I used the Minute PM isolation kit (Table 4.6), which works based on differential centrifugation.

3.3.2.1 Evaluation of plasma membrane isolates

To measure the enrichment of plasma membrane in the isolates, I collected samples from six different stages in the isolation protocol, which have been described by the manufacturer to contain the following:

1. WCL: The whole cell lysate.
2. Nuc: Intact cell nuclei isolated from the whole cell lysate.
3. Cyto: The cytosolic fraction recovered from the supernatant after sedimentation of all membranes.
4. Int: Internal organellar membranes.
5. Pre-W: Plasma membrane prior to the final wash and centrifugation step.
6. PM: Final washed plasma membrane isolate.

I repeated the isolation twice, starting with $2*10^7$ cells grown in 4x 15cm dishes, and collected the above-described six fractions both times. The total protein content in each fraction was measured using the BCA test (section 4.4.2) and sample volumes containing a total of 10 μg protein were used for proteomics (See section 4.7 for a description of methods.)

The proteomics analysis allowed the quantification of 4287 and 4458 proteins in the two replicates of the experiment. A Gene Ontology-based approach was adopted to measure the enrichment of proteins annotated to different cellular components (CC) in the various fractions, as shown in Fig. 3.7A, C for one replicate. The detected proteins were classified according to their cellular component annotation. When they had more than one CC annotation, they were grouped under the 'ambiguous' category. The intensity of all uniquely annotated proteins in each of the fractions was then compared to the whole cell lysate and the fold-changes were averaged by category (Fig. 3.7B, D). From the heatmaps, one can observe a clear enrichment of plasma membrane proteins in the PM fraction. Additionally, one can observe mitochondrial and nuclear proteins enriched in the Nuc fraction, and proteins annotated 'cytoplasm' and 'cytosol' enriched in the Cyto fraction (Fig. 3.7B).

When a more detailed CC annotation is used, one can further resolve proteins into more specific categories (Fig. 3.7D). In this case, one observes that the contamination from 'ER, Golgi, Perox, Lyso' proteins in the isolated plasma membranes observed in Fig. 3.7B arises mainly due to a strong enrichment of lysosomal proteins in the plasma membrane (Fig. 3.7D), whereas proteins annotated to the ER, extracellular matrix, peroxisomes, and the Golgi apparatus are found to be enriched in the Nuc fraction.

Quantitative plots of the fold-changes of individual proteins averaged over the two replicates are provided in Fig. 3.8. On average, proteins annotated uniquely to 'plasma membrane', 'ER, Golgi, Perox, Lyso', 'Mitochondria', and 'Nucleus' were present in the isolated plasma membranes at 5.8, 3.1, 0.7, and 0.4 -fold, relative to the WCL.

Since CC annotations are not specific to membrane proteins, I also performed a similar analysis using a manually-curated list of markers for the plasma membrane and organelle membranes, comprising ER, Golgi, mitochondrial, and nuclear membrane (Fig. 3.9). On average, plasma membrane markers were enriched 6.8-fold in the plasma membrane isolates relative to WCL (Fig. 3.9A), whereas organelle membrane markers were depleted 0.6-fold relative to WCL (Fig. 3.9B), on the whole. Specifically, mitochondrial, nuclear, ER, and Golgi membrane markers showed fold-changes of 0.9, 0.4, 1.6, and 0.5 in the PM fraction, relative to WCL.

Overall, the proteomic analysis revealed a considerable (on average 6-fold) enhancement of plasma membrane proteins over other categories of proteins in the isolated PM fractions, and I proceeded with using this method for the lipidomic analysis of plasma membranes. First, I also assessed the

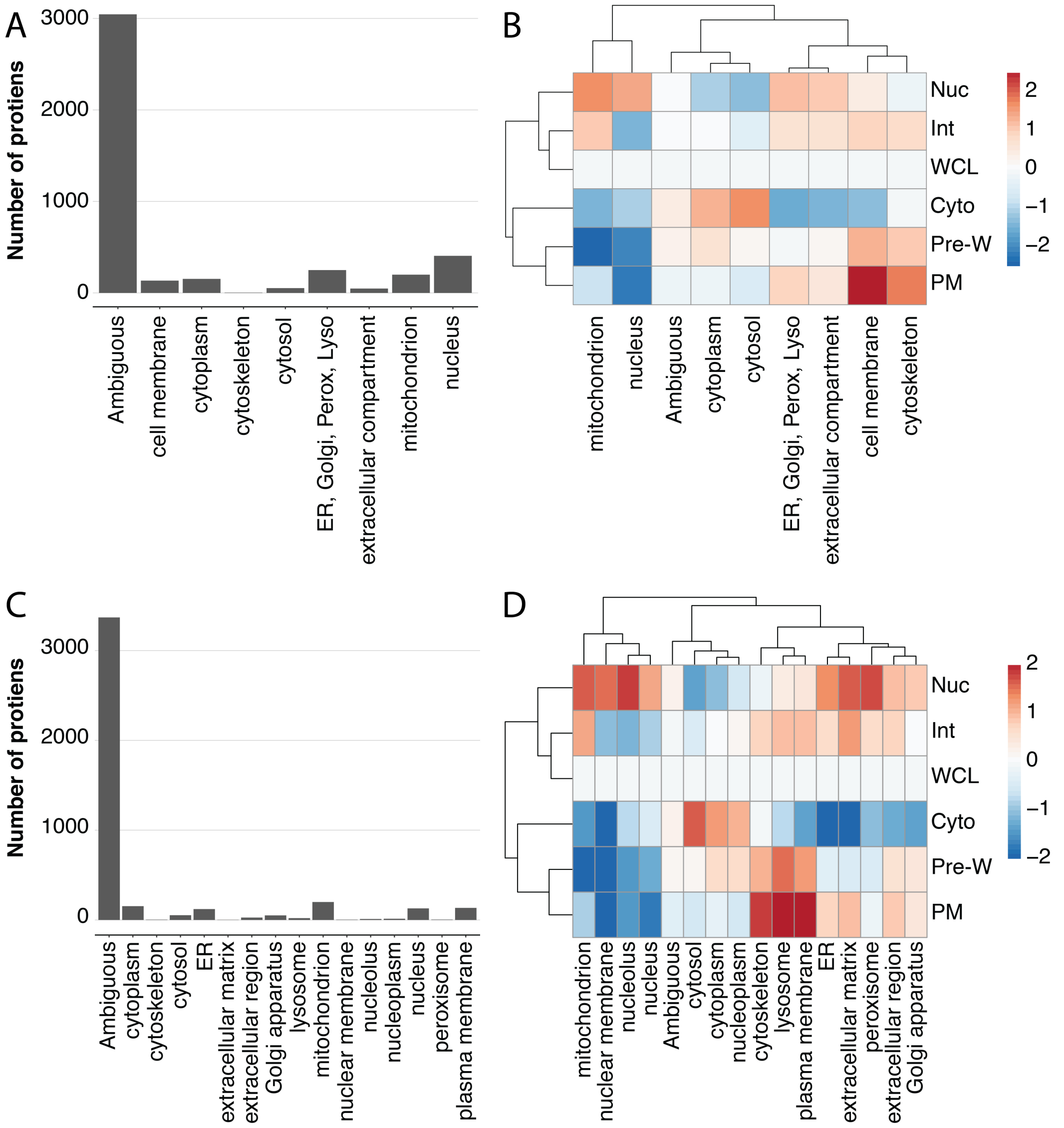

Figure 3.7: Gene ontology-based Proteomics analysis of plasma membrane isolates. A), C) Number of proteins classified into each category according to their Cellular Component GO annotations at two levels. B), D) The average fold-change in the abundance of proteins from each CC category per fraction obtained from PM isolation, relative to the whole cell lysate.

lipid composition of the isolated plasma membranes in relation to the whole cell lipidome (Fig. 3.10).

A total of 823 lipids from 31 lipid classes were quantified and the Student's t-test was used to find significantly altered lipid levels between the two sample groups. 17 lipids showed significant differences between whole cells and PM isolates with $p \leq p_c$, where the cut-off p_c was determined to be 0.0012 by the Benjamini-Hochberg procedure, with a false-positive rate of 5%. Of these 17 lipids, 5 were decreased in abundance (all cardiolipins) and 12 were increased in abundance (8 sphingomyelins and 4 phospholipids) in

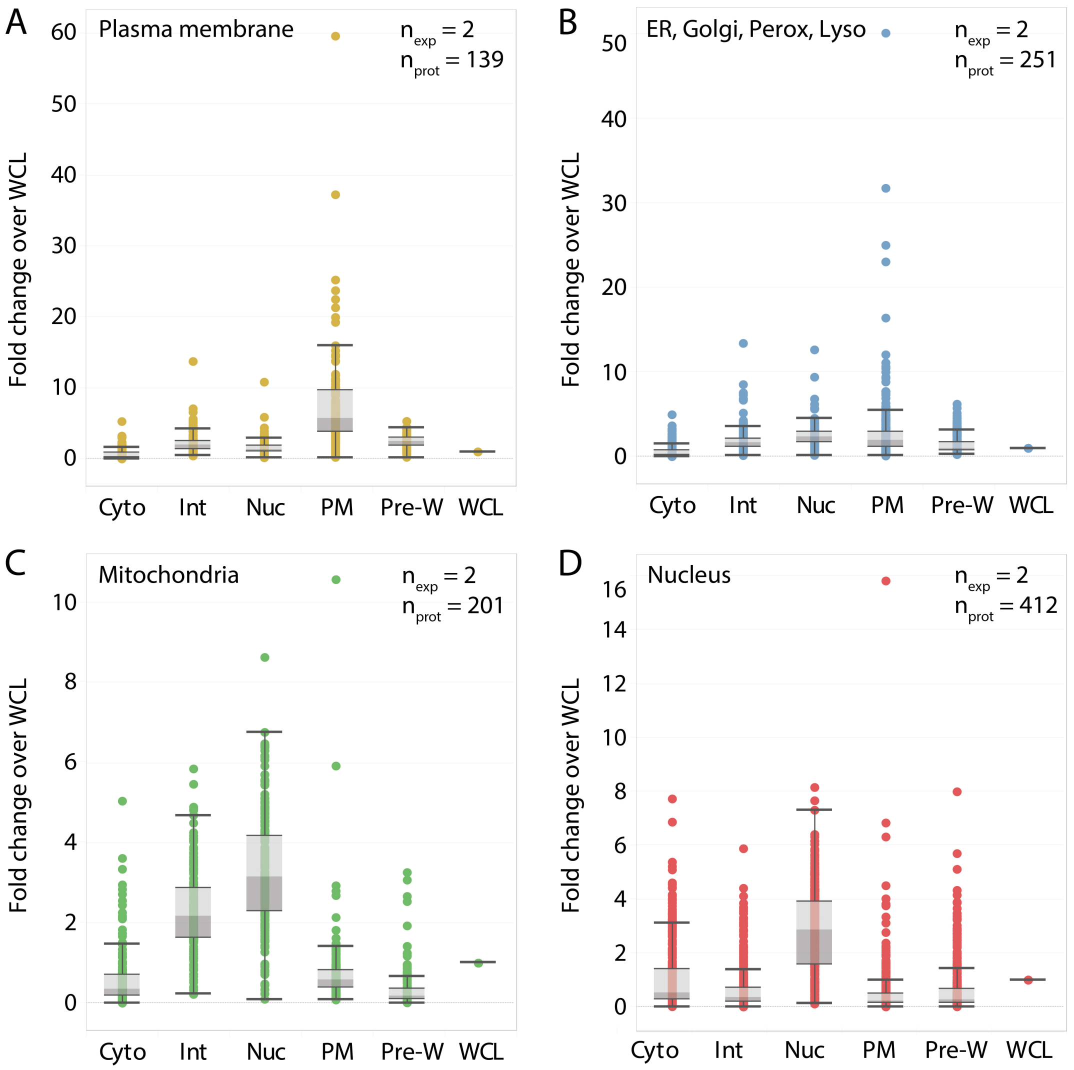

Figure 3.8: Estimation of isolation efficiency using GO analysis. Fold change in the abundance of individual proteins in each fraction relative to the whole cell lysate, for proteins annotated uniquely to the categories 'plasma membrane' (A), 'ER, Golgi, Perox, Lyso' (B), 'Mitochondria' (C) and 'Nucleus' (D).

the PM isolates relative to whole cells. This is shown in Fig. 3.10A as a volcano plot, where each lipid is colored according to its lipid class. Here, cholesterol and sphingolipid are collectively grouped under the 'PM lipid class' category, since they are known to be enriched in the plasma membrane relative to other membranes [47], and cholesterol esters, non-esterified fatty acids, cardiolipins, and monolysocardiolipins are grouped under the 'Non-PM lipid class' category. From this plot, it is clear that the plasma membrane is enriched for cholesterol and sphingolipids, and depleted of lipids not expected to be present in the plasma membrane. The net relative abundances of lipid classes (Fig. 3.10B) further reflect this.

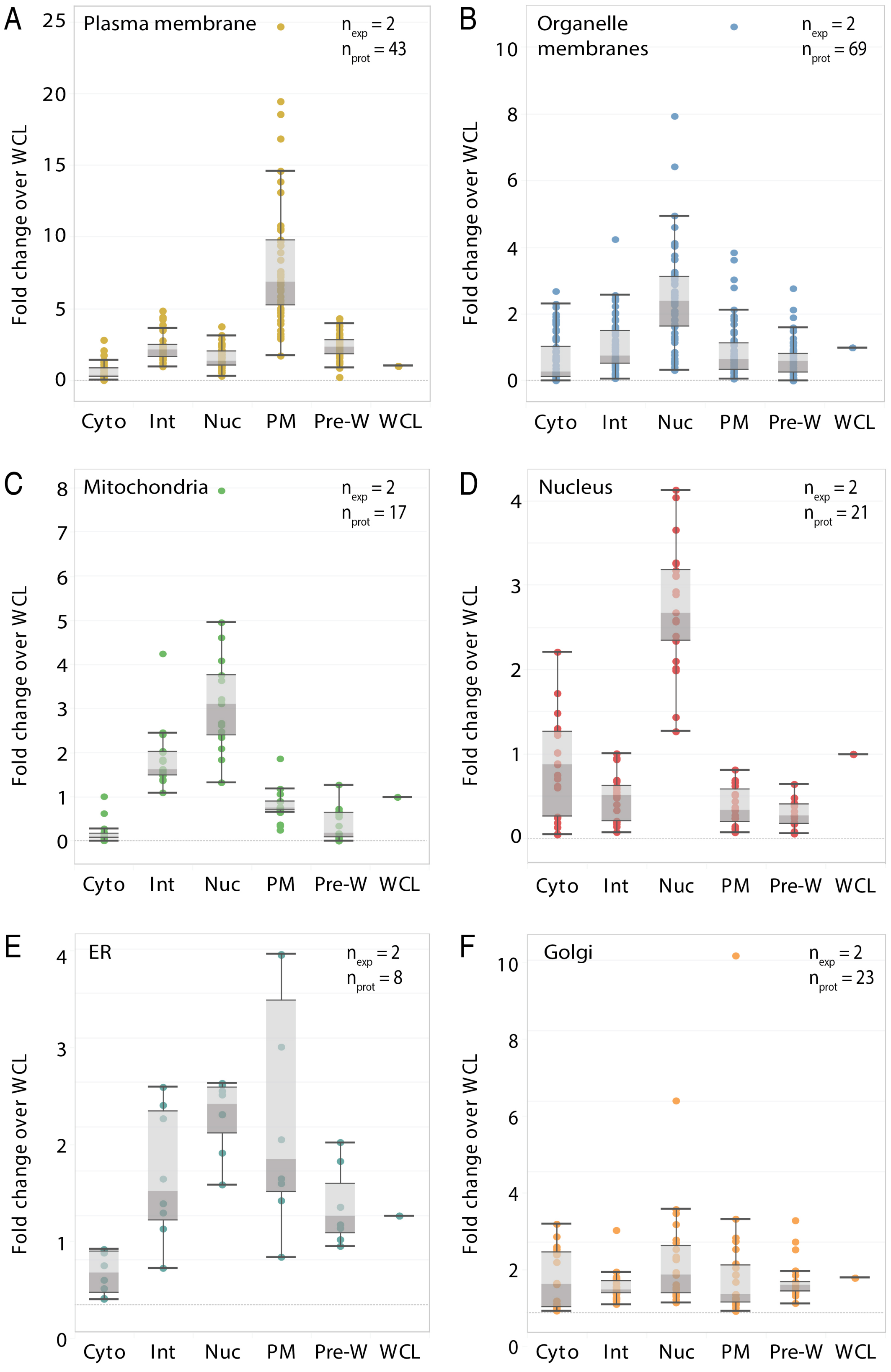

Figure 3.9: Estimation of isolation efficiency using membrane markers. *Contd.*

Figure 3.9: *Contd.* Fold change in the abundance of individual proteins in each fraction relative to the whole cell lysate, for membrane markers of ′=plasma membrane (A), pooled organellar membranes (B), Mitochondria, (C) Nucleus (D), ER (E) and Golgi (F). Lists of membrane markers were curated manually based on commercially available antibodies used for marking the respective membranes in immunostainings and known function in specific membranes as reported on UniProt.

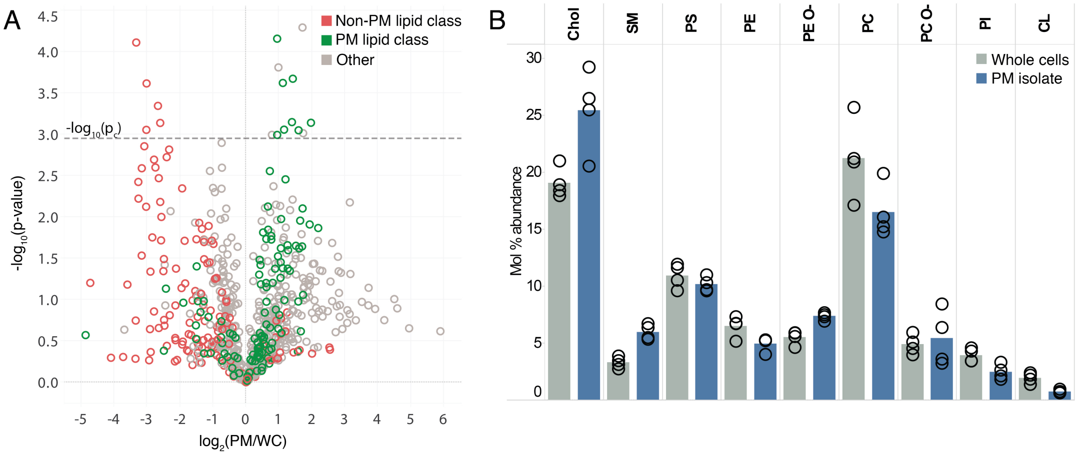

Figure 3.10: Lipidomic analysis of plasma membrane isolates. A) Volcano plot comparing the mol % abundance of individual lipids between isolated plasma membranes and whole-cell lipid extracts. -log$_{10}$(p-value) is plotted against log$_2$(PM/WC) where each circle is an individual lipid species. All p-values were determined using the Student's t-test and the dashed line corresponds to the cut-off p_c = 0.0012 determined by the Benjamini-Hochberg procedure for multiple hypothesis testing. B) Mol % abundance of lipid classes in whole cell lipid extracts and plasma membrane isolates.

3.3.2.2 Characterization of cholesterol-depleted PM

Since the isolation of plasma membranes from 3T3 mouse fibroblasts was successful, I next applied this pipeline to analyze the lipid and protein composition of the plasma membrane in cholesterol-depleted cells. For this, plasma membrane was isolated from cells grown in media containing 10% del FBS for 30 min (ctrl) and from cells treated with 5mM MβCD for 30 minutes and lipidomics and proteomics were performed on these samples.

A total of 1148 lipids from 25 lipid classes were quantified by lipidomics. Cholesterol levels were found to decrease by 24% in the plasma membrane after 30 minutes of treatment with 5mM MβCD (Fig. 3.11). This is not as strong an effect as the 38% decline observed in total cellular cholesterol levels over the same duration of treatment (Fig. 3.6C), indicating that the loss of cholesterol from the plasma membrane is partially compensated by transport of cholesterol from the cells' reserves to the plasma membrane.

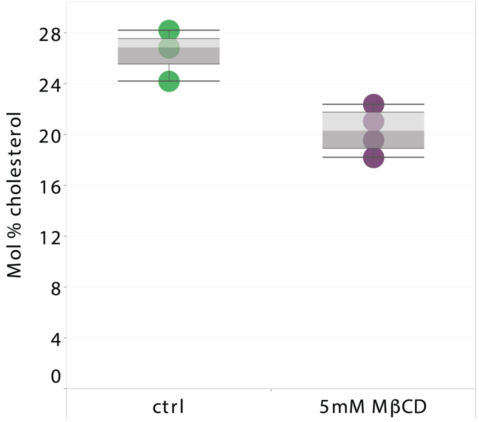

Figure 3.11: Cholesterol depletion in the plasma membrane. Mol % abundance of cholesterol in plasma membranes isolated from control cells incubated in media containing 10% del FBS (ctrl) and cells treated with 5mM MβCD for 30 minutes.

A statistical analysis followed by correcting for multiple hypothesis testing revealed no other significant changes in membrane lipid composition upon cholesterol depletion, similar to what I observed for the whole cell lipidome upon cholesterol depletion. Similarly, a proteomics analysis spanning 3831 proteins in total yielded no significant changes in protein levels between plasma membranes isolated from control and MβCD-treated cells.

Taken together, these results suggest a lack of large-scale lipidomic or proteomic changes at the plasma membrane in response to cholesterol depletion using MβCD, which in itself also acts with high specificity towards cholesterol.

3.4 The cellular response to cholesterol depletion

Having characterized the effect of MβCD on both the cellular lipidome and specifically, the lipid composition of the plasma membrane in 3T3 mouse fibroblasts, I proceeded to characterize the mechanical response at the cell surface resulting from cholesterol depletion.

3.4.1 Fluorescent labeling of the plasma membrane

While studying the cellular response to cholesterol depletion, it became clear to me that it would be advantageous to fluorescently label the plasma membrane of the cells, as it would enable the following:

1. Study of cell morphology in 3D using confocal microscopy.

2. Measurement of membrane viscosity by studying the diffusion of the fluorophores.
3. Imaging and segmentation of the cell cortex distinctly from other actin structures to measure the intensity of cortical proteins.

Therefore, I proceeded to fluorescently label the cell membrane. First, I used the plasma membrane-labeling dye PKH67 (See section 4.3.5 for the staining protocol). However, within 30 min of labeling, most of the dye was internalized by the cell and the plasma membrane staining was weak compared to the signal from vesicles (Fig. 3.12A). Hence, I decided to proceed with expressing a fluorescent protein with a plasma-membrane localization sequence.

For this, I used Green Fluorescent Protein (GFP) tagged with a CAAX domain (GFP-CAAX). The CAAX motif is a sequence of four peptides containing a cysteine (C) followed by two aliphatic amino acids (A1 and A2) and one of several amino acids in the terminal position (X), where the cysteine undergoes isoprenylation and binds to the inner leaflet of the plasma membrane.

Lipofectamine-based transfection was used to transiently express GFP-CAAX (See section 4.3.6 for a detailed description of the method). While this provided more specific staining of the plasma membrane (Fig. 3.12B), the transfection efficiency was poor, yielding heterogeneous and low levels of fluorescence in the cell population as determined by flow cytometry (Fig. 3.12C). To resolve this, I generated a stable cell line expressing GFP-CAAX using lentiviral transduction and sorted a sub-population of the cells to ensure uniform levels of GFP-CAAX expression[6] (sorted-low). These cells are referred to as GFP-CAAX 3T3s in the following sections.

3.4.2 Membrane fluidity

Several studies have previously measured the diffusion coefficient of lipids [281, 304–306], transmembrane proteins [305, 307], proteins that are bound to the inner leaflet of the plasma membrane [305, 306] as well as cell-surface proteins on the outer leaflet [305] under conditions of cholesterol depletion using MβCD. While Goodwin *et al* found that cholesterol depletion did not

---

[6] Done with the help of Ewa Sitarska, and Diana Ordonez from the Flow cytometry core facility at EMBL, Heidelberg.

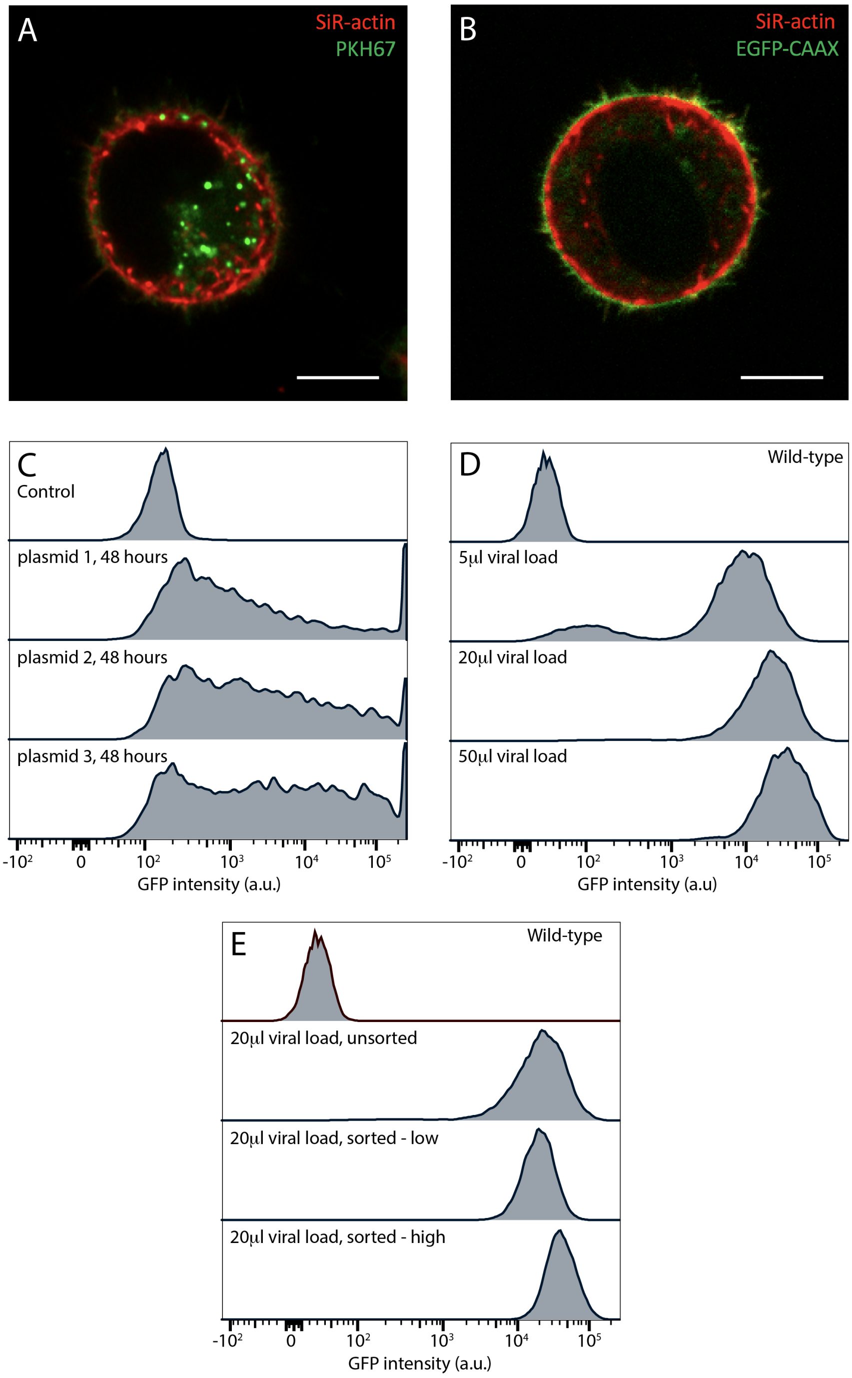

Figure 3.12: Fluorescent labeling of the plasma membrane and generation of the GFP-CAAX-expressing stable cell line. A) A representative confocal slice of a live 3T3 mouse fibroblast labeled with SiR-actin (red) and PKH67 (green) and grown on a 20μm-wide circular micropattern of fibronectin. B) A confocal slice of a live 3T3 mouse fibroblast labeled with SiR-actin (red) and transiently transfected with GFP-CAAX (green), 48 hours post-transfection, on a 20μm-wide circular micropattern of fibronectin. Scale bars in A and B are 10μm long. C) Normalized distribution of fluorescence intensity from GFP-CAAX measured by flow cytometry on cells transfected with plasmids amplified from three different clones of transformed bacteria, 48 hours after transfection. *Contd.*

Figure 3.12: *Contd.* D) Normalized distribution of fluorescence intensity from GFP-CAAX measured by flow cytometry on cells transduced with different viral loads of lentivirus. E) Normalized distribution of fluorescence intensity from GFP-CAAX measured by flow cytometry on cells transduced with lentivirus before and after sorting by intensity.

alter diffusion coefficients of fluorescent lipid probes in a fibroblast-like kidney cell line, all others report a significant reduction in the diffusion coefficient, reflecting a decrease in membrane fluidity.

Using the GFP-CAAX fibroblasts described above, I measured the diffusion of GFP-CAAX in the basal plasma membrane using fluorescence recovery after photobleaching (FRAP). In this method, a region of the field of view is illuminated with high laser power to bleach[7] all the fluorophores in this region in a short timeframe (10-100μs). Thereafter, a movie is recorded where fluorescence is observed to recover in the bleached spot (Fig. 3.13A). Since bleached fluorophores cannot fluoresce again, the recovery is a result of the mixing of fluorescent and bleached fluorophores by diffusion. By modeling the recovery as resulting from diffusion, the diffusion coefficient can be fitted to the experimental recovery curve.

For 2D diffusion in the membrane and considering a circular bleached region, the intensity recovery over time can be modeled as

$$S(t) = S(0) + ae^{\frac{-r^2}{2Dt}} \left(I_0 \left(\frac{r^2}{2Dt} \right) + I_1 \left(\frac{r^2}{2Dt} \right) \right) \tag{3.3}$$

where S is signal intensity, t is the time after bleaching, r is the radius of the bleached spot and I_0 and I_1 are modified Bessel functions arising due to the circular geometry of the bleached region. The factor a accounts for incomplete recovery of the signal and can be expressed as $S(\infty) - S(0)$.

Here, $S(t)$ and $S(0)$ are experimentally measured signal intensity values, and r is the known radius of the bleached region. Therefore, the parameters a and D are the only fitted parameters.

I performed FRAP experiments on control and MβCD-treated cells in media containing 10% del FBS between 20 and 120 minutes of treatment. Normalized and averaged recovery curves measured on control and MβCD-treated cells are shown in Fig. 3.13B. It is clear that the recovery is slower in MβCD-treated cells, indicating slower diffusion in cholesterol-depleted

---

[7] Repeated excitation of the fluorophore to the triplet state with a high power laser leads to chemical changes to the fluorophore such that it loses the ability to fluoresce permanently. This process is called photobleaching.

plasma membranes. Fitting the above equation to the averaged recovery curves per cell further allows quantification of the diffusion coefficient D of GFP-CAAX in individual cells under the two conditions (Fig. 3.13C). An average diffusion coefficient of $0.40 \pm 0.09\ \mu m^2 s^{-1}$ was obtained for control cells, whereas MβCD treatment led to a 30% reduction in D, yielding an average value of $0.28 \pm 0.10\ \mu m^2 s^{-1}$.

As elaborated on in the following section, cells treated with MβCD rounded up over time, leaving very little flat membrane at the basal surface for FRAP. Hence, only cells that did not show extreme rounding could be measured and completely random sampling was not possible. If reduction in membrane fluidity were to correlate with the rounding phenotype, it further stands to reason that D could be overestimated for cholesterol-depleted cells and the overall effect on membrane fluidity could be stronger than that reported here.

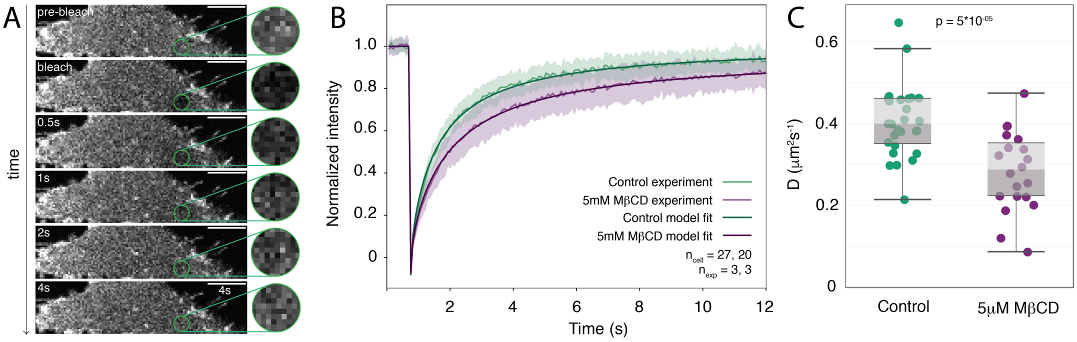

Figure 3.13: Fluorescence Recovery after Photobleaching of GFP-CAAX in cholesterol-depleted cells. A) Representative frames from a FRAP experiment showing the bleached region in the zoomed-in insets. The scale bars are 5μm in length. B) Normalized and averaged FRAP curves for GFP-CAAX control and MβCD-treated cells. C) Diffusion coefficient D from fitting equation 3.3 to normalized and averaged FRAP curves from individual cells.

3.4.3 Cell rounding

When 3T3 mouse fibroblasts were treated with MβCD, they showed a clear morphological change over time, where they rounded up (Fig. 3.14A). In order to characterize cell shape changes in 3D, I used confocal microscopy to acquire images of GFP-CAAX expressing cells treated with 5mM MβCD (Fig. 3.14B) over time. Here I also imaged control cells in media containing 10% del FBS over an identical period of time to control for both the effect of del FBS and any effect of the imaging itself. Whereas control cells showed dynamicity in cell shape and motility, MβCD treatment led to a loss in both dynamicity and motility, eventually resulting in a rounded cell shape. A closer look at the rounding process revealed that the cell body showed rounding first while preserving thin tubes adhered to the substrate (Panel 2, 5mM MβCD, Fig. 3.14B). This was followed by a retraction of the tubes to yield fully rounded cells.

The dynamics of cell rounding were further captured through two shape parameters quantified from fitting a surface to the GFP signal in the confocal images (3.14B), namely cell sphericity and the length difference between the longest and shortest perpendicular axes of the cell.

Cell sphericity (Ψ) is calculated using the equation shown in Fig. 3.15A and is defined as the ratio of the surface area of a sphere with the same volume as the cell in question, to the surface area of the cell, itself. Since a sphere has the smallest ratio of surface area to volume among all 3D geometries, the value of sphericity has an upper bound of one, which is reached when the cell attains a spherical shape. In this case, sphericity was found to increase in cholesterol-depleted cells, while not showing any trend over time in the control cells.

The length difference between the longest and shortest axes of a box bounding the cell surface is a measure of skew between the dimensions of the cells (Fig. 3.15B). This length difference was found to vary between 0-110μm under control conditions and approached zero μm in cholesterol-depleted cells as they rounded up.

The cell rounding behavior observed here is in line with previous reports [255, 256, 262–264, 273]. While these previous reports posit that cell rounding is due to a lowering of cell adhesion to the substrate, it has also been shown by others that cholesterol depletion causes cells to form larger focal adhesions and exert higher traction forces on substrates, despite their rounded morphology [267, 274]. The observation that rounding of the cell body precedes retraction of the substrate-adhered membrane tubes made here further suggests that cell rounding is not a consequence of lowered adhesion to the substrate, but rather originates from pulling forces at the cell surface.

Further, the rounding of the cell body is reminiscent of cell rounding during mitosis, which has been shown to be driven by an increase in cortical tension [308]. This is analogous to the behavior exhibited by liquid droplets, where a spherical shape is adopted to minimize surface tension. This led me to next examine the effect of cholesterol depletion on cortical tension.

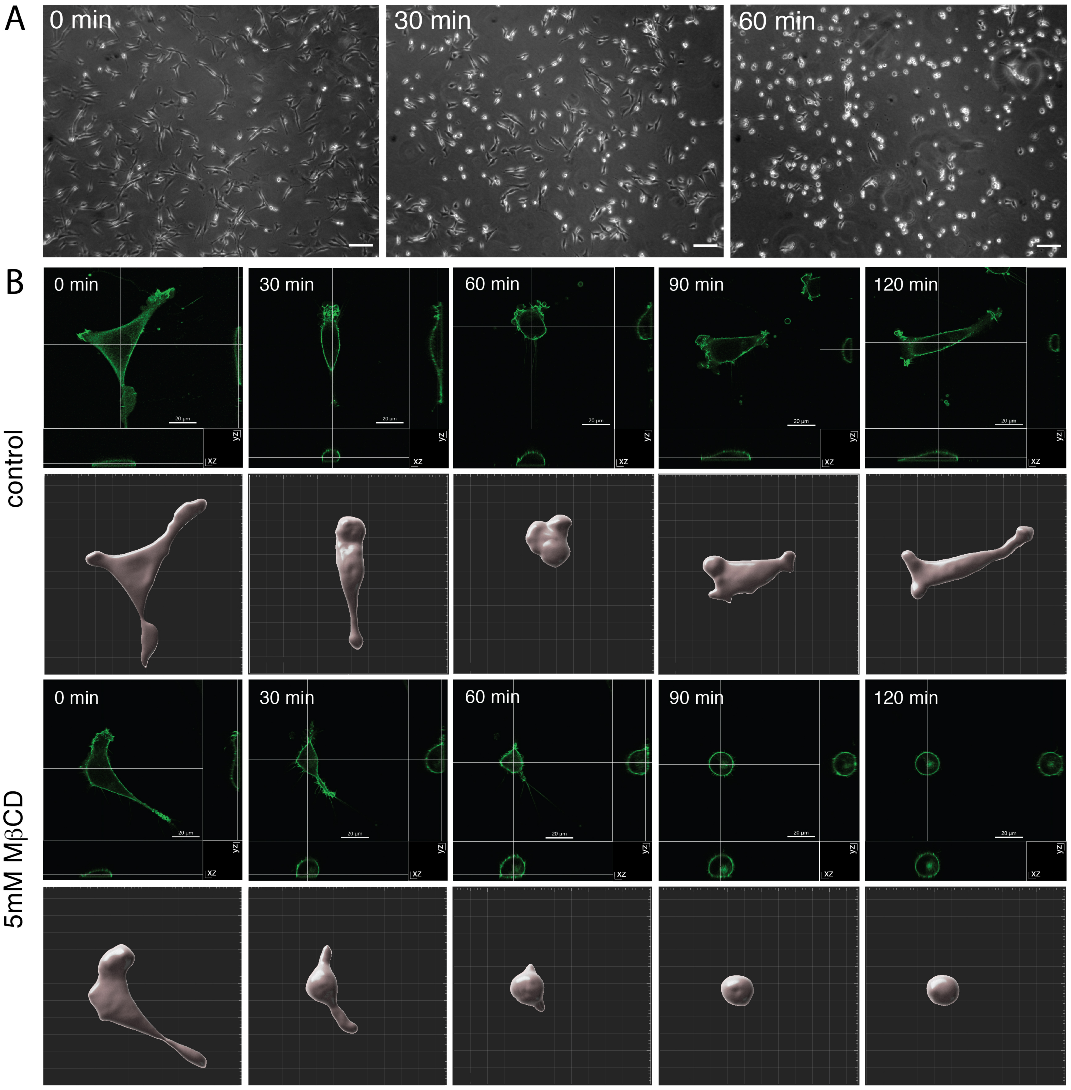

Figure 3.14: Cell rounding in response to MβCD treatment. A) Brightfield images of 3T3 mouse fibroblasts with phase contrast 0, 30min and 60 min into treatment with 5mM MβCD. All scale bars in A are 100μm B) Representative Confocal images of GFP-CAAX fluorescence at various time points of control and MβCD treatment (upper panels) and fitted 3D surfaces for quantification of shape parameters (lower panels). All scale bars in B are 20 μm long.

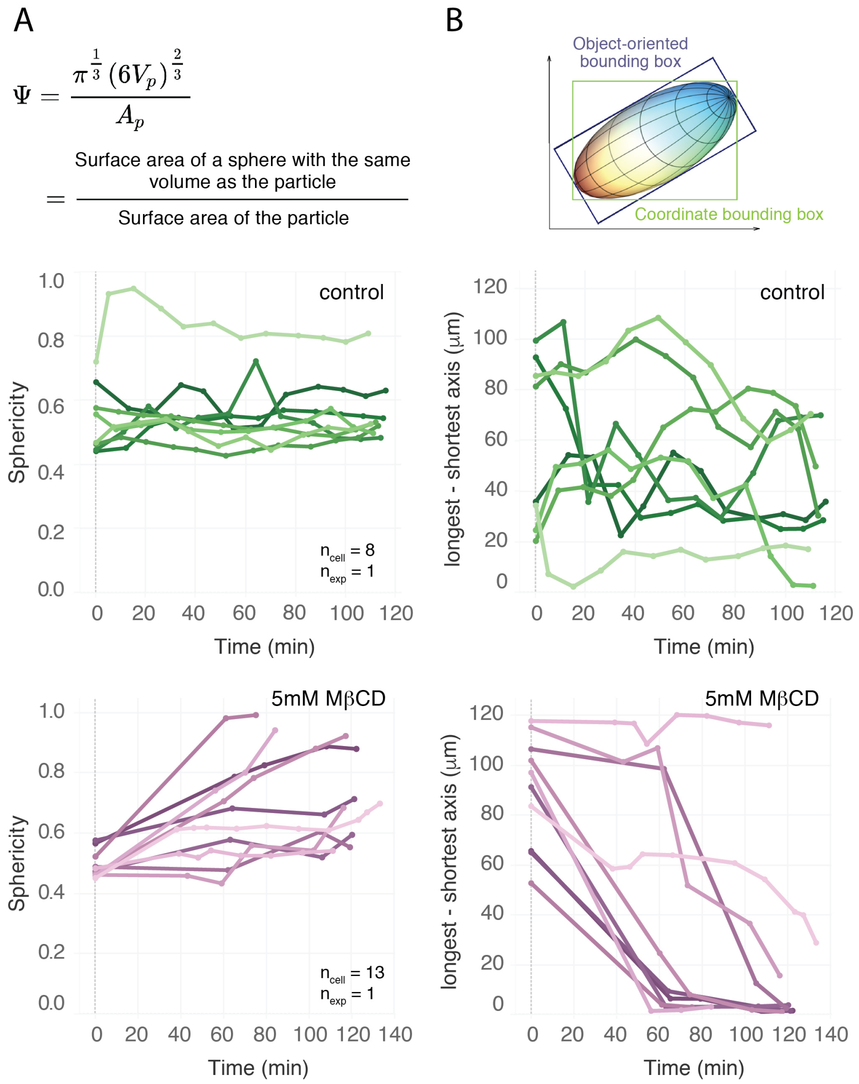

Figure 3.15: Quantification of cell shape parameters during rounding. A) Cell sphericity measured over time for control and MβCD-treated cells. B) Longest-shortest axis of the object-oriented bounding box of the cell surface measured over time for control and MβCD-treated cells.

3.4.4 Cortical tension

For cortical tension measurements, cell spreading was restricted to circles of 20μm diameter on the glass substrate. This was achieved by micropatterning 20μm-wide spots with fibronectin on a background of PLL-PEG[8], which prevents cell adhesion. A schematic for micropatterning is shown in Fig. 3.16A and the procedure is described in detail in section 4.9. Fig. 3.16C and D show representative images of live micropatterned GFP-CAAX cells stained for actin.

---

[8] PLL-PEG is a copolymer of poly(L-lysine) with poly(ethylene glycol) side-chains.

The cortical tension of the micropatterned cells was then probed by indentation using an AFM. Restricting the cell spreading area to 20μm-wide circles and thereby forcing the cell surface to have a spherical geometry provided two advantages:

1. Indentation of a spherical cell surface by a solid sphere has been modeled mathematically [309] and allows for the extraction of cortical tension using a simple relation between force and indentation depth, once the cell radius is known (3.4)[187, 310].
2. Since cholesterol depletion causes cells to round up, micropatterning ensures a similar geometry between control and cholesterol-depleted cells.

To measure cortical tension under the condition of cholesterol depletion, cells were first plated on micropatterned dishes and allowed to adhere to the micropatterns for an hour. Then, they were administered 5mM MβCD and indented between 30 and 120 minutes of treatment. Control cells were incubated in media containing 10% del FBS in place of regular FBS for a similar duration.

A cantilever with a silica bead 10μm in diameter glued to the end was used to indent the micropatterned cell surface, as shown in the schematic in Fig. 3.16B. By measuring the force (f) exerted by the cell as a function of indentation depth (δ), the surface tension can be fitted as a quantity proportional to the slope, using the equation [187, 309, 310].

$$f = 4\pi R_b \left(\frac{1}{R_b} + \frac{1}{R_c} \right) T\delta \tag{3.4}$$

where R_b and R_c are the radii of the bead and cell, respectively, and T is the cortical tension. Since R_b and R_c are known, the value of T can be readily fitted. Here the force exerted by the cell on the cantilever is modeled to vary linearly with indentation depth and hence this model can be applied to obtain values of tension only when such linear force curves are obtained, and when the indentation depth is small compared to the dimensions of the cell.

Cholesterol-depleted cells showed a steeper response to indentation (Fig. 3.16E) compared to control cells. The fitted cortical tension values were 32± 9 pN/μm for control cells and 58± 23 pN/μm for cholesterol-depleted cells, nearly a factor of two higher. Notably, the cell-to-cell variation in measured tension values was 2.6-fold larger for cholesterol-depleted cells than for control cells. Biswas *et al* have previously reported on similarly increased heterogeneity in membrane fluctuations and membrane tension upon cholesterol depletion using MβCD [280].

3.4.5 Cortical F-actin density

The increase in cortical tension observed in response to cholesterol depletion could be brought about by a change in the cortical machinery of the cells. Some studies report an increase in actin stress fibers in response to cholesterol depletion [265, 266], whereas others report a decrease in the same [276]. Further, Chubinskiy-Nadezhdin *et al* report qualitatively on increased F-actin in the cortex of leukemia cells in response to cholesterol depletion [277]. I compared the levels of cortical F-actin in control and MβCD-treated 3T3 mouse fibroblasts using confocal fluorescence microscopy.

While it is difficult to distinguish cortical F-actin in spread adherent cells where stress fibers are the dominant F-actin structures, micropatterned round cells readily provide a means for the quantification of cortical F-actin by confocal microscopy.

Therefore, I used micropatterned GFP-CAAX-expressing cells to quantify cortical F-actin under control and cholesterol-depleted conditions. The respective treatments were performed for 30 minutes, after which the cells were fixed, permeabilized, stained with SiR-actin, and imaged by exciting the fluorescence of GFP-CAAX and SiR-actin in separate channels. Analysis of membrane and F-actin signal was done for an imaging plane 4μm above the bottom surface of the cell, where fluorescence in the membrane channel was used to create a mask (Fig. 3.17A-C, G-I). This mask was then used to generate rings 5, 10, and 15 pixels in width, corresponding to distances of 250, 500, and 750 nm from the cell edge, where the cortex is expected to be. Mean F-actin intensity among all pixels within each of these rings was then calculated and taken to be a measure of F-actin density (Fig. 3.17D-F, J-L). All intensity values were finally normalized to the average intensity obtained for rings of the same width in control cells from individual imaging sessions[9].

In all cases, a 1.2-fold increase in average F-actin intensity was observed for MβCD-treated cells relative to control cells (Fig. 3.17M-O). The increase in actin intensity is in line with that reported qualitatively by Chubinskiy-Nadezhdin *et al* [277]. While changes to the amount of cortical F-actin could

---

[9] The image analysis pipeline was based on the one developed by Léanne Strauss and Christian Tischer at EMBL, Heidelberg.

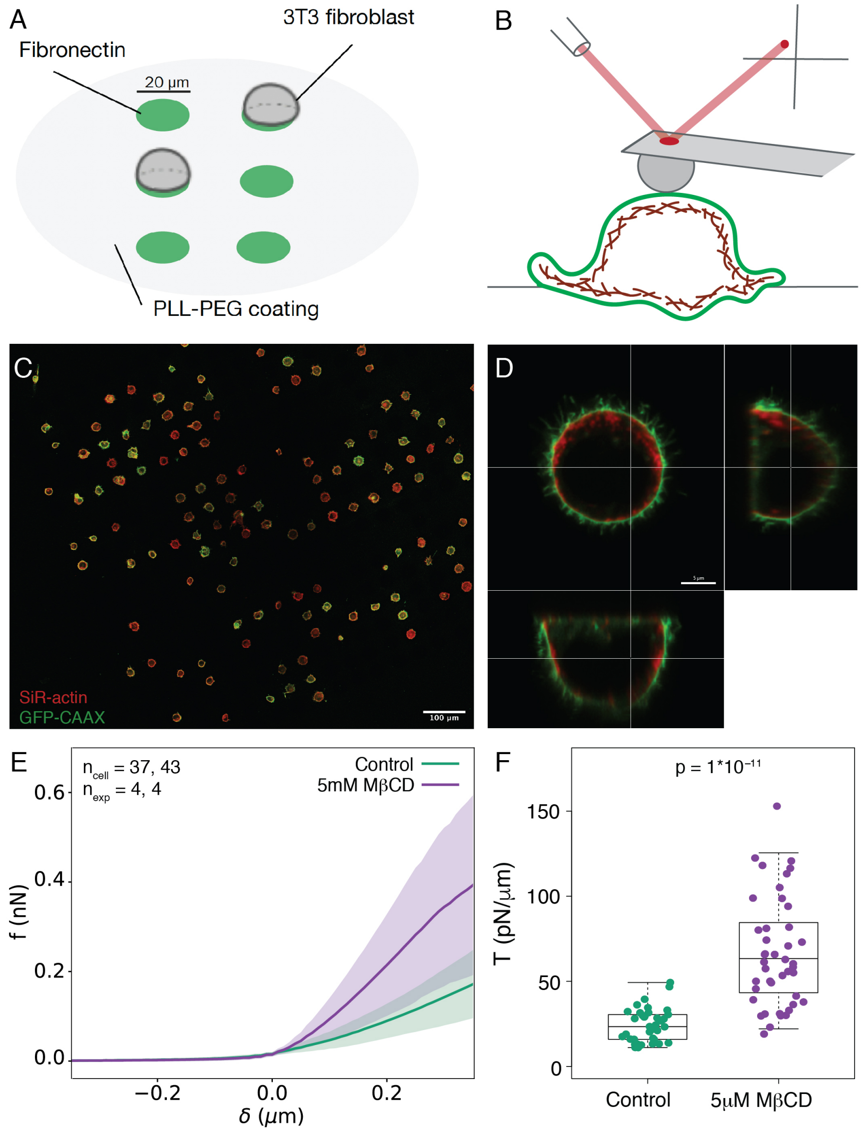

Figure 3.16: Cortical tension measurements on micropatterned 3T3 mouse fibroblasts. A) Schematic of the micropatterning procedure made by Léanne Strauss. In brief, the dish is coated with PLL-PEG which is burned away in the 20μm-wide circular patterns, where fibronectin binds the glass surface. 3T3 mouse fibroblasts seeded on such a dish adhere to the fibronectin in these spots and take on a dome shape. B) Schematic of an indentation experiment using the AFM. The laser light reflected from the top of the cantilever is used to measure the bending of the cantilever when indenting the cell surface. Since the spring constant of the cantilever is calibrated beforehand, this is a direct measure of the force experienced by the cantilever. C) A confocal plane of live GFP-CAAX 3T3 mouse fibroblasts stained with SiR-actin on a micropatterned dish as a representative image. The scale bar has a length of 100μm. D) A confocal z-stack image of a single cell from C. The scale bar has a length of 5μm. E) Force experienced by the cantilever, f as a function of the indentation depth, δ. Averaged force curves are shown for each condition. F) Average cortical tension values per cell obtained from fitting equation 3.4 to individual force curves.

presumably lead to changes in cortical mechanics, mechanical properties

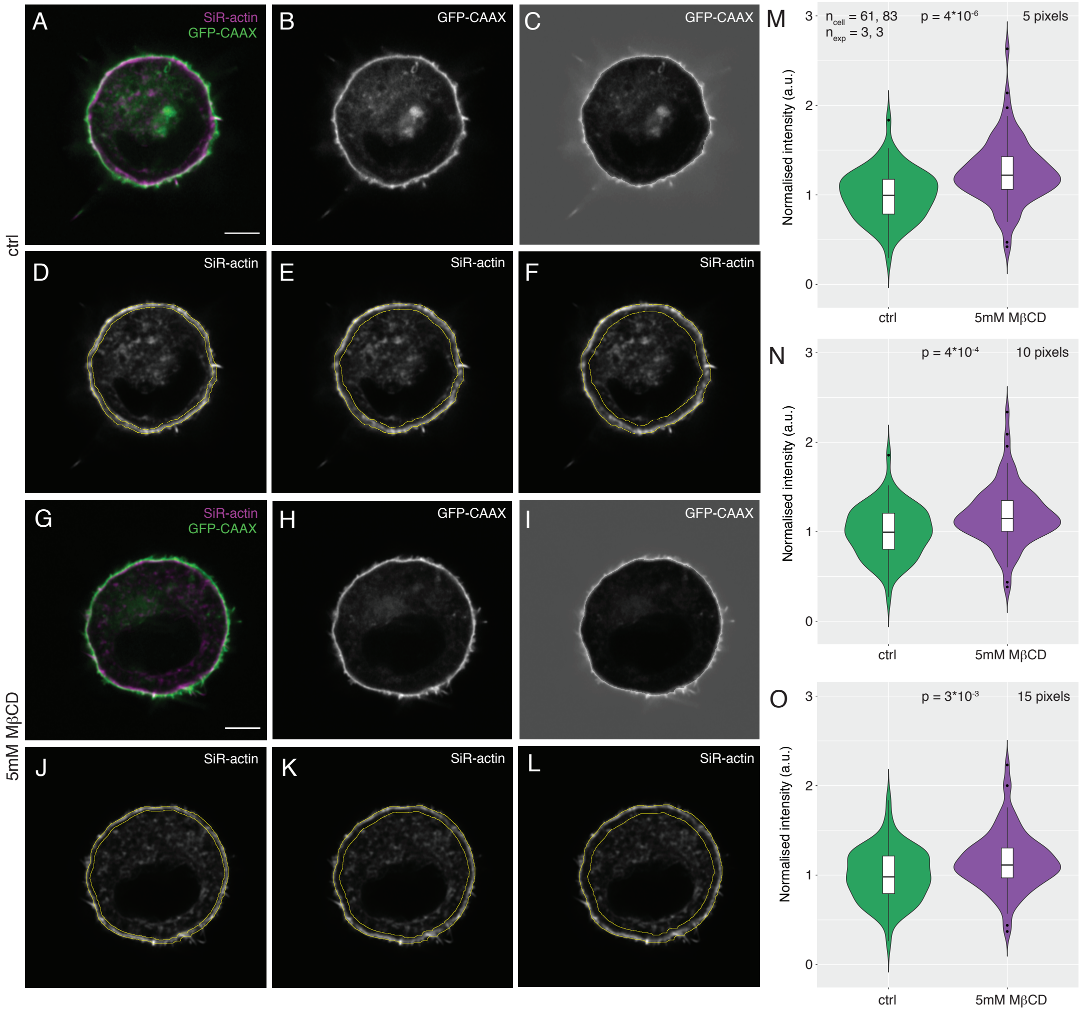

Figure 3.17: Cortical F-actin in micropatterned 3T3 mouse fibroblasts. A) and G) An overlay of the GFP-CAAX (green) and SiR-actin (magenta) channel images from a confocal slice 4μm above the basal surface of representative control (A) and MβCD-treated cells (G). B) and H) GFP-CAAX channel images from A and G, respectively. C) and I) Overlay of GFP-CAAX fluorescence with the mask generated from it. Pixels inside the cell mask are colored black and pixels outside the mask are colored white. D-F and J-L show the rings generated from the masks in C and I, respectively, having a width of 5 (D, J), 10 (E, K), and 15 (F, L) pixels. The outlines of the rings are denoted by yellow lines overlaid with the SiR-actin fluorescence to be quantified. Pixel size = 50nm in x and y. Scale bars are 5 μm in length. M-O) Average pixel intensity in the SiR-actin channel within the 5 (M), 10 (N), and 15 (O) pixel-wide rings. All intensities were normalized to the mean intensity from control cells per experiment. Scale bars are 5μm long and intensities in image panels are not displayed on the same color scale.

emerge from the organization and dynamics of the filaments within the cortex, and there is no direct predictable relationship between F-actin density and properties like cortical tension.

Changes in phosphomyosin[10] density can directly impact cortical tension as phosphomyosin is the active agent that generates stresses in the actin network [71]. However, it has been shown that the actin network architecture, in particular, filament length and crosslinking play a role in the propagation of myosin-generated forces in the network as well [71, 308, 311]. Hence, future work characterizing both cortical phosphomyosin density and features of the actin network architecture at the cortex [311] can provide additional insight into the effect of cholesterol depletion at the cortex.

3.4.6 Summary

I have characterized the following effects of cholesterol depletion using MβCD on 3T3 mouse fibroblasts:

1. A 30% decrease in the diffusion coefficient of plasma membrane-bound cytosolic proteins
2. A 1.2-fold increase in cortical F-actin density
3. A 1.8-fold increase in cortical tension
4. Cell rounding

The question of how cholesterol depletion causes a change in cortical F-actin density and cortical tension remains open. While hypotheses attributing the downstream effects of cholesterol depletion to the disruption of lipid rafts have generally been favored in the past, as described earlier in this chapter [254–268], a handful of papers also point to the change in membrane fluidity as causing the downstream changes [269, 270, 272]. In order to test this hypothesis, I tried to find a different lipid perturbation that could lower membrane fluidity similarly to cholesterol depletion, without altering cholesterol levels. If it is true that cholesterol depletion affects cortical mechanics via lowered membrane fluidity, then the effects of such a treatment on cortical F-actin, tension, and cell morphology would be qualitatively similar to those resulting from cholesterol depletion.

It is known that membrane fluidity depends on membrane lipid saturation, with an increase in the abundance of saturated lipids resulting in a lowering of membrane fluidity and an increase in the abundance of unsaturated lipids resulting in an increase in membrane fluidity [18, 170, 171, 312–314].

---

[10] The ATP-dependent activity of myosin correlates with phosphorylation of the serine 19 residue, and here I refer to myosin phosphorylated at Ser19 as phosphomyosin.

Hence, the next approach I took was to target a change in the membrane lipid saturation levels of 3T3 mouse fibroblasts.

3.5 Membrane lipid saturation and SCD1

The rate-limiting step in the synthesis of monounsaturated fatty acids is catalyzed by the enzyme stearoyl CoA desaturase (SCD), also known as Δ9-desaturase in the endoplasmic reticulum. The isoform SCD1 has been shown to catalyze the insertion of a double bond between the ninth and tenth carbon atoms of both stearic acid (18:0) and palmitic acid (16:0) to generate oleic acid (18:1) and palmitoleic acid (16:1), respectively.

Although perturbations to lipid saturation have not been as widely performed as perturbations to membrane cholesterol, the identification of SCD1 as a potential target in therapies for cancer, obesity, and neurodegenerative diseases has led to the rapid discovery of several small-molecule inhibitors of SCD1 in the past years which have become commercially available[315] (Table 3.1).

Table 3.1: Small molecule inhibitors of SCD1

Drug	Reference
CAY10566	Liu *et al*, 2007 [316]
A939572	Xin *et al*, 2008 [317]
CVT-11127	Kooltun *et al*, 2009 [318]
XEN723	Sun *et al*, 2014 [319]
T-3764518	Imamura *et al*, 2017 [320]
YTX-465	Vincent *et al*, 2018 [321]

Of these, A939572 has been used widely on cultured cell lines, including those derived from mouse [322, 323]. To increase membrane lipid saturation, these studies additionally supplement cells with 200μM BSA-18:0 four hours into the treatment with 1μM A939572 and co-incubate the cells with the drug and fatty acid for 16 hours. Therefore, I decided to perform the same treatment on 3T3 mouse fibroblasts.

3.5.1 The cellular response to SCD1 inhibition

My first observation from the trial of SCD1 inhibition on 3T3 mouse fibroblasts was the cell rounding phenotype (Fig. 3.18). I found that neither drug

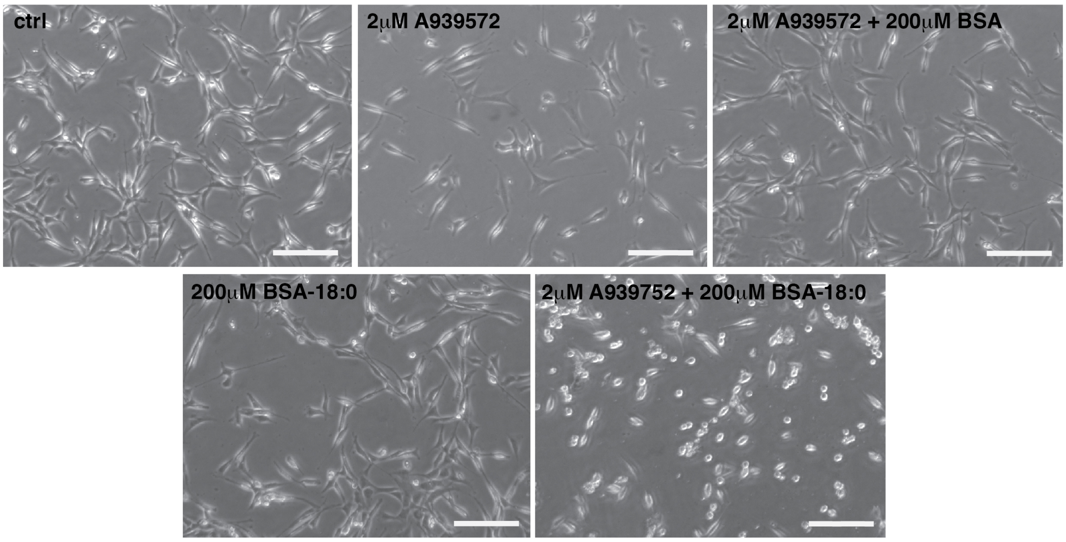

Figure 3.18: Cell rounding in response to SCD1 inhibition and 18:0-loading. Brightfield images of 3T3 mouse fibroblasts with phase contrast. Scale bars are 100μm in length.

treatment nor treatment with BSA-18:0 alone caused the rounding to occur, but when performed simultaneously, they caused cell rounding. At this point, there was no information as to the effect of each of these treatments on membrane saturation, but it was safe to assume that the effect if any, would be strongest in the presence of the SCD1 inhibitor and BSA-18:0, which is where cell rounding was observed.

Since the goal of this treatment was to reduce membrane fluidity by a means orthogonal to cholesterol depletion, I next measured membrane fluidity in cells treated with the SCD1 inhibitor and loaded with BSA-18:0 by FRAP, as described previously (Fig. 3.19A). By fitting eq. 3.3 to the recovery curves, I obtained diffusion coefficient values of 0.42 ± 0.11 μm^{2}s^{-1} for control cells and 0.35 ± 0.07 μm^{2}s^{-1} for treated cells (Fig. 3.19B). Hence, the combined treatment of cells with A939572 and BSA-18:0 causes a 17% reduction in the average values for the diffusion coefficient, D as compared to control cells.

To measure any changes to cortical tension caused by the treatment, I performed indentation experiments on micropatterned cells as described previously. From the indentation force curves (Fig. 3.19C), it is clear that the treatment causes the cells to resist deformation more strongly. Fitting eq. 3.4 to the indentation force curves yielded values for cortical tension in these two conditions (Fig. 3.19D). Cortical tension was found to increase by over two-fold, from 31 ± 12 pNμm^{-1} in control cells to 65 ± 30 pNμm^{-1} in the treated cells.

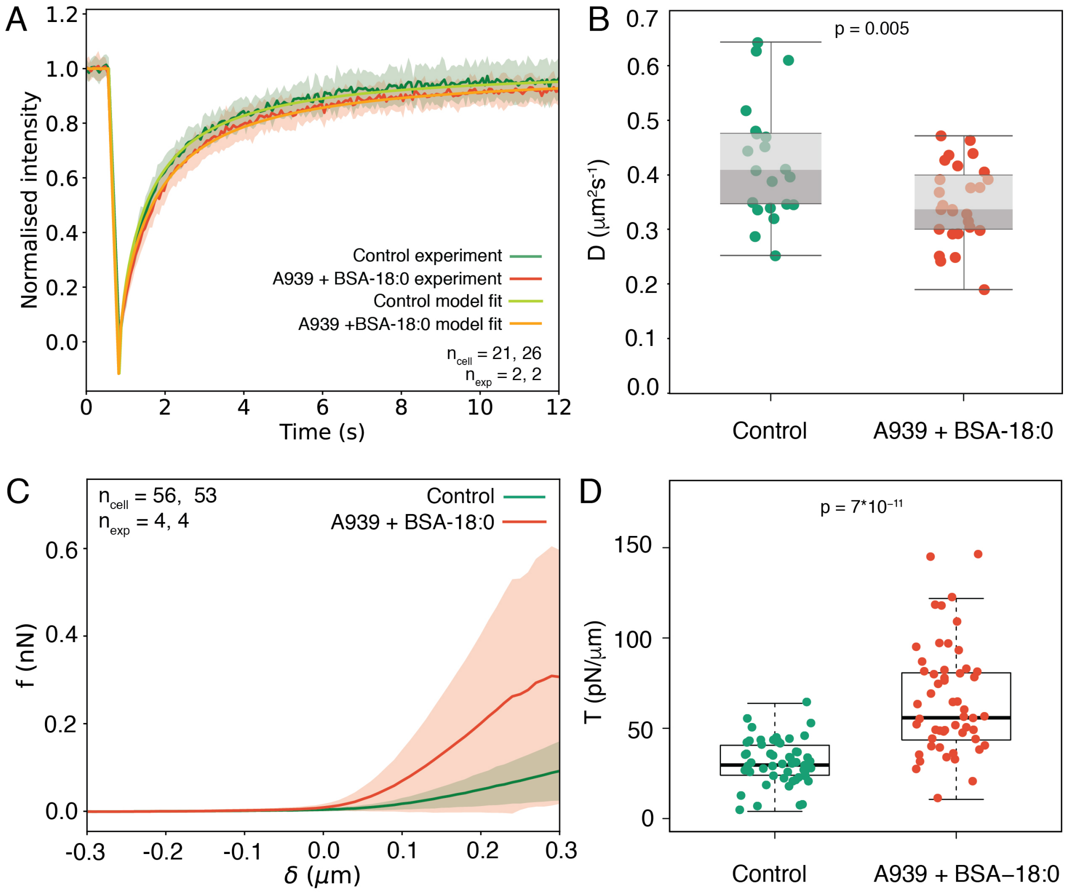

Figure 3.19: The effect of SCD1 inhibition and 18:0-loading at the cell surface. A) Normalized and averaged FRAP curves for GFP-CAAX control cells and cells treated with A939572 + BSA-18:0. B) Diffusion coefficient D from fitting equation 3.3 to normalized and averaged FRAP curves from individual cells. C) Force curves from indentation experiments performed on the AFM. The force experienced by the cantilever, f is plotted as a function of the indentation depth, δ. Averaged force curves are shown for each condition. D) Average cortical tension values per cell obtained from fitting equation 3.4 to individual force curves. A939572 is abbreviated to A939 in the legend labels.

The preliminary finding that SCD1 inhibition and loading with 18:0 has a qualitatively similar effect on membrane fluidity, the cell cortex, and cell shape of 3T3 mouse fibroblasts supports the idea that membrane fluidity could be upstream of these effects. However, it is important to assess the effect of the treatment on the cell and plasma membrane lipidome in order to understand the origin of the change to membrane fluidity and check for any off-target or compensatory effects in the plasma membranes. We next analyzed these cells and their isolated plasma membranes using lipidomics[11].

---

[11] Lipidomics data was collected and analyzed by Richard R. Sprengers at SDU, Odense.

3.5.2 Lipidomic characterization of SCD1 inhibition

Lipid extraction from whole cells and their analysis by mass spectrometry was carried out as described previously. A total of 1119 lipids belonging to 30 lipid classes were quantified.

Grouping lipids by the number of C-C double bonds they contain (double bond index, Fig. 3.20A) allowed me to study the effect of the treatment on lipid saturation. A two-fold increase was observed in the mol % abundance of saturated lipids containing no double bonds, from 7.5 ± 0.7 mol % in control cells to 14.9 ± 0.6 mol % in cells treated with 200μM BSA-18:0. A far more dramatic six-fold increase to 43 ± 3 mol % was observed when the cells were treated with 2μM A939572 to inhibit SCD1 alongside the addition of 200μM BSA-18:0. Both these treatments caused a decrease in lipids containing 4 or more double bonds, but when SD1 was not inhibited, there was a slight increase in lipids containing 1-3 double bonds, presumably as a result of desaturase activity on the supplied 18:0 fatty acid. On the other hand, when SCD1 was inhibited using A939572 alongside the addition of BSA-18:0, there was a decrease in lipids containing any double bonds. Further, the addition of A939572 alone did not have any effect on the distribution of the double bond index, whereas the addition of BSA caused a small decrease in monounsaturated lipids and an increase in lipids containing a total of 2-3 double bonds.

While the treatment caused a clear six-fold increase in the mol % abundance of saturated lipids, as desired, the lipidomics data further shed light on a number of other changes to lipids resulting from the treatment (Fig. 3.20B):

1. ***Non-esterified fatty acids (NEFA).*** Treatment of cells with A939572 + BSA and with BSA-18:0 caused an average 1.5-fold and 3-fold increase in the mol % abundance of free fatty acids, respectively. Contrary to this, treatment with A939572 + BSA-18:0 caused a 35% decrease in the same.

2. ***Neutral glycerolipids (MAG, DAG and TAG).*** Treatment with BSA-18:0 caused an increase in the mol % abundances of MAG, DAG and TAG, with an especially strong effect on TAG, where the increase was on average 9-fold. A more moderate 3-fold increase in TAG was observed in case of treatment with A939572 + BSA and A939572 + BSA-18:0. While

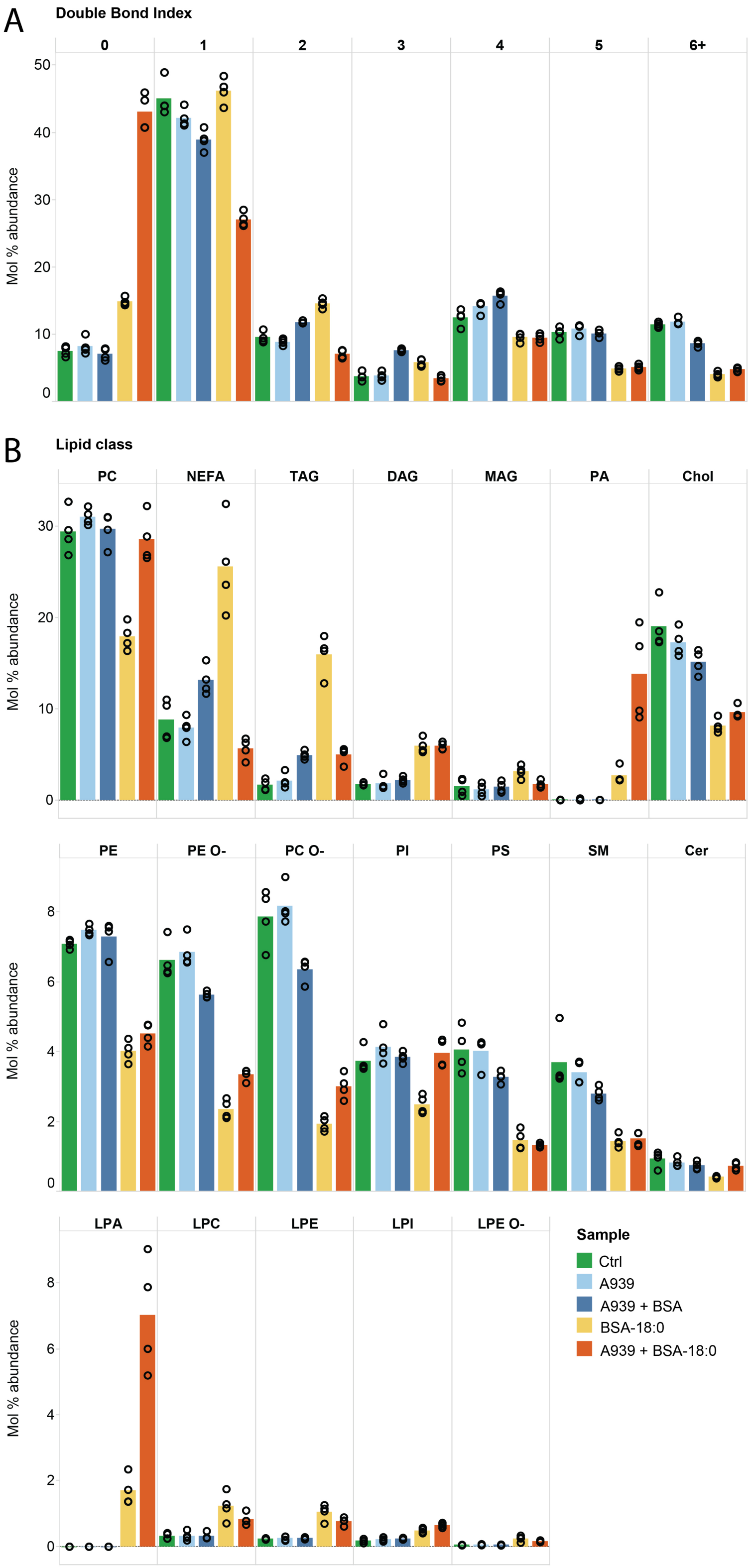

Figure 3.20: The effect of SCD1 inhibition and 18:0-loading on the cell lipidome. A) Mol % abundances of lipids grouped by double bond index across conditions. B) Mol % abundances of lipid classes across conditions. A939572 is abbreviated to A939 in the labels.

no increase was observed in the mol % abundance of DAG upon treatment with A939572 + BSA, treatment with BSA-18:0, both in the presence and absence of A939572, caused a 3-fold increase.

3. ***Phosphatidic acid (PA).*** Present at trace amounts in control cells, PA becomes pronounced in cells treated with BSA-18:0, especially in the presence of A939572, with a mol % abundance of 13 ± 5 mol % among all detected lipids.
4. ***Lysolipids.*** Lysophospholipids, present at low levels in control cells show an increase in abundance when treated with BSA-18:0, both in the presence and absence of A939572. This increase is especially pronounced for LPA, where the mol % abundance is as high as 7 ± 2 mol % in cells treated with A939572 + BSA-18:0.
5. ***Membrane phospholipids and cholesterol.*** Likely as a result of mol % normalization, the relative abundance of other membrane phospholipids (PE, PE O-, PC O-, PS and SM) and cholesterol is found to drop in cells treated with BSA-18:0, both in the presence and absence of A939572.

Additionally, it is clear that SCD1 inhibition using A939572 alone does not impact the lipidome of the cells in any way, while the addition of BSA leads to a few minor changes. The above observations can be interpreted in light of fatty acid uptake and metabolism in the ER (Fig. 3.21). Note that the lipid classes observed to show large increases in mol % abundance upon treatment with BSA-18:0 lie on the triacylglycerol synthesis pathway that leads to the formation of lipid droplets, depicted here. While higher levels of NEFA (reactants) and TAG (end product) are detected when BSA-18:0 is provided in the absence of A939572, the simultaneous inhibition of SCD1 by A939572 results in an increase in the intermediate products along this pathway, namely, LPA, PA and DAG, with much lower levels of NEFA and TAG.

In order to probe the effect of the treatment specifically on the lipid composition of the plasma membrane, I isolated plasma membranes from control cells and cells treated with A939572 + BSA-18:0 using the method described previously (sections 3.3.2 and 4.6). These isolates were then subjected to lipidomics analysis by mass spectrometry.

A total of 954 lipids belonging to 30 lipid classes were quantified. Comparing mol % lipid abundance by double bond index revealed a 4.4-fold increase in the mol % abundance of saturated lipids containing no double

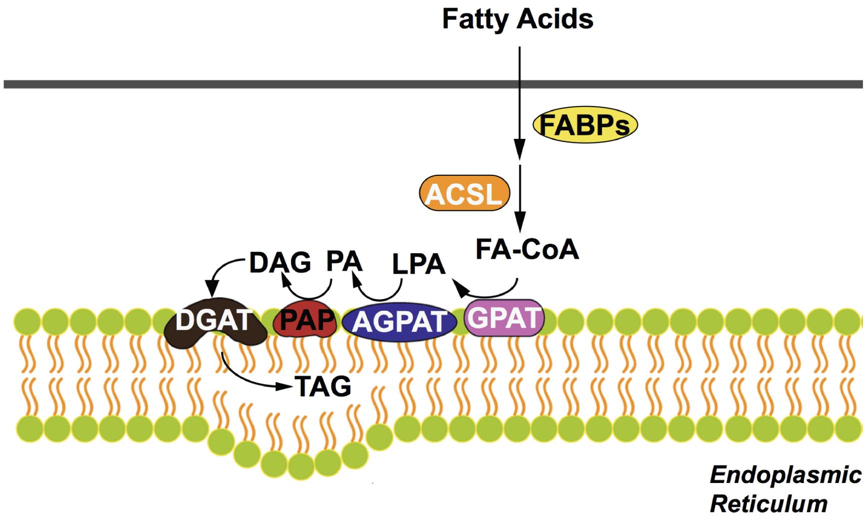

Figure 3.21: Fatty acid uptake and metabolism in the endoplasmic reticulum. Schematic of the triacylglycerol synthesis pathway starting from the uptake of fatty acids in mammalian cells. Fatty acids are transported within the cell by fatty acid binding proteins (FABPs) and are incorporated into TAGs via a series of intermediates. Figure from Chen and Li, 2016 [324]. ACSL, fatty acyl-CoA synthetase; GPAT, glycerol-3-phosphate acyltransferase; AGPAT, acylglycerolphosphate acyltransferase; PAP, phosphatidic acid phosphohydrolase; DGAT, diacylglycerol acyltransferase.

bonds, from 7.5 ± 0.2 mol % in PM from control cells to 33 ± 6 mol % in PM from treated cells. However, increased levels of PA, TAG, DAG, MAG, and LPA and the corresponding decrease in mol % abundances of other membrane phospholipids and cholesterol unexpectedly persisted in data collected on the plasma membrane isolates (Fig. 3.22B). This suggests likely contamination of the PM isolates with ER membranes and lipid droplets, and further investigation is required to tell apart the effects of such contamination from real changes to the plasma membrane lipid composition resulting from this treatment.

3.6 Conclusions and Outlook

An effective way to study the role of a biological process is to make it go awry and observe the consequences for the cell or organism. Genes and proteins are routinely perturbed in this manner to infer their roles in organisms or cells. I took a similar approach and perturbed lipid homeostasis in mouse fibroblasts in order to assess its role in the regulation of the actomyosin cortex. Specifically, I performed two treatments, namely cholesterol depletion using

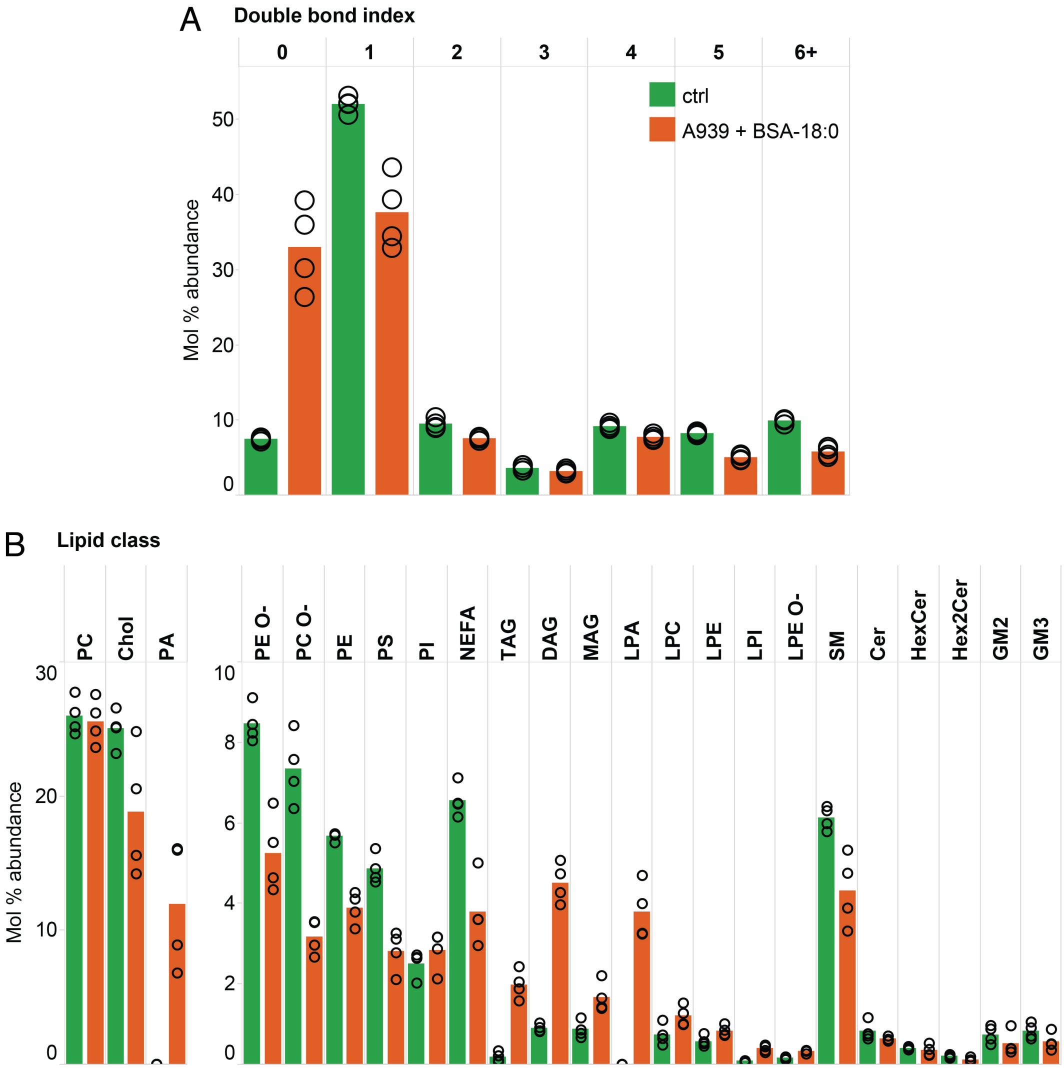

Figure 3.22: The effect of SCD1 inhibition and 18:0-loading on the lipid composition of the plasma membrane. A) Mol % abundances of lipids grouped by double bond index in plasma membranes isolated from control cells and cells treated with A939572 + BSA-18:0. B) Mol % abundances of lipid classes in plasma membranes isolated from control cells and cells treated with A939572 + BSA-18:0. A939572 is abbreviated to A939 in the legend labels.

MβCD and increasing membrane lipid saturation using the drug A939572 along with BSA-18:0.

The effect of each of these treatments on cellular and plasma membrane lipid composition was characterized using mass spectrometry-based lipidomics[12]. This revealed that MβCD acted with high specificity toward cholesterol, resulting in the depletion of 38% of cellular cholesterol and 24% of plasma membrane cholesterol 30 minutes into the treatment. The rest of

---

[12] Lipid extraction and mass spectrometry for these lipidomics experiments were performed by Richard R. Sprenger at SDU, Odense.

the lipidome was unaffected by the treatment. On the other hand, treatment with A939572 + BSA-18:0, while increasing lipid saturation in the cell and plasma membrane 6-fold and 4.4-fold, respectively, also resulted in the build-up of several lipid classes such as LPA, PA, DAG, and TAG. Moreover, although these lipids are expected to be present in the ER membrane, they were also increased in abundance in the plasma membrane isolates. This could be the result of contamination of the isolated plasma membranes with ER membranes and further testing and optimization of the isolation protocol may be necessary for cells treated with A939572 + BSA-18:0.

Over the course of the experiments described here, a couple of valuable resources were generated, which could be useful for work along these lines in the future:

- ***Proteomic characterization of PM isolates.*** In order to characterize the effect of the treatments on the plasma membrane lipid composition in particular, I set up a pipeline for plasma membrane isolation using the commercially available Minute PM isolation kit. The purity of PM isolates thus obtained was thoroughly assessed by proteomics[13]. This dataset is potentially interesting for others using this method to isolate cellular plasma membranes.

- ***GFP-CAAX 3T3 mouse fibroblast cell line.*** I generated a GFP-CAAX-expressing 3T3 mouse fibroblast cell line to measure the lateral diffusive properties of the plasma membrane-bound GFP-CAAX using FRAP[14]. This cell line can be used for similar experiments in the future as well as for fluorescently visualizing the plasma membrane to characterize cell shape.

Biophysical characterization of cells treated with MβCD and A939572 + BSA-18:0 revealed that both of these treatments elicited the following common responses:

- ***Reduced membrane fluidity.*** Both treatments caused a 15-30% decrease in the diffusion coefficient of the plasma membrane-bound fluorescent protein GFP-CAAX.

---

[13] Proteomics data collection and analysis were performed by Per Haberkant, Henrik Hammaren, and Frank Stein at the Proteomics core facility at EMBL, Heidelberg.

[14] Cell line generation using lentiviral transduction was done with the help of Ewa Sitarska, and Diana Ordonez from the Flow cytometry core facility at EMBL, Heidelberg.

- ***Increased cortical tension.*** Both treatments caused a nearly two-fold increase in cortical tension, as measured using indentation experiments on the AFM.

- ***Cell rounding.*** Both treatments caused cells to round up. This could be a result of increased cortical tension, as reported to occur during mitosis [308].

Using micropatterned cells, I could further image cortical F-actin in cholesterol-depleted cells. A 1.2-fold increase in F-actin density was observed at the cortices of cholesterol-depleted cells. It would be interesting to check if a similar increase in F-actin density is observed during treatment with A939572 + BSA-18:0. Similarly, confocal microscopy-based analysis of the concentration of other cortical components such as membrane-to-cortex linkers (pERM), motor proteins (pMyosin), actin nucleators (formins and Arp2/3) and crosslinkers (actinin, fimbrin, fascin, filamin, dystrophin, and spectrin) can provide additional information on the molecular changes occurring at the cell cortex.

Although confocal microscopy-based methods can be used to measure relative changes in the concentrations of molecular components at the cortex, they do not directly inform us of the absolute values of concentrations. Moreover, information on the architecture of the actomyosin network is ultimately critical to obtain a complete picture. The resolution needed to visualize individual actin filaments is well below the resolution limit of light microscopy and difficult to access by super-resolution techniques owing to the high density of the actin meshwork [325]. However, state-of-the-art cryo-electron tomography shows great promise for probing individual actin filaments in the mammalian cell cortex [311]. This method could shed light on changes to actomyosin architecture resulting from altered membrane composition in the future.

Previous studies looking into the effect of cholesterol depletion on the cytoskeleton have attributed these to the disruption of lipid rafts [254–268]. However, treatment with A939572 + BSA-18:0 to increase membrane saturation is not expected to disrupt lipid rafts. If similar mechanisms are responsible for the downstream effects of these two treatments on cortical tension and cell shape, then it is likely that membrane fluidity is the relevant parameter regulating the actomyosin cortex.

However, it is important to bear in mind that the perturbations performed here are not specific to the plasma membrane and affect lipids in all cellular membranes. The development of new tools to perturb plasma membrane fluidity more precisely with spatiotemporal control could help test the above hypothesis with better specificity. Recently, Jiménez-Rojo *et al* have developed a photoswitchable fatty acid, FAAzo4, which gets incorporated into PC in mammalian cells [326]. Photoisomerization of these acyl chains can be used to increase membrane fluidity with high spatiotemporal control, using which Jiménez-Rojo *et al* have studied the impact of ER membrane fluidity on protein secretion at the ER [326]. A similar tool that could enable changes to plasma membrane fluidity in a photoswitchable manner would be ideal for studying the effect of plasma membrane fluidity on the actomyosin cortex in the future.

The hypothesis that membrane fluidity could regulate cortical mechanics is further supported by the findings of my colleagues in minimal membrane-tethered actomyosin networks reconstituted *in vitro* and simulations of the same[15]. Both the architecture and dynamics of actin filaments in these networks are found to depend on the fluidity of the membranes on which the network is assembled via membrane-to-cortex linkers. The simulations show that increased drag on membrane-to-cortex attachment proteins due to an increase in membrane viscosity plays into the dynamics of the filaments. However, it is not yet clear what causes the networks to assemble with different architectures. Importantly, since this experimental system and the model both lack lipid rafts as well as signaling cascades, they allow us to study the effects of altered membrane fluidity in isolation.

At the same time, it is also important to note that the minimal cortex assembled *in vitro* differs from a cell cortex in the following ways:

- ***Actin turnover.*** The minimal cortices used here were assembled from pre-polymerized actin and remained in their polymerized form over the course of the experiments. This is in contrast to the cell cortex, where actin is continuously polymerized and depolymerized such that the cortex is turned over in 10-100 seconds [327, 328].

- ***Filament lengths.*** The actin filaments used for *in vitro* reconstitution were on average 7μm long, whereas, in cells, they are found to be on average 120nm long when nucleated by Arp2/3 and 1.2μm long when nucleated by formins [329]. Both these pools of cellular actin filaments are much shorter than those used to reconstitute the cortex *in vitro*. Studies

---

[15] Unpublished results from Srishti Dar at EMBL, Heidelberg and Annamarie Leske and Julio Belmonte at North Carolina State University.

suggest that the action of myosin motors [330, 331] as well as the mechanical properties of the network [308, 329] both depend on filament length.

- ***Crosslinking.*** The minimal cortices used here were built without crosslinkers, while cells typically express a variety of crosslinking proteins which are known to affect network contractility [332].

The actomyosin cortex is ultimately a complex and dynamic material with several components. Modeling the simplest case lacking turnover and crosslinking provides a foundation over which layers of complexity can be built in order to dissect the role of each additional component. Like tethering to the membrane, imposing other known constraints on the cortex could result in similarly interesting behaviors. Overall, minimally reconstituted actin networks and their simulations are extremely valuable tools that can provide insight into a system with rich underlying physics. To make the best use of these tools in biology, it is equally important to characterize cell cortices in depth and to use this data to build models that better represent the biological structures of interest.

The actomyosin cortex is a paradigmatic biological system where the activity of molecular constituents results in emergent phenomena spanning cellular ($\sim \mu$m) and organismal (μm-m) scales, and one which can shed light on more general principles of biological organization.

Lastly, if it is true that plasma membrane fluidity regulates actomyosin activity as proposed here, then it is likely that cells tune plasma membrane fluidity spatially to control cell shape changes. This has been proposed for migrating cells in the past [269, 270, 272] and is also in line with the finding that anti-metastasis drugs suppress cell motility in breast cancer cells by reducing membrane fluidity [333]. Identifying membrane fluidity as a regulator of the cell cortex and cell migration in cancer cells could further allow the design of new drugs targeted at reducing membrane fluidity in these cells.

More generally, a clear understanding of how the fluidity of organellar and cellular membranes affect the myriad of biological processes occurring at these sites could open up a new paradigm in our understanding of biology. This could possibly lead to the generation of a new class of therapeutic agents that act by specifically modulating membrane fluidity at targeted membranes in the future.

Chapter 4

Materials and Methods

4.1 Materials

Materials used for the experiments described in this thesis are listed in their order of appearance in the methods section. All reagents were stored at conditions recommended by the manufacturer until use.

Table 4.1: Cell lines

Cell line	Cell type	Derived from	Source
MEF	mouse Embryonic Fibroblasts	CD1 mouse embryo	Noh Lab, EMBL
129XC57BL/6J	mouse Embryonic Stem Cells (mESC)	male 129-B13 agouti mouse embryo	Noh Lab, EMBL
NIH/3T3-CRL-1658	mouse Embryonic Fibroblasts	NIH/Swiss mouse embryo	ATCC
GFP-CAAX-NIH/3T3-CRL-1658	mouse Embryonic Fibroblasts	NIH/Swiss mouse embryo	This study
HEK293T	human Embryonic Kidney cells	Human Embryo	Diz-Muñoz lab, EMBL

Table 4.2: Cell culture reagents

Reagent	Source	Identifier
Bovine skin Gelatin type B	Merck	G9391
Knockout DMEM	Gibco	10829018

EmbryoMax Fetal Bovine Serum (FBS)	Merck	ES009-M
Non-essential amino acids (NEAA)	Gibco	11140050
Glutamax	Gibco	35050061
Sodium Pyruvate	Gibco	11360070
Penicillin-Streptomycin (Pen-Strep)	Gibco	15070063
β-Mercaptoethanol (β-ME)	Gibco	21985023
Leukemia inhibitory factor (LIF)	EMBL Protein Expression and Purification Core Facility	
0.05% Trypsin-EDTA	Gibco	25300054
High-glucose DMEM	Gibco	11965092
Fetal Bovine Serum (FBS)	Gibco	26140079
Retinoic acid	Merck	R-2625
Poly-D-Lysine hydrobromine (PDL)	Merck	P6407
Laminin	Merck	L2020-1MG
B27 without vitamin A	Gibco	12587010
N2 supplement	Gibco	17502048
Cytarabine (Ara-C)	Merck	C3350000
DMEM/F12 (without HEPES and with glutamine)	Gibco	131331028
Neurobasal medium	Gibco	21103049
L-glutamine	Gibco	25030149
BSA fraction V	Merck	10735078001
Human recombinant Insulin	Merck	91077C
CHIR99021	Tocris	4423
PD0325901	Tocris	4192
Stearic acid (SA, 18:0)	Merck	S4751
Arachidonic acid (AA, 20:4)	Merck	A3611

Docosahexaenoic acid (DHA, 22:6)	Merck	D2534
Fatty acid-free Bovine Serum Albumin (BSA)	Merck	A7030
Methyl-β-cyclodextrin (MβCD)	Merck	C4555
Delipidated FBS	7BioScience	7-FBS-DL-12B
A939572	Merck	SML2356
Dimethyl sulfoxide (DMSO)	Merck	D2438
Latrunculin A (LatA)	Merck	L5163
Lipofectamine 2000	Thermo Fisher Scientific	11668019
Opti-MEM	Gibco	31985062
TransIT-Lenti	Mirus	MIR6604
Lenti-X concentrator	Takara	631232
Polybrene (10mg/mL)	Merck	TR-1003-G
PLL-g-PEG	SuSoS	PLL(20)-g[3.5]- PEG(2)
Polydimethylsiloxane (PDMS) Sylgard 184	Merck	761028
14.5mg/ml PLPP (4-benzoylbenzyl-trimethylammonium chloride)	Alveole	1904
human Fibronectin	Corning	356008
Concanavalin A	Merck	C5275

Table 4.3: Cell culture plasticware

Plasticware	Source	Identifier
Stericup	Merck	S2GPU05RE
T25 flask	Corning	430639
T75 flask	Corning	430641U
10cm TC-treated dish	Corning	353003
10cm non-adherent petri dish	Greiner Bio-One	633102
10cm Nunclon TC-coated dish	Thermo Fisher Scientific	150350

6cm Nunclon TC-coated dish	Thermo Fisher Scientific	150288
Countess cell counting chamber	Thermo Fisher Scientific	C10228
70μm-cell strainer	Merck	431751
0.45μm PVDF syringe filter	Merck	SLHV033R
2mL cryogenic tubes	Thermo Fisher Scientific	366656
Cell lifter	Corning	CLS3008
35mm glass-bottom dishes (Fluorodish)	World Precision Instruments (WPI)	FD35-100
5 mL Round Bottom Polystyrene Test Tube with Cell Strainer Snap Cap (FACS tube)	Corning	352235

Table 4.4: Lipid standards

Lipid	Source	Identifier
ACar 16:0 (+$^{[2]}H_3$)	Merck	55107
CE 10:0	Merck	C4633
Cer 18:1;2/17:0;1	Avanti Polar Lipids	860517P
CL 14:1/14:1/14:1/15:1	Avanti Polar Lipids	LM-1802
DAG 17:0/17:0 (+$^{[2]}H_5$)	Avanti Polar Lipids	850149P
HexCer 18:1;2/12:0	Avanti Polar Lipids	860543
LPA O-16:0	Avanti Polar Lipids	110683
LPC 16:0 (+$^{[2]}H_3$)	Larodan AB	71-2826
LPE O-16:0	Avanti Polar Lipids	110703
LPI 17:1	Avanti Polar Lipids	850103P
LPS 17:1	Avanti Polar Lipids	800740X
PA 15:0/18:1 (+$^{[2]}H_7$)	Avanti Polar Lipids	791642C
PC 16:0/16:0 (+$^{[2]}H_6$)	Larodan AB	71-3726
PE 15:0/18:1 (+$^{[2]}H_7$)	Avanti Polar Lipids	791638C
PG 15:0/18:1 (+$^{[2]}H_7$)	Avanti Polar Lipids	791640C
PI 15:0/18:1 (+$^{[2]}H_7$)	Avanti Polar Lipids	791641C
PS 15:0/18:1 (+$^{[2]}H_7$)	Avanti Polar Lipids	791639C
SM 18:1;2/18:1 (+$^{[2]}H_9$)	Avanti Polar Lipids	791649C

Cholesterol (+$^{[2]}H_7$)	Avanti Polar Lipids	700041P
SHexCer 18:1;2/12:0	Avanti Polar Lipids	860573P
TAG 17:0/17:1/17:0 (+$^{[2]}H_5$)	Avanti Polar Lipids	110544P

Table 4.5: General reagents and chemicals

Reagent	Source	Identifier
Water for MS sample preparation (LCMS grade)	VWR	83645.320
Ammonium formate	Fluka	17843
Methanol (LCMS grade)	Biosolve	13687802BS
Chloroform (HPLC grade)	Rathburn	RH1009
2-propanol (LCMS grade)	Biosolve	16267802BS
Methylamine	Merck	65568
Flexmix Calibration mix for MS	Pierce	A39239
RIPA Lysis and Extraction Buffer	Thermo Fisher Scientific	89900
Trizma base	Merck	T1503
Glycine	Merck	104201
Tris hydrochloride (Tris-HCl)	Merck	10812846001
Tween 20	Merck	P1379
Roche cOmplete Protease Inhibitor Cocktail	Merck	11697498001
Roche PhosSTOP	Merck	4906845001
3-(N-Morpholino) propanesulfonic Acid (MOPS)	Merck	1132-61-2
Sodium Dodecyl Sulfate (SDS)	Merck	151-21-3
4x Laemmli sample buffer	Bio-Rad	1610747

PAGERuler Prestained Protein Ladder	Thermofisher	26616
Draq7 dye	Thermo Fisher Scientific	D15106
Pluronic F-127	Merck	P2443
16% Paraformaldehyde	Thermo Fisher	28908
Triton-X 100	Carl Roth	3051.4
ProLong Gold	Thermo Fisher Scientific	P36934
4",6-diamidino-2-phenylindole dihydrochloride (DAPI)	Merck	D9542
SiR-actin	Spirochrome	SC001
Sodium chloride	Merck	106404
Potassium Chloride	Merck	104936
Sodium Phosphate Dibasic	Merck	567550
Potassium Phosphate Monobasic	Merck	P0662
Boric Acid	Merck	100165
Sodium Tetraborate	Merck	106306
HEPES-KOH	Merck	H0527
Magnesium Chloride	Merck	814733
TrisHCl	Merck	10812846001
Sodium Phosphate Monobasic	Merck	106580
Ethylenediaminetetraacetic acid (EDTA)	Merck	20-158
HEPES	Biomol	05288
Potassium Phosphate Dibasic	Merck	104873
Sucrose	Merck	S0389
2-(N-morpholino) ethanesulfonic acid (MES)	Merck	69889

ethylene glycol-bis(β-aminoethyl ether)-N,N,N′,N′-tetraacetic acid (EGTA)	HACH	2229726

Table 4.6: Kits

Kit	Source	Identifier
Pierce BCA protein assay kit	Thermo Fisher Scientific	23225
PKH67 Green Fluorescent Cell Linker Kit for General Cell Membrane Labeling	Merck	PKH67GL-1KT
Pierce ECL Western Blotting Substrate	Thermo Fisher Scientific	32106
Minute Plasma Membrane Protein Isolation and Cell Fractionation Kit	Invent Biotechnologies	SM-005

Table 4.7: Primary Antibodies

Antibody against	Clonality	Raised in	Source	Identifier	Use case	Dilution
Phospho-Ezrin (Thr567)/ Radixin (Thr564)/ Moesin (Thr558)	Monoclonal	Rabbit	Cell Signaling	3726	Western Blot	1:2000
Ezrin/ Radixin/ Moesin	Polyclonal	Rabbit	Cell Signaling	3142	Western Blot	1:1000
GAPDH	Monoclonal	Mouse	Novus Biologicals	NB300-221	Western Blot	1:80000

β-Tubulin III	Monoclonal	Mouse	Abcam	ab78078	IF	1:200

Table 4.8: Secondary Antibodies

Antibody	Source	Identifier	Use case	Dilution
Goat-Anti-Mouse-HRP	Jackson Immuno Research	115-035-062	Western Blot	1:100000
Donkey-Anti-Rabbit-HRP	Jackson Immuno Research	711-035-152	Western Blot	1:100000
Goat-Anti-Mouse-Alexa 594	Thermo Fisher Scientific	A-11005	IF	1:500

Table 4.9: Recombinant DNA

Plasmid	Source	Identifier
EGFP-CAAX	Addgene	86056
pHR:GFP-CAAX	Diz-Muñoz lab	DM82
p8.91	Diz-Muñoz lab	DM71
pMD2.G	Diz-Muñoz lab	DM70

Table 4.10: Equipment

Equipment	Source	Identifier
Olympus CKX53 cell culture microscope	Evident Scientific	N/A
Leica DM IL LED epifluorescence microscope	Leica Microsystems	N/A
Countess II FL automated cell counter	Thermo Fisher Scientific	N/A
Table-top Eppendorf tube centrifuge	Eppendorf	5417R
Heraeus Megafuge 16 Centrifuge	Thermo Fisher Scientific	75004230

T 10 basic Ultra-Turrax	IKA	0003737000
Bioruptor Standard	Diagenode	UCD-200
ThermoMixer C	Eppendorf	5382000015
Vacufuge plus Vacuum Concentrator	Eppendorf	N/A
Orbitrap Fusion Tribrid MS	Thermo Fisher Scientific	N/A
TriVersa NanoMate	Advion Biosciences	5305000304
Victor Nivo Multimode Microplate Reader	PerkinElmer	HH35000500
Orbitrap Fusion Lumos Tribrid Mass Spectrometer	Thermo Fisher Scientific	N/A
Mini Gel Tank	Thermo Fisher Scientific	A25977
Mini Blot Module	Thermo Fisher Scientific	B1000
Benchblotter Shaker	Benchmark Scientific	BR1000
Scientific Industries	Thermo Fisher Scientific	SI-0256
ChemiDoc touch imaging system	Bio-Rad	1708370
LSR Fortessa	Becton Dickinson	N/A
MoFlo XDP	Beckman Coulter	N/A
Plasma Cleaner	Gala Instrumente	N/A
PRIMO system	Alveole	N/A
CellHesion 200 Atomic Force Microscope (AFM)	JPK BioAFM, Bruker	N/A
Eclipse Ti inverted light microscope	Nikon	N/A
Zeiss LSM 780 NLO	Zeiss	N/A
Zeiss LSM 880 NLO Airyscan	Zeiss	N/A

Table 4.11: Other materials

Material	Source	Identifier

Bolt 4 to 12%, Bis-Tris, 1.0 mm, Mini Protein Gels	Thermo Fisher Scientific	NW04120BOX
Immun-Blot PVDF membranes	Bio-Rad	1620177
Blot Absorbent Filter Paper	Bio-Rad	1703956
Olympus BioLever	Bruker	OBL-10
MLCT-010 cantilevers	Bruker	MLCT-O10
10μm-borosilicate glass beads	Noovascan	PT.GS

Table 4.12: Software

Software	Version	Source
Excel	16.43	Microsoft
XCalibur	4.2	Thermo Fisher Scientific
ALEX[123]		Ejsing lab
SAS	9.4	SAS Institute Inc.
SAS Enterprise Guide	7.1	SAS Institute Inc.
RStudio	1.1.463	
R	3.6.2	
Tableau Desktop	2020.4	Tableau Software, Inc.
Python	3.6.1	
ImageJ2	2.3.0/1.53f	
FlowJo	v10.7.1	Becton Dickinson
Imaris	9.7.2	Oxford Instruments

4.2 Solutions, buffers and media

4.2.1 Solutions

Table 4.13: AF Solution in LCMS-grade water

Reagent	Concentration (mM)

Ammonium Formate	155

4.2.2 Buffer compositions

Table 4.14: Phosphate Buffer Saline, pH 7.4

Reagent	Concentration (mM)
Sodium chloride	137
Potassium Chloride	2.7
Sodium Phosphate Dibasic	10
Potassium Phosphate Monobasic	1.8

Table 4.15: Borate Buffer

Reagent	Concentration (mM)
Boric Acid	50
Sodium Tetraborate	23.8

Table 4.16: HKM Buffer, pH 7.4

Reagent	Concentration (mM)
HEPES-KOH	150
Potassium Chloride	150
Magnesium Chloride	5

Table 4.17: 10x Transfer Buffer stock, pH 8.3

Reagent	Concentration (mM)
Trizma base	250
Glycine	1920

Table 4.18: 1x Transfer Buffer

Reagent	Volume per 100ml buffer (ml)
10x Transfer buffer, pH 8.3	10
Methanol	20

Table 4.19: 20x Tris-Buffered Saline (TBS), pH 7.5

Reagent	Concentration (mM)
Sodium Chloride	3000
TrisHCl	400

Table 4.20: Tris-Buffered Saline, Tween (TBST)

Reagent	Volume per 100ml buffer (ml)
20x TBS, pH 7.5	5
Tween 20	0.1

Table 4.21: 100mM Phosphate Buffer, pH 7.0

Reagent	Concentration (mM)
Sodium Phosphate Monobasic	19
Sodium Phosphate Dibasic	81

Table 4.22: 20x NuPAGE MOPS SDS Running Buffer, pH 7.7

Reagent	Concentration (mM)
MOPS	1000
Trizma base	1000
Sodium Dodecyl Sulfate (SDS)	70
EDTA	20

Table 4.23: 4x Laemmli Buffer

Reagent	Volume per 100ml buffer (ml)
4x Laemmli sample buffer	90
β-ME	10

Table 4.24: Cytometry buffer

Reagent	Concentration
BSA	37.6 (0.25% w/v)
EDTA	2.5mM

PBS, pH 7.4	1x

Table 4.25: 10x Intracellular buffer, pH 7.4

Reagent	Concentration (mM)
MES	100
Potassium Chloride	1400
Magnesium Chloride	30
EGTA	20

Table 4.26: 2x Fixation-Permeabilization buffer

Reagent	Volume per 100ml buffer (ml)
10x Intracellular buffer, pH 7.4	20
16% Paraformaldehyde	37.5
Tergitol	1
1M Sucrose stock	2

4.2.3 Media compositions

All media were prepared under laminar flow hoods and filtered using stericups with 0.22μm pore size. They were then stored at 4°C and warmed to 37°C using a water bath prior to use on cells. The compositions of various media used in cell culture are listed below in the order in which they appear in the methods section.

Table 4.27: ES media

Reagent	Stock Concentration	Final Concentration	Volume per 100ml media (ml)
Knockout DMEM		80%	80
EmbryoMax FBS		15%	15
NEAA	100x	1x	1
Glutamax	100x	1x	1

Sodium Pyruvate	100mM	1mM	1
Pen-Strep	5000U/ml	50U/ml	1
β -ME	14.3mM	143μM	1
LIF	10μg/ml	20ng/ml	0.2

Table 4.28: CA media

Reagent	Stock Concentration	Final Concentration	Volume per 100ml media (ml)
High-glucose DMEM		85%	85
FBS		10%	10
NEAA	100x	1x	1
Glutamax	100x	1x	1
Sodium Pyruvate	100mM	1mM	1
Pen-Strep	5000U/ml	50U/ml	1
β-ME	14.3mM	143μM	1

Table 4.29: N2 media

Reagent	Stock Concentration	Final Concentration	Volume per 100ml media (ml)
High-glucose DMEM		96%	96
Sodium Pyruvate	100mM	1mM	1
B27 without vitamin A	50x	0.5x	1
N2 supplement	100x	1x	1
Pen-Strep	5000U/ml	50U/ml	1

Table 4.30: 3T3 media

Reagent	Stock Concentration	Final Concentration	Volume per 100ml media (ml)
DMEM containing 4.5g/l glucose	100%	89%	89
FBS	100%	10%	10
Pen-Strep	5000U/ml	50U/ml	1

Table 4.31: HEK media

Reagent	Stock Concentration	Final Concentration	Volume per 100ml media (ml)
DMEM containing 1g/l glucose	100%	89%	89
FBS	100%	10%	10
L-glutamine	200mM	2mM	1
Pen-Strep	5000U/ml	50U/ml	1

4.3 Cell culture

All cultured cells described in this thesis were maintained at 37°C in the presence of 5% CO_2 and the cells were not exposed to air outside the sterile environment of a laminar flow hood. S1 safety measures were followed unless otherwise specified.

4.3.1 Neuronal differentiation of mESCs in embryoid bodies

Culturing and differentiation of mESCs into neurons in embryoid bodies was performed over 20 days [69] as described below.

Day -7: Seeding of MEF feeder cells. A feeder layer of mouse embryonic fibroblast cells (mEFs) from CD1 mice was used as a feeder layer on which mESCs were cultured. For this, T25 flasks were coated with 5ml 0.1% (w/v) gelatin dissolved in PBS for 1 hour at 37°C. MEFs were thawed and seeded on the gelatin-coated flasks at a density of 2.4*10^4 cells/cm^2 in ES media (Table 4.27).

Day -6: Seeding of mESCs. mESCs (129XC57BL/6J generated from male 129-B13 agouti mice) were thawed and seeded on the feeder layer of mEFs in ES media at a density of 4.2*10^4 cells/cm^2.

Day -5 to 0: Maintenance of cells in adherent culture. Media was refreshed on odd days (-5, -3, and -1), and the cells were subcultured on even days (-4 and -2) into new gelatin-coated T75 flasks. For this, cells were washed twice with PBS and treated with 0.05% trypsin-EDTA for 5 minutes at 37°C. Trypsin was then neutralized using ES media and the cells were pelleted by centrifugation at 800g for 3 minutes at RT. They were resuspended in ES media, counted, and seeded in fresh gelatin-coated dishes at a density of 4.2*10^4 cells/cm^2.

Day 0: Feeder depletion and the onset of suspension culture. Day 0 marks the start of cell growth in embryoid bodies. For this, the cells were washed, trypsinized, and pelleted by centrifugation as on previous days. Cells pelleted from one T75 flask were resuspended in 5ml ES media and incubated in a 10cm TC-coated dish for 10 minutes at 37°C to selectively deplete the more adherent MEF feeder cells. The unadhered mESCs were then recovered from these dishes, counted, and once again centrifuged as before. The cells were then resuspended in CA medium and 4*10^6 cells were seeded in 15mL CA media (Table 4.28) in a 10cm non-adherent sterile petri dish. Under these conditions, the mESCs clustered into embryoid bodies that progressively grew progressively larger over the next 8 days.

Day 0 to 4: Growth of mESCs in embryoid bodies. Media was refreshed on day 2 by transferring the suspension culture from the petri dish into a falcon tube and allowing the embryoid bodies to sediment over 5 minutes, after which the supernatant was aspirated. 10ml of fresh media was carefully pipetted into the falcon tubes and the cells were collected from the bottom in one go and transferred into new Petri dishes using a 25μl-serological pipette. It is important to handle the cells gently in this process as sheer forces from quick and repeated pipetting can break up the cell aggregates.

Day 4 to 8: Stimulation with retinoic acid. On days 4 and 6, the media was refreshed as on day 2, but using CA media supplemented with 5μl retinoic acid to induce neuronal differentiation. In preparation for day 8, TC-coated nunclon dishes were incubated overnight on day 6 with 0.1 mg/ml PDL in Borate buffer (Table 4.15). On day 7, the dishes were washed thrice with water and incubated overnight with 2.5μg/ml laminin in PBS at 37°C.

Day 8: Dissociation of embryoid bodies and cell plating. The embryoid bodies were allowed to sediment in a falcon tube and the supernatant was aspirated, as before. The cells were then carefully washed twice with PBS and allowed to sediment for 5 minutes after each wash. The PBS was then aspirated and the cells were treated with 0.05% Trypsin-EDTA for 5 minutes at 37°C to dissociate the embryoid bodies into single cells. The trypsin was then quenched with CA medium, the cells were pipetted up and down repeatedly to further break up any aggregates and passed through a 70μm nylon cell strainer. Cells were seeded at a density of 2*10^5 cells/cm² in N2 media (Table 4.29) on the PDL + laminin-coated dishes. Two hours later, 50% of the media was refreshed.

Day 8-12: Adherent culture of neurons. On day 9 and day 10, 50% of the media was refreshed, taking care not to expose the plated neurons directly to air and on day 10, the media was supplemented with 1μM Ara-C to terminate proliferating non-differentiated cells. Day 12 neurons showed positive staining for the neuronal marker β-Tubulin III (Figure 2.8).

4.3.2 NIH/3T3 mouse fibroblasts

3T3 mouse fibroblasts were seeded on TC-coated dishes at a density of 5-10*10^3 cells/cm^2 in 3T3 media (Table 4.30). They were subcultured every 2-3 days.

4.3.3 Cell freezing and storage

Cells of all types were trypsinized and counted prior to freezing. They were then pelleted by centrifugation at 800g for 3 minutes at room temperature and resuspended in a solution of 10% DMSO in FBS at a concentration of 1-2*10^6 cells/ml and aliquoted into 2ml cryogenic storage tubes such that each tube contained 1-2*10^6 cells. These tubes were then slowly cooled to -80°C over the next two hours by placing in a Mr. Frostie in the -80°C freezer. They were then transferred into liquid nitrogen for long-term storage.

4.3.4 Perturbations to cells in culture

4.3.4.1 Fatty acid supplementation

Fatty acids (FAs) were supplemented to the cells after complexing with BSA [106, 168, 169]. For this, stock solutions of the FAs to be supplemented to cells were prepared by dissolving the lyophilized FAs in ethanol at 4°C (40 mM 18:0, 32.8 mM 20:4 and 60 mM 22:6). Fatty acid-free BSA was dissolved in N2 media at 4°C to a final concentration of 3mM. The FA solutions were pipetted drop-wise into the N2 media containing 3 mM fatty acid-free BSA at 37°C with constant stirring to obtain 100x stocks of FAs bound to BSA (3mM 18:0, 1mM 20:4 and 2mM 22:6), which were aliquoted and stored at -20°C. In this step, it is important to pipette slowly in order to prevent precipitation. On day 8 of neuronal differentiation in embryoid bodies (section 4.3.1), the 100x FA-BSA stock was added to the N2 culture medium in a 1:100 ratio.

4.3.4.2 Cholesterol depletion

Cholesterol was depleted from 3T3 cells using treatment with methyl-β-cyclodextrin (MβCD) [202]. In order to prevent competition to cellular cholesterol from lipids in the media for binding MβCD, the drug was dissolved in 3T3 media made with delipidated FBS in place of regular FBS, to the desired final concentration. Cells were washed twice with PBS before being placed in media containing the drug to wash out any lipid remnants that can interfere with the binding of MβCD to cellular cholesterol and the cells were incubated with the drug for 30-120 min.

4.3.4.3 SCD1 inhibition

SCD1 inhibition was performed using the drug A939572 as described for other cell types previously[322, 323]. For this, lyophilized A939572 was dissolved in DMSO to a stock concentration of 4mM and stored at -20C. Stearic acid (18:0) was complexed with 3mM BSA in 3T3 medium as described for fatty acid supplementation, to a final stock concentration of 6mM. To perform SCD1 inhibition in cells, the A939572 stock was dissolved 1:2000 in 3T3 media to obtain a final concentration of 2μM. Media from the 3T3 cells in culture was aspirated and swapped in for media containing 2μM A939572. 4 hours later, the BSA-18:0 stock was added to the cells at a 1:30 dilution, in order to have final concentrations of 200μM 18:0 and 100μM BSA. The cells were then co-incubated with A939572 and BSA-18:0 over 16-20 hours to achieve increased saturation of their lipids.

4.3.4.4 Inhibition of actin polymerization

The toxin Latrunculin A (LatA), first extracted from the red sea sponge *Latrunculia magnifica* was used for inhibiting actin polymerization in 3T3 fibroblasts [334, 335]. LatA in solid form was dissolved in DMSO to a final stock concentration of 1mM and stored at -20°C. This stock was then dissolved in 3T3 media with 1:1000 dilution to a final concentration of 1μM and the cells were incubated in it for 30 minutes.

4.3.5 Membrane labeling with PKH67 in live cells

The PKH67 kit was used for staining plasma membrane in live 3T3 mouse fibroblasts in a 35mm glass bottom dish for imaging. For this, a 2x solution (500μM) of PKH67 was prepared by dissolving 1μl dye 1000μl of diluent C. Cells were washed once with DMEM and kept in a drop of 125μl diluent C. 125μl of the 2x working solution of PKH67 was added to have a final concentration of 250μM of dye. The cells were incubated in this manner for 5 minutes at room temperature. They were then treated with 250μl FBS to quench labeling. The solution was aspirated, the cells were washed twice with 3T3 media and incubated once again in 3T3 media at 37°C for 30 minutes prior to imaging.

4.3.6 Transient transfection

Transient transfection of 3T3 mouse fibroblasts to express GFP-CAAX was performed by packaging the EGFP-CAAX plasmid in liposomes using lipofectamine 2000 as per the manufacturer's instructions. Briefly, the 3T3 mouse fibroblasts to be transfected were plated a day prior to transfection in a six-well plate with a seeding density of 5*10^3 cells/cm^2. On the day of transfection, 8μl of lipofectamine 2000 was diluted in 150μl of Opti-MEM under the TC hood. 1μg of the EGFP-CAAX plasmid was diluted separately in another 150ul of Opti-MEM. These are the volumes required to transfect one well of the six-well plate and can be scaled up depending on the number of wells needing transfection. The lipofectamine and plasmid solutions were then mixed, vortexed, and incubated at room temperature for 10 minutes. This solution was then gently pipetted drop by drop into the well containing the cells in 2ml media without pipetting up and down. The cells were then grown for 48 hours before measuring the fluorescence from GFP-CAAX.

4.3.7 Stable cell line generation

Lentiviral transduction was used to generate 3T3 mouse fibroblasts with stable expression of GFP-CAAX to allow fluorescent visualization of the cell membrane. Briefly, lentivirus particles carrying the GFP-CAAX gene were first produced from three separate plasmids in HEK293T cells. The particles were then collected from the media of these cells by centrifugation and used to transduce 3T3 cells, which were then sorted by fluorescence-activated cell sorting (FACS) to obtain a population of cells with a homogeneous level of stable GFP-CAAX expression. Each of the steps is explained in the following sections.

4.3.7.1 Lentivirus Production

Lentivirus production was done using the 2nd generation packaging method where the lentiviral genome is distributed into 3 separate plasmids for safety:

1. Lentiviral transfer plasmid encoding GFP-CAAX with pHR backbone (pHR:GFP-CAAX). In this plasmid, the GFP-CAAX sequence is flanked by long terminal repeat (LTR) sequences responsible for integrating the gene of interest into the cell's genome upon transduction.
2. Packaging plasmid p8.91 containing the viral genes Gag, Pol, Rev, and Tat.
3. Envelope plasmid pMD2.G carrying the envelope protein VSV-G.

HEK293T cells were used as hosts for lentivirus production and isolation as described below.

Day -3: Thawing of HEK293T cells. HEK293T cells were thawed and seeded on TC-coated 10cm dishes at a density of $5*10^4$ cells/cm^2 in HEK media (Table 4.31) and allowed to recover for three days.

Day 0: Plating of HEK293T cells for transfection. HEK293T cells were trypsinized as described for 3T3 cells and reseeded into two wells of a 6-well plate at a density of $5*10^4$ cells/cm^2 and 2ml HEK media per well.

Day 1: Transfection of HEK293T cells. The three plasmids encompassing the lentiviral genome were mixed together such that the final mix contained 3μg transfer plasmid, 2.6μg p8.91 and 0.33μg pMD2.G. 400μl opti-MEM and 16μl TransIT-Lenti were added to this mix and incubated for 15 minutes at room temperature. 200μl of the solution was then pipetted drop-wise into each well containing the HEK293T cells and the plate was moved into an incubator in the S2 safety-level lab, as these cells would soon produce lentiviral particles by the combined expression of the transfected plasmids. All further steps were carried out in the S2 cell culture lab following the prescribed additional safety measures.

Day 3: Collection of lentiviral particles. Visual inspection of the HEK293T cells under an epifluorescence microscope with excitation and emission filters for GFP revealed fluorescent signal at the plasma membrane, confirming the expression of GFP-CAAX. Lentiviral particles were harvested from the media of the HEK293T cells. For this, the media (4ml) was collected from the wells and passed through a 0.45μm PVDF syringe filter. 1.4mL Lenti-X was added to concentrate the viruses and mixed gently. The solution was first incubated at 4°C for 30 minutes and then centrifuged at 1500g at 4°C for 45 minutes to pellet the viral particles. The supernatant was then discarded and the pellet was resuspended in 150μl 3T3 media and stored at -20°C.

4.3.7.2 Lentiviral transduction of NIH/3T3 cells

3T3 cells already in culture were seeded into three wells of a 24-well plate at a density of 2*10^{4}cells/ccm^2. One day later, these cells were treated with polybrene to a final concentration of 5μg/ml to neutralize the charge repulsion between the lentiviral particles and the cell surface and thereby facilitate transduction. Then 5, 20, and 50μl of the viral stock solution was added to the three wells. The cells were then kept in culture and expanded over three passages.

During this period, the cells were counted at every passage and carefully observed under the microscope for any phenotypic abnormalities. Cells transduced with 50μl of the lentiviral stock solution were observed to reach confluence more slowly compared to wildtype-cells and cells transduced with lower viral loads, and therefore not selected for the final experiments. Visual inspection under an epifluorescence microscope revealed green fluorescent signal at the plasma membrane, confirming the expression of GFP-CAAX in all three cases, with a very faint signal in cells transduced with 5μl of the lentiviral stock compared to those loaded with higher amounts.

After three passages, the cells were moved back to the S1 safety-level lab. Cells from one 10cm dish for each cell line were frozen at a density of 2*10^6 cells/ml in FBS + 10% DMSO solution and stored at -80°C. Owing to the faint GFP signal observed in the 5μl-lentivirus-transduced cells and the growth defect observed in the 50μl-lentivirus-transduced cells, 20μl-lentivirus-transduced cells were used for further sorting 4.8 to obtain two cell lines with homogeneous expression of GFP-CAAX across the cell population. Of these, the cell line with lower GFP expression was then used for all further experiments and is referred to as the GFP-CAAX-NIH/3T3 cell line in this thesis.

4.4 MS^{ALL}-based shotgun lipidomics

4.4.1 Sample collection for lipidomics

4.4.1.1 Brain tissue

Brain tissue samples were collected at four developmental time points from wild-type CD-1 mice from the EMBL breeding colonies:

1. Embryonic day 10.5 (E10.5)
2. Embryonic day 15.5 (E15.5)
3. Post-natal day 2 (P2)
4. Post-natal day 21 (P21)

The animals were housed at the EMBL mouse facility under standard laboratory conditions including a twelve-hour day/night cycle with *ad lib* access to food and water. Pups were housed with their mother and littermates until P21. At each desired time point, the animals were sacrificed (mothers in case of embryonic stages E10.5 and E15.5) by IACUC-approved methods and the brain tissues were carefully dissected out and washed in PBS. P2 and P21 tissues were additionally dewetted on lens-cleaning tissue, whereas this was found to lead to smearing and loss of the more delicate E10.5 and E15.5 tissues, and hence avoided. The samples were then transferred to 2ml Eppendorf tubes and snap-frozen in liquid nitrogen for storage at -80°C until further processing.

Mouse embryos were surgically removed from the amnion and the outer ectoderm was carefully peeled off from the brain region of E10.5 mice. Individual E10.5 brain samples were found to not yield enough lipids for lipidomics. Therefore, samples consisting of pooled brain regions of five embryos from the same mother were prepared per biological replicate. The rest of the individual E10.5 embryos after removal of the brain tissue were collected in order to compare the lipid composition of brain tissue to the average lipidome of the rest of the tissues in the embryo at this early point in development.

At all other time points, the brain had developed clear hemispherical lobes and therefore allowed further dissection of cerebral hemispheres from the rest of the brain. Here, individual hemispheres and residual brain tissues provided sufficient lipid yield for lipidomics and constituted independent biological replicates.

4.4.1.2 mESCs

mESCs being differentiated into neurons *in vitro* were collected for lipidomics at four different stages of differentiation:

1. Day 0 (undifferentiated mESCs)
2. Day 4 (embryoid bodies)
3. Day 8 (embryoid bodies)
4. Day 12 (*in vitro* differentiated neurons)

On day 0, $3*10^6$ adherent mESCs from about two nearly confluent wells of a 6-well plate were collected after trypsinization, feeder depletion, and counting, prior to the start of suspension culture. On days 4 and 8, embryoid bodies from one 6cm dish were collected by centrifugation at 800g for 3 min at room temperature and on day 12, cells from 3 wells of a six-well plate were pooled to generate a sample for lipidomics.

The cell pellets from days 0, 4, and 8 were washed once with 4ml HKM buffer (Table 4.16) and once more with 1ml HKM buffer, and re-pelleted after each wash. The final cell pellet was then dissolved in 200μl AF solution (Table 4.13). The adherent cells on day 12 were washed twice with 4mL HKM buffer in their respective wells and then scraped in 100μl AF solution using a cell scraper.

All samples in AF solution were transferred to 2ml Eppendorf tubes and snap-frozen in liquid nitrogen for storage at -80°C until further processing. The differentiation procedure was repeated to generate independent biological replicates for all time points.

4.4.1.3 NIH/3T3 mouse fibroblasts

3T3 mouse fibroblasts from one 10cm dish ($3*10^6$ cells) were collected for whole-cell lipidomics. For this, they were trypsinized, counted, and pelleted. The cell pellet was washed once with 4ml HKM buffer and once more with 1ml HKM buffer, and re-pelleted after each wash. The final cell pellet was then dissolved in 200μl AF solution and transferred to a 2ml Eppendorf tube and snap-frozen in liquid nitrogen for storage at -80°C until further processing.

4.4.1.4 Plasma membrane isolates

Protein concentration in isolated plasma membranes was estimated using Bradford or BCA assay (Section 4.4.2) and the samples were diluted to a final protein concentration of 45ng/μl in AF solution, following which they were snap-frozen in liquid nitrogen for storage at -80°C until further processing.

4.4.1.5 Sample homogenization

As tissue samples from mice were freshly snap-frozen after dissection, they required an additional homogenization step before lipid extraction. AF solution was warmed to 85°C using a water bath and 250-1200μl of the warm AF solution was added to the frozen tissue samples, based on total lipid amounts measured in the pilot run [1]. Samples were then homogenized using an ultra-turrax at setting 3-4 for 30s, following which they were incubated in the 85°C water bath for two minutes, and then shifted to ice. Where required, homogenized tissues were further diluted in AF solution.

Tissue and cell samples were also subjected to sonication using the Bioruptor for five minutes with 30s ON/OFF cycles on ice to obtain homogeneous samples, following which their protein content was estimated using either a Bradford or BCA Assay.

4.4.2 Protein estimation

The protein concentration of homogenized samples was determined using one of the two established colorimetric assays described below.

4.4.2.1 Bradford assay

The Bradford assay is based on the binding of the Coomassie G-250 Dye to proteins in an acidic environment, resulting in a shift in the absorbance peak of the dye from 465 nm to 610 nm.

---

[1] For the very first pilot experiment, with no prior information on the sample amount to use, samples were weighed on a weighing scale and 30uL AF solution was added per mg of sample. This was done assuming that brain tissue yields 40-50 μg protein/mg of tissue, and we would like to extract lipids from samples containing 10μg protein, dissolved in a few μl of solution.

The assay was performed in a 96-well glass-bottom plate (Thermo Fisher Scientific, 15041). Since the assay is linear for protein concentrations of 125-1500μg/ml, standard solutions containing 0, 125, 250, 500, 750, and 1000 μg/ml BSA in AF solution were prepared for calibrating the absorbance values to protein concentrations on a standard curve.

Next, 5μl of each standard was pipetted in triplicate into three wells of the 96-well plate. Similarly, 5μl of each unknown sample was pipetted in duplicate. 200μl of Bradford reagent was added into each well and mixed well. The plate was incubated for 15-30 min at room temperature, following which it was placed in a plate reader and the absorbance was measured at 595nm wavelength, where the difference in absorbance between the protein-bound and unbound states of the dye is greatest.

4.4.2.2 BCA assay

The Bicinchoninic acid (BCA) assay is used to determine protein concentrations based on a reaction involving the peptide bonds of proteins. In the alkaline environment of the assay, peptide bonds reduce the Cu^{2+} ions in solution into Cu^{+} ions, which get chelated into a complex with BCA. This complex gives the solution a purple color and strongly absorbs light at 562 nm wavelength.

The assay was performed using the BCA assay kit in 96-well glass-bottom plates. Since the assay is linear for protein concentrations of 20-2000μg/ml, standard solutions containing 0, 25, 125, 250, 500, 750, 1000, 1500, and 2000μg/ml BSA in AF solution were prepared for calibrating the absorbance values to protein concentrations on a standard curve.

Next, 25μl of each standard was pipetted in triplicate into three wells of the 96-well plate. Similarly, 25μl and 5μl of each unknown sample were pipetted in duplicate. To the wells containing 5μl unknown sample, 20μl AF solution was added to achieve 5x dilution. This was done in order to be able to make an estimate in case the undiluted sample contained protein concentrations greater than 2000μg/ml.

Reagents A and B of the kit were mixed 50:1 to obtain the working reagent for the assay and 200μl of this mix was pipetted into each well. The plate was then incubated at 37°C for 30 minutes and then at room temperature for a few minutes, following which it was transferred to the plate reader and absorption was measured in all wells 562nm.

4.4.2.3 Estimation of protein concentration

Protein estimation from absorbance values was performed in the same way for both assays. Absorbance values of all standard and unknown samples were averaged between replicates. The blank absorption (0μg/ml BSA) was subtracted from all values. A standard curve of concentration vs blank-subtracted absorption was plotted for the BSA standards and fitted to a straight line passing through the origin. Measured absorbance values of all samples were divided by the fitted slope to obtain protein concentrations of the unknown samples. When values outside the range covered by the blanks were obtained, the assay was repeated for suitable dilutions of the samples to have reliable estimates of protein concentration.

4.4.3 Internal Standards

Internal standards are synthetic lipids that are spiked into the sample in known amounts and can be used to quantify the absolute amounts of lipids present in the sample, by a comparison of peak intensities in the mass spectra. Since lipids of different classes have different propensities to get partitioned into the organic phase during lipid extraction and to get ionized in the mass spectrometer, a mix of lipid standards belonging to several lipid classes are used, and endogenous lipids are quantified by comparing their peak intensities against the corresponding lipid standard from their class. The internal standards mix (IS mix) was prepared by diluting internal standard stock solutions into methanol (Table 4.32) in the cold room (4°C) using pre-cooled pipette tips under a laminar flow hood and stored in a glass vial at -20°C.

Table 4.32: IS mix composition

Internal standard	Stock Concentration (μM)	Final Concentration (μM)	Volume per 1ml IS mix (μl)
ACar 16:0 (+$^{[2]}$H$_3$)	126.52	1.27	10.0
CE 10:0	920	17.70	19.2
Cer 18:1;2/17:0;1	440.00	3.45	7.8
CL 14:1/14:1/14:1/15:1	89.14	2.33	26.2

DAG 17:0/17:0 (+$^{[2]}H_5$)	200.00	3.66	18.3
HexCer 18:1;2/12:0	450.31	4.50	10.0
LPA O-16:0	648.56	3.70	5.7
LPC 16:0 (+$^{[2]}H_3$)	55.63	0.93	16.8
LPE O-16:0	155.36	6.68	43.0
LPI 17:1	83.10	1.29	15.5
LPS 17:1	47.03	0.43	9.1
PA 15:0/18:1 (+$^{[2]}H_7$)	156.60	3.13	20.0
PC 16:0/16:0 (+$^{[2]}H_6$)	277.00	4.31	15.6
PE 15:0/18:1 (+$^{[2]}H_7$)	162.30	5.10	31.4
PG 15:0/18:1 (+$^{[2]}H_7$)	153.70	1.71	11.1
PI 15:0/18:1 (+$^{[2]}H_7$)	172.90	1.73	50.0
PS 15:0/18:1 (+$^{[2]}H_7$)	128.70	2.27	17.6
SM 18:1;2/18:1 (+$^{[2]}H_9$)	151.90	3.77	24.8
Cholesterol (+$^{[2]}H_7$)	6350.00	100.00	15.8
SHexCer 18:1;2/12:0	67.47	0.75	11.1
TAG 17:0/17:1/17:0 (+$^{[2]}H_5$)	200.00	2.00	10.0

4.4.4 Lipid extraction

Lipid extraction from all samples was carried out by partitioning the sample between an organic and an aqueous solvent and collecting the organic fraction, as previously described [26, 157, 336]. All steps were carried out in the cold room at 4°C and organic solvents were handled under a laminar flow hood.

The volume of each sample to use for lipid extraction was determined by performing a pilot experiment. Here, a sample volume containing 12μg protein (V_{pilot}) was used, as estimated from protein concentrations determined by a Bradford/BCA assay. The net abundance of PC, PC O-, PE, PE O-, SM, and TAG (L_{pilot}) in this sample volume was measured by performing lipid extraction and MS^1 analysis (described in sections 4.4.5, 4.4.6). Accordingly, the volume of sample to use in order to obtain 4.3nmol abundance was calculated as

$$V = V_{pilot}\frac{4.3\,\text{nmol}}{L_{pilot}} \tag{4.1}$$

The calculated amount of sample was pipetted into a fresh 2ml Eppendorf tube. AF solution was added to a final volume of 200μl. Two blank samples containing 200uL of AF solution were included after roughly every 8-10 real samples, in order to control for 'background' lipids and other contaminants incurred during the lipid extraction steps. Each sample was spiked with 30μl of the IS mix containing known amounts of synthetic lipid standards (Table 4.32).

A two-step lipid extraction was performed [336]:

Step 1: Partitioning against 10:1 Chloroform/Methanol. 990μl of 15:1 C/M (v/v) was pipetted into each sample tube (since the IS mix was prepared in by dissolving the lipid standards in methanol, this results effectively in a 10:1 C/M organic phase when mixed with 30μl of IS mix). The sample tubes were then shaken at 1400rpm for 120 min at 4°C to partition the lipids between the 10:1 C/M organic phase and aqueous phase. Following this, the tubes were centrifuged at 5000g for 2 minutes at 4°C and the organic phase was carefully pipetted out into fresh tubes, which were then subjected to vacuum evaporation for 1-2 hours until all the solvent was completely evaporated, resulting in the first set of lipid extracts using 10:1 C/M.

Step 2: Partitioning against 2:1 Chloroform/Methanol. The remaining aqueous phase from step 1 was subjected to another round of partitioning by adding 990 μl of 2:1 C/M (v/v) to each tube and shaking at 1400rpm for 90 min at 4°C. Following this, the tubes were centrifuged at 5000g for 2 minutes at 4°C and the organic phase was carefully pipetted out into fresh tubes. These tubes were then subjected to vacuum evaporation for 1-2 hours until all the solvent was completely evaporated, resulting in the second set of lipid extracts using 2:1 C/M.

Each deposited lipid extract was dissolved in 100μl 1:2 C/M (v/v), mixed by shaking at 700rpm for 3 minutes at 4°C, centrifuged at 13000g for 3 min at 4°C and stored at -20°C.

4.4.5 Acquisition of MS^{ALL} spectra

MS^{ALL} lipidomics analysis was performed as previously described[26]. This involved recording MS^1 (intact ions) and MS^2 (ion fragments) spectra in both positive and negative ion modes, and multiplexed MSX spectra (for cholesterol detection and quantification) in the positive ion mode. Spectra were acquired on an Orbitrap Fusion Tribrid mass spectrometer equipped with a robotic nanoflow ion source, the TriVersa NanoMate. The steps are described below.

4.4.5.1 Sample loading

The lipid extracts were loaded on 96-well PCR plates compatible with the nanomate. These were mixed with other solvents to yield infusates with solvent compositions that favor ionization of the lipids in the spectrometer. Two kinds of samples were prepared from 10:1 C/M extracts for measuring with the positive and negative ion modes, and the 2:1 C/M extracts were prepared for measuring only with the negative ion mode. The samples were prepared as described below.

1. 10:1 Positive ion mode: 10μl of 10:1 C/M extract was mixed with 12.9μl 13.30mM AF in 2-propanol, to yield an infusate containing 7.5mM Ammonium formate in chloroform/methanol/2-propanol in a ratio of 1:2:4 (v/v/v).

2. 10:1 Negative ion mode: 10μl of 10:1 C/M extract was mixed with 12.9μl 1.33mM AF in 2-propanol, to yield an infusate containing 0.75mM Ammonium formate in chloroform/methanol/2-propanol in a ratio of 1:2:4 (v/v/v).

3. 2:1 Negative ion mode: 10μl of 2:1 C/M extract was mixed with 10μl 0.01% methylamine in methanol, to yield an infusate containing 0.005% methylamine in chloroform/methanol in a ratio of 1:5 (v/v).

In addition to the samples, 50μl of Flexmix calibration mix was loaded into one of the wells. The 96-well PCR plate was then covered with an aluminium foil sticker and mounted onto the plate holder at the nanomate. The tip bin under the nanomate was emptied and fresh tips were loaded if required.

4.4.5.2 Instrument Calibration

Nano-Electrospray Ionization (NSI) was used to generate ions for calibration, with the following settings on the TriVersa NanoMate:

- Back-pressure: 1.25 psi
- Ionization voltage: +0.95 kV in positive-ion mode and -0.95 kV in negative-ion mode
- Flow-rate: 200 nl/min

Once a steady ion spray was generated, the calibration program was run for both positive and negative ion modes before starting measurements on samples.

4.4.5.3 Mass Spectrometry

Samples were ionized by NSI, with parameters identical to those for the calibration mix and an Ion Transfer Tube Temperature of 275°C.

The spectrometer was programmed to record the following Fourier-transform mass spectra (FTMS) on the three kinds of samples loaded on the plate:

1. 10:1 Positive ion mode:
   - MS^1 in the m/z range 280-605
   - MS^1 in the m/z range 470-1030
   - MS^1 in the m/z range 975-1400
   - MS^2 (MSX) at m/z 404.39 and m/z 411.43
   - MS^2 at 1 Da m/z windows in the m/z range 400-1000
2. 10:1 Negative ion mode:
   - MS^1 in the m/z range 200-400
   - MS^1 in the m/z range 350-650
   - MS^1 in the m/z range 500-1400
   - MS^2 at 1 Da m/z windows in the m/z range 400-1000

3. 2:1 Negative ion mode:
    - MS^1 in the m/z range 360-675
    - MS^1 in the m/z range 530-1080
    - MS^1 in the m/z range 1000-1400
    - MS^2 at 1 Da m/z windows in the m/z range 400-1000

MS^1 and MSX spectra were jointly acquired for 5 minutes per sample and MS^2 spectra were acquired for another 15 minutes, using the parameters listed in Table 4.33.

Table 4.33: FTMS Acquisition parameters

Acquisition parameters	MS^1	MSX	MS^2
Maximum ion injection time (ms)	100	600	100
Microscans	3	5	3
Automated gain control (AGC) Target	$1*10^5$	$5*10^4$	$5*10^4$
Target resolution	500000	120000	30000

Here, MS^1 refers to the mass spectra of intact ions, automatically generated by a Fourier-transform applied to the current measured in the orbitrap.

MSX refers to the multiplexed isolation of ions at m/z 369.35 ± 0.75 (Cholesterol $+H^+-H_2O$ ion) and m/z 376.40 ± 0.75 (internal standard Cholesterol$+^{[2]}H_7$ $+H^+-H_2O$ ion), which were then subjected to fragmentation by Higher-energy C-trap dissociation (HCD) with 8% collision energy. The fragments were detected on the orbitrap similarly to MS^1.

MS^2 involved fragmentation of all ions within a chosen m/z window with 30% collision energy and a spectrum of the fragment ions was recorded similarly to MS^1 and MSX on the orbitrap.

4.4.6 Analysis of mass spectra

4.4.6.1 Lipid identification

Scripts from the ALEX^{123} framework [24, 25, 150] from the Ejsing lab were used for the analysis of mass spectra in order to annotate peaks to intact lipid ions (in MS^1 spectra) and their fragments (in MSX and MS^2 spectra). The following steps were followed:

1. ***File conversion to txt.*** The ALEX^{123} converter was used to convert mass spectra into individual text files with columns for m/z and measured intensity.

2. ***Targetlist generation*** The ALEX^{123} Target list generator was used to generate lists of m/z values of all relevant lipid ions (and fragment ions in case of MSX and MS^2 spectra) expected within a mass range for the desired (+/-) ionization mode and (10:1 or 2:1 C/M) lipid extract. Ions were chosen for the target lists based on the expected partitioning and ionization properties of the various lipid classes as listed in Table 4.34. The internal standards present in the ISmix (Table 4.32) were also included in the target lists based on their lipid class. m/z values were pulled from the ALEX^{123} database.

Table 4.34: Lipid search lists

Lipid class	Lipid extract	Ionization mode	Adduct	MS^1 m/z range
ACar	10:1 C/M	+ve	+H$^+$	280-605
CE	10:1 C/M	+ve	+NH$_4^+$	470-1030
Cer	10:1 C/M	-ve	+HCOO$^-$	500-1400
CL	2:1 C/M	-ve	-2H$^+$	530-1080
DAG	10:1 C/M	-ve	+HCOO$^-$	500-1400
GM3	2:1 C/M	-ve	-H$^+$	1000-1400
HexCer	10:1 C/M	-ve	+HCOO$^-$	500-1400
LPA	2:1 C/M	-ve	-H$^+$	360-675
LPC	10:1 C/M	-ve	+HCOO$^-$	350-650
LPE	10:1 C/M	-ve	-H$^+$	350-650
LPE O-	10:1 C/M	-ve	-H$^+$	350-650
LPI	2:1 C/M	-ve	-H$^+$	530-1080
LPS	2:1 C/M	-ve	-H$^+$	360-675

MLCL	2:1 C/M	-ve	$-2H^+$	530-1080
PA	2:1 C/M	-ve	$-H^+$	530-1080
PC	10:1 C/M	-ve	$+HCOO^-$	500-1400
PC O-	10:1 C/M	-ve	$+HCOO^-$	500-1400
PE	10:1 C/M	-ve	$-H^+$	500-1400
PE O-	10:1 C/M	-ve	$-H^+$	500-1400
PG	2:1 C/M	-ve	$-H^+$	530-1080
PI	2:1 C/M	-ve	$-H^+$	530-1080
PS	2:1 C/M	-ve	$-H^+$	530-1080
SM	10:1 C/M	+ve	$+H^+$	470-1030
Cholesterol	10:1 C/M	+ve	$+H^+ -H_2O$	369.35 and 376.40
SHexCer	2:1 C/M	-ve	$-H^+$	530-1080
TAG	10:1 C/M	+ve	$+NH_4^+$	470-1030

3. ***Isotope targetlist generation.*** The ALEX^{123} Isotope compiler was used to add m/z entries in order to later compensate for overlapping isotope peaks. The m/z of each entry were one ^{13}C isotope to be lost, was calculated to generate a new entry corresponding to an ion having one less ^{13}C isotope.

4. ***Peak search.*** The ALEX^{123} Extractor was used to run searches through the txt files from step 1 for intensity peaks matching the m/z values in the target lists to within a specified m/z error. This value was set to 0.005. The script returned peak intensity values matched to lipid and fragment ions from the spectra of all samples.

5. ***Unified result file generation.*** The ALEX^{123} Unifier was used to unify results from all searches into one file for MS^1+MSX data and one for MS^2 data, listing all identified lipid ions and their fragments, respectively.

All ALEX^{123} scripts were run on a Windows 10 v20H2 operating system running python 3.6.1 and java 1.8.0_291-b10.

4.4.6.2 Lipid Quantification

SAS pipelines from the Ejsing lab were run on SAS Enterprise Guide for quantifying lipids. The following steps were followed:

1. ***MS^1 deisotoping.*** Since the ^{13}C isotope has a natural abundance of 1.1%, isotope peaks can be significantly large for lipid molecules, which contain tens of C atoms. The deisotoping pipeline was used to identify overlaps between peaks corresponding to a lipid (say, lipid A, with a peak at m/z = a) and an isotope peak of another lipid (lipid B), where B+$^{13}C_1$ has the same m/z, a. Then the intensity of lipid B at m/z = b was used to calculate the contribution from B+$^{13}C_1$ to the intensity at m/z = a and this value was subtracted from the measured intensity at m/z = a to yield the true intensity corresponding to lipid A.

2. ***MS^1 Background subtraction.*** Average peak intensities from the blanks were subtracted from all other samples using the Background Subtraction pipeline.

3. ***Identification of Molecular Lipid Species.*** The MS^2 identification pipeline was used to compile information from the fragment ions identified by ALEX[123] in MS^2 spectra and assign complete side-chain information (called molecular lipid species or MLS identity) to the lipid species (LS) identified from the MS^1 m/z values.

   First, ion fragments with an intensity lower than 250 or an intensity error larger than 10 ppm were filtered out. Similarly, fragments that were not detected in at least half of the measured samples were discarded. The remaining ion fragments were classified into two groups:

   - Lipid class-specific fragments (LCFs) carrying only head-group information about lipid class.
   - Molecular lipid species-specific fragments (MLFs) carrying information on the acyl chain composition of the lipid.

   A list of all MLSs where each piece of structural information (head group and individual acyl chains) was confirmed by the detection of at least one corresponding fragment ion was drawn. Additionally, MLSs were listed only when at least one of the following conditions was met:

   - At least half the calculated fragments for the MLS were detected.
   - At least three fragments were detected per MLS.

4. ***Calculation of relative abundances of MLSs.*** The MS^2 intensity percentage calculation pipeline was used to assign relative abundances for MLSs corresponding to the same LS (ie, having the same MS^1 m/z).

For this, intensities of MLFs from individual MS^2 spectra were summed for each MLS identified in the previous step to obtain I_{MLS}. Next, intensities of MLFs from individual MS^2 spectra were summed across MLSs for each LS to obtain I_{LS}. The relative abundance of each MLS was then calculated to be I_{MLS}/I_{LS}.

5. ***Quantification of LSs and MLSs.*** The peak intensity corresponding to each LS in MS^1 spectra after deisotoping and background subtraction in steps 1 and 2 was used to determine the amount of lipid in pmol (A_{LS}), based on the known pmol abundance of the corresponding internal standard of the same lipid class, A_{IS} as

$$A_{LS} = A_{IS} * \frac{I_{LS}}{I_{IS}} \tag{4.2}$$

Since ISs from some lipid classes were not used, lipids from these classes were quantified based on an IS from a similarly partitioning and ionizing lipid class. Thus, GM3 species were quantified using the PI IS, LPC O-s using the LPC IS, LPEs using the LPE O- IS, MLCLs using the CL IS, and PC O-s, PE O-s, and TAG O-s using the PC IS, PE IS, and TAG IS, respectively.

Once the pmol abundance of each lipid species was quantified, the abundance of MLSs was further determined by multiplying A_{LS} with the relative abundance calculated in step 4.

Finally, since the amount of lipids detected by MS depends on how much of the sample was used for lipid extraction, the pmol amount was normalized to the protein amount in the extracted samples, resulting in the expression of lipid abundance in pmol/μg protein. Based on lipid abundance in pmol/μg protein, the lipids were further grouped by lipid class, and the lipid abundance per lipid class and per all lipid species was determined and expressed in mol % units.

All pipelines were run using Enterprise Guide 7.1 on SAS 9.4 on a windows 10 v20H2 operating system.

4.4.7 Lipidomics analyses

Once the mol % abundances of individual LSs and MLSs were obtained across samples, they were further analyzed to identify significant differences and patterns across samples using the methods outlined below.

1. ***Statistical Tests.*** Depending on the number of conditions being analyzed by lipidomics, one of the following procedures was used to test for statistically significant differences in lipid composition:

    - ***Student's t-test*** Where lipidomics data between two sample groups (*eg*, control and treated) were directly compared, the Student's t-test was used to test for statistically significant differences in the abundance of individual lipids.
    - ***One-way Analysis of Variance (ANOVA).*** In the analysis of time-course data, samples were divided into sample groups, within which all replicates of identical conditions were grouped together. This resulted in nine sample groups among samples obtained from mice and four sample groups from different time points in neuronal differentiation. One-way ANOVA testing with these sample groups was performed to identify significant changes in the mol% abundances of lipids.

    To minimize false positives due to multiple hypothesis testing in both these cases, a Benjamini-Hochberg critical value q was calculated for every p-value with a false positive rate of 0.05. Changes were considered significant for all $p \leq p_c$, where p_c is the largest p-value that is smaller than its corresponding q-value. The statistical tests were performed on R 3.6.2 using Rstudio 1.1.463.

2. ***Principal component analysis.*** A PCA of the mol% abundances of lipids was performed using the ClustVis tool [337]. Here, each sample was considered as a point in the multidimensional space of lipid abundances. First, all values were scaled by unit variance scaling, to identify lipids with large changes between sample groups irrespective of their relative abundance among other lipids. Then, dimensionality reduction was performed by singular value decomposition with imputation for missing values. The PCA scores of samples on the leading components PC1 and PC2 were used to infer the clustering of samples, and the loadings of lipids to PC1 and PC2 were used to infer which lipids were maximally contributing to the differences seen along PC1 and PC2.

3. ***In silico* hydrolysis.** The hydrolysis of lipids results in the formation of fatty acids from their side chains, which can be analysed by chromatography to assess the fatty acyl composition of lipids [338]. Since

the MS^2 data obtained here allows us to identify lipids down to acyl chains, this information can be used to calculate the abundance of fatty acyl chains across lipid classes computationally, lending this analysis pipeline the name *in silico* hydrolysis. An SAS pipeline from the Ejsing lab was used to perform this procedure, where text parsing was used to isolate FA names from the MLS names and the MLS abundance in pmol/μg protein was also taken as the abundance of each FA thus generated from the MLS. These abundances were then summed within each lipid class and MLSs to obtain the absolute (pmol/μg protein) and relative (mol %) abundances of FAs within each lipid class and in the whole of the sample, respectively. Additionally, the distribution of each FA across the various lipid classes was also calculated.

4. ***Lipid Structural Enrichment Analysis.*** Lipid structural Enrichment Analysis was performed as previously described [157] using an SAS pipeline from the Ejsing lab. Here, lists of lipids showing a statistically significant increase or decrease between two indicated sample groups were drawn, constituting the 'increasing' and 'decreasing' lipid clusters. The following structural attributes of these lipids were then determined:

    - Lipid category
    - Lipid class
    - Backbone
    - FA chain[2]

    The occurrence of each structural attribute within the lipid clusters was then compared to its occurrence in the list of all detected lipids and Fisher's exact test was used to determine the probability, p of obtaining the observed occurrences under the null hypothesis that the lipids in the clusters are drawn at random from the pool of all detected lipids. The odds ratio for each feature was calculated as the ratio of occurrence in the lipid cluster to the occurrence in the list of all detected lipids. $p < 0.05$ indicated that the lipid feature was either enriched (odds ratio > 1) or depleted (odds ratio < 1) in the lipid cluster.

All lipidomics data was visualized using Tableau Desktop 2020.4.

---

[2] From MLSs

4.5 Western blotting

Western blotting was used to quantify changes to phosphorylated ERM proteins during serum starvation and cholesterol depletion. The steps are described in the following sections.

4.5.1 Cell lysis

In preparation for the experiment, a 25x stock solution of protease inhibitors (Roche cOmplete) was prepared by dissolving one tablet in 2ml of 100mM phosphate buffer (Table 4.21), and similarly, a 20x stock solution of phosphatase inhibitors (20x, Roche PhosSTOP) was prepared by dissolving one tablet in 100mM phosphate buffer. The stocks were stored at -20°C for up to 4 months. Before cell lysis, they were diluted to final 1x working concentrations in the RIPA lysis buffer.

3T3 mouse fibroblasts were seeded on 6 well plates at a density of $1*10^4$ cells/cm^2 and allowed to grow for two days, after which they were subjected to the desired treatment. Then, the cells were washed with PBS at 4°C and lysed with RIPA buffer containing protease and phosphatase inhibitors at 4°C for 5 minutes. 150μl of lysis buffer was used per well. The lysate was transferred to an Eppendorf tube and centrifuged at 14000g for 5 minutes. The supernatant was transferred to a fresh tube. A small volume of the sample was used to perform the Bradford or BCA assay to determine protein concentrations. The samples were stored at -80°C for as long as required.

4.5.2 SDS-PAGE

Sodium dodecyl sulfate-polyacrylamide gel electrophoresis (SDS-PAGE) was used to denature all proteins in the cell lysates and separate them by molecular weight on a polyacrylamide gel. For this, 30μl of each cell lysate was mixed with 10μl of 4x Laemmli sample buffer (Table 4.23) and boiled for 3 minutes at 95°C. The samples were then centrifuged at 14000g for 3 minutes and placed on ice.

A 10-lane pre-cast SDS gel with 4-12% Bis-Tris gradient was used for SDS-PAGE. It was washed in distilled water and clipped in place in the buffer chamber. Running buffer was prepared by diluting 20ml of 20x MOPS running buffer (Table 4.22) in 380ml of water. The 1x running buffer was filled into the buffer chamber such that it covered the sample wells. Sample wells were washed with running buffer and 20μl of each sample was loaded into separate wells. 5μl of PAGERuler prestained marker was loaded in one of the lanes. The contacts to the power source were secured and the voltage was set to 80V for 20 minutes, and then increased to 150V and run for 1 hour and 30 minutes until the samples ran out the bottom edge of the gel, but preserving all bands above $\sim$20kDa in weight.

4.5.3 Transfer

A PVDF membrane and filter papers were cut to the size of the gel. The membrane was always handled with care and touched only at the edges with tweezers. One corner was cut, so as to know the correct orientation of the membrane later. 1x Transfer buffer was freshly prepared before use, using cold (4°C) milli-Q water (Table 4.18). Used pipet tip boxes were repurposed as soaking chambers for components of the wet transfer step. The PVDF membrane was soaked for 30-45s in methanol, rinsed in distilled water, and then placed in transfer buffer. Filters and sponges were directly soaked in transfer buffer.

After PAGE, the gel was removed from the tank and both the gel and tank were rinsed with distilled water. The gel was removed from its plastic case and the very top and bottom were sliced off to make it flat. The gel was then placed in transfer buffer for 5-10min. The transfer sandwich was carefully assembled as per the instructions in the manual of the transfer chamber, starting from the negative plate and ending with the positive plate on top. A roller was used to ensure that no air bubbles were present between the layers. The membrane was placed with its cut corner at the top-right, and it was ensured that the sandwich sat snugly in the transfer chamber without any gaps. Where required, additional filter papers were inserted to keep tight packing.

The chamber was placed in the electrophoresis tank and filled with transfer buffer. Ice was placed in the tank around the transfer chamber, and a voltage of 20V was applied for an hour.

4.5.4 Blocking and staining

After the transfer step was complete, the membrane was carefully removed from the sandwich and washed once in TBST. It was then placed in a freshly prepared solution of 5% BSA in TBST with gentle shaking for 1 hour at room temperature. Following this, membranes were washed thrice in TBST with gentle shaking over 5-15 minutes for each wash.

In the meantime, the primary antibodies were diluted in TBST containing 5% BSA as required (Table 4.7) to yield 10ml solutions. After the last wash, the membrane was cut as desired, preserving regions around the bands of interest. The individual pieces were then transferred into their respective primary antibody solutions in cleaned pipette tip boxes. They were incubated overnight at 4°C with gentle shaking. The following day, the membranes were rinsed thrice in TBST with gentle shaking over 5-15 minutes for each wash. Following this, they were incubated in solutions of HRP-conjugated[3] secondary antibodies against their organism of origin (Table 4.8), prepared in TBST buffer containing 5% BSA for 1 hour at room temperature with gentle shaking. TBST washes were performed thrice as before.

4.5.5 Detection and Quantification

For detecting protein abundance, the blot was developed using the Pierce ECL Western Blotting substrate whose oxidation is catalyzed by HRP in the secondary antibody and results in a chemiluminescent signal. For this, the two reagents in the kit were mixed 1:1 and kept in the dark. The washed membranes were carefully assembled on a transparency sheet after blotting excess buffer on a paper towel. The ECL agent was pipet drop-wise to cover the area of the membrane and a second transparency sheet was placed over the membrane. The membrane was then kept in the dark for 5 minutes and chemiluminescence was detected on the ChemiDoc touch imaging system. The intensity of the detected bands was quantified using ImageJ2 2.3.0/1.53f as described previously in the literature [339, 340].

4.6 Plasma membrane Isolation

Plasma membrane isolation was performed on the basis of differential centrifugation using the Minute PM isolation kit, as per the instructions of the manufacturer.

Briefly, 3T3 mouse fibroblasts were seeded three days prior to plasma membrane isolation at a density of $5*10^3$ cells/cm^2 on 4x 15cm dishes. Three days later, these cells were trypsinized and centrifuged at 500-600g for 5 minutes at room temperature. Centrifugation was always performed in individual 15ml-Falcon tubes for cells retrieved from each 15cm dish, to ensure efficient pelleting. The cells were washed once with PBS at 4°C, counted, and

---

[3] HRP: Horseradish Peroxidase is an oxidizing agent.

centrifuged again at 500-600g for 5 minutes. The samples were handled on ice after this point. Typically, around 25*10^6 cells were retrieved in this manner.

The supernatant was aspirated completely and the cell pellets were all combined by resuspending in 500 μl Buffer A and incubated on ice for 5-10 minutes, following which they were vortexed for 10-30 seconds. Samples at this stage are termed whole cell lysate (WCL). The WCL was then transferred immediately to a filter cartridge provided in the kit, capped, and centrifuged at 16000g for 30 seconds at 4°C. The pellet thus obtained was resuspended by vigorous vortexing for 10 seconds and passed through the same filter once again by repeating the centrifugation step. Following this, the filter was discarded and the pellet was resuspended once again by vigorous vortexing for 10s.

The sample was centrifuged at 700g for one minute yielding nuclei (Nuc) in the pellet and the rest of the cell in the supernatant. The supernatant was transferred into a fresh 1.5ml Eppendorf tube and centrifuged at 16000g for 30min at 4°C, yielding the cytoplasmic fraction in the supernatant (Cyto) and the total membrane fraction in the pellet. The supernatant was carefully removed and the pellet was resuspended in 200μl buffer B by vigorous vortexing for 30 seconds. The plasma membrane (supernatant; Pre-W) was separated from internal membranes (pellet; Int) by centrifuging at 7800g for 5 minutes at 4°C. The supernatant containing plasma membrane was carefully transferred to a fresh 2ml Eppendorf tube and mixed with 1.6 ml PBS at 4°C by inverting the tube a few times. This mixture was then centrifuged at 16000g for 30 minutes at 4°C. The supernatant was discarded and the pellet containing the isolated and washed plasma membrane fraction (PM) was resuspended in 200μl AF solution.

Similarly, all pellets at various stages of the protocol were resuspended in 200μl AF solution for preparing samples for proteomics.

4.7 Proteomics

Total protein concentrations of all samples were determined using the BCA method (section 4.4.2) prior to Proteomics. Samples were diluted to a final protein concentration of 0.25μg/μl in AF buffer and 40μl of each sample was subjected to tryptic digest. The resulting peptides were labeled with isobaric TMT labels for multiplexing. Following this, the samples were dried down and reconstituted in 100 µl 0.1% formic acid. 2μl volumes of all samples to be multiplexed were then pooled and subjected to a reverse phase clean-up step (OASIS) and analyzed on a 90-minute gradient by LC-MS on an Orbitrap Fusion Lumos Tribrid Mass Spectrometer.

Peaks in the mass spectra were matched to TMT-labeled peptide sequences from the 2020 Uniprot *Mus musculus* database using the isobarquant package [341]. Contaminants and proteins with fewer than 2 unique quantified peptides were filtered out and Variance Stabilising Normalisation was applied [342].

4.8 Flow cytometry

Flow cytometry was used for quantitative analysis of fluorescence from the transfection of GFP-CAAX and the three lentivirus-transduced cell lines expressing GFP-CAAX.

In all cases, the cells were trypsinized, counted, and centrifuged at 800g for 3 minutes at 4°C. They were then resuspended and spun down twice in 2ml of PBS per million cells at 4°C. The cell pellet was then resuspended in ice-cold Cytometry buffer (Table 4.24) to yield a cell density of $2.5*10^5$cells/ml in a minimal volume of 400μl. The cell solution was then transferred to a FACS tube through a cell strainer to filter cell clumps. 5μl of 0.3 M Draq7 was added per ml of each sample and used as a marker for cell death. The cells were always handled on ice and vortexed for 10 seconds before loading the sample on the cytometer.

GFP fluorescence was analyzed using the LSR Fortessa Analyser at the Flow cytometry core facility at EMBL, Heidelberg. Data analysis was performed on FlowJo v10.7.1. Cells were prepared similarly for cell sorting, without the addition of Draq7. Cell sorting was performed on a MoFloe XDP cell sorter at the Flow cytometry core facility at EMBL, Heidelberg.

4.9 Micropatterning

Micropatterning was performed using the PRIMO setup. The various steps of this process are described in the sections that follow.

4.9.1 Micropattern file generation

The first step towards generating micropatterns was to generate an image file with the pattern of interest. ImageJ2 2.3.0 was used to generate such an image. First, the *set scale* option was used to match the pixel size to the 20x objective and camera setting on the microscope with the PRIMO unit. The scale was set to 0.28px/μm. Next, the image type was set to 8-bit greyscale, and the dimensions were set to 1824px * 1140px in width and height. All pixels were first made black. An array of white circles 20μm in diameter were then added with a spacing of 50μm between their centers using ImageJ drawing tools. The image was saved as a .tiff file.

4.9.2 Stencil and dish preparation

Stock solutions of PLL-PEG and fibronectin were prepared prior to micropatterning. For this, PLL-PEG was dissolved in PBS to a final concentration of 0.2mg/ml PLL-PEG. 5mg Fibronectin was dissolved in 5 ml of PBS to make 1mg/ml stock solution. Both these stocks were stored at -20°C until use.

PDMS gels were used to prepare a small well in the middle of the dish for micropatterning. For this, 1-2mm thin PDMS gels were cast on plastic 10cm Petri dishes. A 1cm*1cm square was cut out of this sheet using a cutter. A biopsy plunger 3mm in diameter was used to then cut a circular hole into the middle of the square.

35mm glass-bottomed dishes were prepared for micropatterning by plasma treatment for 1 minute in a plasma cleaner. The PDMS stencil with the 3mm hole was placed in the center of the glass-bottom dish as soon as it was removed from the plasma cleaner and firmly pressed using Dumont tweezers to ensure that no air was trapped between the PDMS stencil and the glass surface. 15μl of 0.2 PLL-PEG was pipetted into the well in the middle of the PDMS stencil and incubated at room temperature for 30 minutes. At the end of 30 minutes, the well was carefully washed five times with 100μl PBS, without touching the glass surface and without completely emptying the liquid in the well.

4.9.3 Micropatterning using PRIMO

The well in the dish to be micropatterned was washed once with 6μl of PLPP and filled with 6μl of PLPP. The PRIMO system was calibrated on an empty dish marked with a yellow highlighter on the inner glass surface. The dish to be micropatterned was mounted on the microscope next and the PDMS well was found by moving the dish in the xy-plane. The image containing the desired pattern was loaded in an array with 4-9 repeats within the well. Dust particles at the upper surface of the glass were used to sharpen the focus in z. Micropatterning along the loaded pattern was performed using a UV illumination dose of 2000 μJmm^{-2}.

After patterning, the stencil well was washed five times with 100μl of PBS. 1μl of the fibronectin stock (1 mg/ml) was diluted in 20μl of PBS to yield a final concentration of 50 ug/ml and pipetted into the stencil well. The solution was incubated for 30 minutes at room temperature and a circle was drawn on the outer surface of the dish to mark the well. The stencil was then carefully removed using tweezers, without touching the micropatterned region and 1ml of PBS was pipetted into the dish. Micropatterned dishes were stored in PBS at 4°C for up to a week.

4.9.4 Cell seeding on micropatterned dishes

The PBS in the micropatterned dish was replaced with 500μl 3T3 media. 3T3 mouse fibroblasts in culture were trypsinized, counted, and centrifuged at 800g for 3 minutes a room temperature. They were resuspended in a volume of media determined by the cell count in order to yield a density of $\sim 1 * 10^7$ cells/ml. They were then pipetted through a cell strainer in a FACS tube to yield single cells. 15μl of the cell solution was then carefully pipetted onto the demarcated micropatterned region of the dish without touching the surface. The dish was placed in the cell incubator and checked under a brightfield microscope every 10 minutes. By gently shaking the dish, it was ascertained whether the micropatterns had been occupied by cells. When they were found to be sufficiently occupied, the dish was washed twice with 2ml media, with gentle pipetting to avoid detaching the cells. The cells were then left on the micropatterns for at least an hour before performing any treatments or measurements on them.

4.10 Atomic force spectroscopy

The atomic force microscope was used to perform two kinds of force measurements at the cell surface, namely measurements of membrane-to-cortex adhesion strength using dynamic tether pulling experiments and cortical tension measurements using cell indentation. These experiments are described in the sections below. All AFM measurements were made on the CellHesion 200 Atomic Force Microscope from JPK BioAFM, Bruker mounted on an Eclipse Ti inverted light microscope from Nikon in an insulated box heated to 37°C with 5% CO_2 supply.

4.10.1 Tether pulling

Dynamic tether pulling was performed as described by Bergert and Diz-Muñoz [302].

4.10.1.1 Cantilever coating and calibration

Olympus BioLevers (spring constant k = 60 pN/nm) from Bruker were calibrated in air using the contact-based method for the calibration of optical light sensitivity (OLS) and thermal noise-based calibration of spring constant. The average value of the spring constant from triplicate measurements was used. The cantilever was then incubated for 1 hour at room temperature in 3mg/ml Concanavalin A dissolved in PBS, after which the cantilever was rinsed twice in PBS and its OLS was recalibrated in PBS.

4.10.1.2 Dynamic tether pulling

Cells were seeded on 35mm glass bottom dishes at a density of $5*10^4$cells/cm^2 one day prior to dynamic tether pulling experiments. The cells were washed twice with PBS and incubated in serum-free 3T3 media (ctrl) or serum-free 3T3 media containing 5mM MβCD for 30 minutes before performing dynamic tether pulling. They were then mounted on the microscope along with the AFM head. The 60x oil-immersion objective was used to locate the cells and the cantilever by bright-field microscopy.

The cantilever was positioned above individual cells and programmed to approach the cell surface and pull dynamic tethers with the following parameters:

- Approach velocity: 0.5μms^{-1}
- Contact force: 100-300 pN
- Contact time: 0.1-10s
- Retraction speed: 2, 5, 10 and 30 μms^{-1}

The contact time with the cell surface was adjusted to obtain at least one dynamic tether, but such that all tethers broke during the retraction phase. At least two tethers were measured per retraction speed per cell, where only tethers that broke during the retraction phase were considered. Measurements were performed for up to an hour per dish in order to not wear out the ConA coating. The order of data acquisition with the various retraction speeds was randomized on each cell and the order of measurement on the two experimental conditions (ctrl vs 5mM MβCD) was randomized in each replicate of the experiment.

4.10.1.3 Data analysis

The force curves from dynamic tether-pulling experiments were analyzed using the JPK SPM data processing software to obtain tether values. The Brochard-Wyart model (eqn. 3.1) [303] was fitted to the Force-velocity plots to obtain the MCA parameter with a Monte Carlo-based error estimation procedure. Data analysis and visualization were performed using R scripts from Martin Bergert at EMBL, Heidelberg.

4.10.2 Cell Indentation

Cortical tension was measured by indenting the surface of micropatterned cells with a spherical indenter. For this, MLCT-O10 cantilevers were modified by the gluing of a borosilicate glass bead 10μm in diameter at the flat tip.

4.10.2.1 Bead gluing and Calibration

Briefly, beads were pipetted onto a glass slide and visualized on the bright-field microscope equipped with the AFM. The AFM head was mounted over the same microscope and lowered to a height of $\sim 80\mu m$ above the glass surface. A thin layer of Epoxy glue was deposited on one side of the glass slide and the cantilever tip was made to approach the surface coated with glue. It was retracted again and aligned to the center of a bead, and the bead surface was approached. Contact with the bead was maintained for 30-45s and the cantilever was retracted. This usually resulted in successful gluing of the bead to the cantilever tip. The cantilever was then calibrated in air as described above for OBL-10 cantilevers.

Then the cantilever was coated for an hour in a 1% solution of F-127 pluronic at 37°C. Following this, it was rinsed once in PBS and its OLS was calibrated in PBS.

4.10.2.2 Cell Indentation

Cells were seeded on micropatterns as described in section 4.9 2 and 21 hours prior to indentation experiments in the case of cholesterol depletion and

SCD1 treatments, respectively. Cholesterol depletion was performed for 30 minutes and SCD1 inhibition with BSA-18:0 was performed overnight before the start of the indentation measurements.

The cells and cantilever were visualized using brightfield imaging with a 60x oil objective and the cantilever was positioned with the center of the bead directly above the cell. Cortical tension was measured by indenting individual cells with the following parameters:

- Approach velocity: 0.4μms^{-1}
- Contact force: 300-1000 pN
- Contact time: 0s
- Retraction speed: 10 μms^{-1}

At least two force curves were obtained per cell. The contact force was varied in order to indent 0.8-1.2μm of the cell surface. The order of measurement on the two experimental conditions being compared was randomized in each replicate of the experiment.

4.10.2.3 Data analysis

The force curves from indentation experiments were analyzed using the JPK SPM data processing software to obtain values of cortical tension by fitting the liquid droplet model to the curves in the 125-250 pN region (eqn. 3.4) [187, 309, 310]. Statistical analysis and visualization through box plots were done using R scripts from Martin Bergert at EMBL, Heidelberg. Averaged force curves from all data per condition were plotted using Python 3.6.1.

4.11 Fluorescence recovery after photobleaching

Fluorescence Recovery After Photobleaching (FRAP) was used to measure the lateral diffusion coefficient of GFP-CAAX in the basal membrane of 3T3 mouse fibroblasts [343]. For this, GFP-CAAX 3T3 cells were seeded on 35mm glass bottom dishes at a density of 3*10^{4}cells/cm^2 two days prior to the experiment. Cells were subjected to the required treatments as described in section 4.3.4.

4.11.1 Data acquisition

FRAP was performed on a Zeiss LSM 780 NLO microscope at the Advanced Light Microscopy Facility at EMBL, Heidelberg. The focus was set to the bottom plane of the cell with maximum green fluorescence, and a circular region 1μm in radius was bleached. A 42-second-long movie was recorded with 16 frames per second starting 10 frames before bleaching. 3-6 FRAP curves were recorded for each cell, making sure to acquire an ROI (region of interest) spanning the bleached region, an unbleached region of the membrane to use as a reference region, and an area outside of the cell to estimate the background signal.

4.11.2 Data Analysis

In addition to the bleached region ($frap$), a similar circular reference region of the membrane (ref) away from the bleached region and a background region outside of the cell (*back*) were chosen manually and the signal intensity in each of the three regions was estimated for each frame of the movie. This was done on the ZEN software during the acquisition of FRAP data.

All further analysis was performed using the FRAPAnalyser software [344]. First, the intensity in the bleached region was background-subtracted and normalized against the reference region at each timepoint as follows[343]:

$$I_{norm}(t) = \frac{I_{frap}(t) - I_{back}(t)}{\langle I_{frap}\rangle_{pre} - \langle I_{back}\rangle_{pre}} . \frac{\langle I_{ref}\rangle_{pre} - \langle I_{back}\rangle_{pre}}{I_{ref}(t) - I_{back}(t)} \tag{4.3}$$

where $I_{norm}(t)$ and $I_{frap}(t)$ are the normalized and non-normalized intensity in the bleached region at time t, $I_{back}(t)$ and $I_{ref}(t)$ are the intensities in the background and reference regions at time t, and $\langle I_{frap}\rangle_{pre}$, $\langle I_{back}\rangle_{pre}$ and $\langle I_{ref}\rangle_{pre}$ are the intensities in the bleached region, background region and reference region averaged over all pre-bleach timepoints, respectively.

An additional normalization was applied to scale the intensity values between 0 and 1 as follows:

$$I_{fullnorm}(t) = \frac{I_{norm}(t) - I_{norm}(t_{bleach})}{\langle I_{norm}\rangle_{pre} - I_{norm}(t_{bleach})} \tag{4.4}$$

where t_{bleach} is the time-point of bleaching.

Following the second normalization, FRAP curves from the same cell were averaged and eqn.3.3 was fit to the averaged FRAP curve to obtain fitted values of the diffusion coefficient, D. Averaged recovery curves from all recorded data per condition were plotted using the Matplotlib package on Python 3.6.1 and box plots of fitted D values per cell were plotted using Tableau Desktop 2020.4.

4.12 Confocal Microscopy

4.12.1 *In vitro*-differentiated neurons

Immunofluorescence (IF) was used to visualize neuron-specific β-Tubulin III in mESCs differentiated into neurons *in vitro*. For this, cells were plated on glass coverslips coated with PDL and laminin on day 8 of differentiation. On day 12, cells were fixed in 4% paraformaldehyde in PBS for twenty minutes at room temperature. Excess paraformaldehyde was then quenched by treating with 30mM glycine for five minutes and the coverslips were washed thrice with PBS. The cells were permeabilized using 0.1% Triton-X 100 in PBS and blocked by incubating the coverslip in a 0.5% (w/v) solution of BSA in PBS for 30 minutes at room temperature. The primary antibody against β-Tubulin III was diluted 1:200 in 0.5% BSA in PBS and the coverslip was incubated in it for one hour at room temperature. An anti-mouse secondary antibody conjugated to Alexa-594 was diluted 1:500 in 5% BSA in PBS and the coverslip was incubated in it for an hour at room temperature. Cell nuclei were stained with 5μg/ml DAPI for five minutes at room temperature and the coverslip was mounted on a glass slide with the ProLong Gold mounting agent. 2-channel fluorescence images of DAPI and Alexa-594 fluorescence were acquired using the 20x objective of a Nikon Eclipse Ti fluorescence microscope.

4.12.2 Live imaging of GFP-CAAX-NIH/3T3 cells

Live GFP-CAAX 3T3 mouse fibroblasts were imaged on the Zeiss LSM 880 microscope with Airyscan using the Airyfast mode to analyze cell shape changes during cholesterol depletion. A number of cells were identified and their corresponding stage positions were saved. The media was carefully aspirated and the cells were washed twice with PBS and had their media replaced with 3T3 media made with 10% del FBS (ctrl) or with 3T3 media made with 10% del FBS + 5mM MβCD. Care was taken to avoid moving the dish. The saved cell positions were revisited and adjusted to account for any movement of the dish or of the cells and a z-stack of each cell was imaged, on average, every 10 minutes. The imaging of live cells was done in a chamber heated to 37°C and supplied with 5% CO_2 with a 40x water objective.

4.12.3 Imaging of fixed GFP-CAAX-NIH/3T3 cells

GFP-CAAX 3T3 cells were fixed, permeabilized and stained with SiR-actin to quantify actin density at the cortex. For this, cells were seeded on fibronectin micropatterns in 35mm glass-bottom dishes as described in section 4.9. The micropatterned cells were washed twice with PBS and incubated in 3T3 media containing 10% del FBS (ctrl) or in 3T3 media containing 10% del FBS + 5mM MβCD for 30 min. At the end of 30 minutes, the cell media was aspirated and 1ml of fresh 3T3 media containing 10% del FBS was added to each dish. 1ml of 2x fixation-permeabilization buffer (Table 4.26) was added to this and the dish was kept at room temperature for 20 minutes to allow fixation and permeabilization. The cells were then incubated in 1x intracellular buffer containing 250nM SiR-actin. SiR-actin was left in solution and the dish was sealed with parafilm to prevent evaporative losses. The cells were imaged after a minimum of 3 hours to allow SiR-actin binding to equilibrate.2-channel images of plasma membrane (GFP-CAAX) and SiR-actin fluorescence were imaged on a plane 4μm above the basal surface of individual micropatterned cells using the airyscan mode and a 40x water objective on the Zeiss LSM 880.

4.13 Image analysis

4.13.1 Analysis of cell shape

Cell shape analysis based on GFP-CAAX signal was performed by fitting a surface to the 3D image of individual cells and calculating the shape parameters of the fitted surfaces. All analysis was performed on Imaris 9.7.2. Tableau Desktop 2020.4. was used for data visualization.

4.13.2 Analysis of F-actin density

F-actin density was analyzed based on the fluorescence intensity of SiR-actin at the cell cortex. Mean pixel intensity was quantified using a macro on ImageJ2 2.3.0/1.53f, based on the analysis pipeline created by Léanne Strauss and Christian Tischer at EMBL, Heidelberg. Briefly, the intensity of the membrane marker GFP-CAAX was used to segment the cell boundary. Ring-shaped masks 5, 10, and 15 pixels wide (i.e., 250, 500, and 750 nm wide) were generated, walking inwards from the cell boundary. The mean fluorescence intensity of SiR-actin in the pixels within the masks was calculated. All intensities were normalized to the mean intensity value from all control cells within each biological replicate.

Bibliography

[1] Robert Hooke. *Micrographia*. 1665.

[2] Paolo Mazzarello. “A unifying concept: the history of cell theory”. In: *Nature cell biology* 1.1 (1999), E13–E15.

[3] Henri Dutrochet. *New research on endosmosis and exosmosis: followed by the experimental application of these physical actions to the solution of the problem of irritability végétal and to the determination of the cause of the ascent of the stems and the descent of the roots*. J.-B. Bailiff, 1828.

[4] Georg Quincke. “Ueber periodische Ausbreitung an Flüssigkeitsoberflächen und dadurch hervorgerufene Bewegungserscheinungen”. In: *Annalen der Physik* 271.12 (1888), pp. 580–642.

[5] Georg Quincke. “Artificial Amœbæ and Protoplasm”. In: *Nature* 49.1253 (1893), pp. 5–6.

[6] Hans Horst Meyer. *Zur Theorie der Alkoholnarkose: 3. Mittheilung; der Einfluss wechselnder Temperatur auf Wirkungsstärke und Theilungscoefficient der Narcotica*. Pharmakologisches Institut, 1899.

[7] Charles Ernest Overton. *Über die osmotischen Eigenschaften der lebenden Pflanzen-und Tierzelle*. Fäsi & Beer, 1895.

[8] E Overton. “Über die allgemeinen osmotischen Eigenschaften der Zelle, ihre vermutlichen Ursachen und ihre Bedeutung für die Physiologie”. In: *Vierteljahrsschrift der Naturforschenden Gesellschaft in Zürich* 44 (1899), pp. 88–135.

[9] Daniel Segré et al. “The lipid world”. In: *Origins of Life and Evolution of the Biosphere* 31.1 (2001), pp. 119–145.

[10] CM Paleos. “A decisive step toward the origin of life”. In: *Trends in biochemical sciences* 40.9 (2015), pp. 487–488.

[11] David Deamer. “The role of lipid membranes in life’s origin”. In: *Life* 7.1 (2017), p. 5.

[12] Charles Tanford. “The hydrophobic effect and the organization of living matter”. In: *Science* 200.4345 (1978), pp. 1012–1018.

[13] Ole G Mouritsen and Luis A Bagatolli. *Life-as a matter of fat: lipids in a membrane biophysics perspective*. Springer, 2015.

[14] Eoin Fahy et al. “A comprehensive classification system for lipids”. In: *Journal of lipid research* 46.5 (2005), pp. 839–861.

[15] Eleonora Muro, G Ekin Atilla-Gokcumen, and Ulrike S Eggert. “Lipids in cell biology: how can we understand them better?” In: *Molecular biology of the cell* 25.12 (2014), pp. 1819–1823.

[16] Eoin Fahy et al. “Lipid classification, structures and tools”. In: *Biochimica et Biophysica Acta (BBA)-Molecular and Cell Biology of Lipids* 1811.11 (2011), pp. 637–647.

[17] Gerhard Liebisch et al. “Shorthand notation for lipid structures derived from mass spectrometry”. In: *Journal of lipid research* 54.6 (2013), pp. 1523–1530.

[18] Takeshi Harayama and Howard Riezman. “Understanding the diversity of membrane lipid composition”. In: *Nature reviews Molecular cell biology* 19.5 (2018), pp. 281–296.

[19] Ashley J Snider, K Alexa Orr Gandy, and Lina M Obeid. “Sphingosine kinase: Role in regulation of bioactive sphingolipid mediators in inflammation”. In: *Biochimie* 92.6 (2010), pp. 707–715.

[20] Sarah Spiegel and Sheldon Milstien. “Sphingosine 1-phosphate, a key cell signaling molecule”. In: *Journal of Biological Chemistry* 277.29 (2002), pp. 25851–25854.

[21] Erhard Bieberich. “It'sa lipid's world: bioactive lipid metabolism and signaling in neural stem cell differentiation”. In: *Neurochemical research* 37.6 (2012), pp. 1208–1229.

[22] *Open Space*. `https://openspace.infohio.org/courseware/lesson/313/student`.

[23] H Alex Brown and Robert C Murphy. “Working towards an exegesis for lipids in biology”. In: *Nature chemical biology* 5.9 (2009), pp. 602–606.

[24] Christer Ejsing. *ALEX*^{123}. `https://git.embl.de/ejsing/alex123`. 2017.

[25] Josch K Pauling et al. “Proposal for a common nomenclature for fragment ions in mass spectra of lipids”. In: *PLoS One* 12.11 (2017), e0188394.

[26] Reinaldo Almeida et al. "Comprehensive lipidome analysis by shotgun lipidomics on a hybrid quadrupole-orbitrap-linear ion trap mass spectrometer". In: *Journal of the American Society for Mass Spectrometry* 26.1 (2014), pp. 133–148.

[27] Charles Tanford. *Ben Franklin stilled the waves: An informal history of pouring oil on water with reflections on the ups and downs of scientific life in general*. OUP Oxford, 2004.

[28] Rob Phillips. "Membranes by the Numbers". In: *Physics of Biological Membranes*. Springer, 2018, pp. 73–105.

[29] Benjamin Franklin and William Brownrigg. "XLIV. Of the stilling of waves by means of oil. Extracted from sundry letters between Benjamin Franklin, LL. DFRS William Brownrigg, MDFRS and the Reverend Mr. Farish". In: *Philosophical Transactions of the Royal Society of London* 64 (1774), pp. 445–460.

[30] John William Strutt. "IV. Measurements of the amount of oil necessary in order to check the motions of camphor upon water". In: *Proceedings of the Royal Society of London* 47.286-291 (1890), pp. 364–367.

[31] Agnes Pockels. "Surface tension". In: *Nature* 43.1115 (1891), pp. 437–439.

[32] Irving Langmuir. "The shapes of group molecules forming the surfaces of liquids". In: *Proceedings of the National Academy of Sciences* 3.4 (1917), pp. 251–257.

[33] Irving Langmuir. "The constitution and fundamental properties of solids and liquids. II. Liquids." In: *Journal of the American chemical society* 39.9 (1917), pp. 1848–1906.

[34] Evert Gorter and FJEM Grendel. "On bimolecular layers of lipoids on the chromocytes of the blood". In: *The Journal of experimental medicine* 41.4 (1925), p. 439.

[35] Mariana Ruiz Villarreal. *Creative commons*. `https://upload.wikimedia.org/wikipedia/commons/c/c6/Phospholipids_aqueous_solution_structures.svg`. 2007.

[36] J David Robertson. "New observations on the ultrastructure of the membranes of frog peripheral nerve fibers". In: *The Journal of biophysical and biochemical cytology* 3.6 (1957), p. 1043.

[37] Robertson JD. "The ultrastructure of cell membranes and their derivatives." In: *Biochemical society symposium*. Vol. 16. 1959, pp. 3–43.

[38] Paul Mueller et al. “Reconstitution of cell membrane structure in vitro and its transformation into an excitable system”. In: *Nature* 194.4832 (1962), pp. 979–980.

[39] Larry D Frye and Michael Edidin. “The rapid intermixing of cell surface antigens after formation of mouse-human heterokaryons”. In: *Journal of cell science* 7.2 (1970), pp. 319–335.

[40] S Jonathan Singer and Garth L Nicolson. “The Fluid Mosaic Model of the Structure of Cell Membranes: Cell membranes are viewed as two-dimensional solutions of oriented globular proteins and lipids.” In: *Science* 175.4023 (1972), pp. 720–731.

[41] Mark S Bretscher. “Asymmetrical lipid bilayer structure for biological membranes”. In: *Nature New Biology* 236.61 (1972), pp. 11–12.

[42] Philippe F Devaux. “Static and dynamic lipid asymmetry in cell membranes”. In: *Biochemistry* 30.5 (1991), pp. 1163–1173.

[43] Philippe F Devaux and Roger Morris. “Transmembrane asymmetry and lateral domains in biological membranes”. In: *Traffic* 5.4 (2004), pp. 241–246.

[44] Akihiro Kusumi and Yasushi Sako. “Cell surface organization by the membrane skeleton”. In: *Current opinion in cell biology* 8.4 (1996), pp. 566–574.

[45] Kai Simons and Elina Ikonen. “Functional rafts in cell membranes”. In: *nature* 387.6633 (1997), pp. 569–572.

[46] Shigeo Takamori et al. “Molecular anatomy of a trafficking organelle”. In: *Cell* 127.4 (2006), pp. 831–846.

[47] Gerrit van Meer, Dennis R Voelker, and Gerald W Feigenson. “Membrane lipids: where they are and how they behave”. In: *Nature reviews Molecular cell biology* 9.2 (2008), pp. 112–124.

[48] Joost CM Holthuis and Anant K Menon. “Lipid landscapes and pipelines in membrane homeostasis”. In: *Nature* 510.7503 (2014), pp. 48–57.

[49] Atsushi Yamashita et al. “Acyltransferases and transacylases that determine the fatty acid composition of glycerolipids and the metabolism of bioactive lipid mediators in mammalian cells and model organisms”. In: *Progress in lipid research* 53 (2014), pp. 18–81.

[50] Takeshi Harayama et al. "Lysophospholipid acyltransferases mediate phosphatidylcholine diversification to achieve the physical properties required in vivo". In: *Cell metabolism* 20.2 (2014), pp. 295–305.

[51] Amy M Hicks et al. "Unique molecular signatures of glycerophospholipid species in different rat tissues analyzed by tandem mass spectrometry". In: *Biochimica et Biophysica Acta (BBA)-Molecular and Cell Biology of Lipids* 1761.9 (2006), pp. 1022–1029.

[52] Bruno Antonny et al. "From zero to six double bonds: phospholipid unsaturation and organelle function". In: *Trends in cell biology* 25.7 (2015), pp. 427–436.

[53] Christian Klose, Michal A Surma, and Kai Simons. "Organellar lipidomics—background and perspectives". In: *Current opinion in cell biology* 25.4 (2013), pp. 406–413.

[54] Kai Simons and Gerrit van Meer. "Lipid sorting in epithelial cells". In: *Biochemistry* 27.17 (1988), pp. 6197–6202.

[55] Deborah A Brown and John K Rose. "Sorting of GPI-anchored proteins to glycolipid-enriched membrane subdomains during transport to the apical cell surface". In: *Cell* 68.3 (1992), pp. 533–544.

[56] Francis O Schmitt, Richard S Bear, and Kenneth J Palmer. "X-ray diffraction studies on the structure of the nerve myelin sheath". In: *Journal of Cellular and Comparative Physiology* 18.1 (1941), pp. 31–42.

[57] JB Finean. "X-ray diffraction studies on the polymorphism of phospholipids". In: *Biochimica et Biophysica Acta* 10 (1953), pp. 371–384.

[58] JB Finean and PF Millington. "Low-angle X-ray diffraction study of the polymorphic forms of synthetic α: β and α: α'-kephalins and α: β-lecithins". In: *Transactions of the Faraday Society* 51 (1955), pp. 1008–1015.

[59] Dennis Chapman. "Phase transitions and fluidity characteristics of lipids and cell membranes". In: *Quarterly reviews of biophysics* 8.2 (1975), pp. 185–235.

[60] Adam Hospital et al. "Molecular dynamics simulations: advances and applications". In: *Advances and applications in bioinformatics and chemistry: AABC* 8 (2015), p. 37.

[61] Egbert Egberts, Siewert-Jan Marrink, and Herman JC Berendsen. "Molecular dynamics simulation of a phospholipid membrane". In: *European biophysics journal* 22.6 (1994), pp. 423–436.

[62] Marieke Kranenburg and Berend Smit. “Phase behavior of model lipid bilayers”. In: *The Journal of Physical Chemistry B* 109.14 (2005), pp. 6553–6563.

[63] Derek Marsh. “Structural and thermodynamic determinants of chain-melting transition temperatures for phospholipid and glycolipids membranes”. In: *Biochimica et Biophysica Acta (BBA)-Biomembranes* 1798.1 (2010), pp. 40–51.

[64] John R Silvius et al. “Thermotropic phase transitions of pure lipids in model membranes and their modifications by membrane proteins”. In: *Lipid-protein interactions* 2 (1982), pp. 239–281.

[65] John F Nagle. “Theory of the main lipid bilayer phase transition”. In: *Annual Review of Physical Chemistry* 31.1 (1980), pp. 157–196.

[66] JF Nagle. “Lipid bilayer phase transition: density measurements and theory”. In: *Proceedings of the National Academy of Sciences* 70.12 (1973), pp. 3443–3444.

[67] Christian Goritz, Daniela H Mauch, and Frank W Pfrieger. “Multiple mechanisms mediate cholesterol-induced synaptogenesis in a CNS neuron”. In: *Molecular and Cellular Neuroscience* 29.2 (2005), pp. 190–201.

[68] Thomas C Südhof. “Synaptic vesicles: an organelle comes of age”. In: *Cell* 127.4 (2006), pp. 671–673.

[69] Miriam Bibel et al. “Generation of a defined and uniform population of CNS progenitors and neurons from mouse embryonic stem cells”. In: *Nature protocols* 2.5 (2007), pp. 1034–1043.

[70] Guillaume Salbreux, Guillaume Charras, and Ewa Paluch. “Actin cortex mechanics and cellular morphogenesis”. In: *Trends in cell biology* 22.10 (2012), pp. 536–545.

[71] Priyamvada Chugh and Ewa K Paluch. “The actin cortex at a glance”. In: *Journal of cell science* 131.14 (2018), jcs186254.

[72] Manasi Kelkar, Pierre Bohec, and Guillaume Charras. “Mechanics of the cellular actin cortex: From signalling to shape change”. In: *Current Opinion in Cell Biology* 66 (2020), pp. 69–78.

[73] Anusha B Gopalan et al. “Lipotype acquisition during neural development in vivo is not recapitulated in stem cell-derived neurons”. In: *bioRxiv* (2022).

[74] Christopher S von Bartheld, Jami Bahney, and Suzana Herculano-Houzel. “The search for true numbers of neurons and glial cells in the human brain: A review of 150 years of cell counting”. In: *Journal of Comparative Neurology* 524.18 (2016), pp. 3865–3895.

[75] Christine Stadelmann et al. “Myelin in the central nervous system: structure, function, and pathology”. In: *Physiological reviews* 99.3 (2019), pp. 1381–1431.

[76] Nikolas Schrod et al. “Pleomorphic linkers as ubiquitous structural organizers of vesicles in axons”. In: *PloS one* 13.6 (2018), e0197886.

[77] Ghulam Hussain et al. “Role of cholesterol and sphingolipids in brain development and neurological diseases”. In: *Lipids in health and disease* 18.1 (2019), pp. 1–12.

[78] Khemissa Bejaoui et al. “SPTLC1 is mutated in hereditary sensory neuropathy, type 1”. In: *Nature genetics* 27.3 (2001), pp. 261–262.

[79] Jennifer L Dawkins et al. “Mutations in SPTLC1, encoding serine palmitoyltransferase, long chain base subunit-1, cause hereditary sensory neuropathy type I”. In: *Nature genetics* 27.3 (2001), pp. 309–312.

[80] Silke Imgrund et al. “Adult ceramide synthase 2 (CERS2)-deficient mice exhibit myelin sheath defects, cerebellar degeneration, and hepatocarcinomas”. In: *Journal of Biological Chemistry* 284.48 (2009), pp. 33549–33560.

[81] Simon N Fewou et al. “Reversal of non-hydroxy: alpha-hydroxy galactosylceramide ratio and unstable myelin in transgenic mice overexpressing UDP-galactose: ceramide galactosyltransferase.” In: *Journal of neurochemistry* 94.2 (2005), pp. 469–481.

[82] Hariharasubramanian Ramakrishnan et al. “Increasing sulfatide synthesis in myelin-forming cells of arylsulfatase A-deficient mice causes demyelination and neurological symptoms reminiscent of human metachromatic leukodystrophy”. In: *Journal of Neuroscience* 27.35 (2007), pp. 9482–9490.

[83] Tadanobu Takahashi and Takashi Suzuki. “Role of sulfatide in normal and pathological cells and tissues”. In: *Journal of lipid research* 53.8 (2012), pp. 1437–1450.

[84] Victoria L Stevens and Jianhua Tang. “Fumonisin B1-induced sphingolipid depletion inhibits vitamin uptake via the glycosylphosphatidylinositol-anchored folate receptor”. In: *Journal of Biological Chemistry* 272.29 (1997), pp. 18020–18025.

[85] Stacey A Missmer et al. “Exposure to fumonisins and the occurrence of neural tube defects along the Texas–Mexico border”. In: *Environmental health perspectives* 114.2 (2006), pp. 237–241.

[86] Ryu-ichi Tozawa et al. “Embryonic lethality and defective neural tube closure in mice lacking squalene synthase”. In: *Journal of Biological Chemistry* 274.43 (1999), pp. 30843–30848.

[87] Ken Ohashi et al. “Early embryonic lethality caused by targeted disruption of the 3-hydroxy-3-methylglutaryl-CoA reductase gene”. In: *Journal of Biological Chemistry* 278.44 (2003), pp. 42936–42941.

[88] Gesine Saher et al. “High cholesterol level is essential for myelin membrane growth”. In: *Nature neuroscience* 8.4 (2005), pp. 468–475.

[89] Mark HG Verheijen et al. “SCAP is required for timely and proper myelin membrane synthesis”. In: *Proceedings of the National Academy of Sciences* 106.50 (2009), pp. 21383–21388.

[90] Daniela H Mauch et al. “CNS synaptogenesis promoted by glia-derived cholesterol”. In: *Science* 294.5545 (2001), pp. 1354–1357.

[91] Lars Fester et al. “Cholesterol-promoted synaptogenesis requires the conversion of cholesterol to estradiol in the hippocampus”. In: *Hippocampus* 19.8 (2009), pp. 692–705.

[92] Elena I Posse de Chaves et al. “Role of lipoproteins in the delivery of lipids to axons during axonal regeneration”. In: *Journal of Biological Chemistry* 272.49 (1997), pp. 30766–30773.

[93] Anna Linetti et al. “Cholesterol reduction impairs exocytosis of synaptic vesicles”. In: *Journal of Cell Science* 123.4 (2010), pp. 595–605.

[94] Shibani Kanungo et al. “Sterol metabolism disorders and neurodevelopment—an update”. In: *Developmental disabilities research reviews* 17.3 (2013), pp. 197–210.

[95] Moneek Madra and Stephen L Sturley. “Niemann–Pick type C pathogenesis and treatment: from statins to sugars”. In: *Clinical lipidology* 5.3 (2010), pp. 387–395.

[96] Robert C Block et al. "Altered cholesterol and fatty acid metabolism in Huntington disease". In: *Journal of clinical lipidology* 4.1 (2010), pp. 17–23.

[97] Gilbert di Paolo and Tae-Wan Kim. "Linking lipids to Alzheimer's disease: cholesterol and beyond". In: *Nature Reviews Neuroscience* 12.5 (2011), pp. 284–296.

[98] Qing Wang et al. "Statins: multiple neuroprotective mechanisms in neurodegenerative diseases". In: *Experimental neurology* 230.1 (2011), pp. 27–34.

[99] Martha Neuringer, Gregory J Anderson, and William E Connor. "The essentiality of n-3 fatty acids for the development and function of the retina and brain". In: *Annual review of nutrition* 8.1 (1988), pp. 517–541.

[100] Sylvie Chalon. "Omega-3 fatty acids and monoamine neurotransmission". In: *Prostaglandins, Leukotrienes and Essential Fatty Acids* 75.4-5 (2006), pp. 259–269.

[101] Sheila M Innis. "Dietary (n-3) fatty acids and brain development". In: *The Journal of nutrition* 137.4 (2007), pp. 855–859.

[102] M Vreugdenhil et al. "Polyunsaturated fatty acids modulate sodium and calcium currents in CA1 neurons." In: *Proceedings of the National Academy of Sciences* 93.22 (1996), pp. 12559–12563.

[103] Frances Calderon and Hee-Yong Kim. "Docosahexaenoic acid promotes neurite growth in hippocampal neurons". In: *Journal of neurochemistry* 90.4 (2004), pp. 979–988.

[104] Mohammed Akbar et al. "Docosahexaenoic acid: a positive modulator of Akt signaling in neuronal survival". In: *Proceedings of the National Academy of Sciences* 102.31 (2005), pp. 10858–10863.

[105] Eisuke Kawakita, Michio Hashimoto, and Osamu Shido. "Docosahexaenoic acid promotes neurogenesis in vitro and in vivo". In: *Neuroscience* 139.3 (2006), pp. 991–997.

[106] Dehua Cao et al. "Docosahexaenoic acid promotes hippocampal neuronal development and synaptic function". In: *Journal of neurochemistry* 111.2 (2009), pp. 510–521.

[107] Klára Kitajka et al. "The role of n-3 polyunsaturated fatty acids in brain: modulation of rat brain gene expression by dietary n-3 fatty acids". In: *Proceedings of the National Academy of Sciences* 99.5 (2002), pp. 2619–2624.

[108] Pauline Coti Bertrand, John R O'Kusky, and Sheila M Innis. "Maternal dietary (n-3) fatty acid deficiency alters neurogenesis in the embryonic rat brain". In: *The Journal of nutrition* 136.6 (2006), pp. 1570–1575.

[109] Mehmet Cansev et al. "Giving uridine and/or docosahexaenoic acid orally to rat dams during gestation and nursing increases synaptic elements in brains of weanling pups". In: *Developmental neuroscience* 31.3 (2009), pp. 181–192.

[110] Carola IF Janssen et al. "Impact of dietary n-3 polyunsaturated fatty acids on cognition, motor skills and hippocampal neurogenesis in developing C57BL/6J mice". In: *The Journal of nutritional biochemistry* 26.1 (2015), pp. 24–35.

[111] Toru Moriguchi, Rebecca Sheaff Greiner, and Norman Salem Jr. "Behavioral deficits associated with dietary induction of decreased brain docosahexaenoic acid concentration". In: *Journal of neurochemistry* 75.6 (2000), pp. 2563–2573.

[112] Norman Salem et al. "Alterations in brain function after loss of docosahexaenoate due to dietary restriction of n-3 fatty acids". In: *Journal of Molecular Neuroscience* 16.2 (2001), pp. 299–307.

[113] Janice Catalan et al. "Cognitive deficits in docosahexaenoic acid-deficient rats." In: *Behavioral neuroscience* 116.6 (2002), p. 1022.

[114] Sun-Young Lim, Junji Hoshiba, and Norman Salem Jr. "An extraordinary degree of structural specificity is required in neural phospholipids for optimal brain function: n-6 docosapentaenoic acid substitution for docosahexaenoic acid leads to a loss in spatial task performance". In: *Journal of neurochemistry* 95.3 (2005), pp. 848–857.

[115] Takashi Takeuchi, Miyoko Iwanaga, and Etsumori Harada. "Possible regulatory mechanism of DHA-induced anti-stress reaction in rats". In: *Brain research* 964.1 (2003), pp. 136–143.

[116] S Gamoh et al. "Chronic administration of docosahexaenoic acid improves reference memory-related learning ability in young rats". In: *Neuroscience* 93.1 (1999), pp. 237–241.

[117] JLW Thudichum. *A Treatise on the Chemical Constitution of the Brain*. Bailliere, Tindall and Cox, 1884.

[118] Irvine H Page. “Chemistry of the Brain: Past Imperfect, Present Indicative, and—Future Perfect?” In: *Science* 125.3251 (1957), pp. 721–727.

[119] Morio Yasuda. “Lipids analysis of the human brain”. In: *The Journal of Biochemistry* 26.2 (1937), pp. 203–210.

[120] WR Bloor. *Biochemistry of the fatty acids and their compounds, the lipids*. 1943.

[121] AC Johnson, AR McNabb, and RJ Rossiter. “Lipids of normal brain”. In: *Biochemical Journal* 43.4 (1948), p. 573.

[122] Heinrich Waelsch. *Biochemistry of the developing nervous system*. Vol. 1. Academic Press, 1957.

[123] FN LeBaron and J Folch. “Structure of brain tissue lipides”. In: *Physiological Reviews* 37.4 (1957), pp. 539–561.

[124] AT James and AJP Martin. “Gas–liquid chromatography: the separation and identification of the methyl esters of saturated and unsaturated acids from formic acid to n-octadecanoic acid”. In: *Biochemical Journal* 63.1 (1956), p. 144.

[125] Krister Fontell, RalphT Holman, and Georg Lambebtsen. “Some new methods for separation and analysis of fatty acids and other lipids”. In: *Journal of Lipid Research* 1.5 (1960), pp. 391–404.

[126] S Balakrishnan, H Goodwin, and JN Cumings. “The distribution of phosphorus-containing lipid compounds in the human brain”. In: *Journal of neurochemistry* 8.3-4 (1961), pp. 276–284.

[127] AN Davison and Martha Wajda. “Analysis of lipids from fresh and preserved adult human brains”. In: *Biochemical Journal* 82.1 (1962), p. 113.

[128] John S O’Brien and E Lois Sampson. “Fatty acid and fatty aldehyde composition of the major brain lipids in normal human gray matter, white matter, and myelin”. In: *Journal of lipid research* 6.4 (1965), pp. 545–551.

[129] John S O’Brien and E Lois Sampson. “Lipid composition of the normal human brain: gray matter, white matter, and myelin”. In: *Journal of lipid research* 6.4 (1965), pp. 537–544.

[130] DT Downing. “The α-Hydroxyacids of Sheep Brain”. In: *Australian Journal of Chemistry* 14.1 (1961), pp. 150–154.

[131] KK Carroll. "The fatty acids of beef brain and spinal cord sphingolipid preparations". In: *Journal of Lipid Research* 3.2 (1962), pp. 263–268.

[132] George Rouser et al. "Lipids in the nervous system of different species as a function of age: brain, spinal cord, peripheral nerve, purified whole cell preparations, and subcellular particulates: regulatory mechanisms and membrane structure". In: *Advances in Lipid Research* 10 (1972), pp. 261–360.

[133] Lars Svennerholm and Marie Therese Vanier. "The distribution of lipids in the human nervous system. II. Lipid composition of human fetal and infant brain". In: *Brain Research* 47.2 (1972), pp. 457–468.

[134] J Tinoco et al. "Linolenic acid deficiency: Changes in fatty acid patterns in female and male rats raised on a linolenic acid-deficient diet for two generations". In: *Lipids* 13.1 (1978), pp. 6–17.

[135] Carl Wayne Cotman et al. "Lipid composition of synaptic plasma membranes isolated from rat brain by zonal centrifugation". In: *Biochemistry* 8.11 (1969), pp. 4606–4612.

[136] WC Breckenridge, G Gombos, and IG Morgan. "The lipid composition of adult rat brain synaptosomal plasma membranes". In: *Biochimica et Biophysica Acta (BBA)-Biomembranes* 266.3 (1972), pp. 695–707.

[137] John B Fenn et al. "Electrospray ionization for mass spectrometry of large biomolecules". In: *Science* 246.4926 (1989), pp. 64–71.

[138] Franz Hillenkamp et al. "Matrix-assisted laser desorption/ionization mass spectrometry of biopolymers". In: *Analytical chemistry* 63.24 (1991), 1193A–1203A.

[139] Stephen J Blanksby and Todd W Mitchell. "Advances in mass spectrometry for lipidomics". In: *Annual Review of Analytical Chemistry* 3 (2010), pp. 433–465.

[140] Dirk Fitzner et al. "Cell-type-and brain-region-resolved mouse brain lipidome". In: *Cell Reports* 32.11 (2020), p. 108132.

[141] Karolina Tulodziecka et al. "Remodeling of the postsynaptic plasma membrane during neural development". In: *Molecular biology of the cell* 27.22 (2016), pp. 3480–3489.

[142] Jia Tu et al. "Absolute quantitative lipidomics reveals lipidome-wide alterations in aging brain". In: *Metabolomics* 14.1 (2018), pp. 1–11.

[143] Xianlin Han, David M Holtzman, and Daniel W McKeel Jr. "Plasmalogen deficiency in early Alzheimer's disease subjects and in animal models: molecular characterization using electrospray ionization mass spectrometry". In: *Journal of neurochemistry* 77.4 (2001), pp. 1168–1180.

[144] Xianlin Han et al. "Substantial sulfatide deficiency and ceramide elevation in very early Alzheimer's disease: potential role in disease pathogenesis". In: *Journal of neurochemistry* 82.4 (2002), pp. 809–818.

[145] Roy G Cutler et al. "Involvement of oxidative stress-induced abnormalities in ceramide and cholesterol metabolism in brain aging and Alzheimer's disease". In: *Proceedings of the National Academy of Sciences* 101.7 (2004), pp. 2070–2075.

[146] Yanhui Xiang, Sin Man Lam, and Guanghou Shui. "What can lipidomics tell us about the pathogenesis of Alzheimer disease?" In: *Biological Chemistry* 396.12 (2015), pp. 1281–1291.

[147] Antonio Veloso et al. "Distribution of lipids in human brain". In: *Analytical and bioanalytical chemistry* 401.1 (2011), pp. 89–101.

[148] Antonio Veloso et al. "Anatomical distribution of lipids in human brain cortex by imaging mass spectrometry". In: *Journal of the American Society for Mass Spectrometry* 22.2 (2011), pp. 329–338.

[149] Reinaldo Almeida et al. "Quantitative spatial analysis of the mouse brain lipidome by pressurized liquid extraction surface analysis". In: *Analytical chemistry* 87.3 (2015), pp. 1749–1756.

[150] Shane R Ellis et al. "Automated, parallel mass spectrometry imaging and structural identification of lipids". In: *Nature methods* 15.7 (2018), pp. 515–518.

[151] Wen Wen, Hui Li, and Jia Luo. "Potential Role of MANF, an ER Stress Responsive Neurotrophic Factor, in Protecting Against Alcohol Neurotoxicity". In: *Molecular neurobiology* 59.5 (2022), pp. 2992–3015.

[152] Ronald W Oppenheim. "Cell death during development of the nervous system". In: *Annual review of neuroscience* 14.1 (1991), pp. 453–501.

[153] M Kristiansen and J Ham. "Programmed cell death during neuronal development: the sympathetic neuron model". In: *Cell Death & Differentiation* 21.7 (2014), pp. 1025–1035.

[154] Astrid G Petzoldt and Stephan J Sigrist. “Synaptogenesis”. In: *Current biology* 24.22 (2014), R1076–R1080.

[155] Travis E Faust, Georgia Gunner, and Dorothy P Schafer. “Mechanisms governing activity-dependent synaptic pruning in the developing mammalian CNS”. In: *Nature Reviews Neuroscience* 22.11 (2021), pp. 657–673.

[156] Jeffrey C Magee and Christine Grienberger. “Synaptic plasticity forms and functions”. In: *Annual review of neuroscience* 43 (2020), pp. 95–117.

[157] Richard R Sprenger et al. “Lipid molecular timeline profiling reveals diurnal crosstalk between the liver and circulation”. In: *Cell reports* 34.5 (2021), p. 108710.

[158] Domenico Russo et al. “Glycosphingolipid metabolic reprogramming drives neural differentiation”. In: *The EMBO journal* 37.7 (2018), e97674.

[159] Laura Capolupo et al. “Sphingolipids control dermal fibroblast heterogeneity”. In: *Science* 376.6590 (2022), eabh1623.

[160] Giovanni D’Angelo and Gioele La Manno. “The lipotype hypothesis”. In: *Nature Reviews Molecular Cell Biology* (2022), pp. 1–2.

[161] CY Lin and Stuart Smith. “Properties of the thioesterase component obtained by limited trypsinization of the fatty acid synthetase multienzyme complex.” In: *Journal of Biological Chemistry* 253.6 (1978), pp. 1954–1962.

[162] Bornali Chakravarty et al. “Human fatty acid synthase: structure and substrate selectivity of the thioesterase domain”. In: *Proceedings of the National Academy of Sciences* 101.44 (2004), pp. 15567–15572.

[163] Christophe AC Freyre et al. “MIGA2 links mitochondria, the ER, and lipid droplets and promotes de novo lipogenesis in adipocytes”. In: *Molecular cell* 76.5 (2019), pp. 811–825.

[164] Steven A Moore et al. “Astrocytes, not neurons, produce docosahexaenoic acid (22: 6ω-3) and arachidonic acid (20: 4ω-6)”. In: *Journal of neurochemistry* 56.2 (1991), pp. 518–524.

[165] Hee-Yong Kim. “Novel metabolism of docosahexaenoic acid in neural cells”. In: *Journal of Biological Chemistry* 282.26 (2007), pp. 18661–18665.

[166] Gregory J Brewer and Carl W Cotman. "Survival and growth of hippocampal neurons in defined medium at low density: advantages of a sandwich culture technique or low oxygen". In: *Brain research* 494.1 (1989), pp. 65–74.

[167] Gregory J Brewer et al. "Optimized survival of hippocampal neurons in B27-supplemented neurobasal™, a new serum-free medium combination". In: *Journal of neuroscience research* 35.5 (1993), pp. 567–576.

[168] Rolf K Berge et al. "In contrast with docosahexaenoic acid, eicosapentaenoic acid and hypolipidaemic derivatives decrease hepatic synthesis and secretion of triacylglycerol by decreased diacylglycerol acyltransferase activity and stimulation of fatty acid oxidation". In: *Biochemical Journal* 343.1 (1999), pp. 191–197.

[169] Kandice R Levental et al. "Lipidomic and biophysical homeostasis of mammalian membranes counteracts dietary lipid perturbations to maintain cellular fitness". In: *Nature communications* 11.1 (2020), pp. 1–13.

[170] Michael Sinensky. "Homeoviscous adaptation—a homeostatic process that regulates the viscosity of membrane lipids in Escherichia coli". In: *Proceedings of the National Academy of Sciences* 71.2 (1974), pp. 522–525.

[171] Robert Ernst, Christer S Ejsing, and Bruno Antonny. "Homeoviscous adaptation and the regulation of membrane lipids". In: *Journal of molecular biology* 428.24 (2016), pp. 4776–4791.

[172] Hanna L Sladitschek and Pierre A Neveu. "A gene regulatory network controls the balance between mesendoderm and ectoderm at pluripotency exit". In: *Molecular Systems Biology* 15.12 (2019), e9043.

[173] Michal Levy and Anthony H Futerman. "Mammalian ceramide synthases". In: *IUBMB life* 62.5 (2010), pp. 347–356.

[174] Krishnan Venkataraman et al. "Upstream of growth and differentiation factor 1 (uog1), a mammalian homolog of the yeast Longevity Assurance Gene 1 (LAG1), regulatesN-Stearoyl-sphinganine (C18-(Dihydro) ceramide) synthesis in a fumonisin B1-independent manner in mammalian cells". In: *Journal of Biological Chemistry* 277.38 (2002), pp. 35642–35649.

[175] Maja Gehre et al. “Lysine 4 of histone H3. 3 is required for embryonic stem cell differentiation, histone enrichment at regulatory regions and transcription accuracy”. In: *Nature genetics* 52.3 (2020), pp. 273–282.

[176] Glyn Dawson. “Measuring brain lipids”. In: *Biochimica et Biophysica Acta (BBA)-Molecular and Cell Biology of Lipids* 1851.8 (2015), pp. 1026–1039.

[177] Elsa Lauwers, Rose Goodchild, and Patrik Verstreken. “Membrane lipids in presynaptic function and disease”. In: *Neuron* 90.1 (2016), pp. 11–25.

[178] Soheil Yousefi et al. “Comprehensive multi-omics integration identifies differentially active enhancers during human brain development with clinical relevance”. In: *Genome medicine* 13.1 (2021), pp. 1–27.

[179] Zehua Wang et al. “Embracing lipidomics at single-cell resolution: Promises and pitfalls”. In: *TrAC Trends in Analytical Chemistry* (2023), p. 116973.

[180] Gele Liu et al. “Advances in pluripotent stem cells: history, mechanisms, technologies, and applications”. In: *Stem cell reviews and reports* 16 (2020), pp. 3–32.

[181] David E Rodríguez-Fuentes et al. “Mesenchymal stem cells current clinical applications: a systematic review”. In: *Archives of medical research* 52.1 (2021), pp. 93–101.

[182] Meritxell Huch and Bon-Kyoung Koo. “Modeling mouse and human development using organoid cultures”. In: *Development* 142.18 (2015), pp. 3113–3125.

[183] Giuliana Rossi, Andrea Manfrin, and Matthias P Lutolf. “Progress and potential in organoid research”. In: *Nature Reviews Genetics* 19.11 (2018), pp. 671–687.

[184] Shiladitya Banerjee, Margaret L Gardel, and Ulrich S Schwarz. “The actin cytoskeleton as an active adaptive material”. In: *Annual review of condensed matter physics* 11 (2020), pp. 421–439.

[185] Oscar M Lancaster et al. “Mitotic rounding alters cell geometry to ensure efficient bipolar spindle formation”. In: *Developmental cell* 25.3 (2013), pp. 270–283.

[186] Jakub Sedzinski et al. “Polar actomyosin contractility destabilizes the position of the cytokinetic furrow”. In: *Nature* 476.7361 (2011), pp. 462–466.

[187] Alba Diz-Muñoz et al. “Control of directed cell migration in vivo by membrane-to-cortex attachment”. In: *PLoS biology* 8.11 (2010), e1000544.

[188] Richard G Fehon, Andrea I McClatchey, and Anthony Bretscher. “Organizing the cell cortex: the role of ERM proteins”. In: *Nature reviews Molecular cell biology* 11.4 (2010), pp. 276–287.

[189] Kevin Carvalho et al. “Cell-sized liposomes reveal how actomyosin cortical tension drives shape change”. In: *Proceedings of the National Academy of Sciences* 110.41 (2013), pp. 16456–16461.

[190] Akihiro Kusumi et al. “Paradigm shift of the plasma membrane concept from the two-dimensional continuum fluid to the partitioned fluid: high-speed single-molecule tracking of membrane molecules”. In: *Annu. Rev. Biophys. Biomol. Struct.* 34 (2005), pp. 351–378.

[191] Antoine Villiers. “Sur la fermentation de la fécule par l’action du ferment butyrique”. In: *Compt. Rend. Acad. Sci* 112 (1891), pp. 536–538.

[192] Mark E Davis and Marcus E Brewster. “Cyclodextrin-based pharmaceutics: past, present and future”. In: *Nature reviews Drug discovery* 3.12 (2004), pp. 1023–1035.

[193] Nadia Morin-Crini et al. “130 years of cyclodextrin discovery for health, food, agriculture, and the industry: A review”. In: *Environmental Chemistry Letters* 19.3 (2021), pp. 2581–2617.

[194] Yoshiro Ohtani et al. “Differential effects of α-, β-and γ-cyclodextrins on human erythrocytes”. In: *European journal of biochemistry* 186.1-2 (1989), pp. 17–22.

[195] Raphael Zidovetzki and Irena Levitan. “Use of cyclodextrins to manipulate plasma membrane cholesterol content: evidence, misconceptions and control strategies”. In: *Biochimica et Biophysica Acta (BBA)-Biomembranes* 1768.6 (2007), pp. 1311–1324.

[196] Kimmo Tanhuanpää and Pentti Somerharju. “γ-Cyclodextrins greatly enhance translocation of hydrophobic fluorescent phospholipids from vesicles to cells in culture: importance of molecular hydrophobicity in phospholipid trafficking studies”. In: *Journal of Biological Chemistry* 274.50 (1999), pp. 35359–35366.

[197] Zhaofeng Li et al. “γ-Cyclodextrin: a review on enzymatic production and applications”. In: *Applied microbiology and biotechnology* 77.2 (2007), pp. 245–255.

[198] Mirkka Koivusalo et al. “Endocytic trafficking of sphingomyelin depends on its acyl chain length”. In: *Molecular biology of the cell* 18.12 (2007), pp. 5113–5123.

[199] Guangtao Li et al. “Efficient replacement of plasma membrane outer leaflet phospholipids and sphingolipids in cells with exogenous lipids”. In: *Proceedings of the National Academy of Sciences* 113.49 (2016), pp. 14025–14030.

[200] Elisabeth PC Kilsdonk et al. “Cellular cholesterol efflux mediated by cyclodextrins”. In: *Journal of Biological Chemistry* 270.29 (1995), pp. 17250–17256.

[201] AE Christian et al. “Use of cyclodextrins for manipulating cellular cholesterol content”. In: *Journal of lipid research* 38.11 (1997), pp. 2264–2272.

[202] Saleemulla Mahammad and Ingela Parmryd. “Cholesterol depletion using methyl-β-cyclodextrin”. In: *Methods in membrane lipids*. Springer, 2015, pp. 91–102.

[203] Ramaswamy Ravichandran and Soundar Divakar. “Inclusion of ring A of cholesterol inside the β-cyclodextrin cavity: evidence from oxidation reactions and structural studies”. In: *Journal of inclusion phenomena and molecular recognition in chemistry* 30.3 (1998), pp. 253–270.

[204] Alekos Tsamaloukas et al. “Interactions of cholesterol with lipid membranes and cyclodextrin characterized by calorimetry”. In: *Biophysical Journal* 89.2 (2005), pp. 1109–1119.

[205] Cesar A López, Alex H De Vries, and Siewert J Marrink. “Molecular mechanism of cyclodextrin mediated cholesterol extraction”. In: *PLoS computational biology* 7.3 (2011), e1002020.

[206] Frédérick de Meyer and Berend Smit. “Effect of cholesterol on the structure of a phospholipid bilayer”. In: *Proceedings of the National Academy of Sciences* 106.10 (2009), pp. 3654–3658.

[207] Milka Doktorova et al. “Cholesterol promotes protein binding by affecting membrane electrostatics and solvation properties”. In: *Biophysical journal* 113.9 (2017), pp. 2004–2015.

[208] Kechuan Tu, Michael L Klein, and Douglas J Tobias. “Constant-pressure molecular dynamics investigation of cholesterol effects in a dipalmitoylphosphatidylcholine bilayer”. In: *Biophysical journal* 75.5 (1998), pp. 2147–2156.

[209] John L Rubenstein, Barton A Smith, and Harden M McConnell. "Lateral diffusion in binary mixtures of cholesterol and phosphatidylcholines." In: *Proceedings of the National Academy of Sciences* 76.1 (1979), pp. 15–18.

[210] David Needham and Rashmi S Nunn. "Elastic deformation and failure of lipid bilayer membranes containing cholesterol." In: *Biophysical journal* 58.4 (1990), pp. 997–1009.

[211] Douglas J Tobias, Kechuan Tu, and Michael L Klein. "Atomic-scale molecular dynamics simulations of lipid membranes". In: *Current opinion in colloid & interface science* 2.1 (1997), pp. 15–26.

[212] Norbert Kučerka et al. "The effect of cholesterol on short-and long-chain monounsaturated lipid bilayers as determined by molecular dynamics simulations and X-ray scattering". In: *Biophysical journal* 95.6 (2008), pp. 2792–2805.

[213] JB Leathes. "Condensing effect of cholesterol on monolayers". In: *Lancet* 208 (1925), pp. 853–856.

[214] YK Levine and MHF Wilkins. "Structure of oriented lipid bilayers". In: *Nature New Biology* 230.11 (1971), pp. 69–72.

[215] NP Franks. "Structural analysis of hydrated egg lecithin and cholesterol bilayers I. X-ray diffraction". In: *Journal of molecular biology* 100.3 (1976), pp. 345–358.

[216] Michael Rappolt et al. "Structural, dynamic and mechanical properties of POPC at low cholesterol concentration studied in pressure/temperature space". In: *European Biophysics Journal* 31.8 (2003), pp. 575–585.

[217] Wei-Chin Hung et al. "The condensing effect of cholesterol in lipid bilayers". In: *Biophysical journal* 92.11 (2007), pp. 3960–3967.

[218] DL Worcester and NP Franks. "Structural analysis of hydrated egg lecithin and cholesterol bilayers II. Neutron diffraction". In: *Journal of molecular biology* 100.3 (1976), pp. 359–378.

[219] Jana Gallová et al. "Bilayer thickness in unilamellar extruded 1, 2-dimyristoleoyl and 1, 2-dierucoyl phosphatidylcholine vesicles: SANS contrast variation study of cholesterol effect". In: *Colloids and Surfaces B: Biointerfaces* 38.1-2 (2004), pp. 11–14.

[220] Jeremy Pencer et al. “Bilayer thickness and thermal response of dimyristoylphosphatidylcholine unilamellar vesicles containing cholesterol, ergosterol and lanosterol: a small-angle neutron scattering study”. In: *Biochimica et Biophysica Acta (BBA)-Biomembranes* 1720.1-2 (2005), pp. 84–91.

[221] MC Phillips. “The physical state of phospholipids and cholesterol in monolayers, bilayers, and membranes”. In: *Progress in surface and membrane science*. Vol. 5. Elsevier, 1972, pp. 139–221.

[222] Harden M McConnell and Arun Radhakrishnan. “Condensed complexes of cholesterol and phospholipids”. In: *Biochimica et Biophysica Acta (BBA)-Biomembranes* 1610.2 (2003), pp. 159–173.

[223] Juyang Huang. “Exploration of molecular interactions in cholesterol superlattices: effect of multibody interactions”. In: *Biophysical journal* 83.2 (2002), pp. 1014–1025.

[224] Michael C Pitman et al. “Molecular-level organization of saturated and polyunsaturated fatty acids in a phosphatidylcholine bilayer containing cholesterol”. In: *Biochemistry* 43.49 (2004), pp. 15318–15328.

[225] Thomas J McIntosh, Alan D Magid, and Sidney A Simon. “Cholesterol modifies the short-range repulsive interactions between phosphatidylcholine membranes”. In: *Biochemistry* 28.1 (1989), pp. 17–25.

[226] Hein Sprong, Peter van der Sluijs, and Gerrit van Meer. “How proteins move lipids and lipids move proteins”. In: *Nature Reviews Molecular Cell Biology* 2.7 (2001), pp. 504–513.

[227] Olaf S Andersen and Roger E Koeppe. “Bilayer thickness and membrane protein function: an energetic perspective”. In: *Annu. Rev. Biophys. Biomol. Struct.* 36 (2007), pp. 107–130.

[228] Mark S Bretscher and Sean Munro. “Cholesterol and the Golgi apparatus”. In: *Science* 261.5126 (1993), pp. 1280–1281.

[229] Joan M Boggs. “Lipid intermolecular hydrogen bonding: influence on structural organization and membrane function”. In: *Biochimica et Biophysica Acta (BBA)-Reviews on Biomembranes* 906.3 (1987), pp. 353–404.

[230] Cojen Ho and Christopher D Stubbs. “Hydration at the membrane protein-lipid interface”. In: *Biophysical journal* 63.4 (1992), pp. 897–902.

[231] T Parasassi et al. “Cholesterol modifies water concentration and dynamics in phospholipid bilayers: a fluorescence study using Laurdan probe”. In: *Biophysical journal* 66.3 (1994), pp. 763–768.

[232] Gora M'Baye et al. "Liquid ordered and gel phases of lipid bilayers: fluorescent probes reveal close fluidity but different hydration". In: *Biophysical journal* 95.3 (2008), pp. 1217–1225.

[233] Akira Ono and Eric O Freed. "Plasma membrane rafts play a critical role in HIV-1 assembly and release". In: *Proceedings of the National Academy of Sciences* 98.24 (2001), pp. 13925–13930.

[234] Robert A Dick and Volker M Vogt. "Membrane interaction of retroviral Gag proteins". In: *Frontiers in Microbiology* 5 (2014), p. 187.

[235] E Evans and W Rawicz. "Entropy-driven tension and bending elasticity in condensed-fluid membranes". In: *Physical review letters* 64.17 (1990), p. 2094.

[236] Jianben Song and Richard E Waugh. "Bending rigidity of SOPC membranes containing cholesterol". In: *Biophysical journal* 64.6 (1993), pp. 1967–1970.

[237] Z Chen and R Peter Rand. "The influence of cholesterol on phospholipid membrane curvature and bending elasticity". In: *Biophysical journal* 73.1 (1997), pp. 267–276.

[238] Michael F Brown et al. "Elastic deformation of membrane bilayers probed by deuterium NMR relaxation". In: *Journal of the American Chemical Society* 124.28 (2002), pp. 8471–8484.

[239] Saptarshi Chakraborty et al. "How cholesterol stiffens unsaturated lipid membranes". In: *Proceedings of the National Academy of Sciences* 117.36 (2020), pp. 21896–21905.

[240] Ole G Mouritsen. "The liquid-ordered state comes of age". In: *Biochimica et Biophysica Acta (BBA)-Biomembranes* 1798.7 (2010), pp. 1286–1288.

[241] Edward J Shimshick and Harden M McConnell. "Lateral phase separations in binary mixtures of cholesterol and phospholipids". In: *Biochemical and biophysical research communications* 53.2 (1973), pp. 446–451.

[242] MR Alecio et al. "Use of a fluorescent cholesterol derivative to measure lateral mobility of cholesterol in membranes." In: *Proceedings of the National Academy of Sciences* 79.17 (1982), pp. 5171–5174.

[243] Florence Trentacosti Presti. "The role of cholesterol in regulating membrane fluidity". In: *Membrane fluidity in biology* 4 (1985), pp. 97–145.

[244] Sriram Subramaniam and Harden M McConnell. “Critical mixing in monolayer mixtures of phospholipid and cholesterol”. In: *Journal of Physical Chemistry* 91.7 (1987), pp. 1715–1718.

[245] Harden M McConnell. “Structures and transitions in lipid monolayers at the air-water interface”. In: *Annual Review of Physical Chemistry* 42.1 (1991), pp. 171–195.

[246] John R Silvius, Denis del Giudice, and Michel Lafleur. “Cholesterol at different bilayer concentrations can promote or antagonize lateral segregation of phospholipids of differing acyl chain length”. In: *Biochemistry* 35.48 (1996), pp. 15198–15208.

[247] Jonas Korlach et al. “Characterization of lipid bilayer phases by confocal microscopy and fluorescence correlation spectroscopy”. In: *Proceedings of the National Academy of Sciences* 96.15 (1999), pp. 8461–8466.

[248] Arun Radhakrishnan and Harden M McConnell. “Cholesterol-phospholipid complexes in membranes”. In: *Journal of the American Chemical Society* 121.2 (1999), pp. 486–487.

[249] Ivan V Polozov and Klaus Gawrisch. “Characterization of the liquid-ordered state by proton MAS NMR”. In: *Biophysical journal* 90.6 (2006), pp. 2051–2061.

[250] Sean Munro. “Lipid rafts: elusive or illusive?” In: *Cell* 115.4 (2003), pp. 377–388.

[251] Andrey S Shaw. “Lipid rafts: now you see them, now you don’t”. In: *Nature immunology* 7.11 (2006), pp. 1139–1142.

[252] Ilya Levental and Sarah L Veatch. “The continuing mystery of lipid rafts”. In: *Journal of molecular biology* 428.24 (2016), pp. 4749–4764.

[253] Ilya Levental, Kandice R Levental, and Frederick A Heberle. “Lipid rafts: controversies resolved, mysteries remain”. In: *Trends in cell biology* 30.5 (2020), pp. 341–353.

[254] Santos Mañes et al. “Membrane raft microdomains mediate front–rear polarity in migrating cells”. In: *The EMBO journal* 18.22 (1999), pp. 6211–6220.

[255] Gopal Pande. “The role of membrane lipids in regulation of integrin functions”. In: *Current Opinion in Cell Biology* 12.5 (2000), pp. 569–574.

[256] P Gopalakrishna et al. "Modulation of $\alpha5\beta1$ integrin functions by the phospholipid and cholesterol contents of cell membranes". In: *Journal of cellular biochemistry* 77.4 (2000), pp. 517–528.

[257] Concepción Gómez-Moutón et al. "Segregation of leading-edge and uropod components into specific lipid rafts during T cell polarization". In: *Proceedings of the National Academy of Sciences* 98.17 (2001), pp. 9642–9647.

[258] Jaime Millán et al. "Lipid rafts mediate biosynthetic transport to the T lymphocyte uropod subdomain and are necessary for uropod integrity and function". In: *Blood, The Journal of the American Society of Hematology* 99.3 (2002), pp. 978–984.

[259] Lynda M Pierini et al. "Membrane lipid organization is critical for human neutrophil polarization". In: *Journal of Biological Chemistry* 278.12 (2003), pp. 10831–10841.

[260] Santos Mañes et al. "From rafts to crafts: membrane asymmetry in moving cells". In: *Trends in immunology* 24.6 (2003), pp. 319–325.

[261] Concepción Gómez-Moutón et al. "Dynamic redistribution of raft domains as an organizing platform for signaling during cell chemotaxis". In: *The Journal of cell biology* 164.5 (2004), pp. 759–768.

[262] Praturi Gopalakrishna, Nandini Rangaraj, and Gopal Pande. "Cholesterol alters the interaction of glycosphingolipid GM3 with $\alpha5\beta1$ integrin and increases integrin-mediated cell adhesion to fibronectin". In: *Experimental cell research* 300.1 (2004), pp. 43–53.

[263] Tanvir Kaur et al. "A correlation between membrane cholesterol level, cell adhesion and tumourigenicity of polyoma virus transformed cells". In: *Molecular and cellular biochemistry* 265.1 (2004), pp. 83–95.

[264] OG Ramprasad et al. "Changes in cholesterol levels in the plasma membrane modulate cell signaling and regulate cell adhesion and migration on fibronectin". In: *Cell motility and the cytoskeleton* 64.3 (2007), pp. 199–216.

[265] Maosong Qi et al. "Cholesterol-regulated stress fiber formation". In: *Journal of cellular biochemistry* 106.6 (2009), pp. 1031–1040.

[266] Barbara Hissa et al. "Membrane cholesterol removal changes mechanical properties of cells and induces secretion of a specific pool of lysosomes". In: *PloS one* 8.12 (2013), e82988.

[267] Barbara Hissa et al. “Cholesterol depletion impairs contractile machinery in neonatal rat cardiomyocytes”. In: *Scientific reports* 7.1 (2017), pp. 1–15.

[268] Shan Sun et al. “Cholesterol-dependent modulation of stem cell biomechanics: application to adipogenesis”. In: *Journal of biomechanical engineering* 141.8 (2019).

[269] Amit Vasanji et al. “Polarization of plasma membrane microviscosity during endothelial cell migration”. In: *Developmental cell* 6.1 (2004), pp. 29–41.

[270] T Kanayasu-Toyoda et al. “Eicosapentaenoic acid abolishes the proatherogenic effects of cholesterol: effects on migration of bovine smooth muscle and endothelial cells in vitro”. In: *Prostaglandins, leukotrienes and essential fatty acids* 48.6 (1993), pp. 463–468.

[271] Atif B Awad, Heinric Williams, and Carol S Fink. “Phytosterols reduce in vitro metastatic ability of MDA-MB-231 human breast cancer cells”. In: *Nutrition and cancer* 40.2 (2001), pp. 157–164.

[272] Prabar K Ghosh et al. “Membrane microviscosity regulates endothelial cell motility”. In: *Nature Cell Biology* 4.11 (2002), pp. 894–900.

[273] Hana Oh et al. “Membrane cholesterol is a biomechanical regulator of neutrophil adhesion”. In: *Arteriosclerosis, thrombosis, and vascular biology* 29.9 (2009), pp. 1290–1297.

[274] Leann L Norman et al. “Modification of cellular cholesterol content affects traction force, adhesion and cell spreading”. In: *Cellular and molecular bioengineering* 3.2 (2010), pp. 151–162.

[275] Silvia Corvera, Carlo DiBonaventura, and Howard S Shpetner. “Cell confluence-dependent remodeling of endothelial membranes mediated by cholesterol”. In: *Journal of Biological Chemistry* 275.40 (2000), pp. 31414–31421.

[276] Jeanne Kwik et al. “Membrane cholesterol, lateral mobility, and the phosphatidylinositol 4, 5-bisphosphate-dependent organization of cell actin”. In: *Proceedings of the National Academy of Sciences* 100.24 (2003), pp. 13964–13969.

[277] Vladislav I Chubinskiy-Nadezhdin, Yuri A Negulyaev, and Elena A Morachevskaya. “Cholesterol depletion-induced inhibition of stretch-activated channels is mediated via actin rearrangement”. In: *Biochemical and biophysical research communications* 412.1 (2011), pp. 80–85.

[278] Fitzroy J Byfield et al. "Cholesterol depletion increases membrane stiffness of aortic endothelial cells". In: *Biophysical journal* 87.5 (2004), pp. 3336–3343.

[279] Nima Khatibzadeh et al. "Effects of plasma membrane cholesterol level and cytoskeleton F-actin on cell protrusion mechanics". In: *PloS one* 8.2 (2013), e57147.

[280] Arikta Biswas et al. "Cholesterol depletion by MβCD enhances cell membrane tension and its variations-reducing integrity". In: *Biophysical journal* 116.8 (2019), pp. 1456–1468.

[281] Mingzhai Sun et al. "The effect of cellular cholesterol on membrane-cytoskeleton adhesion". In: *Journal of cell science* 120.13 (2007), pp. 2223–2231.

[282] Nima Khatibzadeh et al. "Effects of cholesterol on nano-mechanical properties of the living cell plasma membrane". In: *Soft Matter* 8.32 (2012), pp. 8350–8360.

[283] David A Eberhard et al. "Evidence that the inositol phospholipids are necessary for exocytosis. Loss of inositol phospholipids and inhibition of secretion in permeabilized cells caused by a bacterial phospholipase C and removal of ATP". In: *Biochemical Journal* 268.1 (1990), pp. 15–25.

[284] Donald W Hilgemann, Siyi Feng, and Cem Nasuhoglu. "The complex and intriguing lives of PIP2 with ion channels and transporters". In: *Science's STKE* 2001.111 (2001), re19–re19.

[285] Tor Erik Rusten and Harald Stenmark. "Analyzing phosphoinositides and their interacting proteins". In: *Nature methods* 3.4 (2006), pp. 251–258.

[286] Won Do Heo et al. "PI (3, 4, 5) P3 and PI (4, 5) P2 lipids target proteins with polybasic clusters to the plasma membrane". In: *Science* 314.5804 (2006), pp. 1458–1461.

[287] Geert Van Den Bogaart et al. "Membrane protein sequestering by ionic protein–lipid interactions". In: *Nature* 479.7374 (2011), pp. 552–555.

[288] Gerald RV Hammond et al. "PI4P and PI (4, 5) P2 are essential but independent lipid determinants of membrane identity". In: *Science* 337.6095 (2012), pp. 727–730.

[289] Hsin-Yung Yen et al. “PtdIns (4, 5) P2 stabilizes active states of GPCRs and enhances selectivity of G-protein coupling”. In: *Nature* 559.7714 (2018), pp. 423–427.

[290] Pico Caroni. “Actin cytoskeleton regulation through modulation of PI (4, 5) P2 rafts”. In: *The EMBO Journal* 20.16 (2001), pp. 4332–4336.

[291] Helen L Yin and Paul A Janmey. “Phosphoinositide regulation of the actin cytoskeleton”. In: *Annual review of physiology* 65 (2003), p. 761.

[292] O Behnke, J Tranum-Jensen, and B Van Deurs. “Filipin as a cholesterol probe. II. Filipin-cholesterol interaction in red blood cell membranes.” In: *European journal of cell biology* 35.2 (1984), pp. 200–215.

[293] Rania Leventis and John R Silvius. “Use of cyclodextrins to monitor transbilayer movement and differential lipid affinities of cholesterol”. In: *Biophysical journal* 81.4 (2001), pp. 2257–2267.

[294] M Page Haynes, Michael C Phillips, and George H Rothblat. “Efflux of cholesterol from different cellular pools”. In: *Biochemistry* 39.15 (2000), pp. 4508–4517.

[295] Theodore L Steck, Jin Ye, and Yvonne Lange. “Probing red cell membrane cholesterol movement with cyclodextrin”. In: *Biophysical journal* 83.4 (2002), pp. 2118–2125.

[296] Spencer A Freeman et al. “Transmembrane pickets connect cyto-and pericellular skeletons forming barriers to receptor engagement”. In: *Cell* 172.1-2 (2018), pp. 305–317.

[297] Sarah R Barger et al. “Membrane-cytoskeletal crosstalk mediated by myosin-I regulates adhesion turnover during phagocytosis”. In: *Nature communications* 10.1 (2019), pp. 1–18.

[298] Ewa Sitarska and Alba Diz-Muñoz. “Pay attention to membrane tension: Mechanobiology of the cell surface”. In: *Current opinion in cell biology* 66 (2020), pp. 11–18.

[299] Martin Bergert et al. “Cell surface mechanics gate embryonic stem cell differentiation”. In: *Cell Stem Cell* 28.2 (2021), pp. 209–216.

[300] Henry De Belly et al. “Membrane tension gates ERK-mediated regulation of pluripotent cell fate”. In: *Cell Stem Cell* 28.2 (2021), pp. 273–284.

[301] FM Hochmuth et al. "Deformation and flow of membrane into tethers extracted from neuronal growth cones". In: *Biophysical journal* 70.1 (1996), pp. 358–369.

[302] Martin Bergert and Alba Diz-Muñoz. "Quantification of Apparent Membrane Tension and Membrane-to-Cortex Attachment in Animal Cells Using Atomic Force Microscopy-Based Force Spectroscopy". In: *Mechanobiology*. Springer, 2023, pp. 45–62.

[303] Françoise Brochard-Wyart et al. "Hydrodynamic narrowing of tubes extruded from cells". In: *Proceedings of the National Academy of Sciences* 103.20 (2006), pp. 7660–7663.

[304] Mingming Hao, Sushmita Mukherjee, and Frederick R Maxfield. "Cholesterol depletion induces large scale domain segregation in living cell membranes". In: *Proceedings of the National Academy of Sciences* 98.23 (2001), pp. 13072–13077.

[305] Anne K Kenworthy et al. "Dynamics of putative raft-associated proteins at the cell surface". In: *The Journal of cell biology* 165.5 (2004), pp. 735–746.

[306] J Shawn Goodwin et al. "Ras diffusion is sensitive to plasma membrane viscosity". In: *Biophysical journal* 89.2 (2005), pp. 1398–1410.

[307] Marija Vrljic et al. "Cholesterol depletion suppresses the translational diffusion of class II major histocompatibility complex proteins in the plasma membrane". In: *Biophysical journal* 88.1 (2005), pp. 334–347.

[308] Priyamvada Chugh et al. "Actin cortex architecture regulates cell surface tension". In: *Nature cell biology* 19.6 (2017), pp. 689–697.

[309] EB Lomakina et al. "Rheological analysis and measurement of neutrophil indentation". In: *Biophysical journal* 87.6 (2004), pp. 4246–4258.

[310] Michael Krieg et al. "Tensile forces govern germ-layer organization in zebrafish". In: *Nature cell biology* 10.4 (2008), pp. 429–436.

[311] Sergio Lembo et al. "The distance between the plasma membrane and the actomyosin cortex acts as a nanogate to control cell surface mechanics". In: *bioRxiv* (2023), pp. 2023–01.

[312] Philip C Calder et al. "Incorporation of fatty acids by concanavalin A-stimulated lymphocytes and the effect on fatty acid composition and membrane fluidity". In: *Biochemical Journal* 300.2 (1994), pp. 509–518.

[313] PE Tiku et al. "Cold-induced expression of Δ9-desaturase in carp by transcriptional and posttranslational mechanisms". In: *Science* 271.5250 (1996), pp. 815–818.

[314] Itay Budin et al. "Viscous control of cellular respiration by membrane lipid composition". In: *Science* 362.6419 (2018), pp. 1186–1189.

[315] Yoshikazu Uto. "Recent progress in the discovery and development of stearoyl CoA desaturase inhibitors". In: *Chemistry and physics of lipids* 197 (2016), pp. 3–12.

[316] Gang Liu et al. "Discovery of potent, selective, orally bioavailable stearoyl-CoA desaturase 1 inhibitors". In: *Journal of medicinal chemistry* 50.13 (2007), pp. 3086–3100.

[317] Zhili Xin et al. "Discovery of piperidine-aryl urea-based stearoyl-CoA desaturase 1 inhibitors". In: *Bioorganic & medicinal chemistry letters* 18.15 (2008), pp. 4298–4302.

[318] Dmitry O Koltun et al. "Novel, potent, selective, and metabolically stable stearoyl-CoA desaturase (SCD) inhibitors". In: *Bioorganic & medicinal chemistry letters* 19.7 (2009), pp. 2048–2052.

[319] Shaoyi Sun et al. "Systematic evaluation of amide bioisosteres leading to the discovery of novel and potent thiazolylimidazolidinone inhibitors of SCD1 for the treatment of metabolic diseases". In: *Bioorganic & medicinal chemistry letters* 24.2 (2014), pp. 520–525.

[320] Keisuke Imamura et al. "Discovery of novel and potent stearoyl coenzyme a desaturase 1 (SCD1) inhibitors as anticancer agents". In: *Bioorganic & Medicinal Chemistry* 25.14 (2017), pp. 3768–3779.

[321] Benjamin M Vincent et al. "Inhibiting stearoyl-CoA desaturase ameliorates α-synuclein cytotoxicity". In: *Cell reports* 25.10 (2018), pp. 2742–2754.

[322] Justyna Janikiewicz et al. "Inhibition of SCD1 impairs palmitate-derived autophagy at the step of autophagosome-lysosome fusion in pancreatic β-cells". In: *Journal of lipid research* 56.10 (2015), pp. 1901–1911.

[323] Tomasz Bednarski et al. "Stearoyl-CoA desaturase 1 deficiency reduces lipid accumulation in the heart by activating lipolysis independently of peroxisome proliferator-activated receptor α". In: *Biochimica et Biophysica Acta (BBA)-Molecular and Cell Biology of Lipids* 1861.12 (2016), pp. 2029–2037.

[324] Yuanying Chen and Peng Li. "Fatty acid metabolism and cancer development". In: *Science Bulletin* 61.19 (2016), pp. 1473–1479.

[325] Mathias P Clausen et al. "Dissecting the actin cortex density and membrane-cortex distance in living cells by super-resolution microscopy". In: *Journal of physics D: Applied physics* 50.6 (2017), p. 064002.

[326] Noemi Jiménez-Rojo et al. "Optical Control of Membrane Fluidity Modulates Protein Secretion". In: *bioRxiv* (2022), pp. 2022–02.

[327] Marco Fritzsche et al. "Analysis of turnover dynamics of the submembranous actin cortex". In: *Molecular biology of the cell* 24.6 (2013), pp. 757–767.

[328] François B Robin et al. "Single-molecule analysis of cell surface dynamics in Caenorhabditis elegans embryos". In: *Nature methods* 11.6 (2014), pp. 677–682.

[329] Marco Fritzsche et al. "Actin kinetics shapes cortical network structure and mechanics". In: *Science advances* 2.4 (2016), e1501337.

[330] Viktoria Wollrab et al. "Polarity sorting drives remodeling of actin-myosin networks". In: *Journal of cell science* 132.4 (2019), jcs219717.

[331] Camelia G Muresan et al. "F-actin architecture determines constraints on myosin thick filament motion". In: *Nature communications* 13.1 (2022), p. 7008.

[332] Michael P Murrell and Margaret L Gardel. "F-actin buckling coordinates contractility and severing in a biomimetic actomyosin cortex". In: *Proceedings of the National Academy of Sciences* 109.51 (2012), pp. 20820–20825.

[333] Weina Zhao et al. "Candidate Antimetastasis Drugs Suppress the Metastatic Capacity of Breast Cancer Cells by Reducing Membrane FluidityMembrane Fluidity Controls Metastasis". In: *Cancer research* 76.7 (2016), pp. 2037–2049.

[334] Y Kashman, A Groweiss, and U Shmueli. "Latrunculin, a new 2-thiazolidinone macrolide from the marine sponge Latrunculia magnifica". In: *Tetrahedron Letters* 21.37 (1980), pp. 3629–3632.

[335] Martine Coué et al. "Inhibition of actin polymerization by latrunculin A". In: *FEBS letters* 213.2 (1987), pp. 316–318.

[336] Julio L Sampaio et al. “Membrane lipidome of an epithelial cell line”. In: *Proceedings of the National Academy of Sciences* 108.5 (2011), pp. 1903–1907.

[337] Tauno Metsalu and Jaak Vilo. “ClustVis: a web tool for visualizing clustering of multivariate data using Principal Component Analysis and heatmap”. In: *Nucleic Acids Research* 43.W1 (May 2015), W566–W570. ISSN: 0305-1048.

[338] Marta I Aveldano and Lloyd A Horrocks. “Quantitative release of fatty acids from lipids by a simple hydrolysis procedure.” In: *Journal of lipid research* 24.8 (1983), pp. 1101–1105.

[339] Luke Miller. *Analyzing gels and western blots with ImageJ*. `http://www.lukemiller.org/ImageJ_gel_analysis.pdf`. 2010.

[340] Simon Stael et al. “Detection of Damage-Activated Metacaspase Activity Activities by Western Blot in Plants”. In: *Plant Proteases and Plant Cell Death: Methods and Protocols*. Springer, 2022, pp. 127–137.

[341] Holger Franken et al. “Thermal proteome profiling for unbiased identification of direct and indirect drug targets using multiplexed quantitative mass spectrometry”. In: *Nature protocols* 10.10 (2015), pp. 1567–1593.

[342] Wolfgang Huber et al. “Variance stabilization applied to microarray data calibration and to the quantification of differential expression”. In: *Bioinformatics* 18.suppl_1 (2002), S96–S104.

[343] Aliaksandr Halavatyi and Stefan Terjung. “FRAP and other photoperturbation techniques”. In: *Standard and Super-Resolution Bioimaging Data Analysis: A Primer* (2017), pp. 99–141.

[344] Aliaksandr Halavatyi. *FRAPanalyser*. `https://github.com/ssgpers/FRAPAnalyser`. 2016.